ADVANCES IN WIND POWER

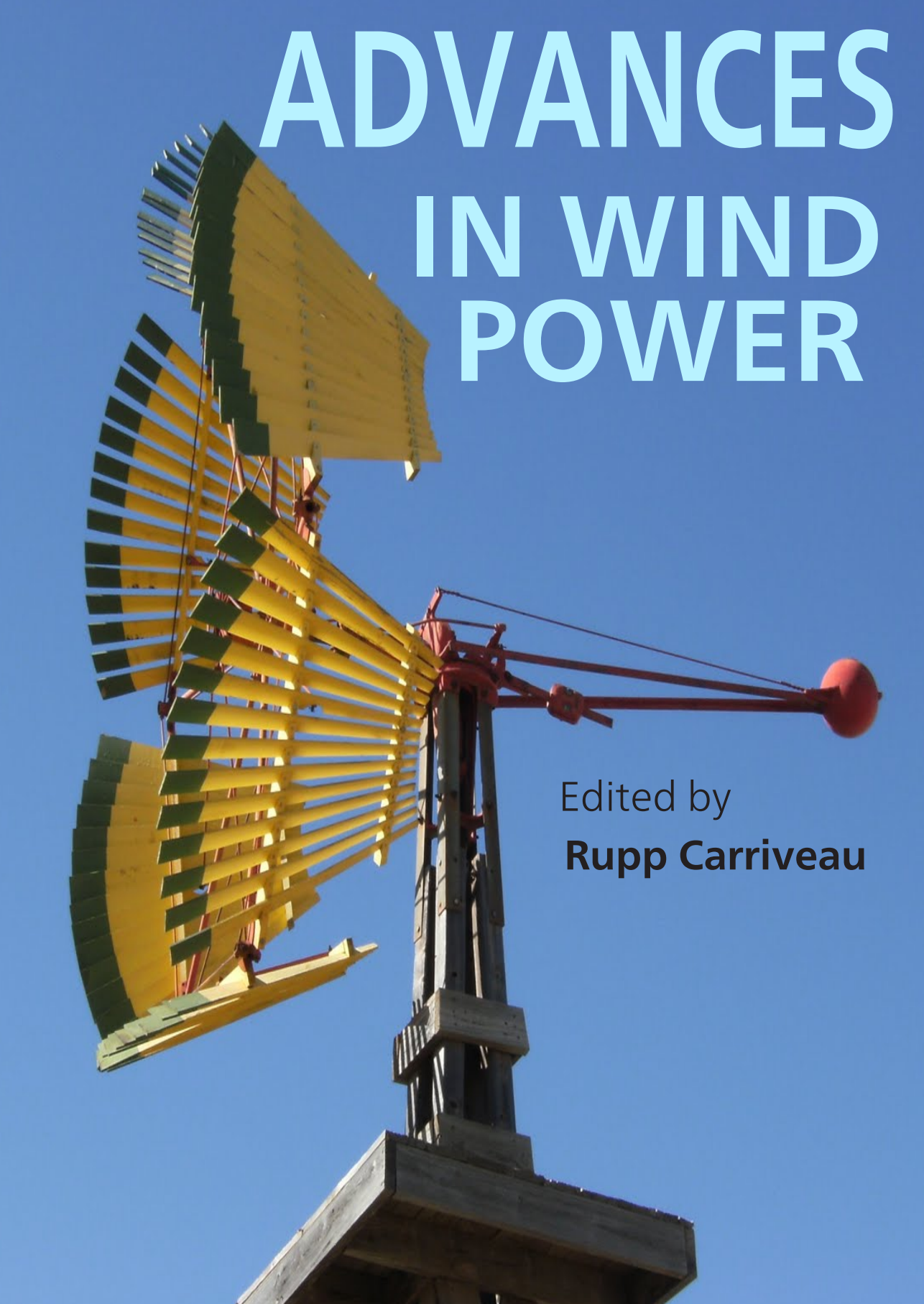

Edited by

Rupp Carriveau

ADVANCES IN WIND POWER

Edited by **Rupp Carriveau**

Advances in Wind Power
http://dx.doi.org/10.5772/3376
Edited by Rupp Carriveau

Contributors

Hengameh Kojooyan Jafari, Mostafa Abarzadeh, Hossein Madadi Kojabadi, Liuchen Chang, Daniel MATT, Emilio Gomez-Lazaro, Sergio Martín Martínez, Angel Molina-Garcia, Antonio Vigueras Rodriguez, Michael Milligan, Eduard Muljadi, Adrian Ilinca, David Wood, Ed Nowicki, Mohamed Fahmy Aner, Samer El Itani, Géza Joós, Mahmoud Huleihil, Karam Youssef Maalawi, Fernando Ponta, Alejandro Otero, Lucas Ignacio Lago, Wenping Cao, Ying Xie, Zheng Tan, Horizon Gitano, João Paulo Vieira, Rupp Carriveau, Tim Newson, Philip McKay, David S-K Ting

Published by InTech

Janeza Trdine 9, 51000 Rijeka, Croatia

Publishing Process Manager Iva Simcic
Technical Editor InTech DTP team
Cover InTech Design team

First published November, 2012
Printed in Croatia

A free online edition of this book is available at www.intechopen.com
Additional hard copies can be obtained from orders@intechopen.com

Advances in Wind Power, Edited by Rupp Carriveau
p. cm.
ISBN 978-953-51-0863-4

Contents

Preface

Today's wind energy industry is at a crossroads. Global economic instability has threatened or eliminated many financial incentives that have been important to the development of specific markets. Such economic sponsorship of energy generation is not unique to renewables; fossil based sources are also subsidized in many different countries. However, for a technology like wind energy whose markets are still developing, incentives can be critical for industry growth. Industry proponents have decreed that long-term energy policy that survives financial swings and changes in government is what is needed to provide the stability that market investors seek. While this may be the case, in the mean time, the pressure is on wind industry designers, manufacturers, and operators to seek the most effectual measures for wind power production.

Like the wind itself, the industry operates on large and small scales. While large commercial wind has traditionally received the most coverage in the literature and the media, small wind has recently established itself as a major player in distributed energy systems. This will become increasingly important as micro grids rapidly find their place in both the developed and developing worlds. In urban and isolated rural settings, small wind is growing rapidly. It is important to emphasize this multi-scale resilience that wind generation provides as an energy solution. The broad range of scales within wind energy is only surpassed by the expansive scope of technologies that cover the spectrum from resource assessment to grid integration. Specialized sub-topics continue to emerge that provide focus for improving critical links in the wind chain. This sort of specificity can be vital for isolating technical elements from the complexity of interconnected wind energy systems. A brief list of emerging specific interest fields include aerodynamic interaction of wind turbine groups, computational modeling of complex composite blades, magnetic speed multiplying converters, generator controls optimized for small wind, disturbance tolerant generators, micro and smart grid integration.

This text details topics fundamental to the efficient operation of modern commercial farms and highlights advanced research that will enable next-generation wind energy technologies. The book is organized into three sections, Inflow and Wake Influences on Turbine Performance, Turbine Structural Response, and Power Conversion, Control and Integration. In addition to fundamental concepts, the reader will be exposed to comprehensive treatments of topics like wake dynamics, analysis of complex turbine blades, and power electronics in small-scale wind turbine systems.

Dr. Rupp Carriveau
Department of Civil and Environmental Engineering,
Windsor, Canada

Section 1

Inflow and Wake Influences on Turbine Performance

Chapter 1

Wind Turbine Power: The Betz Limit and Beyond

Mahmoud Huleihil and Gedalya Mazor

Additional information is available at the end of the chapter

http://dx.doi.org/10.5772/52580

1. Introduction

With a severe energy crisis facing the modern world, the production and utilization of energy has become a vital issue, and the conservation of energy has acquired prime importance. Energy production and consumption are directly related to everyday life in much of human society, and issues of energy research are extremely important and highly sensitive. Being aware of the global warming problem, humans tend to rely more on renewable energy (RE) resources.

1.1. Benefits of wind energy

In [1], scientists and researchers have tried to accelerate solutions for wind energy generation design parameters. Researchers claim that a short time, society, industry, and politics will welcome the use of wind energy as a clean, practical, economical, and environmentally friendly alternative. In an effort to approach a more sustainable world, after the 1973 oil crisis RE sources began to appear on the agenda, and wind energy attracted significant interest. Because of extensive studies on this topic, wind energy has recently been applied in various industries, where it has begun to compete with other energy resources [1].

Among the various renewable energy types as highlighted by [2], wind provides an intermittent but environmentally friendly energy source that does not pollute atmosphere. Wind power calculations are initiated from the kinetic energy definition, and wind power is found to be proportional to half the air density multiplied by the cube of the wind velocity. When seeking to determine the potential usage of wind energy, wind power formulation is derived first by use of kinetic energy definition and then by basic physical definitions of power as the ratio of work over time, work as the force multiplied by the distance, and force as the change of momentum. [2].

1.2. Aerodynamics aspects of wind turbines

Reviews about many of the most important aerodynamic research topics in the field of wind energy are shown in the report of a different study [3] Wind turbine aerodynamics concerns the modeling and prediction of aerodynamic forces, such as performance predictions of wind farms, as well as the design of specific parts of wind turbines, such as rotor-blade geometry. The basics of blade-element momentum theory were presented along with guidelines for the construction of airfoil data. Various theories for aerodynamically optimum rotors were discussed, and recent results on classical models were presented. State-of-the-art advanced numerical simulation tools for wind turbine rotors and wakes were reviewed, including rotor predictions as well as models for simulating wind turbine wakes and flows in wind farms [3].

1.3. Wind power density

Concerning power density and its relation to wind speed, the report given in [4] presented the features of wind power distributions that were analytically obtained from wind distribution functions. Simple equations establishing a relationship between mean power density and wind speed have been obtained for a given location and wind turbine. Different concepts relating to wind power distribution functions were shown—among them the power transported by the wind and the theoretical maximum convertible power from wind, according to the Betz' law. Maximum convertible power from the wind was explained within more realistic limits, including an approximate limit to the maximum power from a wind turbine, was obtained. In addition, different equations were obtained establishing relationships between mean power density and mean wind speed. These equations are simple and useful when discarding locations for wind turbine installation [4].

1.4. Wind power applications

The range of wind power usage is scarce. One of the most important usages is electricity. Hubbard and Shepherd [5] considered wind turbine generators, ranging in size from a few kilowatts to several megawatts, for producing electricity both singly and in wind power stations that encompass hundreds of machines. According to the researchers' claims, there are many installations in uninhabited areas far from established residences, and therefore there are no apparent environmental impacts in terms of noise. The researchers do point out, however, situations in which radiated noise can be heard by residents of adjacent neighborhoods, particularly those who live in neighborhoods with low ambient noise levels [5].

Wind power is used worldwide, not only in developed countries. Specific studies [6, 7] presented a detailed study of a Manchegan windmill while considering the technological conditions of the original Manchegan windmills. In addition, a wind evaluation of the region was carried out, the power and momentum of the windmills were calculated, and the results obtained were discussed, along with a comparison with the type of

http://dx.doi.org/10.5772/52580

Southern Spanish windmill. These windmills were important for wheat milling and had been an important factor in the socio-economic development of rural Spain for centuries [6, 7].

Another example is considered in [8]. This study, conducted with reference to land in Syria, evaluated both wind energy potential and the electricity that could be generated by the wind. An appropriate computer program was especially prepared and designed to perform the required calculations, using the available meteorological data provided by the Syrian Atlas. The program is capable of processing the wind data for any specific area that is in accordance with the needed requirements in fields of researches and applications. Calculations in the study show that a significant energy potential is available for direct exploitation. The study also shows that approximately twice the current electricity consumption in Syria can be generated by wind resources [8].

The potential usage of wind power at Kudat and Labuan for small-scale energy demand was given in [9]. According to their statement, the acquisition of detailed knowledge about wind characteristics at a site is a crucial step in planning and estimating performance for a wind energy project. From this study, the researchers concluded that sites at Kudat and Labuan that they had considered during the study years were unsuitable for large-scale wind energy generation. However, they did confirm that small-scale wind energy could be generated at a turbine height of 100 meters [9]. In light of their findings, James and others [10] reported that the potential impact of the UK's latest policy instrument, the 2010 micro-generation tariffs, is considered applicable to both micro-wind and photovoltaics.As the researchers observed, building-mounted micro-wind turbines and photovoltaics have the potential to provide widely applicable carbon-free electricity generation at the building level. Because photovoltaic systems are well understood it is easy to predict performance using software tools or widely accepted yield estimates. Micro-wind research, however, is far more complex, and in comparison, it is poorly understood [10].

Abdeen [11] addresses another example of wind power usage. As the researcher observed, the imminent exhaustion of fossil energy resources and the increasing demand for energy were the motives for Sudanese authorities to put into practice an energy policy based on rational use of energy. The authorities also based their conclusions on exploitation of new and renewable energy sources. It was pointed out that after 1980, as the supply of conventional energy has not been able to follow the tremendous increase in production demand in rural areas of Sudan; a renewed interest for the application of wind energy has been shown in many places. Therefore, the Sudanese government began to pay more attention to wind energy utilization in rural areas. Because the wind energy resource in many rural areas is sufficient for attractive application of wind pumps, although as fuel it is insufficient, the wind pumps will be spread on a rather large scale in the near future. Wind is a form of renewable energy that is always in a non-steady state due to the wide temporal and spatial variations of wind velocity. Results suggested that wind power would be more profitably used for local and small-scale applications, especially for remote rural areas. The study finds that Sudan has abundant wind energy [11]. Another recent study [12] considered the wind power

in Iran. According to the study's claims, climate change, global warming, and the recent worldwide economic crisis have emphasized the need for low carbon emissions while also ensuring economic feasibility. In their paper, the researchers investigated the status and wind power potential of the city of Shahrbabak in Kerman province in Iran. The technical and economic feasibility of wind turbine installation was presented, and the potential of wind power generation was statistically analyzed [12].

1.5. Types of wind turbines

There are different types of wind turbines: bare wind turbines, augmented wind turbines, horizontal axis wind turbines, and vertical axis wind turbines, just to mention a few.

1.5.1. Bare wind turbines

According to research findings as given by [13], the derivation of the efficiency of an ideal wind turbine is attributed to the three prominent scientists associated with the three principal aerodynamic research schools in Europe during the first decades of the previous century: Lanchester, Betz, and Joukowsky. According to this study, detailed reading of their classical papers had shown that Lanchester did not accept that the velocity through the disc is the average of the velocities far upstream and far downstream, by which his solution is not determined. Betz and Joukowsky used vortex theory to support Froude's result and derived the ideal efficiency of a wind turbine at the same time. This efficiency has been known as the Joukowsky limit in Russia and as the Betz limit everywhere else. As the researchers suggested, because of the contribution of both scientists, this result should be called the Betz-Joukowsky limit everywhere [13]. The maximal achievable efficiency of a wind turbine is found to be given by the Betz number $B = 16/27$. Derivation of the classical Betz limit could be followed as given by [14] and [15].

The question of the maximum wind kinetic energy that can be utilized by a wind turbine, which is of fundamental importance for employment of wind energy, was reconsidered in [16]. According to their study, the researchers observed that in previous studies, an answer to this question was obtained only for the case of an infinite number of turbine-rotor blades, in the framework of application of the one-dimensional theory of an ideal loaded disk without loss for friction and turbulence taken into account. This implies that for an ideal wind turbine, the maximum energy that can be extracted from the wind kinetic energy, or the power coefficient, does not exceed the Betz limit. Based on the exact calculation of the Goldstein function, the researchers determined the maximum power coefficient of an ideal wind turbine having a finite number of blades. As was expected, the maximum turned out to be always lower than the absolute Lanchester-Betz-Joukowski limit. According to their findings, with an increase in the number of blades, the power coefficient rises approaching the estimate of Glauert for a rotor with an infinite number of blades, only if by taking wake flow twisting into account [16].

In a different proposal, Cuerva and Sanz-Andre´s presented an extended formulation of the power coefficient of a wind turbine [17]. Their formulation was a generalization of the Betz-

Lanchester expression for the power coefficient as a function of the axial deceleration of the wind speed provoked by the wind turbine in operation. The extended power coefficient took into account the benefits of the power produced and the cost associated to the production of this energy. By means of the proposed simple model, the researchers evidenced that the purely energetic optimum operation condition giving rise to the Betz-Lanchester limit (maximum energy produced) does not coincide with the global optimum operational condition (maximum benefit generated) if cost of energy and degradation of the wind turbine during operation is considered. The new extended power coefficient, according to the researchers claim, is a general parameter useful to define global optimum operation conditions for wind turbines, considering not only the energy production but also the maintenance cost and the economic cost associated to the life reduction of the machine [17].

1.5.2. Augmented wind turbines

It was suggested in [18] that one could extract more power from the wind by directing the wind by a diffuser that could be incorporated into the system. The benefit of such a device is to decrease the size of the system and thus decrease its cost [18].

According to [19], the performance of a diffuser-augmented wind turbine has been established by matching the forces acting on the blade element to overall momentum and energy balances. Good agreement with experimental data was obtained [19]. Based on computational fluid dynamics (CFD), an actuator disc CFD model of the flow through a wind turbine in a diffuser was developed and validated [20, 21]. Their research presumed a flow increase could be induced by a diffuser. They showed that from a one-dimensional analysis the Betz limit could be exceeded by a factor that is proportional to the relative increase in mass flow through the rotor. This result was verified by theoretical one-dimensional analysis by the CFD model [20, 21]. Supporting the same idea, [22] Sharpe stated that it is theoretically possible to exceed the Lanchester-Betz limit. His study presented a general momentum theory for an energy-extracting actuator disc that modeled a rotor with blades having radially uniform circulation. The study included the effects of wake rotation. Although the study reports that the general momentum theory is well known, the fall in pressure that is caused by the rotation of the wake that the theory predicts, is not usually recognized. Accounting for the wake rotational pressure drop changes some of the established conclusions of the momentum theory that appear in the literature. The conclusion from the study is that the theory establishes no loss of efficiency associated with the rotating wake [22]. Experimental and numerical investigations for flow fields of a small wind turbine with a flanged diffuser were carried out in [23].

The considered wind-turbine system gave a power coefficient higher than the Betz limit, which they attributed to the effect of the flanged diffuser. The experimental and numerical results gave useful information about the flow mechanism behind a wind turbine with a flanged diffuser. In particular, a considerable difference was seen in the destruction process of the tip vortex between the bare wind turbine and the wind turbine with a flanged diffuser [23]. According to the findings given in [24], suitable techniques to convert a country's wind availability (mostly in the low-speed regimes) as a renewable energy source must be scruti-

nized in order to achieve effective and efficient conversion. In this study, the researchers described efforts to step up the potential power augmentation offered by the Diffuser Augmented Wind Turbine (DAWT). Modification of the internal profile of the diffuser occurred by replacing the interior profile of the diffuser with an optimized airfoil shape as the interior profile of the diffuser. Additional velocity augmentation of approximately 66% could be achieved with the optimized profile when compared to a diffuser with an original flat interior [24]. As was pointed out in [25, 26], although there is an increase in maximum performance of a DAWT that is proportional to the mass flow of air, with application of simple momentum theory, the amount of energy extracted per unit of volume with a DAWT is the same as for an ordinary bare wind turbine [25, 26].

1.6. Modeling controversy

Debate is ongoing around the issue of DAWT. In a recent study, a general momentum theory to study the behavior of the classical free vortex wake model of Joukowsky was used [27]. This model, as the researchers reported, has attained considerable attention as it shows the possibility of achieving a power performance that greatly exceeds the Lanchester-Betz limit for rotors running at low tip speed ratios. This behavior was confirmed even when including the effect of a center vortex, which, without any simplifying assumptions, allowed azimuthal velocities and the associated radial pressure gradient to be taken into account in the axial momentum balance. In addition, a refined model that remedies the problem of using the axial momentum theorem was proposed. Using this model the power coefficient never exceeds the Lanchester-Betz limit, but rather tends to zero at a zero tip speed ratio [27]. As asserted in [28], for reasons of energy and momentum conservation a conventional diffuser system, as it is commonly used in water turbines cannot augment the power of a wind turbine beyond the Betz limit. However, if the propeller of the turbine is embedded into an external flow of air from which by means of its static structure energy can be transferred to the internal flow through the propeller, the propeller can supersede the Betz limit with respect to this internal flow [28]. Features of such practical methods toward achieving such improvements in wind power are discussed in [29].

1.7. Blades design

According to the report given by [30], the main problem of a wind turbine generator design project is the design of blades capable of satisfying, with optimum performance, the specific energy requirement of an electric system [30]. Simulations are very important to facilitate engineering and design of wind turbines for many reasons, especially those that concentrate upon reducing cost and saving human time. With regard to the designing the rotor blades, a CFD model for the evaluation of energy performance and aerodynamic forces acting on a straight-bladed vertical-axis Darrieus wind turbine was presented [31]. A modified blade element momentum theory for the counter-rotating wind turbine was developed [32]. This enabled the investigation of the effects of design parameters such as the combinations of the pitch angles, rotating speeds, and radii of the rotors on the aerodynamic performance of the counter-rotating wind turbine [32].

1.8. Wind farms

Vermeer and others surveyed wind farms. The focus of this study was on standalone turbines and wind farm effects. The survey group suggested that when assembling many wind turbines together, several issues should be considered [33]. Other research studies discussed the issue of optimizing the placement of wind turbines in wind farms [34]. Factors considered included multidirectional winds and variable wind speeds, the effect of ambient turbulence in the wake recovery, the effect of ground, variable hub height of the wind turbines, and different terrains [34]. A review of the state of the art and present status of active aeroelastic rotor control research for wind turbines was presented in [35]. A wind farm controller was reported in [36]. That controller distributes power references among wind turbines while it reduces their structural loads.

In this study the effect of losses are considered and discussed for bare wind turbines and for shrouded wind turbines.

2. One-dimensional fluid dynamics models

In this section, one-dimensional fluid dynamics models are analyzed and formulated based on the extended Bernoulli equation [37], accounting for losses that are assumed to be proportional to the square of the velocity of the air crossing the rotor blades of the wind turbine. The performance characteristics of the wind turbine are given by the power and thrust coefficients. The efficiency of the wind turbine is addressed and its relation to the power coefficient is discussed.

While developing a model to describe the performance of a wind turbine, common assumptions regarding the fluid flow are as follows [18]:

1. The entire field is one-dimensional.
2. The fluid considered is not compressible.
3. The flow field in the proximity of the turbine is a pure axial flow.

Other assumptions are given for the specific models.

2.1. Bare wind turbine

Consider a wind turbine that intercepts the flow of air moving with velocity V_0. The different quantities involved in the physics of the moving air are the pressure, p, the velocity, V, the cross section area, A (at different locations along the stream lines), and the thrust on the blades of wind turbine, T. The upstream condition is identified with a subscript of zero, the downstream condition is identified with a subscript of 3, and the turbine locations are identified by subscripts of 1, 2, and t (see Figure 1).

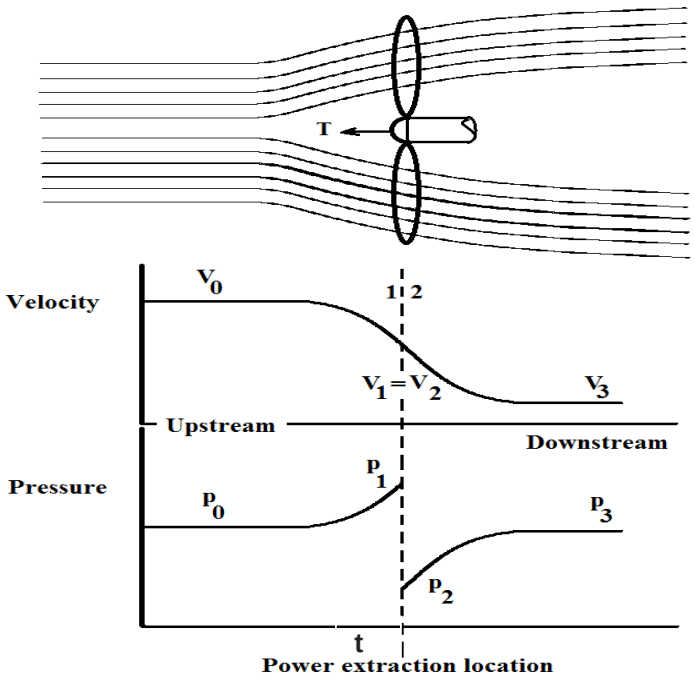

Figure 1. Schematics of the bare wind turbine. In the upper part, airstream lines are shown crossing the turbine's rotor. The velocity of the air at the rotor is the same based on the mass flow rate: V_1=V_2=V_t.The pressure drop is determined by Δp=p_1-p_2.

The steady state mass flow rate is given by:

$$\dot{m} = \rho VA = const. \tag{1}$$

The modified Bernoulli equation (with reference to the turbine head), which describes the energy balance through the wind turbine, is written between the entrance and exit sections, and is given by:

$$\frac{p_0}{\gamma} + \frac{1}{2}\frac{V_0^2}{g} = \frac{p_0}{\gamma} + \frac{1}{2}\frac{V_3^2}{g} + h_t + h_{loss} \tag{2}$$

In this equation h_t is the head of the turbine (related to the amount of power extraction), h_{loss} represents the head losses, and γ is the specific weight. The loss term in the energy equation

http://dx.doi.org/10.5772/52580

accounts for friction (mechanical and fluid) and is assumed proportional to the kinetic energy of the rotor blades, expressed as follows:

$$h_{loss} = C_{loss} \frac{V_t^2}{2g} \tag{3}$$

Equations (2) and (3) are rearranged and the head of the turbine is given by:

$$h_t = \frac{1}{2}\frac{V_0^{\,2}}{g} - \frac{1}{2}\frac{V_3^{\,2}}{g} - C_{loss}\frac{V_t^2}{2g} \tag{4}$$

The power output from the turbine, P, is given by:

$$P = \gamma V_t A_t h_t = \frac{1}{2}\rho V_0^3 A_t \frac{V_t}{V_0}\left(1 - \left(\frac{V_3}{V_0}\right)^2 - C_{loss}\left(\frac{V_t}{V_0}\right)^2\right) \tag{5}$$

From equation (5) we can determine the power coefficient, $C_{P,}$ by:

$$C_P = \frac{P}{\frac{1}{2}\rho V_0^3 A_t} = \frac{V_t}{V_0}\left(1 - \left(\frac{V_3}{V_0}\right)^2 - C_{loss}\left(\frac{V_t}{V_0}\right)^2\right) \tag{6}$$

The developed thrust, T, on the turbine blades is given by the linear moment equation (see [15] for more details), as follows:

$$T = \rho V_t A_t (V_0 - V_3) \tag{7}$$

The thrust coefficient, $C_{T,}$ based on equation (7), is given by:

$$C_T = \frac{T}{\frac{1}{2}\rho V_0^2 A_t} = 2\frac{V_t}{V_0}\left(1 - \frac{V_3}{V_0}\right) \tag{8}$$

Equations (5) and (7) are governed by the following relationship:

$$P = TV_t \tag{9}$$

By observation, the velocity of air decreases toward the downstream. Therefore, we can simplify calculations by introducing the parameter, a, to express the velocity at the cross section of the turbine, and the upstream velocity can be determined by:

$$V_t = (1-a)V_0 \qquad 0 < a < 1 \tag{10}$$

Equating equations (5) and (9) gives the velocity of the air, V_3, at the downstream, and after some algebraic manipulation, it could be shown to be given by:

$$V_3 = \left(1 - a - \sqrt{\left(a^2 - C^*_{loss}\left(1-a\right)^2\right)}\right)V_0 \tag{11}$$

The normalized loss coefficient is defined by:

$$C^*_{loss} = C_{loss}V_0^2 \tag{12}$$

Equations (11) and (12) are useful to calculate the power coefficient (equation (6)) and the thrust coefficient (equation (8)). For the case where the losses are negligible, the known results in the literature are reproduced and given by the following equations:

The downstream velocity is given by:

$$V_3 = 1 - 2a \tag{13}$$

The power coefficient is given by:

$$C_P = 4a\left(1-a\right)^2 \tag{14}$$

The thrust coefficient is given by:

$$C_T = 4a\left(1-a\right) \tag{15}$$

Inversing the relation given in equation (15), the parameter, a, is given as a function of C_T by:

$$a = \frac{1-\sqrt{1-C_T}}{2} \tag{16}$$

Finally, the power coefficient as a function of the thrust coefficient is given by:

$$C_P = \frac{C_T + C_T\sqrt{1-C_t}}{2} \tag{17}$$

2.2. Augmented wind turbine

In order to exploit wind power as economically as possible, it was suggested that the wind turbine should be enclosed inside a specifically designed shroud [38, 39]. Several models were reported in the literature to analyze wind turbine rotors surrounded by a device (shroud), which was usually a diffuser [18, 25, and 26]. Others suggested different approaches [28].

In this section, the extended Bernoulli equation and mass and momentum balance equations are used to analyze the augmented wind turbine. The power coefficient and the thrust coefficients are derived, accounting for losses in the same manner as was done for the bare turbine case. The efficiency of the wind turbine could be defined as the ratio of the net power output to the energy input to the system. The efficiency based on this definition agrees with the Betz limit.

The schematics of the shrouded wind turbine are shown in Figure 2.

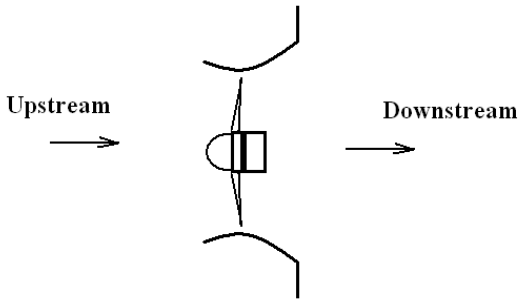

Figure 2. Schematics of the shrouded wind turbine. There is a vertical element at the exit of the wind turbine. This element contributes to reducing the power at the downstream side of the turbine, an effect that extracts more air through the wind turbine. (Idea reproduced similar to the description given by Ohya [40].)

This type of design has been recently reported [40], and it was shown that the power coefficient is about 2-5 times greater when compared to the performance of the bare wind turbine. The vertical part at the exit of the shroud reduces the pressure and therefore, the wind turbine draws more mass.

The balance equations are followed in the same manner as for the bare wind turbine. The modified Bernoulli equation differs by the pressure at the exit and is given by:

$$\frac{p_0}{\gamma}+\frac{1}{2}\frac{V_0^{\,2}}{g}=\frac{p_3}{\gamma}+\frac{1}{2}\frac{V_3^{\,2}}{g}+h_t+h_{loss} \tag{18}$$

The pressure drop between inlet and outlet (p_0-p_3) is rewritten as proportional (with C_F proportionality coefficient) to the difference in kinetic energies and it is given by:

$$\Delta p=p_0-p_3=\frac{1}{2}\rho\left(V_0^2-V_3^2\right)C_F \tag{19}$$

The power coefficient for the shrouded wind turbine is given by:

$$C_P=\frac{P}{\frac{1}{2}\rho V_0^3 A_t}=\frac{V_t}{V_0}\left(\left(C_F+1\right)\left(1-\left(\frac{V_3}{V_0}\right)^2\right)-C_{loss}\left(\frac{V_t}{V_0}\right)^2\right) \tag{20}$$

The thrust coefficient is given by:

$$C_T=\frac{T}{\frac{1}{2}\rho V_0^2 A_t}=2\left(C_F+1\right)\frac{V_t}{V_0}\left(1-\frac{V_3}{V_0}\right) \tag{21}$$

Manipulating equations (9)-(12) makes it possible to produce sample plots to consider in the next section.

2.3. Wind turbine efficiency

Usually, efficiency is defined as the ratio between two terms: the amount of net work, w, to the input, $q_{in,}$ energy to the device. Efficiency can be alternatively defined as the ratio between the derived power, $P_{out,}$ and the rate of energy flowing to the system, P_{in}. Based on these definitions, the efficiency of power generating machine is given by:

$$\eta=\frac{w_{net}}{q_{in}}=\frac{P_{out}}{P_{in}} \tag{22}$$

As was observed by Betz, the maximal achievable efficiency of the bare wind turbine is given by the Betz number B = 16/27. In section 2.1, the power coefficient of the bare turbine was considered under the assumption of frictional losses. In this case, the power coefficient can also be identified as the efficiency of the wind turbine in this case. However, the power coefficient for the shrouded wind turbine as considered in section 2.2 is not efficiency. Based on

the definition of efficiency, one could observe that if we divide the power coefficient by the factor (CF + 1) (taking into account the increased mass flow to the system due to pressure drop), a similar expression of the shrouded wind turbine could be given by equation (6). Thus, according to the modeling assumptions and with special care in treatment of the loss coefficient, one could conclude that the efficiency of the wind turbine could not exceed the Betz limit, although the power coefficient in general could exceed the Betz limit, as was observed previously by others.

2.4. Maximum windmill efficiency in finite time

In a different approach, a model to estimate the efficiency of a wind turbine was introduced [41] and the efficiency at maximum power output $\eta_{mp}$was derived. Although the power developed in a wind turbine derives from kinetic energy rather than from heat, it was possible to view the basic model of the wind turbine in a schematic way, which is similar to the heat engine picture. After the wind turbine accepts energy input in its upstream side, it extracts power at the turbine blades and ejects energy at the downstream. Details of this approach are given elsewhere [41].

The derived value for the efficiency at maximum power operation was shown to be a function of the Betz number, B, and is given by the following formula:

$$\eta_{mp} = 1 - \sqrt{1 - B} \tag{23}$$

This value is 36.2%, which agrees well with those for actually operating wind turbines.

With an algebraic manipulation this expression could be approximated by:

$$\eta_{mp} = \frac{B}{2 - \frac{B}{2}} \tag{24}$$

The expression given in equation (24) differs by only a small percentage when compared to equation (23). With the aid of equation (24), one could estimate the efficiency as 8/23.

As compared to the efficiency of heat engines, the system efficiency could be defined as the mean value between the maximum efficiency (Carnot efficiency) and the efficiency at maximum power point (Curzon-Ahlborn efficiency). Thus, the efficiency of the wind turbine system η_{ts}could be given by:

$$\eta_{ts} = \frac{\left(B + 1 - \sqrt{1 - B}\right)}{2} \tag{25}$$

If equation (23) is used while neglecting the contribution of the Number $B/2$ compared to 2, the turbine efficiency given by equation (24) would be approximated by:

$$\eta_{ts} = \frac{3}{4}B \tag{26}$$

2.5. Wind turbine efficiency and the golden section

The golden section has been considered in different disciplines as a measure of beauty [42-49]. The schematics of the golden section are given in Figure 3.

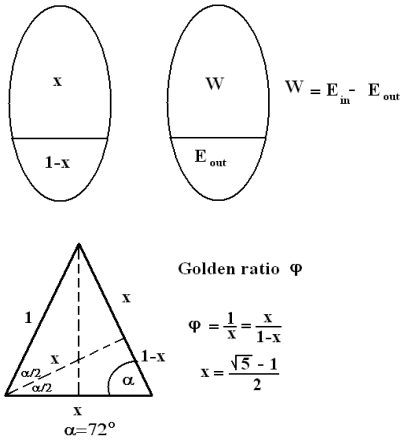

Figure 3. Schematics of the golden ratio. In the upper part to the left, the oval shape is divided into two parts, *x* and 1-*x*. in the upper part to the right, the same oval is divided into two parts with the following engine parameters: *W* represents the net work output; E_{out} represents the energy left the machine. E_{in} represents the energy that was put into the machine. In the lower part, a construction of the golden section is depicted by the isosceles triangle with a base angle of 72°. Comparing the different parts, *x* is defined as W/E_{in} or E_{out}/E_{in}, depending upon parts that have been produced and rejected.

In the upper part of the figure, the oval shape is divided into two parts, x and 1-x (as can be seen in the left side of the figure). In the right side, the same oval shape depicts the relation to quantities considered in engine machines. In the lower part of Figure 3, a golden section construction is depicted using the isosceles triangle with sides of unity and base triangle of 72°. If we apply the result of the golden section ratio (the golden section ratio is related to the sine of the angle of 18º, thus $2\sin(18) = \frac{\sqrt{5}-1}{2}$) to wind power efficiency, which is usually defined as the work gained divided by the energy input to the system, we can observe that the Betz limit agrees very well to the golden section (0.593 compared to 0.618). We can also

see that the practical efficiencies of wind turbines in the proximity of 40% are comparable with the smaller part of the golden section 38.2%.

The golden section beauty can be related to wind turbines if we recall that the kinetic energy of the wind usually splits into two parts: useful and rejected. According to the Betz limit, about 60% of the energy is used to produce electric power and the rest is rejected. On the other hand, the real wind turbines extract about 40% and the rest is wasted. These findings are in match with the golden section division (61.8% and 38.2%). One could conclude by asking: Is this just a fortuitous result or is there something more deep and inherent in the beauty of nature?

2.6. Factors that affect the efficiency of the wind turbine

In terms of wind turbine efficiency, it is possible to highlight different parts of the turbine when estimating its value. Most of the studies discussed above considered extracting power from the kinetic energy of the wind. This could be defined as kinetic energy efficiency η_{KE}. Other considerations should be accounted for, such as the mechanical efficiency, η_{me} (when power is decreased due to mechanical friction), the conversion to electricity efficiency, η_{con}, and the blockage efficiency, η_{bl} (which is defined as the amount of air blocked by the turbine blades as depicted by Figure 4). The overall turbine efficiency is given by:

$$\eta_{net} = \eta_{bl}\eta_{con}\eta_{me}\eta_{KE} \tag{27}$$

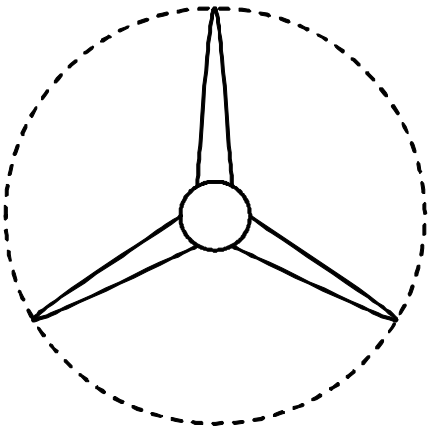

Figure 4. Schematic of the cross section of the rotor blades. The cross section illustrates the fact that the physical body of the rotor blades blocks some of the air particles, reducing potential power production from the air. The blocking efficiency can be defined as $\eta_{bl} = 1 - \frac{A_{rotor}}{A_{cross}}$. In this equation, A_{rotor} is the projected cross section of the rotor blades and A_{cross} is the cross section without the rotor blades.

3. Numerical considerations

In this section sample, plots of the results are considered.

3.1. The ideal bare wind turbine model

The one-dimensional bare wind turbine model without losses has been treated extensively and is well documented in textbooks [15]. The velocity of the air crossing the wind turbine velocity is assumed to be a fraction of the upstream air velocity. This fraction is introduced as a parameter, a, which expresses the ratio between the latter and the former. Parameter a is assigned a value in the range of numbers between zero and one. It is important to note that the physical range of this parameter is limited, for example, $0<a<0.5$, otherwise the velocity at the downstream becomes negative. To help clarify this point, calculations were performed covering the full range of parameter a. Equations (6) and (8) give the power coefficient and the thrust coefficient, respectively. Figure 5 shows these coefficients as functions of parameter a (a very well-known result in the professional literature in the field).

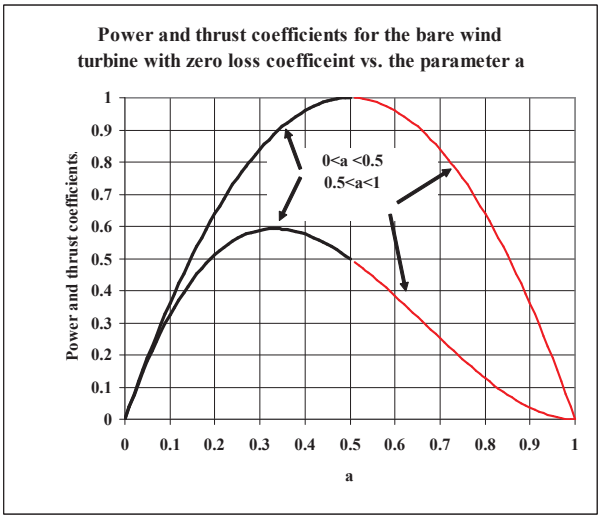

Figure 5. Power and thrust coefficients for the ideal bare wind turbine as a function of the parameter a (the ratio between the air velocity crossing the turbine blades and the upstream velocity of the air). The plot is reproduced similar to what is known in the literature, but highlighting the physical region ($0<a<0.5$) with thicker black color and the non-physical region ($0.5<a<1$) with thinner red color.

For explicit presentation, the physical range of parameter a (up to the value of 1/2) was drawn in a thick black color, while the rest of the plot was prepared using a thinner red col-

http://dx.doi.org/10.5772/52580

or. It is clear from the figure that the coefficients vanish at the zero and one values of the parameter. In between, the maximum thrust coefficient (with a value of unity) occurs at the value of a=1/2. On the other hand, the maximum value of the power coefficient occurs at the value of a=1/3, for which the Betz limit is given ($C_P = B = 16/27$). If we plot the power coefficient as a function of the thrust coefficient, as Figure 6 shows, a loop shape would be produced. Again, the physical range was highlighted using a thick black color.

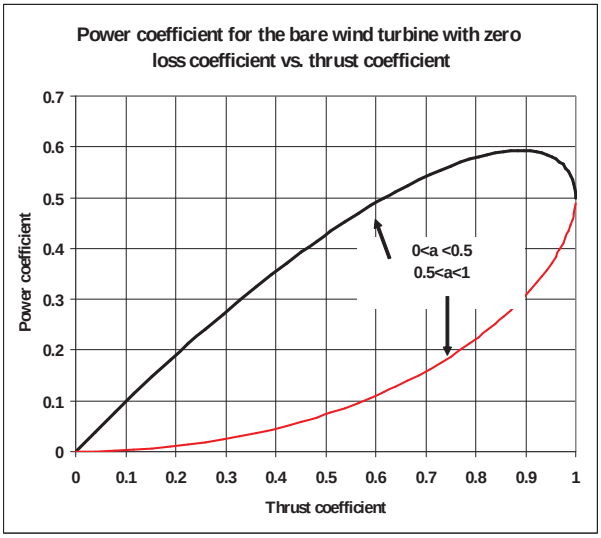

Figure 6. Power coefficient for the ideal bare wind turbine as a function of the thrust coefficient. The plot has been extended to include the non-physical region as was done in Figure 5 for reasons of consistency.

Two important points must be noted on such a plot: the maximum power coefficient (the Betz limit) for which the thrust coefficient receives a value of 8/9; and the maximum thrust (with the value of unity), for which the power coefficient gets a value of 1/2. These relations can be checked using equation (9), or more explicitly by using equation (17).

3.2. The bare wind turbine with losses

In this section, sample plots are given to demonstrate the effect of the losses as modeled in section 2.2. The losses are due to friction and are modeled as proportional to the velocity of the square of the velocity of the air flowing through the wind turbine. The plots are prepared for three different values of the non-dimensional loss coefficient C^*_{loss}: 0, 0.05, and 0.1. Figure 7 shows a plot of the power coefficient and of the thrust coefficient as a function of parameter a, covering the physical range while accounting for losses.

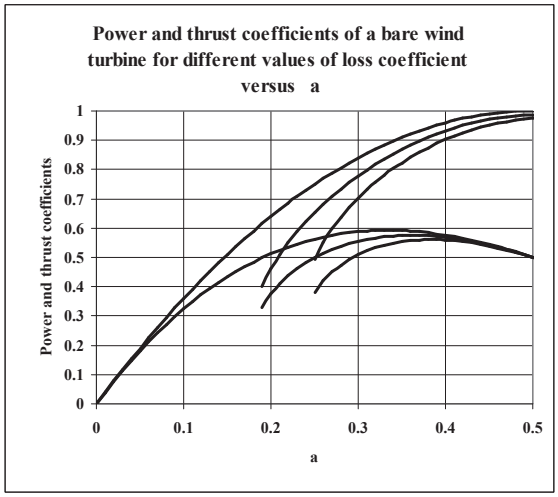

Figure 7. Power and thrust coefficients for the bare wind turbine as a function of parameter *a*, accounting for frictional losses, with different values.

It is clear from the figure that there is degradation in both coefficients in the order of a few percentage points. The two points (maximum power coefficient and maximum thrust coefficient) can be better visualized as illustrated by Figure 8.

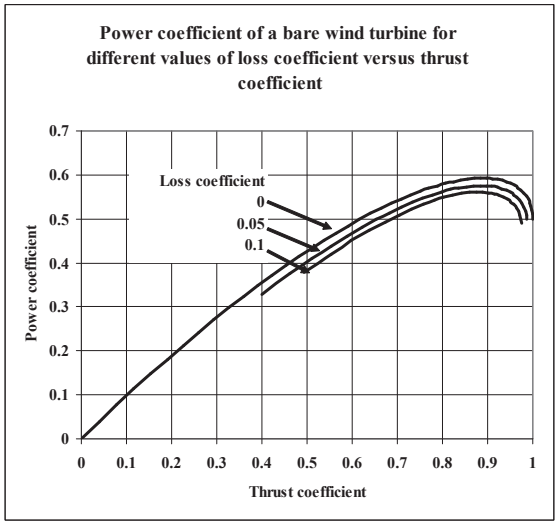

Figure 8. Power coefficient for the bare wind turbine as a function of the thrust coefficient, accounting for frictional losses, with different values.

http://dx.doi.org/10.5772/52580

3.3. The shrouded wind turbine

The shrouded wind turbine was analyzed based on the extended Bernoulli equation, while accounting for frictional losses in the same manner as was done for the bare wind turbine. The increased air mass flow due to the larger drop in pressure was modeled as proportional to the kinetic energy difference, using the coefficient C_F (pressure drop coefficient—see equation (17)). As can be seen from Figure 9 and Figure 10 (equations (18) and (19) respectively), the power coefficient and the thrust coefficient are increased proportionally to the pressure coefficient, which is in agreement with the findings in the literature.

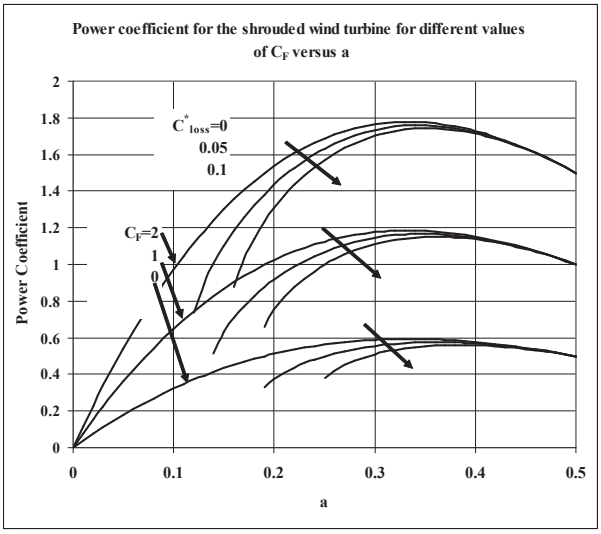

Figure 9. Power coefficient for the shrouded wind turbine as a function of parameter *a*, accounting for frictional losses and for augmentation coefficient C_F.

The maximum power coefficient and the maximum thrust points are illustrated in Figure 11.

By consulting Figure 11, one can observe that both maximum points are degraded by an increasing loss coefficient.

3.4. Efficiency of the wind turbine

As was considered by Betz, the power coefficient as originally defined agrees with the definition of efficiency for a device that extracts work from a given amount of energy. Thus, for the bare wind turbine, the maximum efficiency that could be extracted is actually given by the Betz limit. The effect of friction on wind turbine efficiency, as was expressed through the power coefficient, decreases with friction. A similar observation could be stated for the shrouded wind turbine if we use the definition as given by equation (22). Accordingly, the Betz limit is exceeded, that is, the shrouded wind turbine produces more power, but the

amount of energy extracted per unit of volume with a shroud is the same as for an ordinary bare wind turbine. These results were found to be in agreement with results observed in [Van Bussel, 2007]. The efficiency of maximum power output that was observed by the finite time analysis was approximately 36%, which is comparable to experimental findings [14]. When compared to heat engines, the efficiency of the wind turbine could be expressed in terms of the Betz number by using equation (23). If the Betz number is substituted, the efficiency could be approximated as 47%, but if the other factors are taken into account, the practical efficiency could reach much lower values.

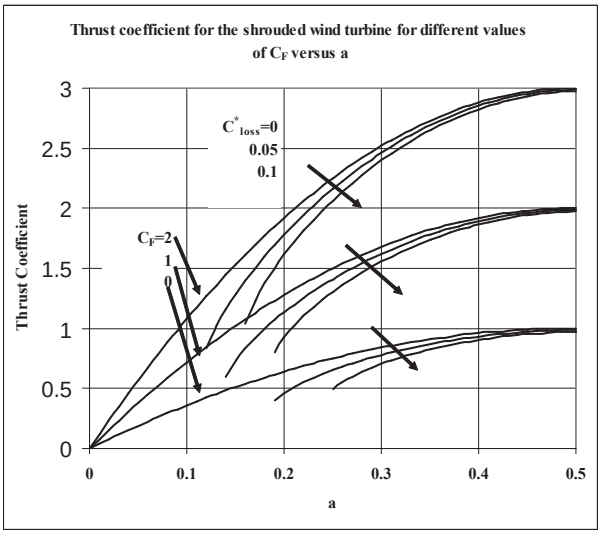

Figure 10. Thrust coefficient for the shrouded wind turbine as a function of parameter *a,* accounting for frictional losses and for augmentation coefficient C_F with different values.

4. Wind turbine arrangements

One could suggest ideas to increase power extraction from the wind, thus decreasing the overall cost. One suggestion is the bottoming wind turbine; another is the *flower leaves* arrangement of wind turbines. Both are discussed in the following sections.

4.1. Bottoming wind turbines

According to Betz, the maximal power extraction efficiency is 16/27. If it is possible to extract energy from the downstream expelled air, assuming the same limit exists, one could estimate an extra amount of 11/27*16/27 which is approximately 24%. This estimate suggests adding a smaller bottoming rotor behind the main larger rotor. The idea of the bottoming wind turbine is depicted schematically in Figure 12.

http://dx.doi.org/10.5772/52580

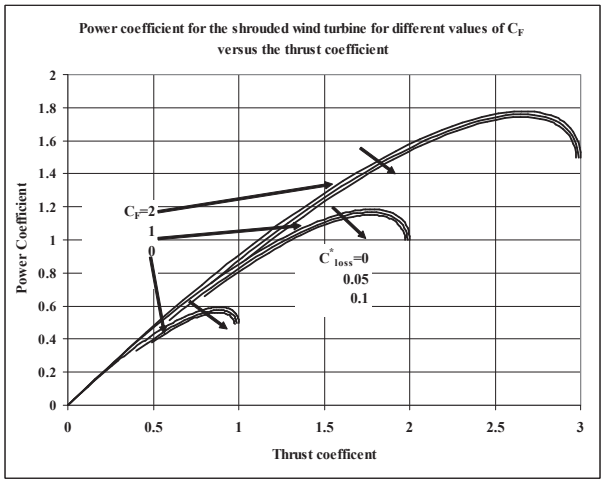

Figure 11. Power and coefficients for the shrouded wind turbine as a function of the thrust coefficient, accounting for frictional losses and for augmentation coefficient C_F, with different values.

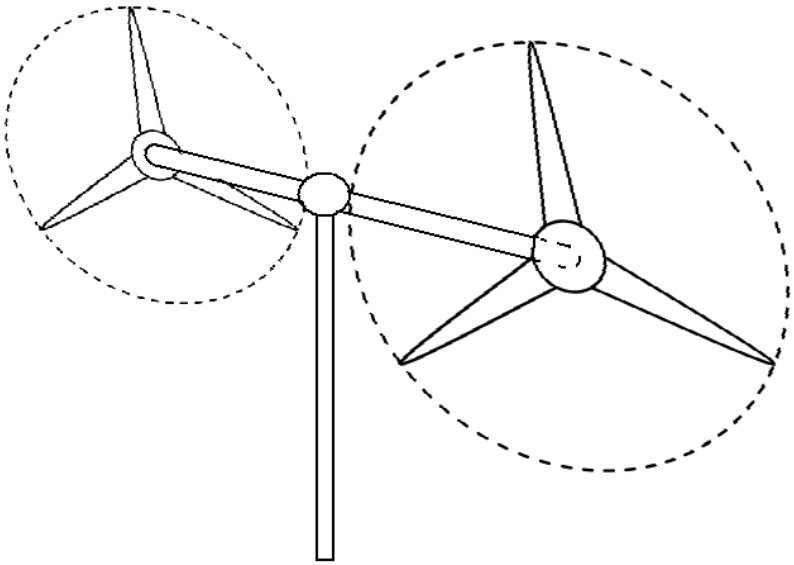

Figure 12. Schematics of the bottoming wind turbine idea. The main rotor is the first to intercept the airflow. Outlet air is then directed to the secondary rotor. The attractiveness of this idea is to gain more output with the same tower installation, reducing the inherently larger cost of erecting multiple towers.

4.2. Flower leaves arrangement of wind turbines

Considering the shrouded wind turbine as being a relatively small device is given (sometimes called flower power while searching the web), one could suggest installing different devices on the same tower. Such an arrangement reduces the cost of the installation. The idea is depicted schematically in Figure 13.

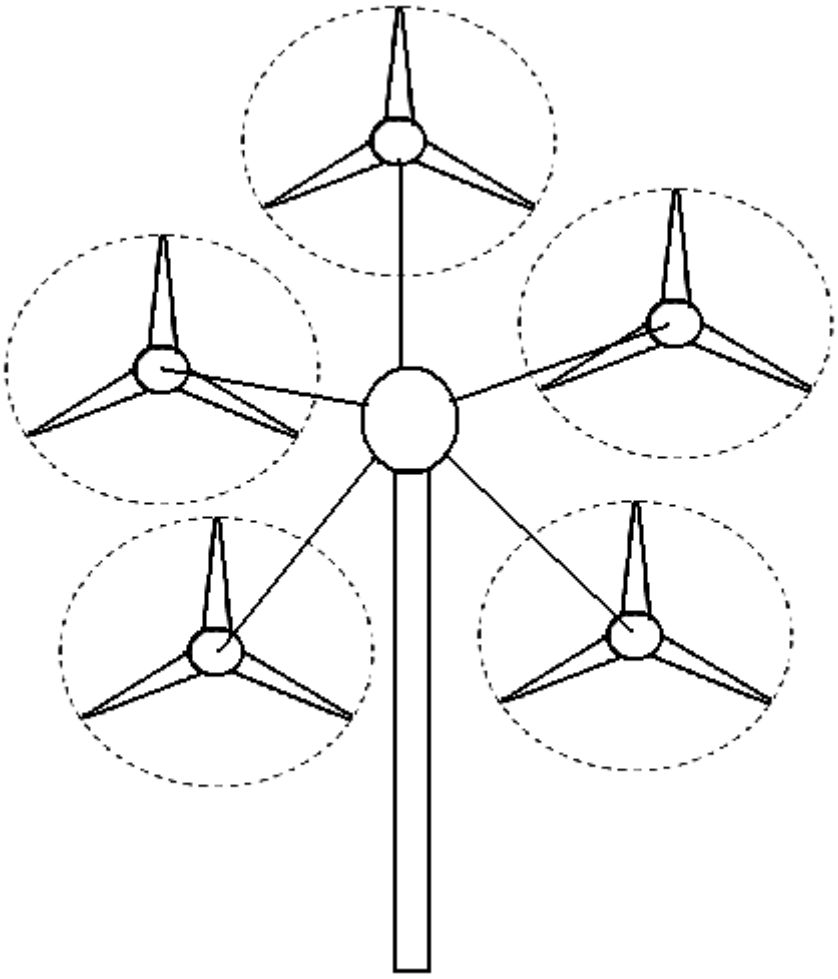

Figure 13. Schematics of *flower leaves* arrangement of wind turbines. Because they are small devices, it should be possible to install more of these shrouded systems on a single tower. While the concept of reducing installation costs is

similar to that of the bottoming wind turbine, the attractiveness of the flower leaves configuration is that many smaller turbines can be accommodated on a single tower, with significant cost reductions.

5. Summary and conclusions

In this study, wind turbine power was reconsidered. At the beginning, a literature review was given with relation to the potentiality of wind power, worldwide applications of wind power, and different factors that affect the performance of wind turbines, especially those related to one-dimensional modeling of the flow through the wind turbine. Later, different models were addressed, taking into account the effect of friction, which is usually neglected in the literature. In this study, friction is modeled to be proportional to the square of the velocity of the air crossing the wind turbine blades. The bare wind turbine model and the shrouded wind turbine model were analyzed based on the following balance equations: the mass balance equation, the momentum balance equation, and the energy balance equation that is exposed in the form of an extended (modified) Bernoulli equation. Through the analysis it was observed that both the power coefficient and the thrust coefficient degrade with friction. As was noticed in previous studies, the power coefficient given by the Betz number is the efficiency of the wind turbine (originally derived for the bare wind turbine). Following the same type of definition, a similar expression for the shrouded wind turbine could be derived. In a different approach, the wind turbine could be analyzed using finite time methods, as was given by [14]. In this study, the results were briefly summarized.

The well-known golden ratio usually is considered as a measure of beauty. It is interesting to notice that the Betz number differs from the golden ratio by only 4% (0.618 compared to 16/27=0.593).

In an effort to explain the discrepancy between theoretical efficiency and practical or measured efficiencies, different factors that affect the extraction of wind power are considered. These include mechanical friction, conversion efficiency to electricity, and blockage efficiency, which accounts for the blocked amount of air (usually is not mentioned in the literature), thus reducing the power output.

Finally, plots were given to suggest ways of assembling wind turbines to gain more of wind power for each tower installation.

Author details

Mahmoud Huleihil[1,2] and Gedalya Mazor[1]

1 Department of Mechanical Engineering, Sami Shamoon College of Engineering, Be'er Sheva, Israel

2 Arab Academic Institute for Education, Beit Berl College, Kfar Sava, Israel

References

[1] Sahin A. D., "Progress and recent trends in wind energy," Progress in Energy and Combustion Science 30, pp. 501–543, 2004.

[2] Şen Z., "Modified wind power formulation and its comparison with Betz limits," Int. J. Energy Res., pp. unknown, 2012, http://onlinelibrary.wiley.com/doi/10.1002/er.2900/full, last visited on 22/6/2012.

[3] Sorensen J. N., "Aerodynamic aspects of wind energy conversion," Annu. Rev. Fluid Mech. 43, pp. 427–48, 2011.

[4] Villanueva D., Feijoo A., "Wind power distributions: A review of their applications," Renewable and Sustainable Energy Reviews 14, pp. 1490–1495, 2010.

[5] Hubbard H. H., and Shepherd K. P., "Wind turbine acoustics," NASA technical paper 3057, DOE/NASA/2030-77, pp. 1-54, 1990.

[6] Rojas-Sola J. I., Juan Manuel A., "Southern Spanish windmills: Technological aspects," Renewable Energy, 30, 1943–1953, 2005.

[7] Rojas-Sola J. I., Gonzalez M., Martın E. P.," Computer-aided design and engineering: A study of windmills in la Mancha (Spain)," Renewable Energy, 31, 10, pp. 1471-1656, 2006.

[8] Al-Mohamad A., Karmeh H., "Wind energy potential in Syria," Renewable Energy 28, pp. 1039–1046, 2003.

[9] Islam M.R., Saidur R., Rahim N.A., "Assessment of wind energy potentiality at Kudat and Labuan, Malaysia using Weibull distribution function," Energy 36, pp. 985-992, 2011.

[10] James P. A. B., Sissons M.F., Bradford J., Myers L. E., Bahaj A.S., Anwar A., Green S., "Implications of the UK field trial of building mounted horizontal axis micro-wind turbines," Energy Policy, 38, pp. 6130–6144, 2010.

[11] Abdeen M. O., "On the wind energy resources of Sudan," Renewable and Sustainable Energy Reviews, 12, pp. 2117–2139, 2008.

[12] Mostafaeipour A., Sedaghat A., Dehghan A.A. N., Kalantar V., "Wind energy feasibility study for city of Shahrbabak in Iran," Renewable and Sustainable Energy Reviews 15, pp. 2545– 2556, 2011.

[13] Okulov V. L., Sørensen J. N., "An Ideal Wind Turbine with a Finite Number of Blades", Doklady Physics, Vol. 53, No. 6, pp. 337–342. 2008.

[14] Rauh A., Seelert W., "The Betz optimum efficiency for windmills," Applied Energy, 17 pp. 15-23, 1984.

[15] Shames, I. H. Shames, Mechanics of Fluids, 2nd ed., pp. A26 –A31,McGraw-Hill, New York, 1982.

[16] Okulov V. L., Sørensen J. N., "An Ideal Wind Turbine with a Finite Number of Blades," Doklady Physics, Vol. 53, No. 6, pp. 337–342. 2008.

[17] Cuerva A., Sanz-Andre´s A., "The extended Betz-Lanchester limit," Renewable Energy 30, pp. 783–794, 2005.

[18] Igra, O., "Research and development for shrouded wind turbines," Energy Conv. & Mgmt., 21 pp. 13-48, 1981.

[19] Fletcher C. A. J., "Diffuser-augmented wind turbine analysis," 7th Australasian hydraulics and fluid mechanics conference, Brisbane, 18-22 August 1980, pp. 435-438, 1980.

[20] Philips D. G., Richards P. J. Mallinson G. D. and Flay R. G. J., "Computational modeling of diffuser for a diffuser augmented wind turbine," 13thAustralAsian fluid mechanics conference, Monash university, Melbourne Australia, 13-18 December 1998, pp. 207-210, 1998.

[21] Hansen M. O. L., Sørensen N. N., Flay R. G. J., "Effect of Placing a Diffuser around a Wind Turbine," Wind Energy, 3, pp. 207–213, 2000.

[22] Sharpe D. J., "A general momentum theory applied to an energy-extracting actuator disc," Wind Energy, 7, pp. 177–188, 2004.

[23] Abe K., Nishida M., Sakurai A., Ohya Y., Kihara H., Wada E., Sato K., " Experimental and numerical investigations of flow fields behind a small wind turbine with a flanged diffuser," J. Wind Eng. Ind. Aerodyn. 93, pp. 951–970, 2005.

[24] Nasutiona A., Purwantoa D. W., "Optimized Curvature Interior Profile for Diffuser Augmented Wind Turbine (DAWT) to increase its energy-conversion performance," 2011 IEEE First Conference on Clean Energy and Technology CET, pp. unknown, 2011.

[25] Van Bussel, G.J.W, "An Assessment of the Performance of Diffuser Augmented Wind Turbines (DAWT's)," 3rd ASME/JSME Fluid Engineering Conference FEDSM99-7830, San Francisco, USA, 1999.

[26] Van Bussel, G. J. W., "The science of making more torque from wind: Diffuser experiments and theory revisited," J. Phys.: Conf. Ser. 75 012010, pp. 1-12, 2007.

[27] Sørensen J. N., Van Kuik G. A. M., "General momentum theory for wind turbines at low tip speed ratios," Wind Energy, 14, pp. 821–839, 2011.

[28] Bet F., Grassmann H., "Upgrading conventional wind turbines," Renewable Energy 28, pp. 71–78, 2003.

[29] Grassmann H., Bet F., Ceschia M., Ganis M.L., "On the physics of partially static turbines," Renewable Energy, 29, pp. 491–499, 2003.

[30] Vitale A.J., Rossi A.P., "Software tool for horizontal-axis wind turbine simulation," International Journal of Hydrogen Energy 33, pp. 3460-3465, 2008.

[31] Castelli M. R., Englaro A., Benini E., "The Darrieus wind turbine: Proposal for a new performance prediction model based on CFD," Energy 36, pp. 4919-4934, 2011.

[32] Seungmin L., Hogeon K., Eunkuk S., Soogab L., "Effects of design parameters on aerodynamic performance of a counter-rotating wind turbine," Renewable Energy 42, pp. 140-144, 2012.

[33] Vermeer L.J., Sorensen J.N., Crespo A., "Wind turbine wake aerodynamics," Progress in Aerospace Sciences 39, 467–510, 2003.

[34] Carlos M. Ituarte-Villarreal, Espiritu J. F., "Optimization of wind turbine placement using a viral based optimization algorithm," Procedia Computer Science 6, pp. 469–474, 2011.

[35] Barlas T.K., van Kuik G.A.M., "Review of state of the art in smart rotor control research for wind turbines," Progress in Aerospace Sciences 46, pp. 1–27, 2010.

[36] Maryam Soleimanzadeh, Rafael Wisniewski, "Controller design for a wind farm, considering both power and load aspects," Mechatronics 21, pp. 720–727, 2011.

[37] Sabersky, R. H., Acosta, A. J., Hauptmann, E. G., Fluid flow, 2nd ed., 1971, Macmillan Publishing Co, Inc., Printed in the USA.

[38] Igra O., "Compact shrouds for wind turbines," Energy conversion, 16, pp. 149-157, 1977.

[39] Igra O., "The shrouded aerogenerator," Energy, 2, pp. 429-439, 1977.

[40] Ohya Y., Karasudani, T., "A shrouded wind turbine generating high output power with wind-lens technology," Energies, 3, pp. 634-649, 2010.

[41] Huleihil M., "Maximum windmill efficiency in finite time," J. Appl.Phys., 105, Issue 10, pp. 104908,1-4, 2009.

[42] BEJAN, A., "The golden ratio predicted: Vision, cognition and locomotion as a single design in nature," Int. J. of Design & Nature and Ecodynamics. Vol. 4, No. 2, 97–104, 2009.

[43] Markowsky G., "Book – review: the golden ratio," Notices of the AMS, vol. 52, 3, pp. 344-347, 2005.

[44] Kaplan A., Tortumlu N. and Hizarci S., "A Simple Construction of the Golden Ratio," World Applied Sciences Journal 7 (7): 833-833, 2009.

[45] Shechtman, "Crystals of golden proportions," The Nobel prize in chemistry, the royal Sweedish academy of sciences, 2011.

[46] Xu, L., Zhong, T., "Golden Ratio in Quantum Mechanics," Nonlinear Science Letters B: Chaos, Fractal and Synchronization, pp. 24, 2011.

[47] Nikolic, S. T., Cosic I., Pecujlija, M., Miletic A., "The effect of the 'golden ratio' on consumer behavior", African Journal of Business Management Vol. 5 (20), pp. 8347-8360, 2011.

[48] Seebregts, A., J., "Gas-Fired power," ©IEA ETSAP - Technology Brief E02, pp. 1-5, April 2010.

[49] Michel Spira, "On the golden ratio," 12th International Congress on Mathematical Education Program Name XX-YY-zz (pp. abcde-fghij) 8 July – 15 July, 2012, COEX, Seoul, Korea.

Chapter 2

Effect of Turbulence on Fixed-Speed Wind Generators

Hengameh Kojooyan Jafari

Additional information is available at the end of the chapter

http://dx.doi.org/10.5772/51407

1. Introduction

The influence of wind energy connection to the grid has increased greatly and turbulence or unreliable characteristics of wind energy are expected to produce frequency and voltage changes in power systems and protection system equipment. To prevent these changes, it is necessary to study the working point change due to turbulence. In other papers, the voltage and transient stability analysis have been studied during and after turbulence [2] and the impact of WTGs (wind turbine generators) on the system frequency, inertia response of different wind turbine technologies, and comparison between inertia response of single-fed and doubly-fed induction generators have been examined. Moreover study of the frequency change alone was conducted using Dig-SILENT simulator for FSWTs (fast-speed wind turbines) with one-mass shaft model [2].

In this chapter both frequency and grid voltage sag change are presented with MATLAB analytically and also by SIMULINK simulation in FSWTs with one- and two-mass shaft turbine models to compare both results and a new simulation of induction machine without limiter and switch blocks is presented as a new work. The first part of study is frequency change effect on wind station by SIMULINK that shows opposite direction of torque change in comparison with previous studies with Dig-SILENT. The second part of study is effect of frequency and voltage sag change on wind station torque due to turbulence in new simulation of induction generator that is new idea.

2. Wind turbine model

The equation of wind turbine power is

$$P = \frac{1}{2}\rho A C_p \upsilon_w{}^3 \tag{1}$$

whereρ is air density, $A$is area of turbine, $C_p$is power coefficient and $\upsilon_w$is wind speed.

The C_p curve and equation are shown in Fig. 1 and given by equation (2) and (3)

$$C_p = c_1\left(c_2\frac{1}{\left(\frac{1}{\lambda + c_8\theta_{pitch}} - \frac{c_9}{1+\theta^3{}_{pitch}}\right)} - c_3\theta_{pitch} - c_4\theta^5{}_{pitch} - c_6\right)e^{-c_7\left(\frac{1}{\lambda+c_8\theta_{pitch}} - \frac{c_9}{1+\theta^3{}_{pitch}}\right)} \tag{2}$$

$$C_p = 0.44\left(125\left(\frac{1}{\lambda}+0.002\right) - 6.94\right)\cdot e^{-16.5\left(\frac{1}{\lambda}+0.002\right)} \tag{3}$$

whereθ_{pitch} is blade pitch angle, $\lambda$is the tip speed ratio described by equation (4). The parameters are given in Table 1.

$$\lambda = \frac{\omega_M R}{v_w} \tag{4}$$

where R is blade radius.

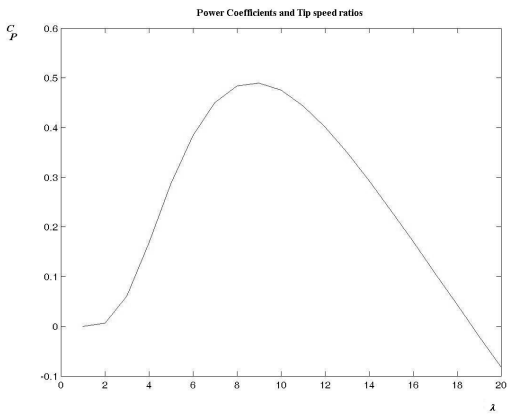

Figure 1. Curve of C_p for different tip speed ratios λ .

http://dx.doi.org/10.5772/51407

The curve of Fig.1 has positive slope before $C_{p\ \max}$ and it has negative slope after $C_{p\ \max}$.

3. One-Mass Shaft Wind Station Model

Induction machine equation is

$$T_e - T_m = J\frac{d\omega_m}{dt} + C\omega_m \tag{5}$$

Where, $T_m$is the mechanical torque, $T_e$is the generator torque, $C$is the system drag coefficient and J is the total inertia.

Table 1 shows the parameters of the one-mass shaft turbine model and induction generator.

Generator	Wind Turbine
R_s = .011Ω	c_1=.44
L_s = .000054H	c_2 = 125
L_m = .00287H	c_3 = 0
L'_r = .000089H	c_4 = 0
R'_r = .0042 [Ω]	c_5 = 0.1
J_m =.5 to 20.26 [kgm^2]	c_6 = 6.94
p(#*pole pairs*) = 2	c_7 = 16.5
P_n = 2e6 [w]	c_6 = 0.1
	c_9 = -.002
	R = 35 [m]
	$A = \pi R^2$ [m^2]
	ρ =1.2041 [kg/m^3]
	v_w = 6, 10, 13 [m/s]
	θ_{pitch} = 0 [°]

Table 1. Parameters of one- mass shaft turbine model and generator.

4. Two-Mass Shaft Induction Machine Model

This model is used to investigate the effect of the drive train or two-mass shaft, i.e., the masses of the machine and the shaft, according to the equation (8) [3], [4]. In this equation,J_t is wind wheel inertia, $J_G$is gear box inertia and generator's rotor inertia connected through

the elastic turbine shaft with a κ as an angular stiffness coefficient and C as an angular damping coefficient.

The angular shaft speed ω_t can be obtained from equations (6) and (7) [1], [3], [4].

$T_G$is the torque of the machine, $T_t$is the turbine torque, $\delta_t$is the angular turbine shaft angle, $\delta_G$is the angular generator shaft angle, $\nu$is the inverse of the gear box ratio and $J_G$andJ_t are the inertia of the machine shaft and turbine shaft, respectively.

The Parameters, defined above, are given in Table 2.

This model is described as equation (8).

$$T_G = J_G \frac{d\omega_G}{dt} - \frac{\kappa}{\nu}(\delta_t - \delta_{GB}) - \frac{C}{\nu}(\omega_t - \omega_{GB}) \tag{6}$$

$$T_t = J_t \frac{d\omega_t}{dt} + \kappa(\delta_t - \delta_{GB}) + C(\omega_t - \omega_{GB}) \tag{7}$$

$$\begin{pmatrix} \dot{\omega}_G \\ \dot{\omega}_t \\ \omega_G \\ \omega_t \end{pmatrix} = \begin{pmatrix} \frac{-\nu^2.C}{J_G} & \frac{-\nu.C}{J_G} & \frac{-\nu^2.\kappa}{J_G} & \frac{\nu\kappa}{J_G} \\ \frac{\nu.C}{J_t} & \frac{-C}{J_t} & \frac{-\nu\kappa}{J_t} & \frac{-\kappa}{J_t} \\ 1 & 0 & 0 & 0 \\ 0 & 1 & 0 & 0 \end{pmatrix} \begin{pmatrix} \omega_G \\ \omega_t \\ \delta_G \\ \delta_t \end{pmatrix} + \begin{pmatrix} \frac{1}{J_G} & 0 \\ 0 & \frac{1}{J_t} \\ 0 & 0 \\ 0 & 0 \end{pmatrix} \begin{pmatrix} T_G \\ T_t \end{pmatrix} \tag{8}$$

υ	1/80
J_G **[kg.m²]**	.5
J_t **[kg.m²]**	1
C **[Nm/rad²]**	1e6
κ **[Nm/rad]**	6e7

Table 2. Parameters of two-mass shaft model.

5. Induction Machine and Kloss Theory

In a single-fed induction machine, the torque angular speed curve of equation (12) [1] is nonlinear, but by using the Kloss equation (13), equations (9), (10), and (11), this curve is linearly modified [1], [2] as shown in Fig. 2. Therefore, the effect of frequency changes in wind power stations can be derived precisely by equation (12) and approximately using equation (13), as shown in Figs. 2–6.

http://dx.doi.org/10.5772/51407

$$G = \pm \sqrt{\frac{\left(\frac{f_s}{f_b}\right)^{-2} R_s{}^2 + X_{ss}{}^2}{\left(X_m{}^2 - X_{ss}X'_{rr}\right)^2 \left(\frac{f_s}{f_b}\right)^2 + R_s{}^2 X'_{rr}{}^2}} \tag{9}$$

$$s_k = R'_r G \tag{10}$$

$$T_k = \frac{\frac{f_s}{f_b} X^2{}_m G V_s{}^2}{\left(R_s + G\left(\frac{f_s}{f_b}\right)^2 \left(X_m{}^2 - X_{ss}X'_{rr}\right)\right)^2 + \left(\frac{f_s}{f_b}\right)^2 \left(X_{ss} + GR_s X'_{rr}\right)^2} \tag{11}$$

$$T_e = \frac{\frac{f_s}{f_b} X_m{}^2 R'_r s V_s{}^2}{\left(R_s + G\left(\frac{f_s}{f_b}\right)^2 \left(X_m{}^2 - X_{ss}X'_{rr}\right)\right)^2 + \left(\frac{f_s}{f_b}\right)^2 \left(X_{ss} + GR_s X'_{rr}\right)^2} \tag{12}$$

$$T_e = 2T_k \frac{s}{s_k};\ \text{s<<sk} \tag{13}$$

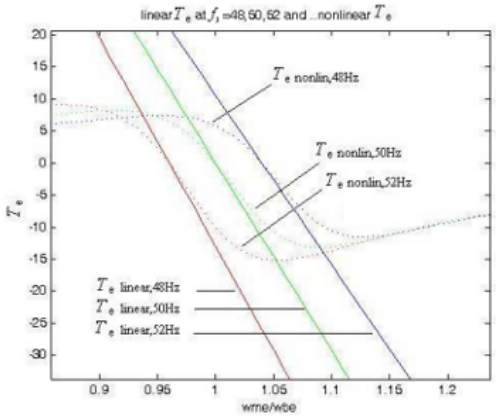

Figure 2. Electrical torque (nonlinear and linear) versus speed (slip).

Equations (11) and (12) are given in per unit, but the associated resistances are in ohms.

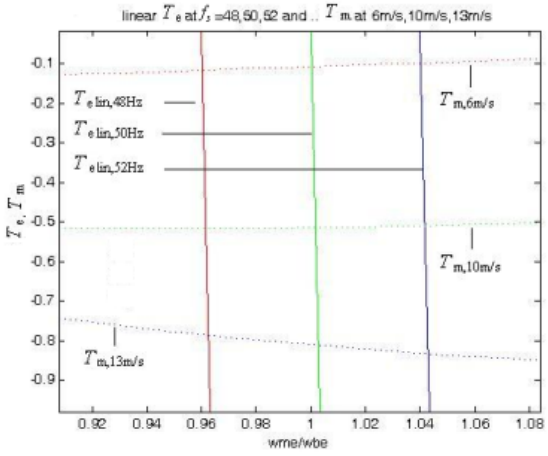

Figure 3. Mechanical and linear electrical torque versus slip.

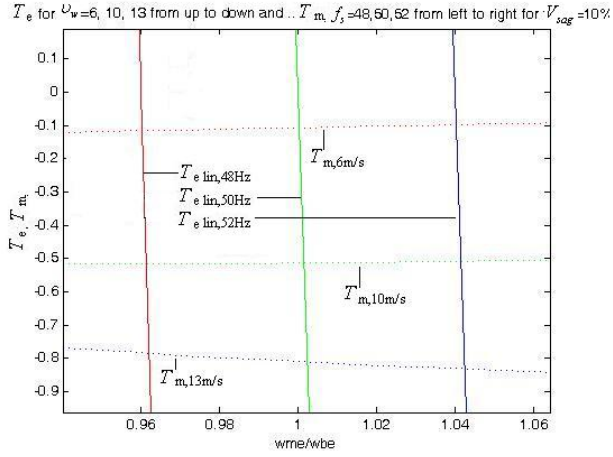

Figure 4. Mechanical and electrical torque versus frequency curves per unit with V_{sag} = 10% .

http://dx.doi.org/10.5772/51407

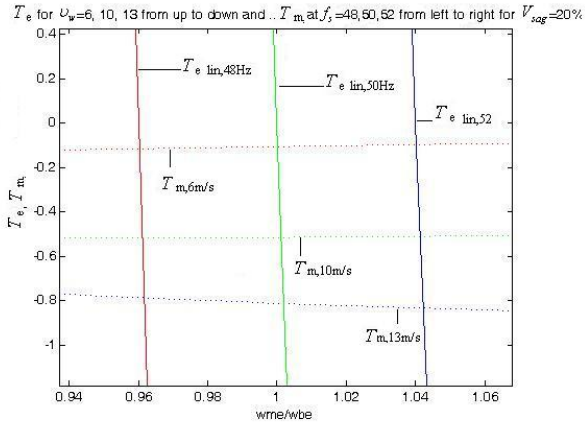

Figure 5. Mechanical and electrical torque versus frequency per unit with V_{sag} = 20%.

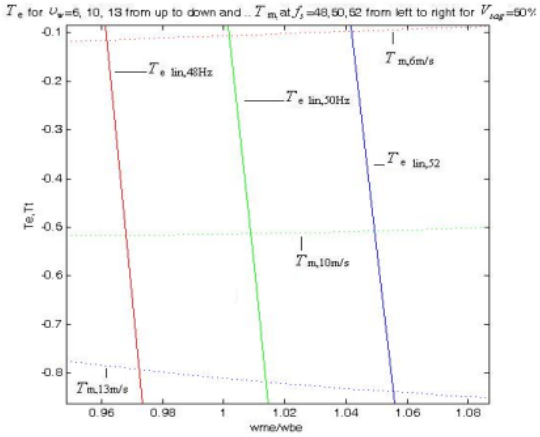

Figure 6. Mechanical and electrical torque versus frequency per unit with V_{sag} = 50%.

Figs. 3, 4, 5, and 6 illustrate that for lower wind speeds of 6 and 10 m/s, as the synchronous frequency f_s and V_{sag} change, the T_e and T_m values of the rotor change in the same direction as the frequency of the network, as shown in Tables III, IV, V, and VI. These figures and tables give the results for V_{sag} = 0% (i.e., only the frequency changes), 10%, 20%, and 50%. However, for a higher wind speed of 13 m/s, as f_s and V_{sag} change, the T_e and T_m values of the rotor change in the opposite direction to the changes in the frequency of the network.

For small changes in the slip according to the Kloss approach in equation (13), the torque changes as follows [2]:

$$T_{m1} = T_{m0} + K_{\alpha}\Delta\omega \tag{14}$$

Then:

$$T_{m1} = 2\frac{T_k}{s_k}\left(1 - \frac{\omega_{m0} + \Delta\omega}{\omega_e}\right) \tag{15}$$

and

$$K_{\alpha} = \frac{\partial T}{\partial \omega} = \frac{\partial T}{\partial \lambda} \cdot \frac{\partial \lambda}{\partial \omega} \tag{16}$$

or

$$K_{\alpha} = \frac{1}{\omega_{M0}}\left(\frac{1}{2}\rho R^4 v_{\omega 0}\frac{\partial C_p}{\partial \lambda}\Big|_{\lambda_0, v_0} - T_{M0}\right) \tag{17}$$

Thus, the new angular operation speed[2] is

$$\Delta\omega = \frac{-T_{m0} + 2\frac{T_k}{s_k} - 2\frac{T_k}{s_k}\frac{\omega_{m0}}{\omega_e}}{k_{\alpha} + 2\frac{T_k}{s_k\omega_e}} \tag{18}$$

v_w	f_s= 48		f_s = 50		f_s= 52	
	ω_m[pu]	T_e[pu]	ω_m[pu]	T_e[pu]	ω_m[pu]	T_e[pu]
6	.96050	-.1157	1.0005	-.1064	1.0405	-.0974
10	.9621	-.5337	1.0021	-.491	1.0421	-.4493
13	.9631	-.7863	1.0035	-.8122	1.0439	-.8331

Table 3. Analytical MATLAB results for different frequencies.

υ_w	$f_s = 48$		$f_s = 50$		$f_s = 52$	
	$\omega_m[pu]$	$T_e[pu]$	$\omega_m[pu]$	$T_e[pu]$	$\omega_m[pu]$	$T_e[pu]$
6	.9606	-.1156	1.0006	-.1064	1.0406	-.0974
10	.9625	-.5163	1.0027	-.5137	1.0429	-.5086
13	.9738	-.7868	1.0043	-.8127	1.0448	-.8335

Table 4. Analytical MATLAB results for V_{sag}= 10%.

υ_w	f_s= 48		f_s= 50		f_s= 52	
	$\omega_m[pu]$	$T_e[pu]$	$\omega_m[pu]$	$T_e[pu]$	$\omega_m[pu]$	$T_e[pu]$
6	.9607	-.1156	1.0007	-.1064	1.0407	-.0974
10	.9632	-.5163	1.0034	-.5136	1.0437	-.5085
13	.9648	-.7875	1.0054	-.8134	1.0461	-.8341

Table 5. Analytical MATLAB results for V_{sag}= 20%

υ_w	f_s= 48		f_s= 50		f_s= 52	
	$\omega_m[pu]$	$T_e[pu]$	$\omega_m[pu]$	$T_e[pu]$	$\omega_m[pu]$	$T_e[pu]$
6	.9618	-.1153	1.0018	-.1061	1.0418	-.0971
10	.9681	-.5161	1.0088	-.5131	1.0494	-.5076
13	.9724	-.7927	1.0139	-.8181	1.0555	-.8382

Table 6. Analytical MATLAB results for V_{sag}= 50%

6. Simulation of wind generator with frequency change

During turbulence and changes in the grid frequency, the torque speed (slip) curves change in such a way that as the frequency increases, the torque is increased at low wind speeds; 6 and 10 m/s, in contrast to Fig. 6 and decreases at a high speed of 13 m/s [2], as shown in Table 7 and Figs. 7–15.

υ_w	$f_s = 48$		$f_s = 50$		$f_s = 52$	
	$\omega_m[pu]$	$T_e[pu]$	$\omega_m[pu]$	$T_e[pu]$	$\omega_m[pu]$	$T_e[pu]$
6	.9619	-.1148	1.0019	-.1057	1.0418	-.0969
10	.9684	-.5179	1.0091	-.5134	1.0494	-.5076
13	.9724	-.7945	1.0147	-.8177	1.0559	-.8373

Table 7. Simulink simulation results for one- and two-mass shaft models

Figs. 7–15 show the electrical torque and mechanical speed of the induction machine for the one- and two-mass shaft turbine models at wind speeds of 6, 10, and 13 m/s to validate Table 7.

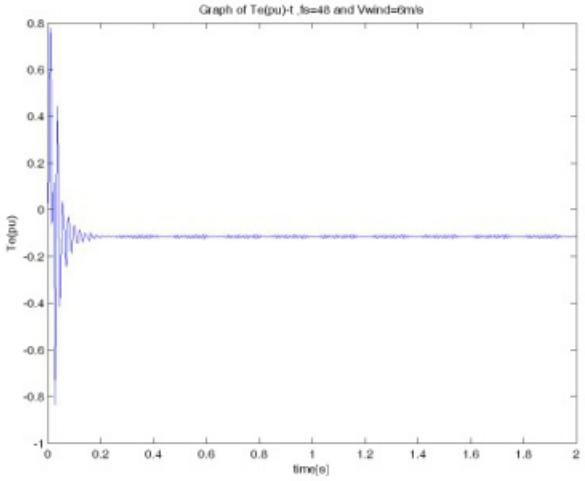

Figure 7. Electrical torque when = 48 and = 6m/s.

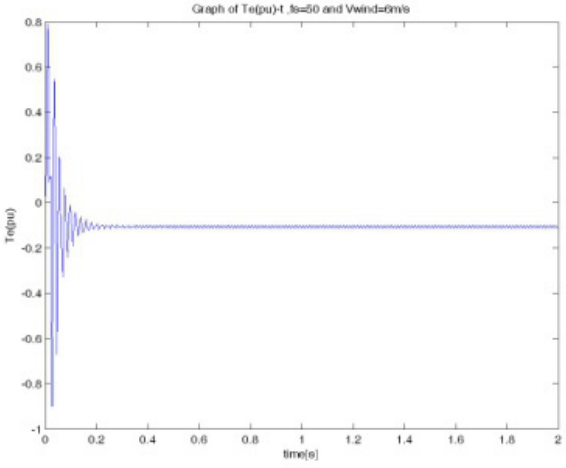

Figure 8. Electrical torque when f_s = 50 and υ_w = 6m/s.

http://dx.doi.org/10.5772/51407

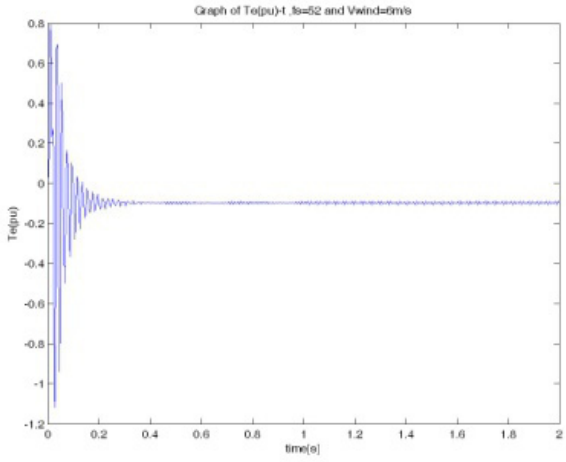

Figure 9. Electrical torque when $f_s = 52$ and $u_w = 6$m/s.

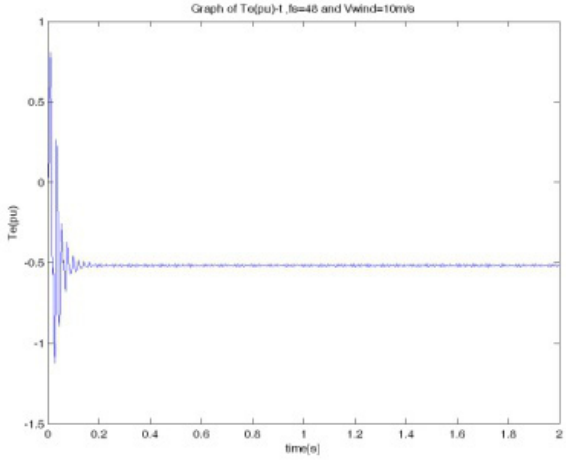

Figure 10. Electrical torque when $f_s = 48$ and $u_w = 10$m/s.

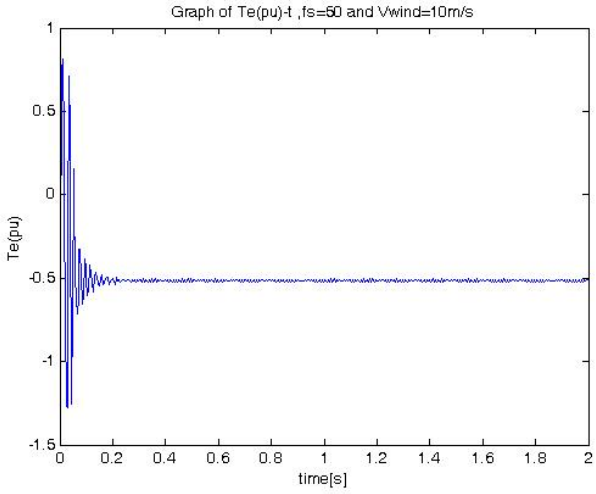

Figure 11. Electrical torque when f_s= 50 and u_w= 10m/s.

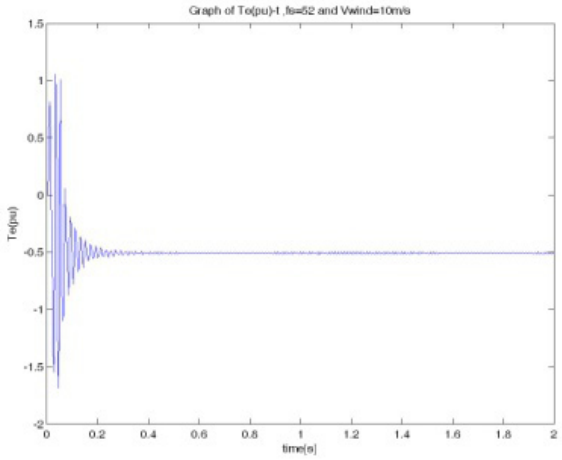

Figure 12. Electrical torque when f_s= 52 and u_w= 10m/s.

http://dx.doi.org/10.5772/51407

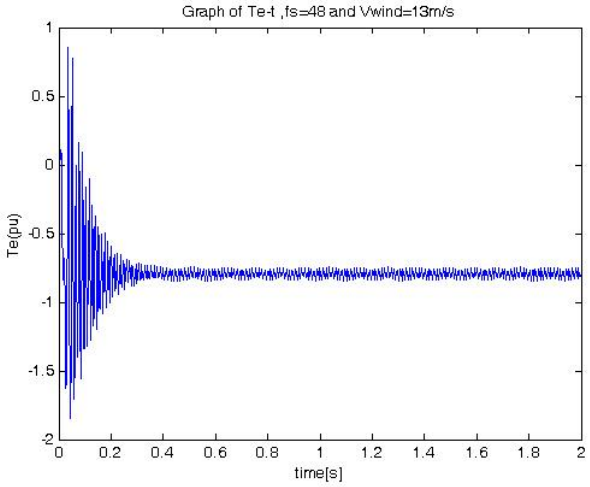

Figure 13. Electrical torque when f_s= 48 and u_w= 13m/s.

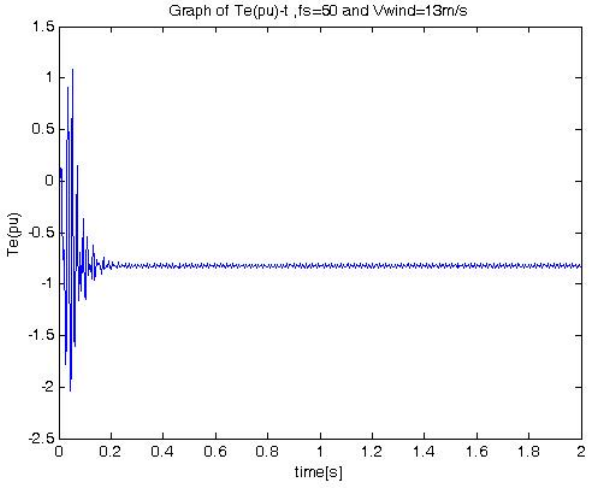

Figure 14. Electrical torque when f_s= 50 and u_w= 13m/s.

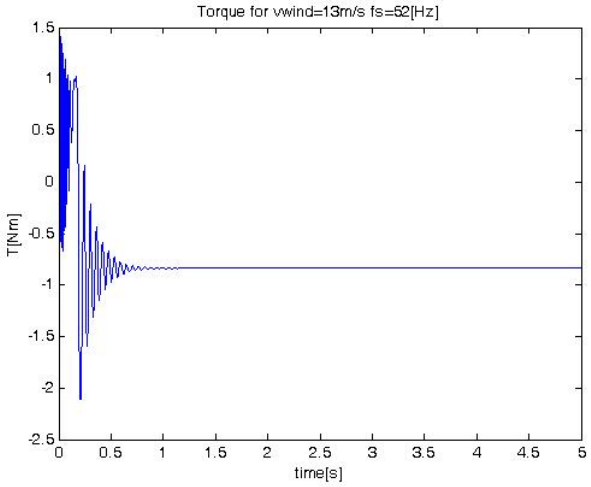

Figure 15. Electrical torque when f_s= 52 and u_w= 13m/s.

7. Simulation of wind station with one-mass and two-mass shaft turbine models

The results of simulations of a simple grid, fixed-speed induction machine, and one-mass and two-mass shaft turbines are given in Tables 8 -10 and Figs. 16–42. For an induction wind generator using the induction block in SIMULINK with high voltage sag i.e. 50% with frequencies 50 and 52 and equal to 13, C_p becomes negative, and the results are unrealistic. Then results of 50% voltage sag are realistic in new simulation of induction machine in Tables 8 -10.

u_w	f_s= 48		f_s= 50		f_s= 52	
	$\omega_m[pu]$	$T_e[pu]$	$\omega_m[pu]$	$T_e[pu]$	$\omega_m[pu]$	$T_e[pu]$
6	.9624	-.1152	1.0024	-.106	1.0423	-.097
10	.9703	-.516	1.0111	-.5128	1.0519	-.5071
13	.9757	-.795	1.0176	-.8201	1.0595	-.8399

Table 8. Simulation results by SIMULINK for one and two mass shaft model for V_{sag}= 10%

http://dx.doi.org/10.5772/51407

υ_w	f_s= 48		f_s= 50		f_s= 52	
	$\omega_m[pu]$	$T_e[pu]$	$\omega_m[pu]$	$T_e[pu]$	$\omega_m[pu]$	$T_e[pu]$
6	.963	-.1151	1.003	-.1059	1.043	-.0969
10	.973	-.5159	1.014	-.5125	1.055	-.5066
13	.9799	-.7977	1.0223	-.8226	1.0648	-.842

Table 9. Simulation results by SIMULINK for one and two mass shaft model for V_{sag}= 20%

υ_w	f_s= 48		f_s= 50		f_s= 52	
	$\omega_m[pu]$	$T_e[pu]$	$\omega_m[pu]$	$T_e[pu]$	$\omega_m[pu]$	$T_e[pu]$
6	.9674	-.114	1.0074	-.1048	1.0474	-.0959
10	.9933	-.5146	1.0364	-.5096	1.0796	-.502
13	1.0248	-.8239	1.0474	-.8347	1.0917	-.85

Table 10. Simulation results by SIMULINK for one and two mass shaft model for V_{sag}= 50%

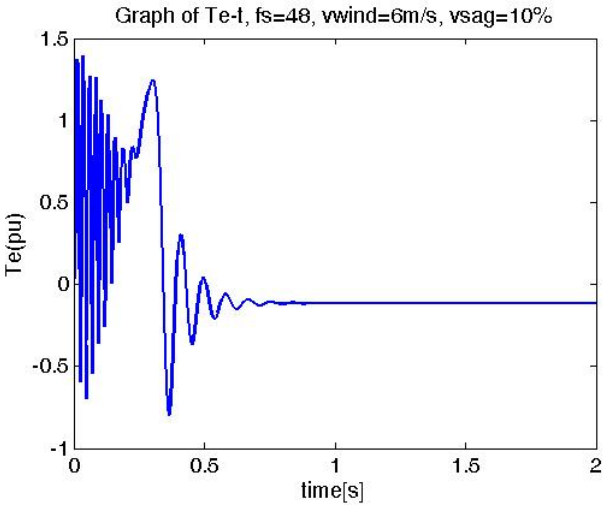

Figure 16. Torque-time in per unit while V_{sag}= 10% and υ_w = 6m/s, f_s=48

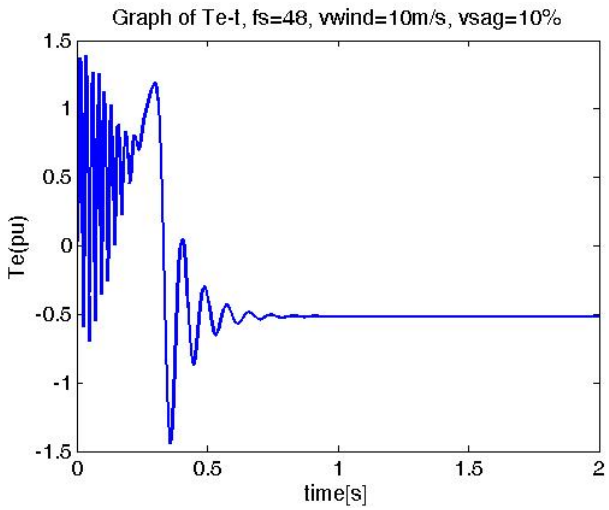

Figure 17. Torque-time in per unit while V_{sag}= 10% and υ_w = 10m/s, f_s= 48

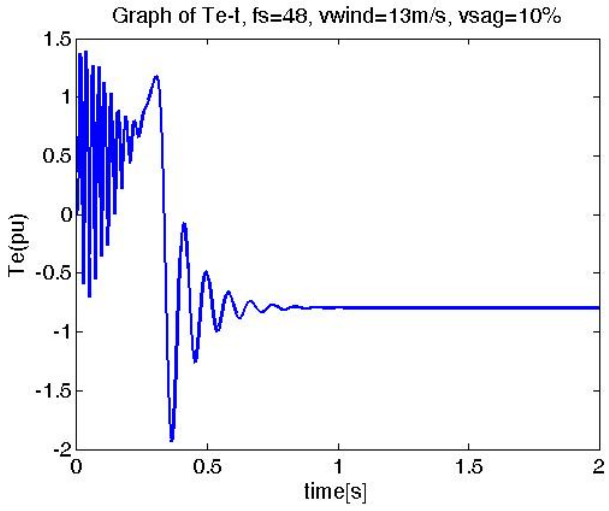

Figure 18. Torque-time in per unit while V_{sag}= 10% and υ_w = 13m/s, f_s= 48

http://dx.doi.org/10.5772/51407

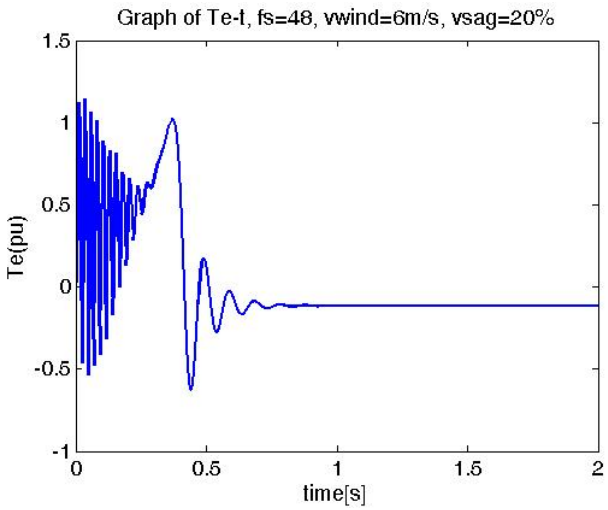

Figure 19. Torque-time in per unit while V_{sag}= 20% and υ_w = 6m/s, f_s= 48

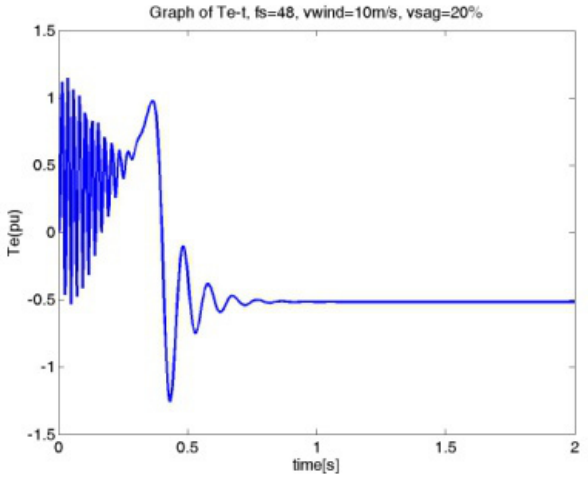

Figure 20. Torque-time in per unit while V_{sag}= 20% and υ_w = 10m/s, f_s= 48

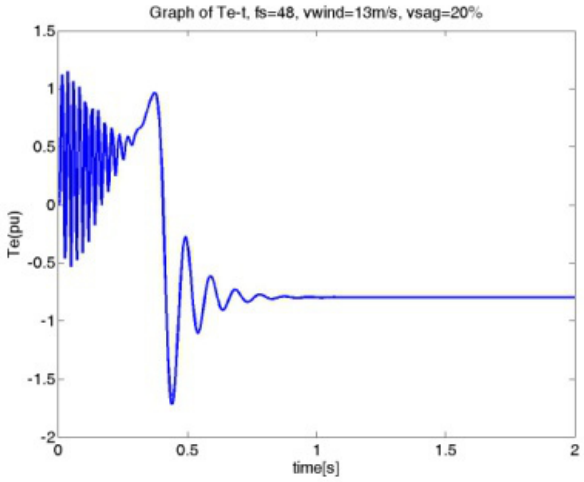

Figure 21. Torque-time in per unit while V_{sag}= 20% and u_w = 13m/s, f_s= 48

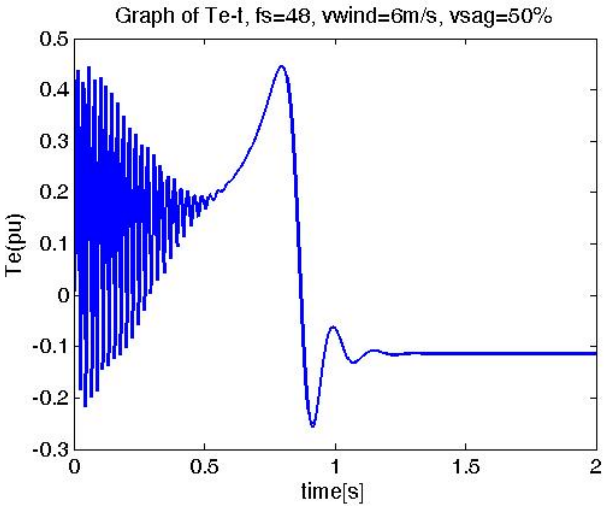

Figure 22. Torque-time in per unit while V_{sag}= 50% and u_w = 6m/s, f_s= 48

http://dx.doi.org/10.5772/51407

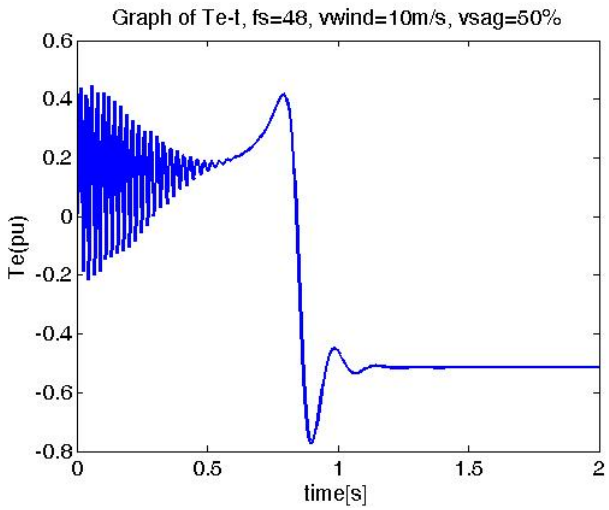

Figure 23. Torque-time in per unit while V_{sag}= 50% and υ_w = 10m/s, f_s= 48

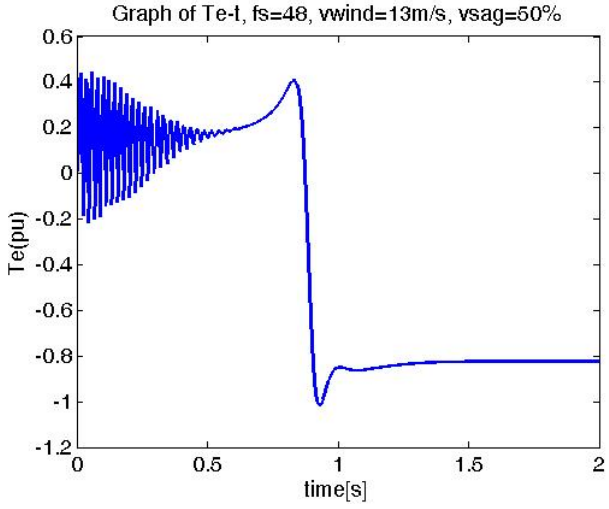

Figure 24. Torque-time in per unit while V_{sag}= 50% and υ_w = 13m/s, f_s= 48

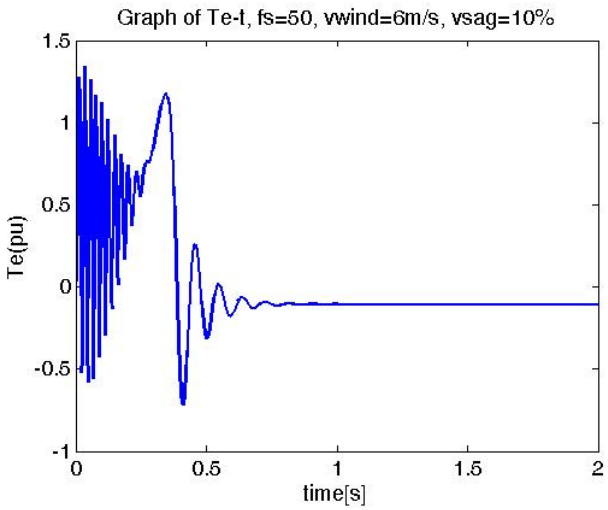

Figure 25. Torque-time in per unit while V_{sag}= 10% and υ_w = 6m/s, f_s= 50

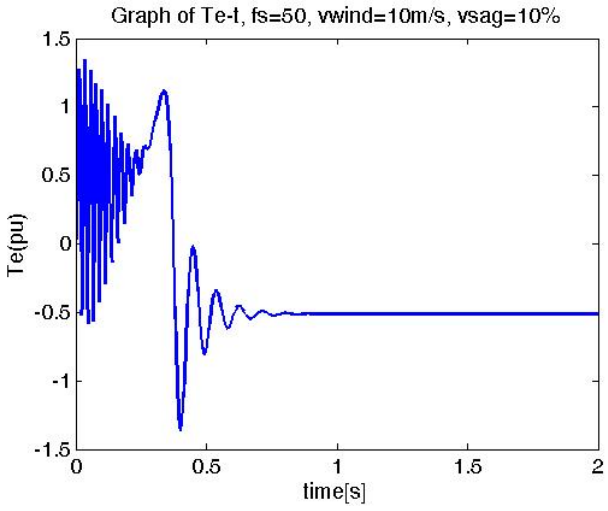

Figure 26. Torque-time in per unit while V_{sag}= 10% and υ_w = 10m/s, f_s= 50

http://dx.doi.org/10.5772/51407

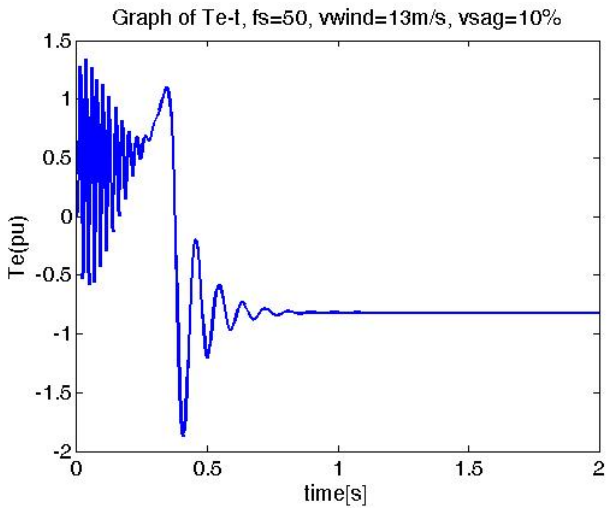

Figure 27. Torque-time in per unit while V_{sag}= 10% and υ_w = 13m/s, f_s= 50

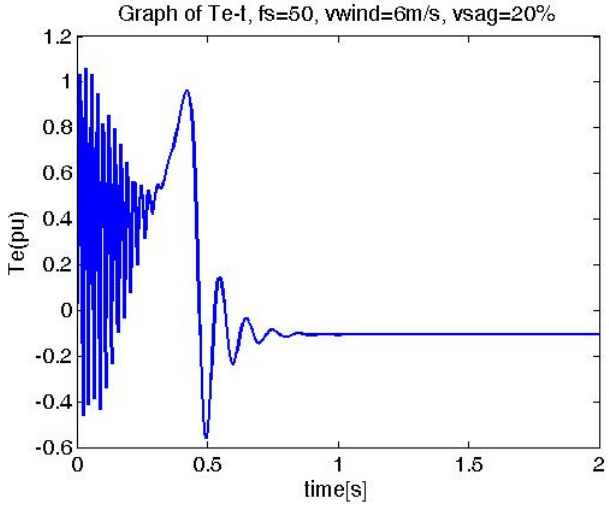

Figure 28. Torque-time in per unit while V_{sag}= 20% and υ_w = 6m/s, f_s= 50

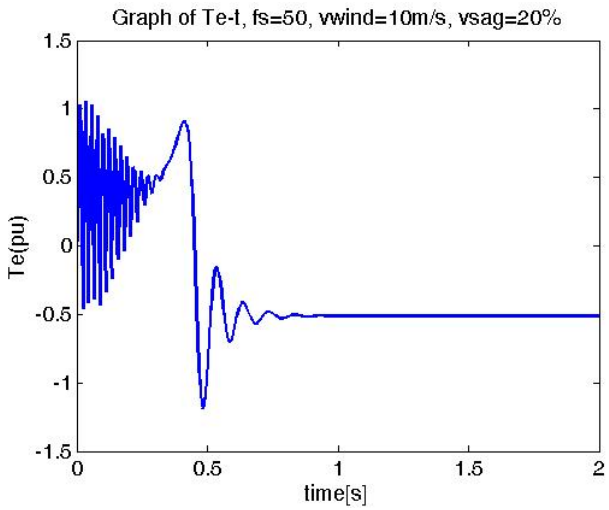

Figure 29. Torque-time in per unit while V_{sag}= 20% and υ_w = 10m/s, f_s= 50

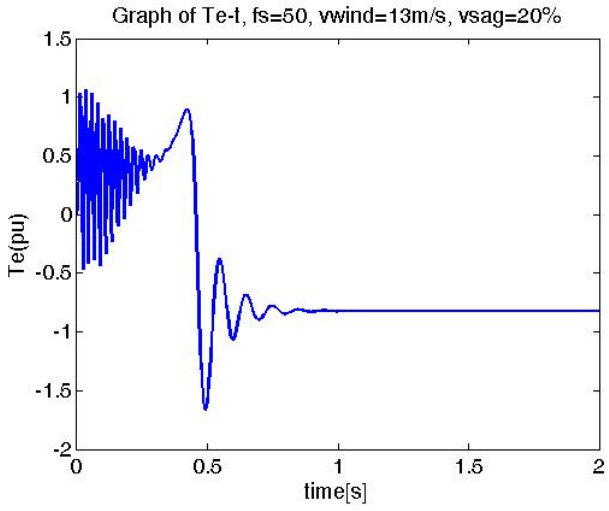

Figure 30. Torque-time in per unit while V_{sag}= 20% and υ_w = 13m/s, f_s= 50

http://dx.doi.org/10.5772/51407

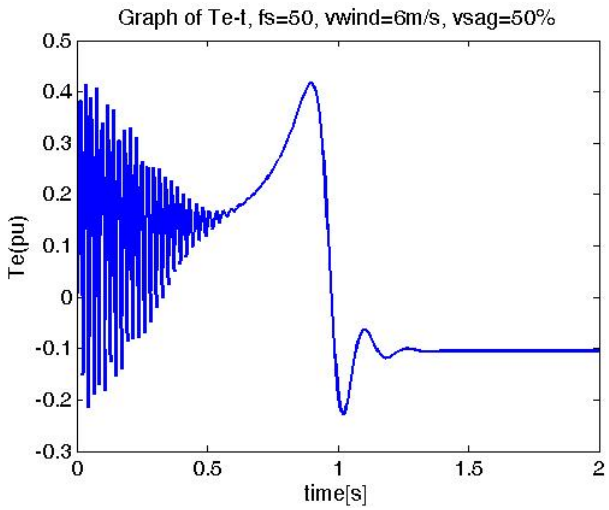

Figure 31. Torque-time in per unit while V_{sag}= 50% and υ_w = 6m/s, f_s= 50

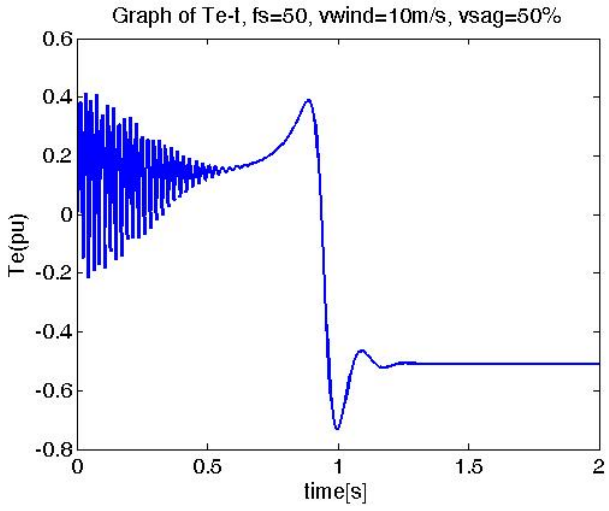

Figure 32. Torque-time in per unit while V_{sag}= 50% and υ_w = 10m/s, f_s= 50

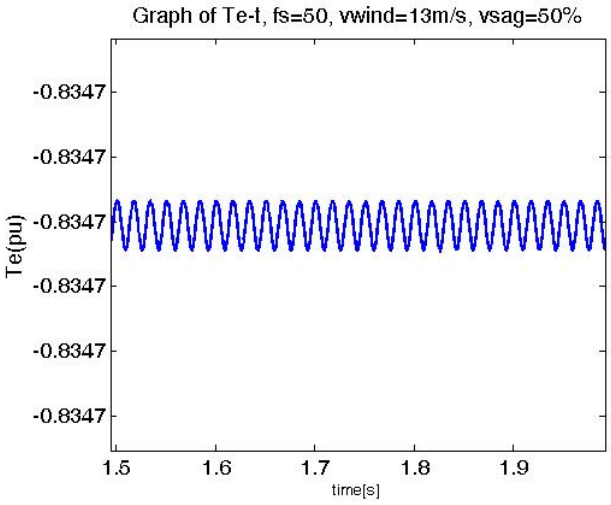

Figure 33. Torque-time in per unit while V_{sag}= 50% and υ_w = 13m/s, f_s= 50 in new simulation of wind generator

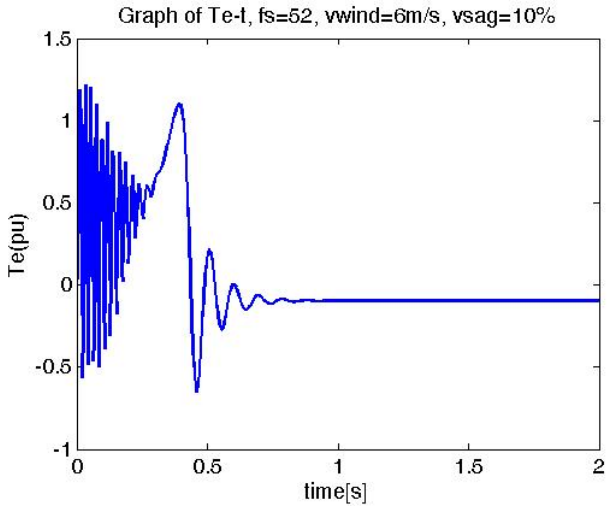

Figure 34. Torque-time in per unit while V_{sag}=10% and υ_w = 6m/s, f_s= 52

http://dx.doi.org/10.5772/51407

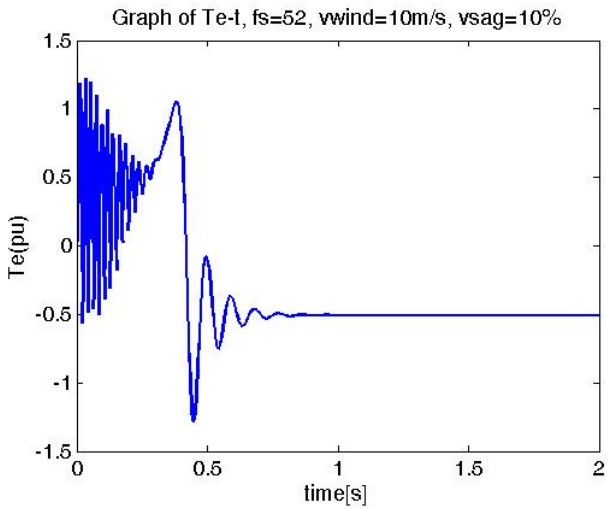

Figure 35. Torque-time in per unit while V_{sag}=10% and u_w = 10m/s, f_s= 52

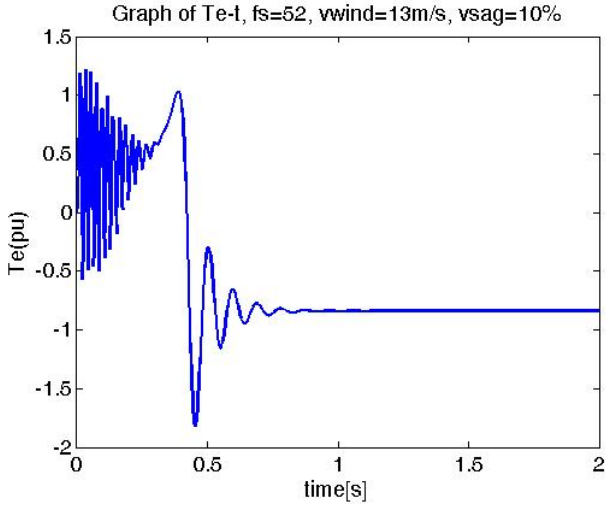

Figure 36. Torque-time in per unit while V_{sag}= 10% and u_w = 13m/s, f_s= 52

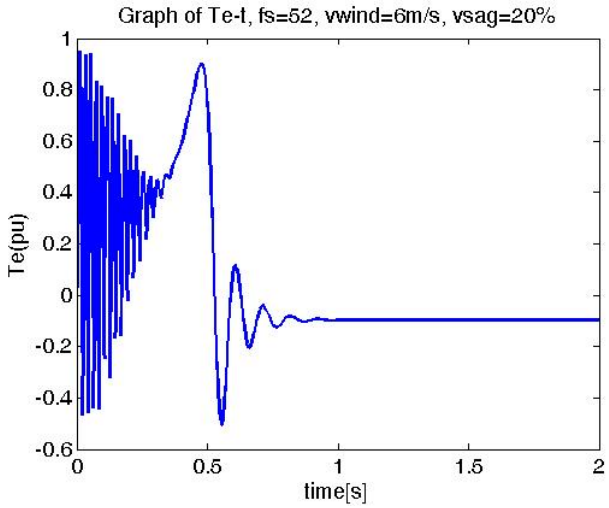

Figure 37. Torque-time in per unit while V_{sag}= 20% and υ_w = 6m/s, = 52

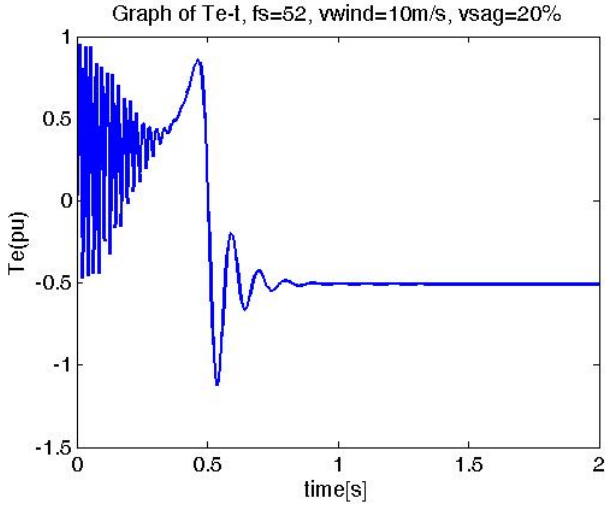

Figure 38. Torque-time in per unit while V_{sag}= 20% and υ_w = 10m/s, f_s= 52

http://dx.doi.org/10.5772/51407

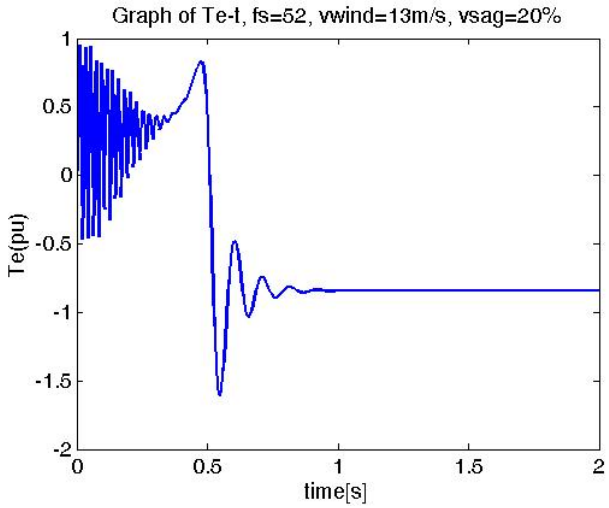

Figure 39. Torque-time in per unit while V_{sag}= 20% and υ_w = 13m/s, f_s= 52

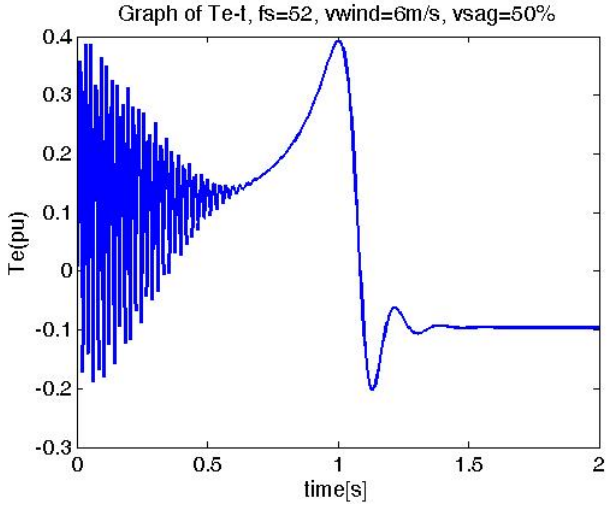

Figure 40. Torque-time in per unit while V_{sag}= 50% and υ_w = 6m/s, f_s= 52

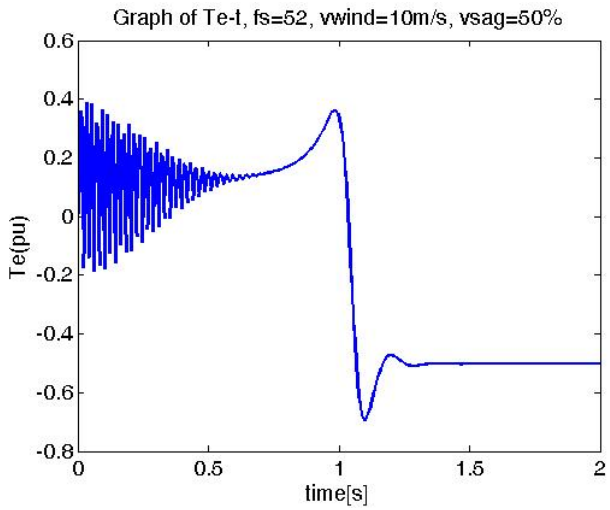

Figure 41. Torque-time in per unit while V_{sag}= 50% and υ_w = 10m/s, f_s= 52

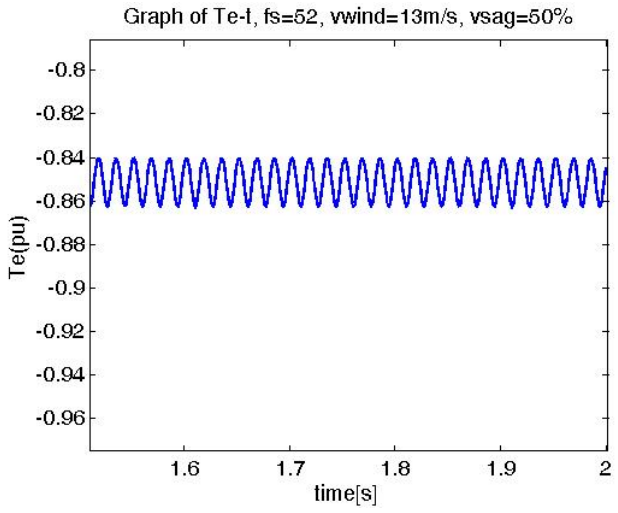

Figure 42. Torque-time in per unit while V_{sag}= 50% and υ_w = 13m/s, f_s= 52 in new simulation of wind generator

http://dx.doi.org/10.5772/51407

8. New Simulation of Induction Machine

Figs. 33 and 42 show the results of new simulation of the induction machine model illustrated in Fig. 43 [1]. The new simulation, which has no limiters and switches, is used because at high grid voltage drop-down or sag, the Simulink induction model does not yield realistic results.

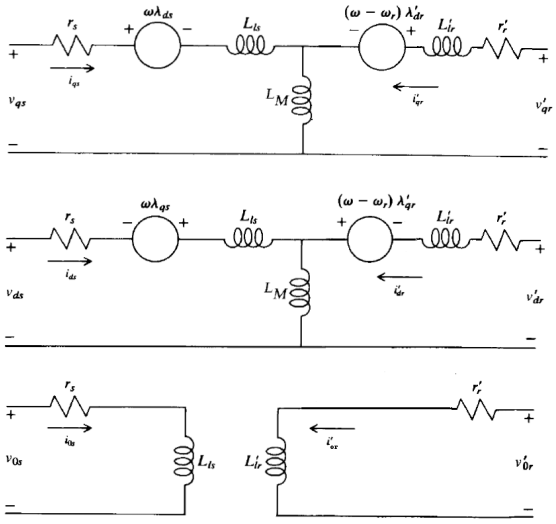

Figure 43. Induction machine Model in *dqo* system

The new simulation of induction machine is in *dqo* system and synchronous reference frame simulation on the stator side; *n* (Transfer coefficient) is assumed to be 1. Circuit theory is used in this simulation, and it does not have saturation and switch blocks, unlike the MATLAB–SIMULINK Induction block. In Fig. 43, L_M is the magnetic mutual inductance, and *r* and L are the ohm resistance and self-inductance of the *dqo* circuits, respectively. The machine torque is given by equation (19). In this equation, $i_{d,qs}$ and $\lambda_{d,qs}$, the current and flux parameters, respectively, are derived from linear equations (20)–(23); they are sinusoidal because the voltage sources are sinusoidal.

$$T_e = \left(\frac{3}{2}\right)\left(\frac{P}{2}\right)\left(\lambda_{ds} i_{qs} - \lambda_{qs} i_{ds}\right) \tag{19}$$

Where P is poles number, λ_{ds} and λ_{qs} are flux linkages and leakages, respectively, and i_{qs} and i_{ds} are stator currents in q and d circuits of *dqo* system, respectively.

Then i matrix produced by the λ matrix is given by equation (20).

$$\begin{bmatrix} \lambda_{qdos} \\ \lambda'_{qdor} \end{bmatrix} = \begin{bmatrix} K_s L_s \left(K_s\right)^{-1} & K_s L'_{sr} \left(K_r\right)^{-1} \\ K_r \left(L'_{sr}\right)^T \left(K_s\right)^{-1} & K_r L'_r \left(K_r\right)^{-1} \end{bmatrix} \cdot \begin{bmatrix} i_{qdos} \\ i'_{qdor} \end{bmatrix} \tag{20}$$

where the inductance matrix parameters are given by (21), (22), (23).

$$K_s L_s \left(K_s\right)^{-1} = \begin{bmatrix} L_{ls} + L_M & 0 & 0 \\ 0 & L_{ls} + L_M & 0 \\ 0 & 0 & L_{ls} \end{bmatrix} \tag{21}$$

$$K_r L'_r \left(K_r\right)^{-1} = \begin{bmatrix} L'_{lr} + L_M & 0 & 0 \\ 0 & L'_{lr} + L_M & 0 \\ 0 & 0 & L'_{lr} \end{bmatrix} \tag{22}$$

$$K_s L'_{sr} \left(K_r\right)^{-1} = K_r \left(L'_{sr}\right)^T \left(K_s\right)^{-1} = \begin{bmatrix} L_M & 0 & 0 \\ 0 & L_M & 0 \\ 0 & 0 & 0 \end{bmatrix} \tag{23}$$

The linkage and leakage fluxes are given by (24) to (29).

$$\lambda_{qs} = L_{ls} i_{qs} + L_M \left(i_{qs} + i'_{qr}\right) \tag{24}$$

$$\lambda_{ds} = L_{ls} i_{ds} + L_M \left(i_{ds} + i'_{dr}\right) \tag{25}$$

$$\lambda_{os} = L_{ls} i_{os} \tag{26}$$

$$\lambda'_{qr} = L'_{lr} i'_{qr} + L_M \left(i_{qs} + i'_{qr}\right) \tag{27}$$

$$\lambda'_{dr} = L'_{lr} i'_{dr} + L_M \left(i_{ds} + i'_{dr}\right) \tag{28}$$

$$\lambda'_{or} = L'_{lr} i'_{or} \tag{29}$$

http://dx.doi.org/10.5772/51407

To create the torque in equation (19), it is necessary to determine the currents in equations (30)–(33) from the stator and rotor currents by using current meters.

$$v_{qs} = r_s i_{qs} + \omega\lambda_{ds} + \frac{d\lambda_{qs}}{dt} \tag{30}$$

$$v_{ds} = r_s i_{ds} - \omega\lambda_{qs} + \frac{d\lambda_{ds}}{dt} \tag{31}$$

$$v'_{qr} = r'_r i'_{qr} + (\omega - \omega_r)\lambda'_{dr} + \frac{d\lambda'_{qr}}{dt} \tag{32}$$

$$v'_{dr} = r'_r i'_{dr} - (\omega - \omega_r)\lambda'_{qr} + \frac{d\lambda_{dr}}{dt} \tag{33}$$

9. Conclusion

As frequency changes and voltage sag occurs because of turbulence in wind stations in ride-through faults, the system's set point changes. The theoretical and simulation results results are similar for one mass shaft and two mass shaft turbine models. At lower wind speeds; 6 and 10 m/s, the directions of the changes in the new working point are the same as those of the frequency changes. At a higher wind speed; 13 m/s, the directions of these changes are opposite to the direction of the frequency changes. Simulation results of high grid voltage sag with SIMULINK induction block has error and new simulation of wind induction generator in synchronous reference frame is presented without error and in 50% voltage sag, new simulation of wind generator model has higher precision than that in 10% and 20% voltage sags; however, this model can simulate wind generator turbulence with voltage sags higher than 50%. Although results of new simulation of induction machine with wind turbine for 50% voltage sag and frequencies 50 and 52 have been presented in this chapter.

10. Nomenclature

P = Generator power

ρ = Air density

A = Turbine rotor area

C_p = Power Coefficient

v_w = Wind speed

θ_{pitch} = Pitch angle

T_e = Electrical torque

T_m = Mechanical torque

J = Inertia

ω_m = Mechanical speed

C = Drag coefficient

v = Gear box ration

R = Blade radius

R_s = Stator resistance

L_s = Stator inductance

L_m = Mutual inductance

L'_r = Rotor inductance

R'_r = Rotor resistance

p = Pole pairs

κ = Stiffness

$\lambda_{r,s}$ = Rotor and stator flux

$K_{r,s}$ = Rotor and stator park transformation in synchronous reference frame

$i_{r,s}$ = Rotor and stator current

$v_{r,s}$ = Rotor and stator voltage

11. Future Work

The new simulation of induction generator will be tested by new innovative rain turbine theory and model of the author.

http://dx.doi.org/10.5772/51407

Acknowledgements

I appreciate Dr. Oriol Gomis Bellmunt for conceptualization, Discussions and new information and Dr. Andreas Sumper for discussions about first part of chapter, with special thanks to Dr. Joaquin Pedra for checking reference frame and starting point in new simulation of induction machine.

Author details

Hengameh Kojooyan Jafari*

Address all correspondence to: kojooyan@iiau.ac.ir

Department of Electrical Engineering, Islamic Azad University, Islamshahr Branch, Iran

References

[1] Krause, Paul C. (1986). Analysis of Electric Machinery. MCGraw-Hill, Inc.

[2] Sunmper, A., Gomis-Bellmunt, O., Sudria-Andreu, A., et al. (2009). Response of Fixed Speed Wind Turbines to System Frequency Disturbances. *ICEE Transaction on Power Systems*, 24(1), 181-192.

[3] Junyent-Ferre, A., Gomis-Bellmunt, O., Sunmper, A., et al. (2010). Modeling and control of the doubly fed induction generator wind turbine. *Simulation modeling practice and theory journal of ELSEVIER*, 1365-1381.

[4] Lubosny, Z. (2003). Wind Turbine operation in electric power systems. *Springer publisher*.

Chapter 3

Turbine Wake Dynamics

Phillip McKay, Rupp Carriveau, David S-K Ting and Timothy Newson

Additional information is available at the end of the chapter

http://dx.doi.org/10.5772/53968

1. Introduction

The extraction of energy from wind across a turbine rotor produces an aerodynamic wake region downstream from the rotor. The wake region is generally associated with a few key characteristics. These include:

- a velocity deficit
- a pressure differential
- an expanding area
- rotation of the wake field
- increased turbulence

Studies of wind turbine wakes range from simplified mathematical approaches to complex empirical models. Wind farm developers also vary in their application of these models for the prediction of losses caused by wakes within a multi-turbine project. While much has been learned in recent years, research continues to reduce uncertainty and increase the accuracy of wake loss calculations. This chapter provides a brief introduction to the accepted principles of wake behaviour, introduces several advanced topics and covers the current state of the art and direction for the future of wake research.

2. Wake fundamentals

Wake influences from one turbine to the next have received the majority of attention in this field of study due to the significant influence this has on performance and reliability. Down-

stream wake effects are frequently quantified through the use of rotor disc theory and the conservation of linear momentum. The rotor disc refers to the total swept area of the rotor as shown in Figure 1. The expanding wake downstream of the turbine in conjunction with a decrease in wind speed U is also shown.

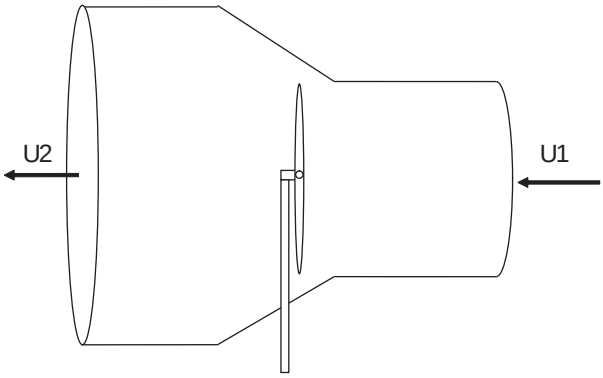

Figure 1. Swept area of wind turbine rotor with expanding wake section [1].

For conservation of mass:

$$\rho A_1 U_1 = \rho A_2 U_2 \tag{1}$$

where ϱ is the air density, A is the cross sectional area, U_1 is the free stream wind speed and U_2 is the wind speed downstream from the turbine. A decrease in wind speed across the rotor area results in a greater downstream area. From elementary energy conservation principles, it can be shown that a high pressure area is formed upstream of the rotor disc and a lower pressure area is formed downstream. This pressure change is due to the work of the rotor blades on the air passing over them. The force of the air on the blades results in an opposing force on the air stream causing a rotation of the air column. This low pressure column of rotating air expands as it moves downstream of the turbine and eventually dissipates as equilibrium is reached with the surrounding airflow [2, 3]. This simplified explanation constitutes what is known as the "wake effect" of a wind turbine [1]. An increase in downstream turbulence is caused by wake rotation, disruption of the air flow across the rotor blades and the vortices formed at the blade tips. This results in less power being available for subsequent turbines.

The Bernoulli equation can also applied to wind turbine wake analysis. The equation follows the concept of conservation of energy:

$$\frac{\rho U_1^2}{2} + \; p = H \tag{2}$$

http://dx.doi.org/10.5772/53968

where p is pressure and H is the total energy for the constant streamline. Using the Bernoulli equation and conservation of momentum together the following equation can be developed:

$$U_2 = U_1\sqrt{1 - C_T} \tag{3}$$

Here C_T refers to the thrust coefficient of the wind turbine. In this way we have a simple wake model for the representation of downstream wind velocity based on the free stream wind speed and the characteristics of the turbine being considered. For more information refer to [4]. While this does include wake expansion it does not consider other factors such as wake rotation. Several other models are currently in use and under development.

The study of wind turbine wakes is broken into two parts: near wake and far wake. The near wake region is concerned with power extraction from the wind by a single turbine, whereas the far wake is more concerned with the effect on the downstream turbines and the environment [7]. Opinions on near wake length have varied, but can be considered to fall in the range of 1 to 5 rotor diameters (1D to 5D) downstream from the rotor disc [5-6], with far wake regions dependent on terrain and environmental conditions. The full extent of far wake length is currently still under study, but may range from up to 15D for onshore sites [8] and up to 14 km for offshore [9]. The 5D to 15D wake region has been defined as an intermediate wake region by some [10], with the far wake pertaining to distances farther than 15D.

Data from an array of turbines within a commercial scale wind farm are given in Figure 2. The turbines are in a straight line with a separation of 4 rotor diameters. Time series data for nacelle position, wind speed and power are given for a wake event affecting 4 turbines. This specific event has a wind direction moving from 120 to 170 degrees from north, clockwise as positive, over a time span of approximately 10 hours. This can be seen in the nacelle position plot for all four turbines in Figure 2a. During this time period the wind direction passes through the alignment condition of 145 degrees from north. An alignment condition refers to a wind direction measured by the lead (upwind) turbine that is coincident with the straight line formed by the turbine row. The nacelle position plot shows the turbines tracking the wind direction while the wind speed plot (Figure 2b) reveals a drop in wind speed for the downstream turbines between the nacelle position range of TA +/- 15 degrees, where TA refers to direct turbine alignment. In addition, the power is shown to drop along the with wind speed (Figure 2c). This is evidence of wake interaction between the four machines. Vermeer et al. [5] found that the wake velocity recovers more rapidly after the first turbine leaving the most dominant effect between the upstream and primary downstream turbine.

The profile of the measured velocity deficit caused by the wake in an array of 4 wind turbines is given in Figure 3. The upstream nacelle position was used as the reference wind direction. The wind speeds of the downstream turbines are given with respect to this wind direction and show the wake centerline as well as the profile of the outer edges of the region. Upstream wind speeds less than 5 m/s are not included due to the added complexity of low wind conditions and cut-in behaviour of the turbines. Wind speeds greater than 11

m/s are also neglected due to the lack of data at these higher speeds and the reduction in wake pronunciation. The wake region extends across a range of 30 degrees (TA +/- 15 degrees) on average for a wind speed range of 5-11 m/s. A number of features are evident in this Figure. The first downstream turbine exhibits the greatest drop in wind speed at approximately 35 %. The second downstream turbine appears to recover by approximately 5 % with respect to free stream velocity under direct turbine alignment. The third in the row shows similar behaviour to the second.

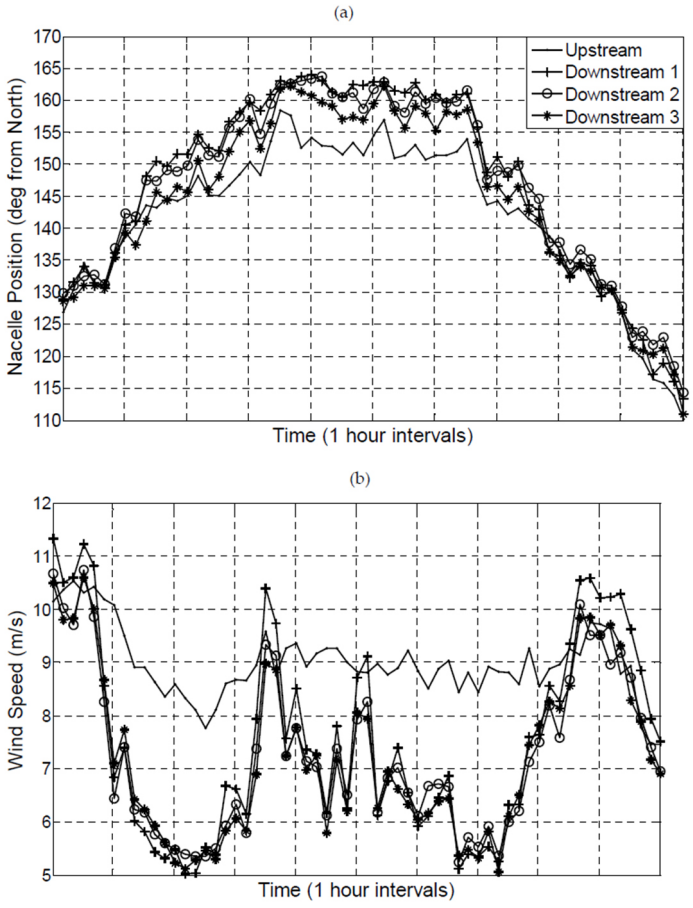

http://dx.doi.org/10.5772/53968

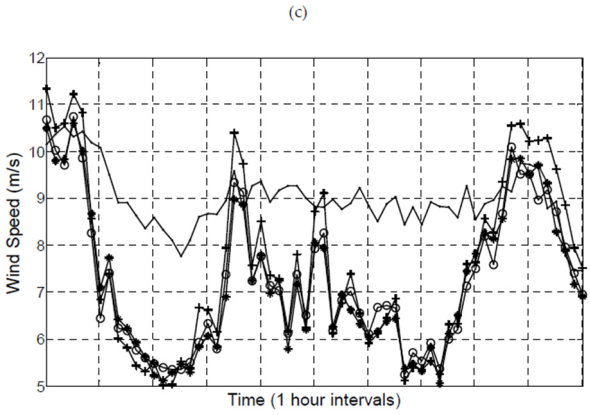

Figure 2. Time series SCADA data for a period containing a case of turbine alignment. a) nacelle position, b) wind speed and c) power [11].

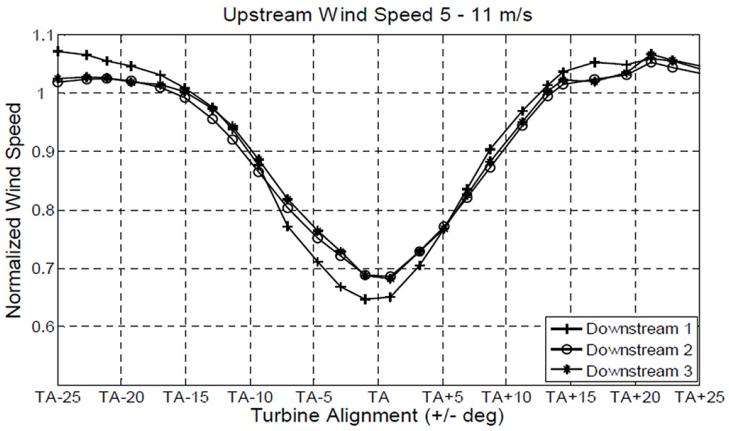

Figure 3. Array wake profile for an upstream turbine wind speed range of 5-11 m/s, considered her e as the free stream wind speed. The data are averaged over 6 months. Wind speed is normalized by the upstream turbine (free stream) wind speed: downstream wind speed/upstream (free stream) wind speed [11].

This recovery is also observed by Barthelmie et al. [12] where momentum drawn into the wake by lateral or horizontal mixing of the air external to the wake region is attributed to the recovery of wind velocity. In the case of Barthelmie et al. the offshore wind farms of Nysted and Horns Rev in Denmark were used to profile the wake regions in the farm's grid style arrangement. The findings revealed the largest wind velocity deficit after the first turbine with a smaller relative wind speed loss after the initial wake interaction with the first downstream machine. Here the velocity continues to decrease for downstream turbines due to wake mixing from neighboring turbine rows.

It has proven useful to concentrate analysis on more narrow bands of wind speeds as each wind speed tends to produce a measurably different result in turbine behaviour. The wind response for the wind speed range of 8-9 m/s is given in Figure 4. This exhibits the same trends as shown in Figure 3 for a more narrow wind speed range. The power coefficient profile for the same wind speeds is shown in Figure 5 where the power coefficient is taken as:

$$C_P = \frac{8P}{\pi\rho U_\infty^3 D^2} \tag{4}$$

The values were estimated using the upstream wind speed reading as free stream velocity,, with P representing power produced by the turbine, ϱ is the air density, and D is the rotor diameter. The coefficients are plotted for each turbine including the upstream lead turbine. The wake boundaries produce a power coefficient in the range of 0.40 or greater with a minimum at the wake center of 0.14.

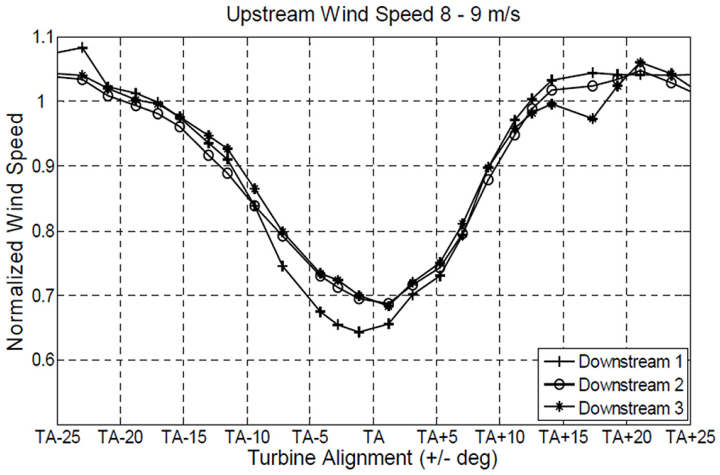

Figure 4. Normalized wind speed for an upstream turbine (free stream) wind speed of 8-9 m/s averaged over 6 months [11].

In Figure 6, turbulence intensity is implied through consideration of the standard deviation of wind speed. Deviations were calculated by the wind farm SCADA system and provided at 10 minute intervals. For the wind turbines discussed above, the downstream wind speed standard deviation is shown. A clear peak in deviation occurs approximately at turbine alignment +/- 10 degrees with a trend in nominal deviation towards the outer edges of the wake region. Turbulence increases are not excessive and are much less than observed for some special weather events; however, the trend shown in Figure 6 is consistent and may have potential to cause issues over the long term life of the turbine. This is due to the in-

http://dx.doi.org/10.5772/53968

creased fatigue loading caused by the frequent fluctuations. In addition, increased variation in wind speed along the length of the rotor may contribute to damaging loads. It can also be seen that the greatest wind speed standard deviation does not necessarily correspond with the greatest loss in power. For example, downstream 3 experiences the highest standard deviation under wake conditions but shows the lowest power deficit in Figure 5.

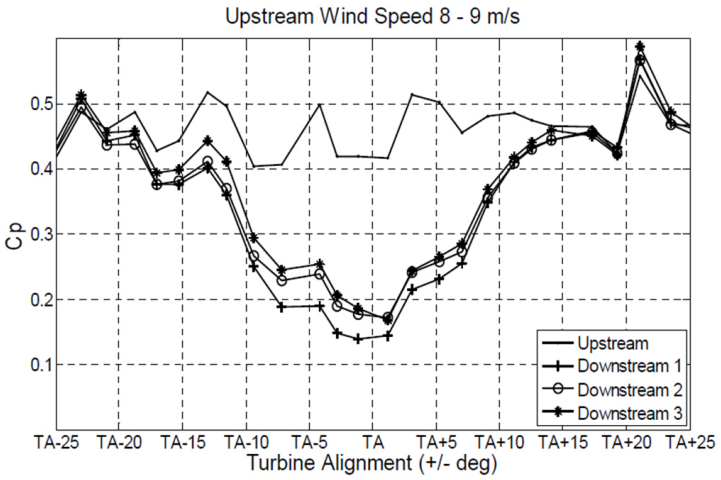

Figure 5. Array power coefficient profile for an upstream turbine wind speed of 8-9 m/s averaged over 6 months [11].

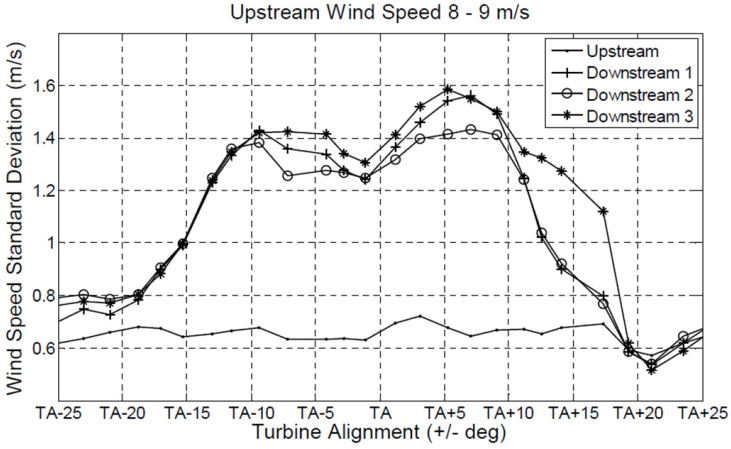

Figure 6. Wind speed standard deviation for upstream wind speeds of 8-9 m/s averaged over 6 months [11].

It is evident that there are other external factors that contribute to the definition of these profiles as they show irregularities and do not exhibit a smooth shape. It is expected that the 6 month averaged data has reduced the effects of short term, isolated fluctuations in wind speed, humidity, temperature, air density and inhomogeneous wake at the downstream turbine and so there is a consistent fluctuation in the wind speed under turbine alignment conditions. Seasonal and site specific wind conditions are likely to contribute to the small scale unpredictability of wake velocity deficit and turbulence intensity. Inter-turbine wake effects are quantifiable and are accounted for in all major wind farms projects. However, there is still a large amount of uncertainty and error in the modeling of wind turbine wakes and associated power losses. The next section discusses wind farm siting and its importance in minimizing uncertainty in the planning stages of a wind project.

3. Siting

Locating and assessing the feasibility of a wind farm is one of the most critical elements in a wind farm business plan. Maximum energy extraction from the investment is dependent on where the site is located and where each individual turbine is positioned within that site. Wake interactions between wind turbines and nearby wind farms can substantially impact power output.

Wind farm developers expend significant resources collecting data for site assessments. Topography, surface roughness, the local wind profile, turbine types, power curves, municipal site restrictions and other data are collected and processed to maximize profitability. Wind Farmer and WindPRO are commonly used software packages delivering a range of services from wake modeling to visual impact studies. While much of the assessment is based on available data and numerical calculations, a portion of the analysis is dependent on user preferences. Depending on the investors and farm developers, varying levels of uncertainty may be accepted in different areas of the study. For example, a developer may choose to install a single meteorological tower for profiling of the wind resource at the center of the site under consideration to reduce costs. Another developer may choose to install two or three towers to drive down uncertainty caused by extrapolation of the recorded data across the area of the site. Some sites can have unique curtailment requirements depending on neighboring properties or bat and bird migration.

A variety of models have been developed to simulate wakes within a wind farm. The most widely used models include the:

- Park
- Modified Park
- Eddy Viscosity
- Deep-Array Wake Model

http://dx.doi.org/10.5772/53968

Brower [13] summarizes these models and their differences. The WAsP software commonly used for analysis of wake within a wind farm by site assessment tools makes use of the Park model. By accounting for geographical and ground surface conditions, the variation in wind speed profiles can be estimated along with expected wake propagation intensity. This estimation allows for "micro-siting" or individual placement of turbines within a wind farm while minimizing wake losses.

The addition of wakes in an array is difficult to model. A simple model for wake region overlap is shown in Johnson and Thomas [14]. The model indicates a 42% loss in power production for a turbine 3.75D downwind of the first and a 70% loss in power for a 3rd turbine 6.25D from the first and 2.5D from the second. However, experimental data, as summarized by Vermeer et al. [5], would indicate that the third turbine in the row sees little effect from the first, but is significantly affected by the second. It is concluded here that a turbine is only noticeably affected by the closest upstream machine. It is difficult to quantify the addition of wakes while siting a wind farm. Ideally turbines are spaced at distances great enough to negate wake effects; however, this is not always economically feasible due to the cost and availability of real estate in addition to the expense of laying cables and the interconnection of machines and substations. The staggering of turbines can be used to minimize effects but it is difficult to avoid interaction completely because of the conical nature of wind turbine wakes [15]. As a result, wind farms are typically arranged for maximum turbine spacing in the directions of the prevailing winds with closer spacing in the directions receiving less frequent winds. In general, the spacing in the prevailing wind direction ranges from 6-10 rotor diameters and 3-4 diameters in cross-wind directions. Figure 7 illustrates a wind rose with a distinctly dominant wind sector.

The study of wake is not restricted to inter-turbine relations. As the number of wind farms increase globally, the distance between wind farms has been gaining importance. Offshore wake from a small wind farm has been seen to propagate for 14 km [14] over the water. Christian and Hasager [16] used satellite imaging to study wake effects of two large wind farms, Horns Rev and Nysted, off the coast of Denmark. The images show a trail downwind of the farm that propagates for 20 km before near-neutral conditions are reached. Offshore wind farm wake dynamics have been considered to propagate farther than onshore due to less atmospheric turbulence; which is required for wind speed recovery [9]. Without this turbulence, mixing of the wake area with the surrounding atmosphere takes longer and can result in wake effects at a greater distance from the farm. Inter-farm effects for offshore is currently becoming a significant issue in Europe where planned offshore wind capacity has been growing. Corten and Brand [17] discussed the planned installation of 6 GW of capacity over 25 farms of offshore wind in a 10,000 square kilometer area. By the methods described in their work it has been concluded that an inter-farm loss of 5-14% is probable. This is substantial and raises many concerns especially in situations where wind farms are not owned and operated by the same company and the possession of wind resources is debated.

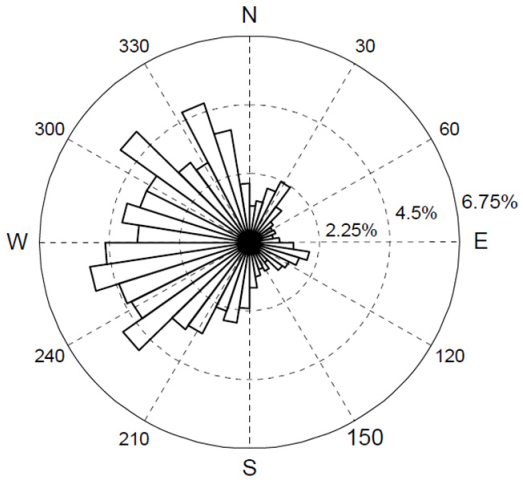

Figure 7. Wind rose indicating percentage of wind direction probability. Data are for the upstream turbine over the six month data set for all power producing winds (3-25 m/s) [11].

Onshore wind farm wake propagation is reduced by complex terrain and vegetation. As stated above, onshore wake propagation has been measured up to 15 rotor diameters downstream of a turbine. While optimal wind turbine spacing has been studied [7, 15Bryony L.D.P and Cagan, J., An Extended Pattern Search Approach to Wind Farm Layout Optimization, Proceedings of ASME IDETC: Design Automation Conference, 2010, 1-10.] further work on the limit of minimum wind farm footprint to maximize profitability may be necessary.

4. Special topics in WAKE

4.1. Wind sector management

Wind sector management refers to a process of attempting to maximize the cumulative wind farm output through an active optimization of wind turbine energy capture. There are currently two common approaches to this technique. One form of wind sector management is concerned with the shutting down of wind turbines downstream of a machine, which is creating a turbulent wake large enough to increase fatigue loads on the turbine. This can be more broadly stated as the curtailment of a wind turbine or turbines during special wind conditions that could cause fatigue damage [18]. The second approach refers to the curtailment of an upstream wind turbine that is producing influential turbulence to increase the

http://dx.doi.org/10.5772/53968

production of downstream turbines and therefore increase the overall production of the farm [14]. Kjaer et al. [19] briefly discussed the concept of stopping a turbine for the purpose of preventing damage upstream or downstream while Neilsen et al. [18] gave an actual method for quantification of the reduction of turbulence intensity for protection of the downstream machines. These approaches will generally result in a decrease of wind farm power production as well. The concept of increasing wind farm production by reducing axial induction has gained most of its attention from Corten and Schaak [20] of the Energy Research Centre of the Netherlands (ECN). A patent has been granted for the strategies developed at ECN [21] after wind tunnel testing showed an overall increase in production of 4.5% in a 6 row arrangement of turbines. The concept was explained in Schepers and Pijl [22] where results from ECN's full scale experimental wind farm were also given. The results from the full scale farm show power gains of less than 0.5% when averaged over all wind conditions. However, performance increase is most noticeable when wind direction causes alignment of turbine wakes and also when wind speeds are below optimum rated speeds. This concept was also discussed in Johnson and Thomas [14] where a theoretical study was completed and control strategy developed which showed gains in wind farm power output. Although the overall increase in power production is not large it is important to note that very little alteration is required to achieve this improvement. A strategic change in control methods with no modification to hardware has the potential to make economic sense. Future research in this area is anticipated.

4.2. Wake influenced yaw positioning

Wind turbines are typically independently controlled, relying on the data collected from the meteorological station situated on the back of the nacelle to dictate response. The turbine continually adjusts the orientation of the nacelle in order to face the best consistent wind direction. They typically only initiate a yaw movement after the new wind direction has been observed for a specified time to avoid constant "hunting" under rapid wind direction fluctuations. The turbines under consideration decrease the necessary consistent wind speed duration required to command a change in yaw position as the wind speed increases. Figure 8 shows data for a range of wind speeds. The Figures represent the downstream nacelle positions subtracted from the upstream nacelle position where a difference of zero represents perfect alignment with the lead upstream turbine. As the wind direction measured by the upstream turbine approaches direct alignment with the turbine array, the downstream turbine increases its yaw misalignment with respect to the upstream turbine. However, there are angles showing consistently large differences in yaw position that are not direct alignment. The Figures show that the nacelle direction offsets change as wind speeds decrease. A nacelle position offset with a greater positive magnitude indicates the downstream turbine remains at an angle counter clockwise from the upstream turbine while a negative offset corresponds with the downstream turbine positioning itself clockwise from the lead upstream machine.

Some patterns can be observed in the different plots although there is significant variation from one wind speed to the next. A steady increase in nacelle position misalignment for the

array occurs in the wake zone, with greater offsets more likely to occur at TA +/- 5 to TA +/- 20 degrees (off wake centre). The first downstream turbine shows the least offset and the third downstream turbine shows the greatest offset. There is a large amount of variation in magnitude and profile of turbine misalignment for each upstream (free stream) wind speed range shown, however a distinct increase is evident for the nacelle position range encompassing the wake zone as defined above. One possible cause of misalignment peaks are the vortex streets on the outer edges of the upstream wake profile. When free stream wind speed is not at turbine alignment (i.e. not coincident with the turbine array line) the downstream turbine instrumentation may experience increased turbulence and rotational velocity in the wind. This could be due to the wake's outer edge of tip vortices passing over the wind speed and direction sensors of the downstream turbine. Similar results are evident for other arrays within the wind farm. An array of six wind turbines with identical linear alignment and spacing shows an increase in yaw misalignment within the wake region (Figure 9). The first downstream turbine has the smallest offset with progressively larger offsets down the array. There are distinct peaks in the alignment offset with an approximate return to 0 (+/- 2 deg). However, the two additional turbines for this arrangement complicate the interactions. As shown in Figure 9, the third downstream turbine agrees with the pattern in magnitude but its direction of rotation is opposite to the rest of the turbines in the array. Furthermore, the separation of nacelle position offset between the downstream turbines is less defined. This adds to the unpredictability of the yaw behaviour within the array, since it is not obvious which turbine will show the greatest offset or at what wind direction it will occur. A potential source of some of these complications may be due to the mixing of each subsequent turbine vortex street when not in direct turbine alignment as discussed earlier. This lack of distinction is further evidenced in the power coefficient profile shown in Figure 10. Although similar to the power coefficient profile given for the array of four turbines in Figure 5, the separation of the lines for each downstream turbine is less defined. The third downstream turbine once again exhibits unique behaviour.

4.3. Turbine operational sensitivity to wake

With wake interactions accepted as an unavoidable fact it becomes useful to quantify the sensitivity of the operation of two turbines to this interaction. The purpose of quantification relates to the mitigation of negative effects and optimization of performance within the wake region. McKay et al. [23] presents the application of the Extended Fourier Amplitude Sensitivity Test method for determination of downstream turbine power output to upstream turbine operational parameters.

A global sensitivity analysis of eight fundamental operating parameters on wind turbine power output is performed. By comparing the sensitivities of normal operation to wake conditions, a better understanding of group turbine behavior is obtained. The most significant characteristic that is evident in the presented analysis is the effect that the introduction of wake has on turbine performance. For a turbine operating in the wake of an upstream machine, power production is most sensitive to wind speed standard deviation above all parameters included in this study, excluding wind speed itself as shown in Figure 11.

http://dx.doi.org/10.5772/53968

(a)

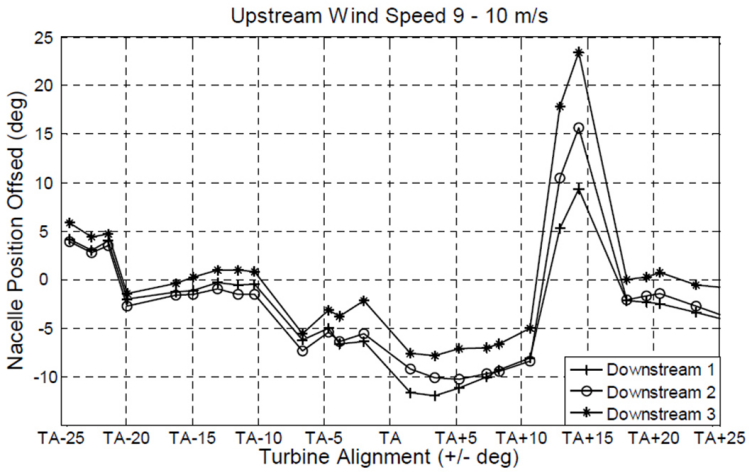

(b)

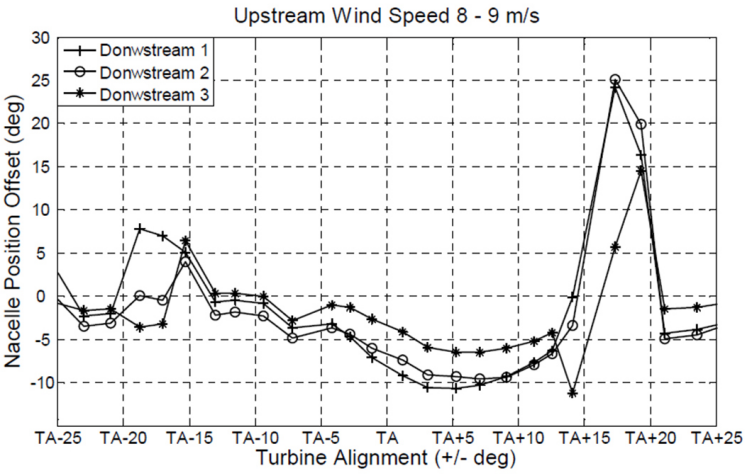

(c)

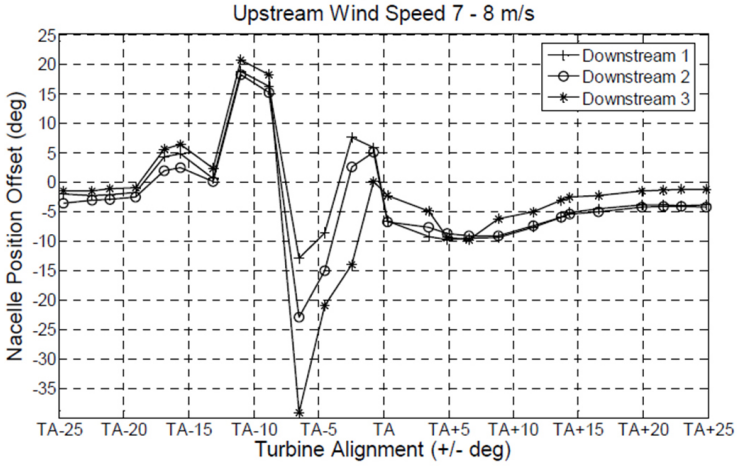
Upstream Wind Speed 7 - 8 m/s
Downstream 1
Downstream 2
Downstream 3
Nacelle Position Offset (deg)
25
20
15
10
5
0
-5
-10
-15
-20
-25
-30
-35
TA-25 TA-20 TA-15 TA-10 TA-5 TA TA+5 TA+10 TA+15 TA+20 TA+25
Turbine Alignment (+/- deg)

(d)

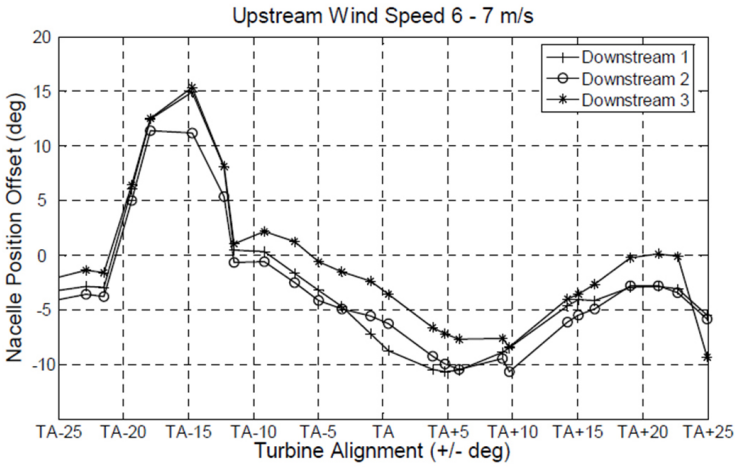
Upstream Wind Speed 6 - 7 m/s
Downstream 1
Downstream 2
Downstream 3
Nacelle Position Offset (deg)
20
15
10
5
0
-5
-10
TA-25 TA-20 TA-15 TA-10 TA-5 TA TA+5 TA+10 TA+15 TA+20 TA+25
Turbine Alignment (+/- deg)

http://dx.doi.org/10.5772/53968

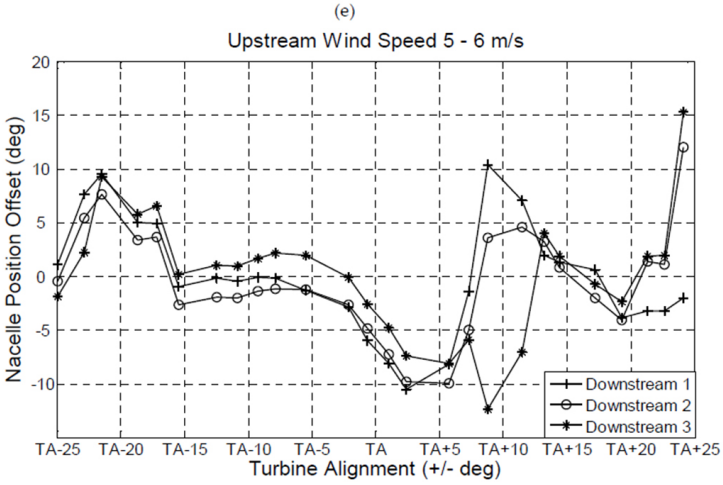

Figure 8. Nacelle misalignment between wind turbines for 6 months averaged data. a) 9-10 m/s, b) 8-9 m/s, c) 7-8 m/s, d) 6-7 m/s, e) 5-6 m/s/ Lead upstream nacelle position is subtracted from each downstream turbine nacelle position [11].

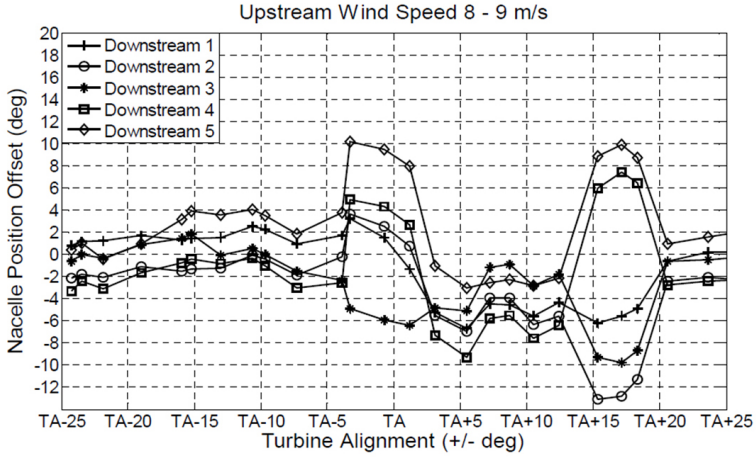

Figure 9. Nacelle misalignment between wind turbines in array of 6 machines for 6 months averaged data. Lead upstream nacelle position is subtracted from each downstream turbine nacelle position [11].

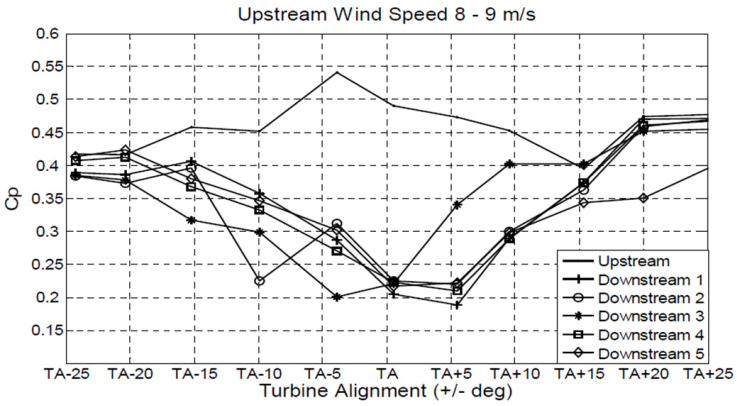

Figure 10. Six turbine array power coefficient profile for an upstream turbine wind speed of 8-9 m/s averaged over 6 months [11].

In essence, the method assigns a frequency to the upstream turbine operational parameters under consideration. The frequency data is input into a model which provides a power output signal related to the downstream turbine containing all of the frequency data in varying proportions. A Fourier transform is performed on the output and the resulting frequency content is ranked according to the operational parameters significance. This is shown in Figure 11. The parameters chosen for the study along with their significance rankings are given in Table 1.

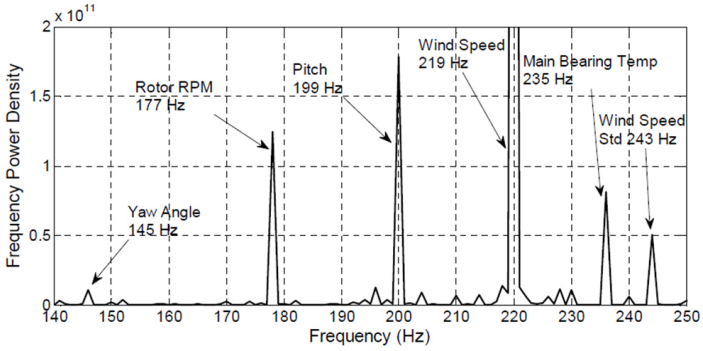

Figure 11. Frequency content of power signal extracted from wake condition data [23].

http://dx.doi.org/10.5772/53968

Input factor	Total Sensitivity Index ($S_{Ti\ wake}$)
Wind Speed	0.0438
Pitch	0.0234
Rotor RPM	0.0268
Main Bearing Temperature	0.0263
Wind Speed Std	0.0309
Ambient Temperature	0.0206
Yaw Angle	0.0203
Yaw Angle Std	0.0172

Table 1. Sensitivity indices for eFAST method applied to wake conditions [23].

The comparison of results from the single turbine and wake conditions is given in Figure 12. Rotor RPM and wind speed are clearly the dominant features in the Figure followed by relatively similar magnitudes for each of the remaining parameters. Two main features become apparent. Firstly power output is more sensitive to rotor speed than wind speed under normal operating conditions while the reverse is true under wake conditions. The turbines under study are designed to operate at an optimum tip speed ratio therefore the control systems will work to keep the rotor speed at specific RPMs depending on the wind conditions. This links rotor rpm directly to power output. In other words any changes in rotor speed will directly affect the power output of the turbine resulting in high sensitivity. The same is true of wake conditions as well. However, it has been shown above that for a turbine experiencing wake, changes in wind speed cause changes in power loss. Very high wind speeds reduce the power losses due to wake while wind speeds falling between 5 and 11 m/s can have a substantial effect on production. As a result, the power output becomes dependent on wind speed for power losses in wake in addition to the dependence of normal, non-wake operation.

Secondly, the wind speed standard deviation's increases in sensitivity under wake. This is expected since the extraction of power by the upstream turbine leaves a turbulent rotating wake region. Therefore, variance in wind speed and direction increases. The increase is directly linked to a loss in power for the downstream turbine, increasing sensitivity. By quantifying the sensitivity it is shown that changes in wind speed standard deviation are more critical to power production than all other parameters other than wind speed.

Utilization of this method to identify other power output sensitivities is possible. By further applying this method to more complex data sets, qualitative comparisons can be quantified, and subsequently, priorities can be placed on turbine operational parameters. This can be used for the purpose of optimizing performance or increasing turbine reliability. The results also suggest that through monitoring sensitivity indices, downstream machines may be able

to determine whether or not they are in a wake. Depending on the severity of the turbulence in the wake the turbine could be controlled to mitigate negative effects or improve performance. Additionally, the method could provide another tool to assess the efficacy of the original siting of existing wind farms.

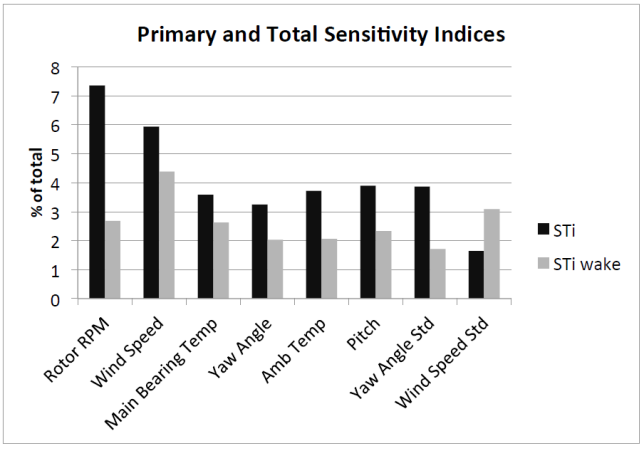

Figure 12. Sensitivity index comparison for wake and non-wake conditions [23].

5. Moving forward

As the wind industry matures major wind farm developers continue to add to their experience in wake loss estimation. These individual organizations continue to refine their predictions and add to databases based on this experience promoting an improved understanding of wake effects and reduced uncertainty in the planning stages. Academic research continues in this area. However, strong demand continues for larger and larger wind farms, particularly offshore. With increased wind farm densities both on and offshore, inter-farm wake dynamics have become a growing concern. Subsequently, there is a notable need for highly reliable wake mixing and long distance wake propagation models. As evidenced in this Chapter, opportunities remain for continued commercial wind farm optimization.

Author details

Phillip McKay[1], Rupp Carriveau[2], David S-K Ting[3] and Timothy Newson[4]

1 Wind Energy Institute of Canada, Canada

2 Department of Civil and Environmental Engineering, University of Windsor, Canada

http://dx.doi.org/10.5772/53968

3 Department of Mechanical, Automotive, and Materials Engineering, University of Windsor, Canada

4 Department of Civil and Environmental Engineering, University of Western Ontario, Canada

References

[1] McKay, P., Carriveau, R. and Ting, D. S-K., Farm Wide Dynamics: The Next Critical Wind Energy Frontier, Wind Engineering, 2011, 35(4), 397-418.

[2] Burton, T., Sharpe, D., Jenkins, N. and Bossanyi, E., Wind Energy Handbook, John Wiley & Sons Ltd, Chichester, 2001.

[3] Manwell, J.F., McGowan, J.G. and Rogers, A.L., Wind Energy Explained, John Wiley & Sons Ltd, Chichester, 2002.

[4] Thørgensen, M., Sørensen, T., Nielsen, P., Grotzner, A. and Chun S., Introduction to Wind Turbine Wake Modeling and Wake Generated Turbulence. EMD International A/S, 2006, 1-2.

[5] Vermeera, L.J., Sørensen, J.N. and Crespoc, A., Wind turbine wake aerodynamics, Progress in Aerospace Sciences, 2003, 39, 467-510.

[6] Helmis, C. G., Papadopoulos, K. H., Asimakopoulos, D. N., Papageorgas, P. G. and Soilemes, A. T., An experimental study of the near-wake structure of a wind turbine operating over complex terrain, Solar Engineering, 1995, 54, (6), 413-428.

[7] Marmidis, G., Lazarou, S. and Pyrgioti, E., Optimal placement of wind turbines in a wind park using Monte Carlo simulation, Renewable Energy, 2008, 33, 1455-1460.

[8] Hojstrup, J., Spectral coherence in wind turbine wakes, Journal of Wind Engineering and Industrial Aerodynamics, 1999, 80, 137-146.

[9] Department of Wind Energy, Risoe National Laboratory Analytical Modelling of Large Wind Farm Clusters, Roskilde, 2002.

[10] Frandsen, S. and Barthelmie, R., Local Wind Climate Within and Downwind of Large Offshore Wind Turbine Clusters, Wind Engineering, 2002, 26, (1), pp 51-58.

[11] McKay, P., Carriveau, R. and Ting, D. S-K., Wake Impacts on Elements of Wind Turbine Performance and Yaw Alignment. To appear in Wind Energy 2012. *Published online in Wiley Online Library (wileyonlinelibrary.com). DOI: 10.1002/we.544.*

[12] Barthelmie RJ, Pryor SC, Frandsen ST, Hansen KS, Schepers JG, Rados K, Schlez W, Neubert A, Jensen LE and Neckelmann S, Quantifying the Impact of Wind Turbine Wakes on Power Output at Offshore Wind Farms, Journal of Atmospheric and Oceanic Technology, 2010, 27, 1302-1319.

[13] Brower, A. Wind Resource Assessment: A Practical Guide to Developing a Wind Project. *John Wiley & Sons Inc. Hoboken, New Jersey, USA 2012*; 250-256

[14] Johnson, K.E. and Thomas, N., Wind farm control: addressing the aerodynamic interaction amoung wind turbines, 2009 American Control Conference, 2009, 2104 - 2109.

[15] Bryony L.D.P and Cagan, J., An Extended Pattern Search Approach to Wind Farm Layout Optimization, Proceedings of ASME IDETC: Design Automation Conference, 2010, 1-10.

[16] Christiansen, M.B. and Hasager, C., Wake effects of large offshore wind farms identified from satellite SAR, Remote Sensing of Environment, 2005, 98, 251-268.

[17] Corten, G.P. and Brand, A.J., Resource Decrease by Large Scale Wind Farming, 2004,

[18] Nielsen, M., Jørgensen, H.E. and Frandsen, S.T., Wind and wake models for IEC 61400-1 site assessment, 2009,

[19] Kjaer, C., Douglas, B. and Luga, D., EWEA Wind Energy - The Facts, Earthscan, London, 2009,

[20] Corten, G.P. and Schaak, P., Heat and Flux - Increase of Wind Farm Production by Reduction of the Axial Induction, European Wind Energy Conference, 2003, 1-8.

[21] Corten, G.P. and Schaak, P., Heat and Flux, Patent Number WO2004111446, 2003,

[22] Schepers, J.G. and van der Pijl, S.P., Improved modelling of wake aerodynamics and assessment of new farm control strategies, Journal of Physics: Conference Series, 2007, 75, 1-8.

[23] McKay, P., Carriveau, R., Ting, D. S-K. and Johrendt, J. Application of the Extended Fourier Amplitude Sensitivity Test to Turbine Wakes, Poster Presentation, WINDPOWER 2012, Atlanta, GA, June 3-6 2012.

Section 2

Turbine Structural Response

Chapter 4

Aeroelasticity of Wind Turbines Blades Using Numerical Simulation

Drishtysingh Ramdenee, Adrian Ilinca and
Ion Sorin Minea

Additional information is available at the end of the chapter

http://dx.doi.org/10.5772/52281

1. Introduction

With roller coaster traditional fuel prices and ever increasing energy demand, wind energy has known significant growth over the last years. To pave the way for higher efficiency and profitability of wind turbines, advances have been made in different aspects related to this technology. One of these has been the increasing size of wind turbines, thus rendering the wind blades gigantic, lighter and more flexible whilst reducing material requirements and cost. This trend towards gigantism increases risks of aeroelastic effects including dire phenomena like dynamic stall, divergence and flutter. These phenomena are the result of the combined effects of aerodynamic, inertial and elastic forces. In this chapter, we are presenting a qualitative overview followed by analytical and numerical models of these phenomena and their impacts on wind turbine blades with special emphasize on Computational Fluid Dynamics (CFD) methods. As definition suggests, modeling of aeroelastic effects require the simultaneous analysis of aerodynamic solicitations of the wind flow over the blades, their dynamic behavior and the effects on the structure. Transient modeling of each of these characteristics including fluid-structure interaction requires high level computational capacities. The use of CFD codes in the preprocessing, solving and post processing of aeroelastic problems is the most appropriate method to merge the theory with direct aeroelastic applications and achieve required accuracy. The conservation laws of fluid motion and boundary conditions used in aeroelastic modeling will be tackled from a CFD point of view. To do so, the chapter will focus on the application of finite volume methods to solve Navier-Stokes equations with special attention to turbulence closure and boundary condition implementation. Three aeroelastic phenomena with direct application to wind turbine blades are then studied using the proposed methods. First, dynamic stall will be used as case study to illustrate

the traditional methodology of CFD aeroelastic modeling: mathematical analysis of the phenomenon, choice of software, computational domain calibration, mesh optimization and turbulence and transition model validation. An S809 airfoil will be used to illustrate the phenomenon and the obtained results will be compared to experimental ones. The divergence will be then studied both analytically and numerically to emphasize CFD capacity to model such a complex phenomenon. To illustrate divergence and related study of eigenvalues, an experimental study conducted at NASA Langley will be analyzed and used for comparison with our numerical modeling. In addition to domain, mesh, turbulence and transition model calibration, this case will be used to illustrate fluid-structure interaction and the way it can be tackled in numerical models. Divergence analysis requires the modeling of flow parameters on one side and the inertial and structural behavior of the blade on the other side. These two models should be simultaneously solved and continuous exchange of data is essential as the fluid behavior affects the structure and vice-versa.

This chapter will conclude with one of the most dangerous and destructive aeroelastic phenomena – the flutter. Analytical models and CFD tools are applied to model flutter and the results are validated with experiments. This example is used to illustrate the application of aeroelastic modeling to predictive control. The computational requirements for accurate aeroelastic modeling are so important that the calculation time is too large to be applied for real time predictive control. Hence, flutter will be used as an example to show how we can use CFD based offline results to build Laplacian based faster models that can be used for predictive control. The results of this model will be compared to experiments.

2. Characteristics of aeroelastic phenomena

Aeroelasticity refers to the science of the interaction between aerodynamic, inertial and elastic effects. Aeroelastic effects occur everywhere but are more or less critical. Any phenomenon that involves a structural response to a fluid action requires aeroelastic consideration. In many cases, when a large and flexible structure is submitted to a high intensity variable flow, the deformations can be very important and become dangerous. Most people are familiar with the “auto-destruction” of the Tacoma Bridge. This bridge, built in Washington State, USA, 1.9 km long, was one of the longest suspended bridges of its time. The bridge connecting the Tacoma Narrows channel collapsed in a dramatic way on Thursday, November 7, 1940. With winds as high as 65-75 km/h, the oscillations increased as a result of fluid-structure interaction, the base of Aeroelasticity, until the bridge collapsed. Recorded videos of the event showed an initial torsional motion of the structure combined very turbulent winds. The superposition of these two effects, added to insufficient structural dumping, amplified the oscillations. Figure 1 below illustrates the visual response of a bridge subject to aeroelastic effects due to variable wind regimes. The simulation was performed using multiphysics simulation on ANSYS-CFX software. Some more details on similar aeroelastic modelling can be viewed from [1], [2], [3] and [4].

http://dx.doi.org/10.5772/52281

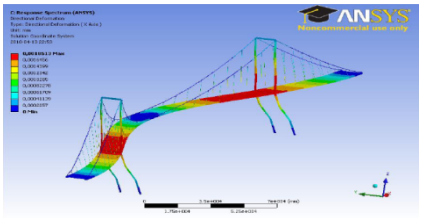

Figure 1. Aeroelastic response of a bridge

In an attempt to increase power production and reduce material consumption, wind turbines' blades are becoming increasingly large yet, paradoxically, thinner and more flexible. The risk of occurrence of damaging aeroelastic effects increases significantly and justifies the efforts to better understand the phenomena and develop adequate design tools and mitigation techniques. Divergence and flutter on an airfoil will be used as introduction to aeroelastic phenomena. When a flexible structure is subject to a stationary flow, equilibrium is established between the aerodynamic and elastic forces (inertial effects are negligible due to static condition). However, when a certain critical speed is exceeded, this equilibrium is disrupted and destructive oscillations can occur. This is illustrated with Figure 2 where α is the angle of attack due to a torsional movement as a result of aerodynamic solicitations.

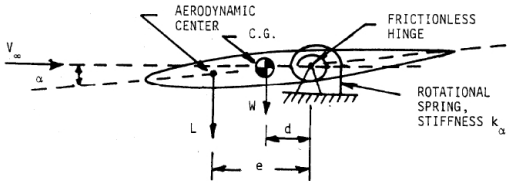

Figure 2. Airfoil model to illustrate aerodynamic flutter

If we consider an angle of attack sufficiently small such that $cos\alpha \approx 1$ and $sin\alpha \approx \alpha$, and writing the equilibrium of the moments, M, with respect to the centre of the rotational spring, we have:

$\sum M=0$

$$Le + Wd - K_{\alpha}\alpha=0 \quad (1)$$

Where the lift L is:

$$L = qSC_l=qSM_0\alpha \quad (2)$$

S, surface area of the profile, C_l is the lift coefficient, M_0 is the moment coefficient. This leads to an angle of attack at equilibrium corresponding to:

$$\alpha = \frac{Wd}{K_\alpha - qSM_0e} \tag{3}$$

For a zero flow condition, the angle of attack α_z, is such that:

$$\alpha_Z = \frac{Wd}{K_\alpha} \tag{4}$$

Divergence occurs when denominator in equation (3) becomes 0 and this corresponds to a dynamic pressure, q_D expressed as:

$$q_D = \frac{K_\alpha}{eSM_0} \tag{5}$$

Therefore:

$$\alpha = \frac{\alpha_z}{\left[1 - \left(\frac{q}{q_D}\right)\right]} \tag{6}$$

When velocity increases such that dynamic pressure q approaches critical dynamic pressure q_D, the angle of attack dangerously increases until a critical failure value – divergence. This is solely a structural response due to increased aerodynamic solicitation due to fluid-structure interaction. This is an example of a *static* aeroelastic phenomenon as it involves no vibration of the airfoil. Flutter is an example of a *dynamic* aeroelastic phenomenon as it occurs when structure vibration interacts with fluid flow. It arises when structural damping becomes insufficient to damp aerodynamic induced vibrations. Flutter can appear on any flexible vibrating object submitted to a strong flow with positive retroaction between flow fluctuations and structural response. When the energy transferred to the blade by aerodynamic excitation becomes larger than the normal dynamic dissipation, the vibration amplitude increases dangerously. Flutter can be illustrated as a superposition of two structural modes – the angle of attack (pitch) torsional motion and the plunge motion which characterises the vertical flexion of the tip of the blade. Pitch is defined as a rotational movement of the profile with respect to its elastic center. As velocity increases, the frequencies of these oscillatory modes coalesce leading to flutter phenomenon. This may start with a rotation of the blade section (at t=0 s in Figure 3). The increased angle amplifies the lift such that the section undertakes an upward vertical motion. Simultaneously, the torsional rigidity of the structure recoils the profile to its zero-pitch condition (at t=T/4 in Figure 3). The flexion rigidity of the structure tends to retain the neutral position of the profile but the latter then tends to a negative angle of attack (at t = T/2 in Figure 3). Once again, the increased aerodynamic force imposes a downward vertical motion on the profile and the torsional rigidity of the latter tends to a zero angle of attack. The cycle ends when the profile retains a neutral position with a positive angle of attack. With time, the vertical movement tends to damp out whereas the rotational movement diverges. If freedom is given to the motion to repeat, the rotational forces will lead to blade failure.

http://dx.doi.org/10.5772/52281

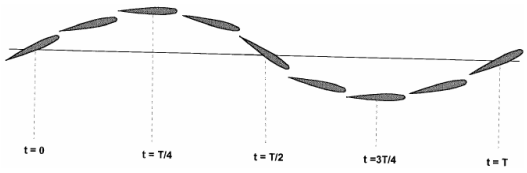

Figure 3. Illustration of flutter movement

3. Mathematical analytical models

Several examples of aeroelastic phenomena are described in the scientific literature. When it comes to aeroelastic effects related to wind turbines, three of the most common and dire ones are dynamic stall, aerodynamic divergence and flutter. In this section, we will provide a summarized definition of these aeroelastic phenomena with associated mathematical analytical models. Few references related to analytic developments of aeroelastic phenomena are [10], [11] and [12].

3.1. Dynamic stall

In fluid dynamics, the stall is a lift coefficient reduction generated by flow separation on an airfoil as the angle of attack increases. Dynamic stall is a nonlinear unsteady aerodynamic effect that occurs when there is rapid change in the angle of attack that leads vortex shedding to travel from the leading edge backward along the airfoil [14]. The analytical development of equations characterizing stall will be performed using illustrations of Figures 4 and 5. The lift per unit length, expressed as L is given by:

$$L = c_L \frac{1}{2} \rho V^2 c \tag{7}$$

Where

- c_L is the lift coefficient
- ρ is the air density
- c is the chord length of the airfoil

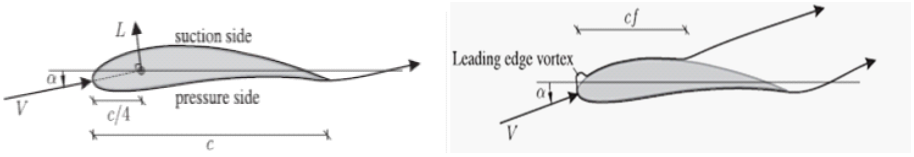

Figure 4. Illustration of an airfoil used for analytical development of stall related equations

We will, first, present static stall as described in [13]. During stationary flow conditions, no flow separation occurs and the lift, L, acts approximately at the quarter cord distance from the leading edge at the pressure (aerodynamic) centre. For small values of α, L varies linearly with α. Stall happens at a critical angle of attack whereby the lift reaches a maximum value and flow separation on the suction side occurs.

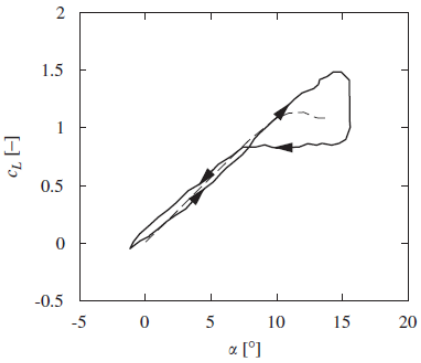

Figure 5. Lift coefficient under static and dynamic stall conditions (dashed line for steady conditions, plain line for unsteady conditions)

For unsteady conditions, a delay exists prior to reaching stability and is an essential condition for building analytical stall models [15]. In such case, we can observe a smaller lift for an increasing angle of attack (AoA) and a larger one for decreasing AoA when compared with a virtually static condition. In a flow separation condition, we can observe a more significant delay which expresses itself with harmonic movements in the flow which affects the aerodynamic stall phenomenon. Figure 5, an excerpt from [16], shows that for harmonic variations of the AoA between 0^o and 15^o, the onset of stall is delayed and the lift is considerably smaller for the decreasing AoA trend than for the ascending one. Hence, as expressed by Larsen et al. [17], dynamic stall includes harmonic motion separated flows, including formation of vortices in the vicinity of the leading edge and their transport to the trailing edge along the airfoil. Figures 6-9, which are excerpts from [18], illustrate these phenomena.

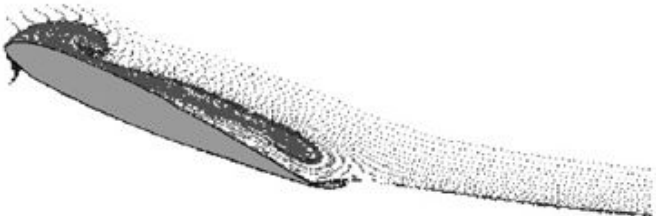

Figure 6. Aerodynamic stall mechanism- Onset of separation on the leading edge

http://dx.doi.org/10.5772/52281

Figure 7. Aerodynamic stall mechanism- Vortex creation at the leading edge

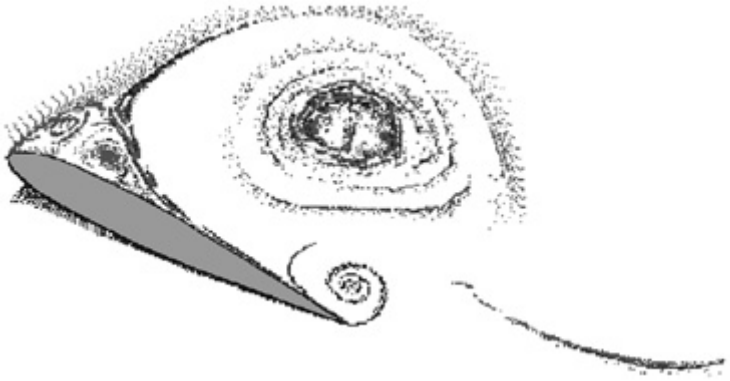

Figure 8. Aerodynamic stall mechanism- Vortex separation at the leading edge and creation of vortices at the trailing edge

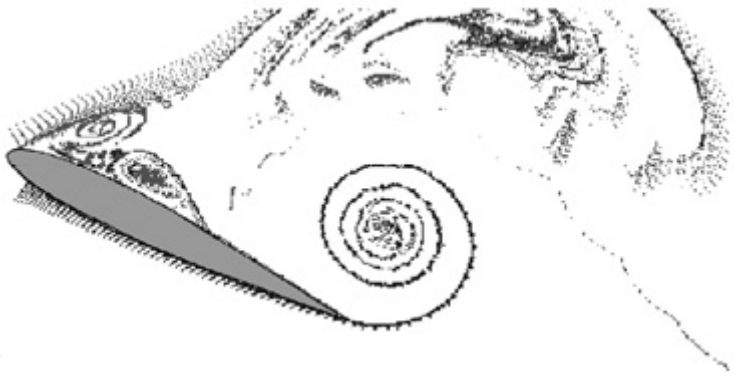

Figure 9. Aerodynamic stall mechanism – Vortex shedding at the trailing edge

Stall phenomenon is strongly non-linear such that a clear cut analytical solution model is impossible to achieve. This complex phenomenon requires consideration of numerous parameters, study of flow transport, boundary layer analysis (shape factor and thickness), vortex creation and shedding as well as friction coefficient consideration in the boundary layer. The latter helps in the evaluation of separation at the leading edge and is important for aeroelastic consideration. The proper modelling of transition from laminar to turbulent flow is also essential for accurate prediction of stall parameters.

3.2. Divergence

We consider a simplified aeroelastic system of the NACA0012 profile to better understand the divergence phenomenon and derive the analytical equation for the divergence speed. Figure 10 illustrates a simplified aeroelastic system, the rigid NACA0012 profile mounted on a torsional spring attached to a wind tunnel wall. The airflow over the airfoil is from left to right. The main interest in using this model is the rotation of the airfoil (and consequent twisting of the spring), α, as a function of airspeed. If the spring were very stiff and/or airspeed very slow, the rotation would be rather small; however, for flexible spring and/or high flow velocities, the rotation may twist the spring beyond its ultimate strength and lead to structural failure.

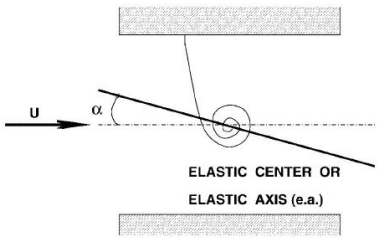

Figure 10. Simplified aeroelastic model to illustrate divergence phenomenon

The airspeed at which the elastic twist increases rapidly to the point of failure is called the divergence airspeed, U_D.. This phenomenon, being highly dangerous and prejudicial for wind blades, makes the accurate calculation of U_D very important. For such, we define C as the chord length and S as the rigid surface. The increase in the angle of attack is controlled by a spring of linear rotation attached to the elastic axis localized at a distance e behind the aerodynamic centre. The total angle of attack measured with respect to a zero lift position equals the sum of the initial angle α_r and an angle due to the elastic deformation θ, known as the elastic twist angle.

$$\alpha = \alpha_r + \theta \tag{8}$$

The elastic twist angle is proportional to the moment at the elastic axis:

http://dx.doi.org/10.5772/52281

$$\theta = C^{\theta\theta} T \tag{9}$$

where $C^{\theta\theta}$ is the flexibility coefficient of the spring. The total aerodynamic moment with respect to the elastic axis is given by:

$$T = (C_l e + C_m c) qS \tag{10}$$

where

- C_l is the lift coefficient
- C_m is moment coefficient
- q is the dynamic pressure
- S is the rigid surface area of the blade section

The lift coefficient is related to the angle of attack measured with respect to a zero lift condition as follows:

$$C_l = \frac{\partial C_l}{\partial \alpha}\left(\alpha_r + \theta\right) \tag{11}$$

Here $\frac{\partial C_l}{\partial \alpha}$ represents the slope of the lift curve. The elastic twist angle θ, can be obtained by simple mathematical manipulations of the three previous equations:

$$T = \left[\frac{\partial C_l}{\partial \alpha}(\alpha_r + \theta).e + C_m c\right] qS \tag{12}$$

Hence,

$$\theta = C^{\theta\theta}\left[\frac{\partial C_l}{\partial \alpha}(\alpha_r + \theta).e + C_m c\right] qS \tag{13}$$

$$\theta = C^{\theta\theta}\left[\frac{\partial C_l}{\partial \alpha}\alpha_r eqS + \frac{\partial C_l}{\partial \alpha}\theta eqS + C_m cqS\right] \tag{14}$$

Regrouping θ :

$$\theta\left[1 - \frac{\partial C_l}{\partial \alpha} C^{\theta\theta} eqS\right] = C^{\theta\theta}\left[\frac{\partial C_l}{\partial \alpha}\alpha_r eqS + C_m cqS\right] \tag{15}$$

This leads to:

$$\theta = C^{\theta\theta}\frac{\frac{\partial C_l}{\partial \alpha}\alpha_r eqS + C_m cqS}{1 - \frac{\partial C_l}{\partial \alpha} C^{\theta\theta} eqS} \tag{16}$$

We can note that for a given value of the dynamic pressure q, the denominator tends to zero such that the elastic twist angle will then tend to infinity. This condition is referred to as aerodynamic divergence. When the denominator tends to zero:

$$1 - \frac{\partial C_l}{\partial \alpha} C^{\theta\theta} eqS = 0 \tag{17}$$

The dynamic pressure is given by:

$$q = \frac{1}{2}\rho v^2 \tag{18}$$

Thus, we come up with:

$$1 - \frac{\partial C_l}{\partial \alpha} C^{\theta\theta} e \frac{1}{2}\rho v^2 S = 0 \tag{19}$$

Hence, the divergence velocity can be expressed as:

$$U_D = \sqrt{\frac{1}{C^{\theta\theta}\frac{\partial C_l}{\partial \alpha} e \frac{1}{2}\rho S}} \tag{20}$$

To calculate the theoretical value of the divergence velocity, certain parameters need to be found. These are $C^{\theta\theta}$, which is specific to the modeled spring, S and e being inherent to the airfoil, ρ depends upon the used fluid and $\frac{\partial C_l}{\partial \alpha}$ depends both on the shape of the airfoil and flow conditions [23]. We note that as divergence velocity is approached, the elastic twist angle will increase in a very significant manner towards infinity [24]. However, computing is finite and cannot model infinite parameters. Therefore, the value of the analytical elastic twist angle is compared with the value found by the coupling. In the case wherein the elastic twist angle introduces no further aerodynamic solicitations, by introducing $\alpha = \alpha_r$, and resolving for the elastic twist angle, we have:

$$\theta_r = C^{\theta\theta} T = C^{\theta\theta}\left(\frac{\partial C_l}{\partial \alpha} e\, \alpha_r + C_m c\right) qS \tag{21}$$

Hence:

$$\theta = \frac{\theta_r}{1 - \frac{\partial C_l}{\partial \alpha} C^{\theta\theta} eqS} \tag{22}$$

which leads to:

http://dx.doi.org/10.5772/52281

$$\theta = \frac{\theta_r}{1 - \frac{q}{q_D}} = \frac{\theta_r}{1 - \left(\frac{U}{U_D}\right)^2} \tag{23}$$

Hence, we note that the theoretical elastic twist angle depends on the divergence speed and the elastic twist angle calculated whilst considering that it triggers no supplementary aerodynamic solicitation. The latter is calculated by solving for the moment applied on the profile at the elastic axis (T) during trials in steady mode. These trials are conducted using the k-ω SST intermittency transitional turbulence model with a 0.94 intermittency value [25]. In this section, we will present only the expression used to calculate the divergence speed. The development of this expression and the analytical calculation of a numerical value of the divergence speed are detailed in [28]:

$$U_D = \sqrt{\frac{1}{C^{\theta\theta} \frac{\partial C_l}{\partial \alpha} \frac{\rho}{2} eS}} \tag{24}$$

Detailed eigen values and eigenvectors analysis related to divergence phenomenon is presented in [27].

3.3. Aerodynamic flutter

As previously mentioned, flutter is caused by the superposition of two structural modes – pitch and plunge. The pitch mode is described by a rotational movement around the elastic centre of the airfoil whereas the plunge mode is a vertical up and down motion at the blade tip. Theodorsen [16-18] developed a method to analyze aeroelastic stability. The technique is described by equations (61) and (62). α is the angle of attack (AoA), α_0 is the static AoA, C(k) is the Theodorsen complex valued function, h the plunge height, L is the lift vector positioned at 0.25 of the chord length, M is the pitching moment about the elastic axis, U is the free velocity, ω is the angular velocity and a, b, d_1 and d_2 are geometrical quantities as shown in Figure 11.

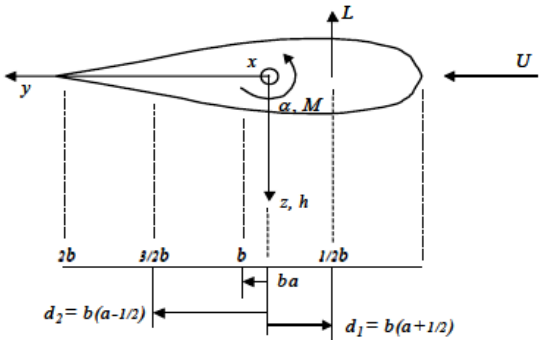

Figure 11. Model defining parameters

$$L = 2\pi\rho U^2 b\left\{\frac{i\omega C(k)h_0}{U} + C(k)\alpha_0 + [1 + C(k)(1 - 2a)]\frac{i\omega b\alpha_0}{2U} - \frac{\omega^2 b h_0}{2U^2} + \frac{\omega^2 b^2 a\alpha_0}{2U^2}\right\} \tag{25}$$

$$M = 2\pi\rho U^2 b\left\{d_1\left[\frac{i\omega C(k)h_0}{U} + C(k)\alpha_0 + [1 + C(k)(1 - 2a)]\frac{i\omega b\alpha_0}{2U}\right] + d_2\frac{i\omega b\alpha_0}{2U} - \frac{\omega^2 b^2 a}{2U^2}h_0 + \left(\frac{1}{8} + a^2\right)\frac{\omega^2 b^3\alpha_0}{2U^2}\right\} \tag{26}$$

Theodorsen's equation can be rewritten in a form that can be used and analyzed in Matlab Simulink as follows:

$$L = 2\pi\rho U^2 b\left\{\frac{C(k)}{U}\dot{h} + C(k)\alpha + [1 + C(k)(1 - 2a)]\right]\frac{b}{2U}\dot{\alpha} + \frac{b}{2U^2}\ddot{h} - \frac{b^2 a}{2U^2}\ddot{\alpha}\Big\} \tag{27}$$

$$M = 2\pi\rho U^2 b\left\{d_1\left[\frac{C(k)\dot{h}}{U} + C(k)\alpha + \left[1 + C(k)\left(1 - 2a\right)\frac{b}{2U}\dot{\alpha}k\right]\right] + d_2\frac{b}{2U}\dot{\alpha} + \frac{ab^2}{2U^2}\ddot{h} - \left(\frac{1}{8} + a^2\right)\frac{b^3\ddot{\alpha}}{2U^2}\right\} \tag{28}$$

3.3.1. Flutter movement

The occurrence of the flutter has been illustrated in Section 2 (Figure 3). To better understand this complex phenomenon, we describe flutter as follows: aerodynamic forces excite the mass – spring system illustrated in Figure 12. The plunge spring represents the flexion rigidity of the structure whereas the rotation spring represents the rotation rigidity.

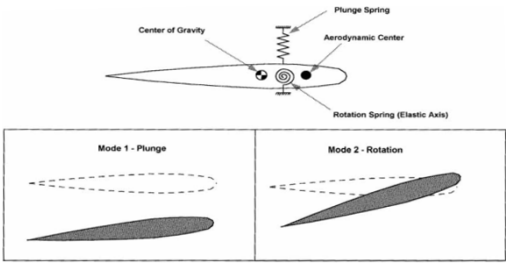

Figure 12. Illustration of both pitch and plunge

3.3.2. Flutter equations

The flutter equations originate in the relation between the generalized coordinates and the angle of attack of the model that can be written as:

$$\alpha(x, y, t) = \theta_T + \theta(t) + \frac{\dot{h}(t)}{U_0} + \frac{l(x)\dot{\theta}(t)}{U_0} - \frac{w_g(x, y, t)}{U_0} \tag{29}$$

The Lagrangian form equations are constructed for the mechanical system. The first one corresponds to the vertical displacement z and the other is for the angle of attack α:

http://dx.doi.org/10.5772/52281

$$J_0\ddot{\alpha} + mdcos(\alpha)\ddot{z} + c(\alpha - \alpha_0) = M_0 \tag{30}$$

$$m\ddot{z} + mdcos(\alpha)\ddot{\alpha} - msin(\alpha)\dot{\alpha}^2 + kz = F_Z \tag{31}$$

Numerical solution of these equations requires expressing F_z and M_o as polynomials of α. Moreover, $F_z(\alpha) = \frac{1}{2}\rho S V^2 C_z(\alpha)$ and $M_o(\alpha) = \frac{1}{2}\rho L S V^2 C_{m0}(\alpha)$ for S being the surface of the blade, C_z, the lift coefficient, C_{m0} being the pitch coefficient, F_z being the lift, M_o, the pitch moment. C_z and C_m values are extracted from NACA 4412 data. Third degree interpolations for C_z and C_m with respect to the AoA are given below:

$C_z = -0.0000983\,\alpha^3 - 0.0003562\alpha^2 + 0.1312\alpha + 0.4162$

$C_{m0} = -0.00006375\alpha^3 + 0.00149\alpha^2 - 0.001185\,\alpha - 0.9312$

These equations will be used in the modeling of a lumped representation of flutter presented in the last section of this chapter.

4. Computational fluid dynamics (CFD) methods in aeroelastic modeling

Aeroelastic modeling of wind blades require complex representation of both fluid flows, including turbulence, and structural response. Fluid mechanics aims at modeling fluid flow and its effects. When the geometry gets complex (flow becomes unsteady with turbulence intensity increasing), it is impossible to solve analytically the flow equations. With the advent of high efficiency computers, and improvement in numerical techniques, computational fluid dynamics (CFD), which is the use of numerical techniques on a computer to resolve transport, momentum and energy equations of a fluid flow has become more and more popular and the accuracy of the technique has been an a constant upgrading trend. Aeroelastic modeling of wind blades includes fluid-structure interaction and is, in fact, a science which studies the interaction between elastic, inertial and aerodynamic forces. The aeroelastic analysis is based on modeling using ANSYS and CFX software. CFX uses a finite volume method to calculate the aerodynamic solicitations which are transmitted to the structural module of ANSYS. Within CFX, several parameters need to be defined such as the turbulence model, the reduced frequency, the solver type, etc. and the assumptions and limitations of each model need to be well understood in order to validate the quality and pertinence of any aeroelastic model. These calibration considerations will be illustrated in the stall modeling section as an example.

4.1. Dynamic stall

In this section of the chapter, we will illustrate aeroelastic modeling of dynamic stall on a S809 airfoil for a wind blade. The aim of this section, apart from illustrating this aeroelastic phenomenon is to emphasize on the need of parameter calibration (domain size, mesh size,

turbulence and transition model) in CFD analysis.The different behaviour of lift as the AoA increases or decreases leads to significant hysteresis in the air loads and reduced aerodynamic damping, particularly in torsion. This can cause torsional aeroelastic instabilities on the blades. Therefore, the consideration of dynamic stall is important to predict the unsteady blade loads and, also, to define the operational boundaries of a wind turbine. In all the following examples, the CFD based aeroelastic models are run on the commercial ANSYS-CFX software. CFX, the fluid module of the software, models all the aerodynamic parameters of the wind flow. ANSYS structural module defines all the inertial and structural parameters of the airfoil and calculates the response and stresses on the structure according to given solicitations. The MFX module allows fluid-structure modelling, i.e., the results of the aerodynamic model are imported as solicitations in the structural module. The continuous exchange of information allows a multi-physics model that, at all time, computes the action of the fluid on the structure and the corresponding impact of the airfoil motion on the fluid flow.

4.1.1. Model and convergence studies

4.1.1.1. Model and experimental results

In an attempt to calibrate the domain size, mesh size, turbulence model and transition model, an S809 profile, designed by NREL, was used.

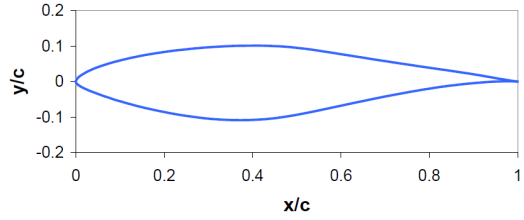

Figure 13. S809 airfoil

This airfoil has been chosen as experimental results and results from other sources are available for comparison. The experimental results have been obtained at the Low Speed Laboratory of the Delft University [31] and at the Aeronautical and Astronautical Research Laboratory of the Ohio State University [32]. The first work [31], performed by Somers, used a 0.6 meters chord model at Reynolds numbers of 1 to 3 million and provides the characteristics of the S809 profile for angles of incidence from -20^0 to 20^0. The second study [32], realized by Ramsey, gives the characteristics of the airfoil for angles of incidence ranging from -20^0 to 40^0. The experiments were conducted on a 0.457 meters chord lenght for Reynolds numbers of 0.75 to 1.5 million. Moreover, this study provides experimental results for the study of the dynamic stall for incidence angles of (8^0, 14^0 and 20^0) oscillating at ($\pm 5.5^0$ and $\pm 10^0$) at different frequencies for Reynolds numbers between 0.75 and 1.4 million.

http://dx.doi.org/10.5772/52281

4.1.1.2. Convergence studies

In this section, we will focus on the definition of a calculation domain and an adapted mesh for the flow modelling around the mentioned airfoil. This research is realized by the study of the influence of the distance between the boundaries and the airfoil, the influence of the size of the chord for the same Reynolds number and finally, the influence of the number of elements in the mesh and computational time.

4.1.1.3. Computational domain

The computational domain is defined by a semi-disc of radius I_1×c around the airfoil and two rectangles in the wake, of length I_2×c. This was inspired from works conducted by Bhaskaran presented in Fluent tutorial. As the objective of this study was to observe how the distance between the domain boundary and the airfoil affects the results, only I_1 and I_2 were varied with other values constant. As these two parameters will vary, the number of elements will also vary. To define the optimum calculation domain, we created different domains linked to a preliminary arbitrary one by a homothetic transformation with respect to the centre G and a factor b. Figure 14 gives us an idea of the different parameters and the outline of the computational domain whereas table 1 presents a comparison of the different meshed domains.

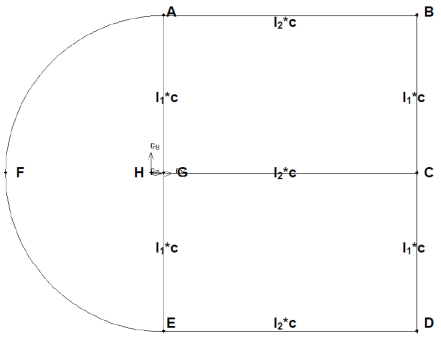

Figure 14. Shape of the calculation domain

Figure 15 below respectively illustrates the drag and lift coefficients as a function of the homothetic factor b for different angles of attack.

Trial	Trial 1	Trial 2	Trial 3	Trial 4	Trial 5	Trial 6
b	1	0.75	0.5	0.25	2	4
I_1	12.5	9	6.25	3.125	25	50
I_2	20	15	10	5	40	80
Number of elements	112680	106510	97842	84598	128142	143422

Table 1. Description of the trials through homothetic transformation

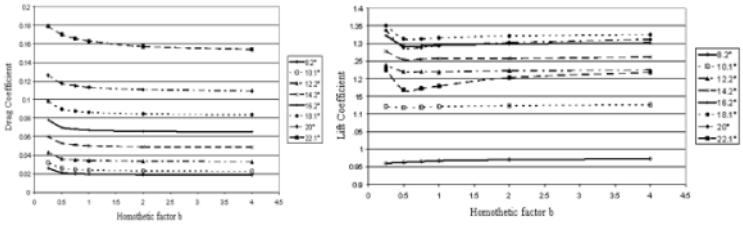

Figure 15. Drag and lift coefficients vs. homothetic factor for different angles of attack

The drag coefficient diminishes as the homothetic factor increases but tends to stabilize. This stabilization is faster for low angles of attack (AoA) and seems to be delayed for larger homothetic factors and increasing AoA. The trend for the lift coefficients as a function of the homothetic factor is quite similar for the different angles of attack except for an angle of 8.2^0. The evolution of the coefficients towards stabilization illustrate an important physical phenomenon: the further are the boundary limits from the airfoil, this allows more space for the turbulence in the wake to damp before reaching the boundary conditions imposed on the boundaries. Finally, a domain having a radius of semi disc 5.7125 m, length of rectangle 9,597 m and width 4.799 m was used.

4.1.1.4. Meshing

Unstructured meshes were used and were realized using the CFX-Mesh. These meshes are defined by the different values in table 2. We kept the previously mentioned domain.

Description	Symbol	Value
Size of the elements along the profile (between I and G)	a_1	0.001m
Size of the first element in the boundary layer	a_3	0.00001m
Size of the elements on the boundary limits	a_7	0.2m
Number of layers in the boundary layer	n_3	17
Inflation factor in the boundary layer	f_1	1.19
Inflation factors near the boundary limits	f_2	1.19

Table 2. Mesh parameters

Figure 16 gives us an appreciation of the mesh we have used of in our simulations:

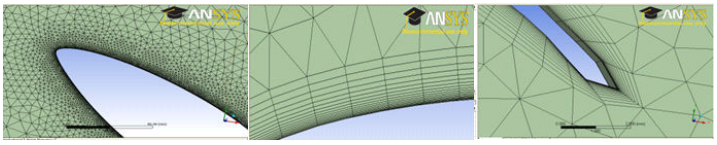

Figure 16. Unstructured mesh along airfoil, boundary layer at leading edge and boundary layer at trailing edge

http://dx.doi.org/10.5772/52281

Several trials were performed with different values of the parameters describing the mesh in order to have the best possible mesh. Lift and drag coefficient distributions have been computed according to different AoA for a given Reynolds number and the results were compared with experiments. The mesh option that provided results which fitted the best with the experimental results was used. The final parameters of the mesh were 66772 nodes and 48016 elements.

4.1.1.5. Turbulence model calibration

CFX proposes several turbulence models for resolution of flow over airfoils. Scientific literature makes it clear that different turbulence models perform differently in different applications. CFX documentation recommends the use of one of three models for such kind of applications, namely the k-ω model, the k-ω BSL model and the k-ω SST model. The Wilcox k-ω model is reputed to be more accurate than k-ε model near wall layers. It has been successfully used for flows with moderate adverse pressure gradients, but does not succeed well for separated flows. The k-ω BSL model (Baseline) combines the advantages of the Wilcox k-ω model and the k-ε model but does not correctly predict the separation flow for smooth surfaces. The k-ω SST model accounts for the transport of the turbulent shear stress and overcomes the problems of k-ω BSL model. To evaluate the best turbulence model for our simulations, steady flow analyses at Reynolds number of 1 million were conducted on the S809 airfoil using the defined domain and mesh. The different values of lift and drag obtained with the different models were compared with the experimental OSU and DUT results. D'Hamonville et al. [24] presents these comparisons which lead us to the following conclusions: the k-ω SST model is the only one to have a relatively good prediction of the large separated flows for high angles of attack. So, the transport of the turbulent shear stress really improves the simulation results. The consideration of the transport of the turbulent shear stress is the main asset of the k-ω SST model. However, probably a laminar-turbulent transition added to the model will help it to better predict the lift coefficient between 6° and 10°, and to have a better prediction of the pressure coefficient along the airfoil for 20°. This assumption will be studied in the next section where the relative performance of adding a particular transitional model is studied.

4.1.1.6. Transition model

ANSYS-CFX proposes in the advanced turbulence control options several transitional models namely: the fully turbulent k-ω SST model, the k-ω SST intermittency model, the gamma theta model and the gamma model. As the gamma theta model uses two parameters to define the onset of turbulence, referring to [33], we have only assessed the relative performance of the first three transitional models. The optimum value of the intermittency parameter was evaluated. A transient flow analysis was conducted on the S809 airfoil for the same Reynolds number at different AoA and using three different values of the intermittency parameter: 0.92, 0.94 and 0.96. Figure 17 illustrates the drag and lift coefficients obtained for these different models at different AoA as compared to DUT and OSU experimental data. We note that for the drag coefficient, the computed results are quite similar and only dif-

fer in transient mode exhibiting different oscillations. For large intermittency values, the oscillations are larger. Figure 18 shows that for the lift coefficients, the results from CFX differ from 8.2^0. For the linear growth zone, the different results are close to each other. The difference starts to appear near maximum lift. The k-ω SST intermittency model with γ=0.92, under predicts the lift coefficients as compared with the experimental results. The results with γ=0.94 predicts virtually identical results as compared to the OSU results. The model with γ= 0.96 predicts results that are sandwiched between the two experimental ones. Analysis of the two figures brings us to the conclusion that the model with γ=0.94 provides results very close to the DUT results. Therefore, we will compare the intermittency model with γ=0.94 with the other transitional models.

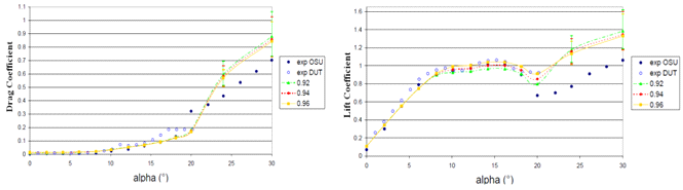

Figure 17. Drag and lift coefficients for different AoA using different intermittency values

Figure 18 illustrates the drag and lift coefficients for different AoA using different transitional models.

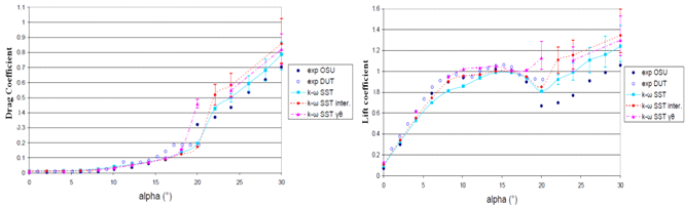

Figure 18. Drag and lift coefficients for different AoA using different transitional models

Figure 18 shows that the drag coefficients for the three models are very close until 18^0 after which the results become clearly distinguishable. As from 20^0, the γ-θ model over predicts the experimental values whereas such phenomena appear only after 22.1^0 for the two other models. For the lift coefficients, Figure 18 shows that the k-ω SST intermittency models provide results closest to the experimental values for angles smaller than 14^0. The k-ω SST model under predicts the lift coefficients for angles ranging from 6^0 to 14^0. For angles exceeding 20^0, the intermittency model does not provide good results. Hence, we conclude that the transitional model helps in obtaining better results for AoA smaller than 14^0. However, for AoA greater than 20^0, a purely turbulent model needs to be used.

http://dx.doi.org/10.5772/52281

4.1.2. Results

In order to validate the quality of stall results, the latter are compared with OSU experimental values and with Leishman-Beddoes model. Moreover, modelling of aeroelastic phenomena is computationally very demanding such that we have opted for an oscillation of 5.5^0 around 8^0, 14^0 and 20^0 for a reduced frequency of $k=\frac{\omega c}{2U_\infty}=0.026$, where c is the length of the chord of the airfoil and U_∞ is the unperturbed flow velocity. From a structural point of view, the 0.457 m length profile will be submitted to an oscillation about an axis located at 25% of the chord. The results which follow illustrates the quality of our aeroelastic stall modelling at three different angles, all with a variation of 5.5 sin(w)*t.

$$\alpha = 8^0 \pm 5.5\sin(\omega t)^0$$

Figure 19 illustrates the evolution of the aerodynamic coefficients with oscillation of the AoA around 8^0 with amplitude 5.5^0 and a reduced frequency of 0.026. When the angle is less than 14^0, the transitional k-ω SST intermittency model was used.

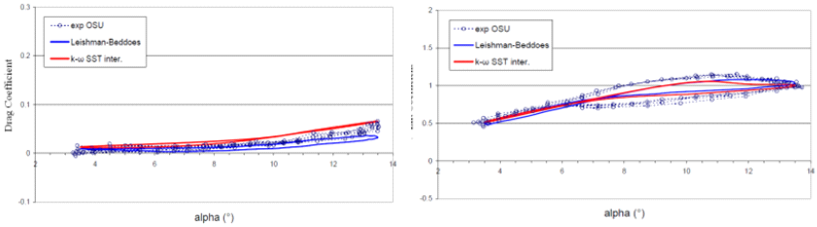

Figure 19. Drag and lift coefficients vs. angle of attack for stall modelling

For the drag coefficient, the results are very close to experimental ones and limited hysteresis appears. As for the lift coefficient, we note that the «k-ω SST intermittency» transitional turbulent model underestimates the hysteresis phenomenon. Furthermore, this model provides results with inferior values as compared to experimental ones for increasing angle of attack and superior values for decreasing angle of attack. We, also, notice that the onset of the stall phenomenon is earlier for the «k-ω SST intermittency» model.

$$\alpha = 14^0 \pm 5.5\sin(\omega t)^0$$

Figure 20 illustrates the evolution of the aerodynamic coefficients with oscillation of the AoA around $14^0$with amplitude of 5.5^0 and a reduced frequency of 0.026. As the angle exceeds 14^0, the purely turbulent k-ω SST model was used.

We note that before 17°, the model overestimates the drag coefficient, both for increasing and decreasing AoA. For angles exceeding 17°, the model approaches experimental results. As for the drag coefficient, the model provides better results for the lift coefficient when the angle of attack exceeds 17°. Furthermore, we note that the model underestimates the lift coefficient for both increasing and decreasing angles of attack. Moreover, the predicted lift coefficients are closer to experimental results for AoA less than 13°.

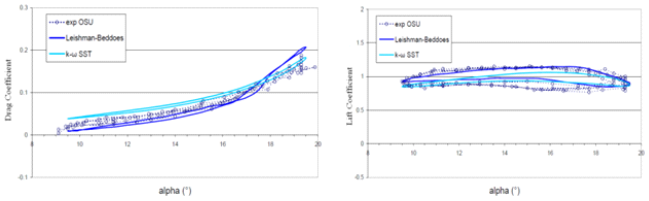

Figure 20. Drag and lift coefficients vs. angle of attack for stall modelling

$$\alpha = 20^0 \pm 5.5\mathbf{sin}(\omega \mathbf{t})^0$$

Figure 21 illustrates the evolution of the aerodynamic coefficients with oscillation of the Ao Aaround $20^0$with amplitude of 5.5^0 and reduced frequency of 0.026. As the angle exceeds 14^0, the purely turbulent k-ω SST model was used. For the drag coefficients, the results provided by the k-ω SST model are quite close to the experimental results but predict premature stall for increasing AoA and reattachment for decreasing AoA. Furthermore, we note oscillations of the drag coefficient for the experimental data showing higher levels of turbulence. The k-ω SST model under predicts the value of the lift coefficient for increasing AoA. Furthermore, due to vortex shedding, we note oscillations occurring in the results. Finally, the model prematurely predicts stall compared to the experiments.

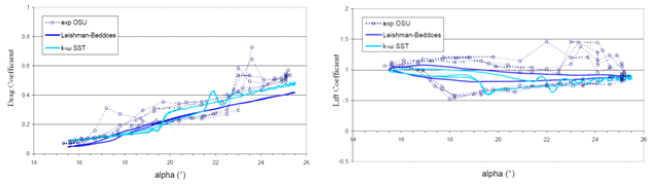

Figure 21. Drag and lift coefficients vs. angle of attack for stall modelling

4.1.3. Conclusions on stallmodelling

In this section, we presented an example of aeroelastic phenomenon, the dynamic stall. We have seen through this section the different steps to build and validate the model. Better results are obtained for low AoA but as turbulence intensity gets very large, the results diverge from experimental values or show oscillatory behaviour. We note that, though, the CFD models show better results than the relatively simple indicial methods found in literature, refinements should be brought to the models. Moreover, this study allows us to appreciate the complexity of fluid structure interaction and the calibration work required upstream. It should be emphasized that the coupling were limited both by the structural and aerodynamic models and refinements and better understanding of all the parameters that can help achieve better results. This study allows us to have a very good evaluation of the different turbulence models offered by CFX and their relative performances.

http://dx.doi.org/10.5772/52281

4.2. Aerodynamic divergence

In this section we will illustrate the different steps in modeling another aeroelastic phenomenon, the divergence and whilst using this example to lay emphasis on the ability of CFX-ANSYS software to solve fluid-structure interaction problems. As from the 1980s, national and international standards concerning wind turbine design have been enforced. With the refinement and growth of the state of knowledge the "Regulation for the Certification of Wind Energy Conversion Systems" was published in 1993 and further amended and refined in 1994 and 1998. Other standards aiming at improving security for wind turbines have been published over the years. To abide to such standards, modelling of the aeroelastic phenomena is important to correctly calibrate the damping parameters and the operation conditions. For instance, Nweland [34] makes a proper and complete analysis of the critical divergence velocity and frequencies. These studies allow operating the machines in secure zones and avoid divergence to occur. Such studies' importance is not only restrained to divergence but also apply to other general dynamic response cases of wind turbines. Wind fluctuations at frequencies close to the first flapwise mode blade natural frequency excite resonant blade oscillations and result in additional, inertial loadings over and above the quasi-static loads that would be experienced by a completely rigid blade. Knowledge of the domain of such frequencies allows us to correctly design and operate the machines within IEC and other norms. We here present a case where stall can be avoided by proper knowledge of its parameters and imposing specific damping. As the oscillations result from fluctuations of the wind speed about the mean value, the standard deviation of resonant tip displacement can be expressed in terms of the wind turbulence intensity and the normalized power spectral density at the resonant frequency, $R_u(n1)$ [34]:

$$\frac{\sigma_{x1}}{\bar{x}_1} = \frac{\sigma_u}{\bar{U}} \frac{\pi}{\sqrt{2\delta}} \sqrt{R_u(n1)} \sqrt{K_{sx}(n1)} \tag{32}$$

where:

$$R_u(n1) = \frac{n.S_u(n1)}{\sigma^2_u} \tag{33}$$

- $\bar{x}_1$ is the first mode component of the steady tip displacement.
- $\bar{U}$ is the mean velocity (usually averaged over 10 minutes)
- δ is the logarithmic decrement damping
- $K_{sx}(n1)$ is the size of the reduction factor which is present due to lack of correlation of wind along the blade at the relevant frequency.

It is clear from equation (32) that a key determinant of resonant tip response is the value of damping present. If we consider for instance a vibrating blade flat in the wind, the fluctuating aerodynamic force acting on it per unit length is given by:

$$\frac{1}{2}\rho\left(\bar{U}-\dot{x}\right)^2 C_d \cdot C(r) - \frac{1}{2}\rho \bar{U}^2 C_d.C(r) \cong \rho \bar{U}\dot{x}C_d C\left(r\right) \tag{34}$$

where $\dot{x}$ is the blade flatwise velocity, C_d is the drag coefficient and C(r) is the local blade chord. Hence the aerodynamic damping per unit length, $\hat{C}_a(r)=\rho\bar{U}C_d C(r)$ and the first aerodynamic damping mode is:

$$\varepsilon_{a1}=\frac{C_{a1}}{2m_1\omega_1}=\frac{\int_0^R \hat{C}_a(r)\mu_1^2(r)dr}{2m_1\omega_1}=\frac{\rho\bar{U}C_d\int_0^R C(r)\mu_1^2(r)dr}{2m_1\omega_1} \tag{35}$$

$\mu_1(r)$ is the first mode shape and m_1 is the generalized mass given by:

$$m_1=\int_0^R m(r)\mu_1^2(r)dr \tag{36}$$

Here, ω_1 is the first mode natural frequency given in radian per second. The logarithmic decrement is obtained by multiplying the damping ratio by 2 π. To properly estimate operating conditions and damping parameters, knowledge of the vibration frequencies and shape modes are important. The need to know these limits is again justified by the fact that when maximum lift is theoretically achieved toward maximum power when stall and other aeroelastic phenomena are also approached.

4.2.1. ANSYS-CFX coupling

To achieve the fluid structure coupling study, we make use of the ANSYS multi-domain (MFX). This module was primarily developed for fluid-structure interaction studies. On one side, the structural part is solved using ANSYS Multiphysics and on the other side, the fluid part is solved using CFX. The study needs to be conducted on a 3D geometry. If the geometries used by ANSYS and CFX need to have common surfaces (interfaces), the meshes of these surfaces can be different. The ANSYS code acts as the master code and reads all the multi-domain commands. It recuperates the interface meshes of the CFX code, creates the mapping and communicates the parameters that control the timescale and coupling loops to the CFX code. The ANSYS generated mapping interpolates the solicitations between the different meshes on each side of the coupling. Each solver realizes a sequence of multi-domain, time marching and coupling iterations between each time steps. For each iteration, each solver recuperates its required solicitation from the other domain and then solves it in the physical domain. Each element of interface is initially divided into n interpolation faces (IP) where n is the number of nodes on that face. The 3D IP faces are transformed into 2D poly-

http://dx.doi.org/10.5772/52281

gons. We, then, create the intersection between these polygons, on one hand, the solver diffusing solicitations and on the other hand, the solver receiving the solicitations. This intersection creates a large number of surfaces called control surfaces as illustrated in Figure 22. These surfaces are used in order to transfer the solicitation between the structural and fluid domains.

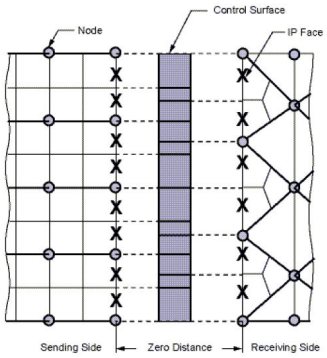

Figure 22. Transfer Surfaces

The respective MFX simultaneous and sequential resolution schemes are presented in figure 23.

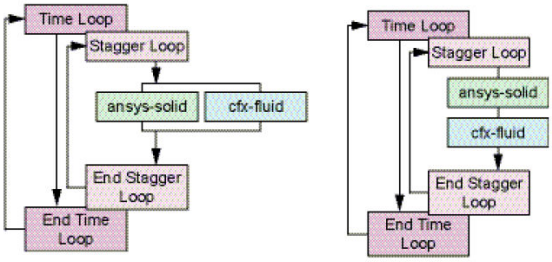

Figure 23. Simultaneous or sequential resolution of CFX and ANSYS

We can make use of different types of resolutions, either using a simultaneous scheme or using a sequential scheme, in which case we need to choose which domain to solve first. For lightly coupled domains, CFX literature recommends the use of the simultaneous scheme. As for our case, the domains are strongly coupled and for such reasons, we make use of the sequential scheme. This scheme has as advantage to ensure that the most recent result or solicitation of a domain solver is applied to the other solver. In most simulations; the physics of one domain imposes the requirements of the other domain. Hence, it is essential to ade-

quately choose the code to solve first in the sequential scheme. In the case of the divergence, it is the fluid that imposes the solicitations on the solid such that the CFX code will be the first to be solved followed by the ANSYS code. The ANSYS workbench flow-charts that illustrates such interaction is illustrated in Figure 24 below:

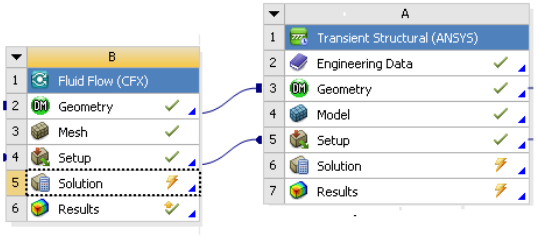

Figure 24. ANSYS workbench divergence flow-chart

4.2.2. Comparison with experimental results

4.2.2.1. Overview of the experimental results

An aeroelastic experiment was conducted at the Duke University Engineering wind tunnel facility [35]. The goals of this test were to validate the analytical calculations of non-critical mode characteristics and to explicitly examine the aerodynamic divergence phenomenon.

4.2.2.2. Configuration description

The divergence assessment testbed (*dat*) wind tunnel model consists of a typical section airfoil with a flexible mount system providing a single degree of freedom structural dynamic mode. The only structural dynamic mode of this model is torsional rotation, or angle of attack. The airfoil section is a NACA 0012 with an 8-inch chord and a span of 21 inches. The ratio of the trailing edge mass to the total mass is 0.01.This spans the entire test section from the floor to ceiling. The structural dynamic parameters for this model are illustrated in table 3:

Kα (N•m/rad)	**ω_α (rads/sec)**	**$_\alpha$ (Hz)**	**ζ**
5.8262	49.5	7.88	0.053

Table 3. Excerpt from Table 5 in "Jennifer Heeg" [35]: Structural dynamic parameters associated with wind tunnel model configurations

Table 4 lists the analytical calculations for divergence conditions for the considered model presented in [35].

http://dx.doi.org/10.5772/52281

Velocity			Dynamic Pressure	
(in/sec)	(mph)	(m/s)	(psf)	(N/m^2)
754	42.8	19.15	4.6	222

Table 4. Analytical calculations for divergence conditions for the considered model presented

However, some parameters were unavailable in [35] such that an iterative design process was used to build the model in ANSYS. Using parameters specified in [35], a preliminary model was built and its natural frequencies verified using ANSYS. The model was successively modified until a model as close as possible to the model in the experiment was obtained.The aims of the studies conducted in [35] were to: 1) find the divergence dynamic pressure;2)examine the modal characteristics of non-critical modes, both sub-critically and at the divergence condition; 3) examine the eigenvector behaviour. Heeg[35] obtained several interesting results among which the following graphic showing the variation of the angle of attack with time. The aim of our simulations was to determine how the numerical ANSYS-CFX model will compare with experiments.

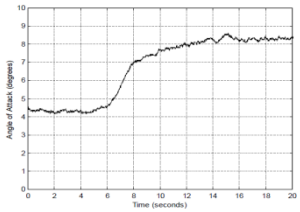

Figure 25. Divergence of wind tunnel model configuration #2

The test was conducted by setting as close as possible to zero the rigid angle of attack, α_0, for a zero airspeed. The divergence dynamic pressure was determined by gradually increasing the velocity and measuring the system response until it became unstable. The dynamic pressure was being slowly increased until the angle of attack increased dramatically and suddenly. This was declared as the divergence dynamic pressure, 5.1 psf (244 N/m2). The time history shows that the model oscillates around a new angle of attack position, which is not at the hard stop of the spring. It is speculated that the airfoil has reached an angle of attack where flow has separated and stall has occurred [35].

4.2.2.3. The ANSYS-CFX model

The model used in the experiment was simulated using a reduced span-wise numerical domain (quasi 2D). The span of the airfoil was reduced 262.5 times, from 21 inches to 0.08 inches or 2.032 mm, while the chord of the airfoil was maintained at 8 inch or 203.2 mm. We used a cylinder to simulate the torsion spring used in the experiment.

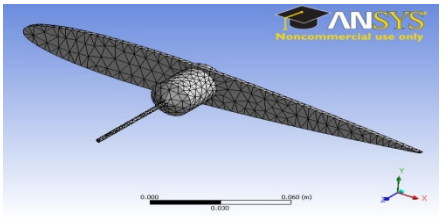

Figure 26. ANSYS built geometry with meshing

4.2.2.4. Results

In [23], the authors have derived the analytical mathematical equation to calculate the divergence velocity, U_D. The expression was:

$$U_D = \sqrt{\frac{1}{C^{\theta\theta}\frac{\partial C_l}{\partial \alpha} e \frac{1}{2}\rho S}} \tag{37}$$

In order to calculate the theoretical value of the divergence velocity, certain parameters need to be found first. These are $C^{\theta\theta}$, which is specific to the modeled spring, S being inherent to the profile, e, which depends both on the profile (elastic axis) and on the aerodynamic model, ρ, which is dependent upon the used fluid and $\frac{\partial C_l}{\partial \alpha}$ which depends both on the shape of the profile but, also, on the turbulent model [23]. We note that, as divergence velocity is approached, the elastic twist angle will increase in a very significant manner and tend to infinity [24]. However, numerical values are finite and cannot model infinite parameters. We will, therefore, formulate the value of the analytical elastic twist angle in order to compare it with the value found by the coupling. In the case wherein the elastic twist angle introduces no further aerodynamic solicitations, by introducing $\alpha = \alpha_r$, and resolving for the elastic twist angle, we have:

$$\theta_r = C^{\theta\theta} T = C^{\theta\theta}\left(\frac{\partial C_l}{\partial \alpha} \mathrm{e}\, \alpha_r + C_m c\right) qS \tag{38}$$

Algebraic manipulations of the expressions lead us to the following formulation:

$$\theta = \frac{\theta_r}{1 - \frac{\partial C_l}{\partial \alpha} C^{\theta\theta} eqS} \tag{39}$$

This leads to:

$$\theta = \frac{\theta_r}{1 - \frac{q}{q_D}} = \frac{\theta_r}{1 - \left(\frac{U}{U_D}\right)^2} \tag{40}$$

http://dx.doi.org/10.5772/52281

Hence, we can note that the theoretical elastic twist angle depends on the divergence speed and the elastic twist angle calculated whilst considering that it triggers no supplementary aerodynamic solicitation. To calculate the latter, we will solve for the moment applied on the profile at the elastic axis (T) during trials in steady mode. These trials are conducted using the k-ω SST intermittency transitional turbulence model with a 0.94 intermittency value [24]. To model the flexibility coefficient of the rotational spring $C^{\theta\theta}$, used in the NASA experiments we used a cylinder as a torsion spring. The constant of the spring used in the experiment is K_α = 5.8262 N•m/rad and since we used a reduced model, with an span 262.5 times smaller than the original, the dimensions and properties of the cylinder are such that:

$$K_{\alpha r} = \frac{5.8262}{262.5} N \bullet \frac{m}{rad} = 0.022195 \text{ N} \bullet \text{ m} \Big/ \text{ rad} \tag{41}$$

and the flexibility coefficient is:

$$C^{\theta\theta} = \frac{1}{K_{\alpha r}} = 45.0552 \; rad \Big/ N \bullet m \tag{42}$$

The slope of the lift $\frac{\partial C_l}{\partial \alpha}$, can be calculated for an angle $\alpha = 5^0$ in the following way:

$$\frac{\partial C_l}{\partial \alpha} = \frac{C_{l,\alpha>5^0} - C_{l,\alpha<5^0}}{\alpha>5^0 - \alpha<5^0} \tag{43}$$

We have calculated the lift coefficient at 4.0^0 and 6.0^0 such that:

$C_{l,\alpha=4.0^0} = 0.475$

and $C_{l,\alpha=6.0^0} = 0.703$

Hence the gradient can be expressed and calculated as follows:

$\frac{\partial C_l}{\partial \alpha} = \frac{0.703 - 0.475}{6.0 - 4.0} = 0.114 \; deg^{-1} = 6.532 \; rad^{-1}$

The distance *e*, between the elastic axis and the aerodynamic centre for the model is 0.375•*b*. The rigid area is calculated to be S, being the product of the chord and the span and is calculated as follows:

$S = 0.2032 \bullet 0.5334 = 0.0004129024 m^2$

Hence the divergence velocity is calculated as:

$$U_D = \sqrt{\frac{1}{C^{\theta\theta} \frac{\partial C_l}{\partial \alpha} \frac{\rho}{2} eS}} = 18.78 \text{ m} \Big/ \text{s} \tag{44}$$

The theoretical divergence speed given in Table 4 of the NASA experiment [35] is 19.15 m/s. This slight difference is due to the value of slope of the lift profile $\frac{\partial C_l}{\partial \alpha}$ taken into consideration, which in the NASA work was 2π, or 6.283 rad^{-1}, whereas we used a value of 6.532 rad^{-1} . Furthermore, a difference between our calculated speed and that presented in [35] might also be explained by the size of the used tunnel and the possible wall turbulence interaction. Furthermore, using the model, domain and mesh parameters detailed in the previous sections of this article, divergence was modelled as follows: the airfoil used in [35] was fixed and exempted from all rotational degrees of liberty and subjected to a constant flow of velocity 15 m s^{-1}. Suddenly, the fixing is removed and the constant flow can be then compared to a shock wave on the profile. The profile then oscillates with damped amplitude due to the aerodynamic damping imposed. Figure 27 illustrates the response portrayed by ANSYS-CFX software. We can extract the amplitude and frequency of oscillation of around 8 Hz which is close to the 7.9 Hz frequency presented in [35].

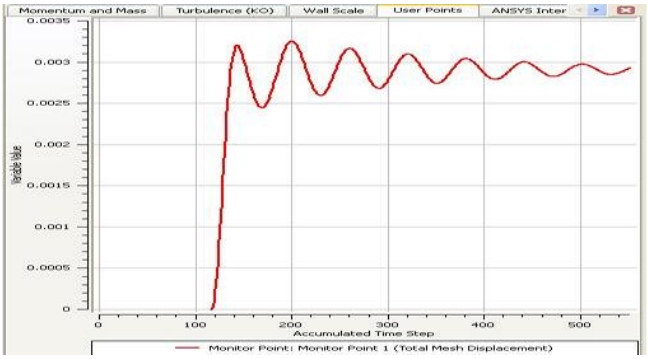

Figure 27. Oscillatory response to sudden subject to a constant flow of 15m/s

4.3. Aerodynamic flutter

In this section, we illustrate a CFD approach of modeling the most complex and the most dangerous type of aeroelastic phenomenon to which wind turbine blades are subjected. While illustrating stall phenomenon, we calibrated the CFD parameters for aeroelastic modeling. In the divergence section, the example was used to reinforce the notion of multiphysics modeling, more precisely, emphasis was laid on fluid structure interaction modeling within ANSYS-CFX MFX. Flutter example will be used to illustrate the importance of using lumped method.

4.3.1. Computational requirement and Lumped model

Aeroelastic modeling requires enormous computational capacity. The most recent quad core 16 GB processor takes some 216 hours to simulate flutter on a small scale model and that for a 12 second real time frame. The aim of simulating and predicting aeroelastic effects on

http://dx.doi.org/10.5772/52281

wind blades has as primary purpose to apply predictive control. However, with such enormous computational time, this is impossible. The need for simplified lumped (2D Matlab based) models is important. The CFD model is ran preliminarily and the lumped model is built according to simulated scenarios. In this section we will illustrate flutter modeling both from a CFD and lumped method point of view.

4.3.2. Matlab-Simulink and Ansys-CFX tools

For flutter modelling, again, ANSYS-CFX model was used to simulate the complex fluid-structure interaction. However, due to excessively important computational time that rendered the potential of using the predictive results for the application of mitigation control impossible, the results of the CFD model was used to build a less time demanding lumped model based on Simulink. Reference [36] describes the Matlab included tool Simulink as an environment for multi-domain simulation and Model-Based Design for dynamic and embedded systems. It provides an interactive graphical environment and a customizable set of block libraries that let you design, simulate, implement, and test a variety of time-varying systems. For the flutter modelling project, the aerospace blockset of Simulink has been used. The Aerospace Toolbox product provides tools like reference standards, environment models, and aerospace analysis pre-programmed tools as well as aerodynamic coefficient importing options. Among others, the wind library has been used to calculate wind shears and Dryden and Von Karman turbulence. The Von Karman Wind Turbulence model uses the Von Karman spectral representation to add turbulence to the aerospace model through pre-established filters. Turbulence is represented in this blockset as a stochastic process defined by velocity spectra. For a blade in an airspeed V, through a frozen turbulence field, with a spatial frequency of Ω radians per meter, the circular speed ω is calculated by multiplying V by Ω. For the longitudinal speed, the turbulence spectrum is defined as follows:

$$\psi_{lo} = \frac{\sigma^2_{\omega}}{V L_{\omega}} \cdot \frac{0.8\left(\frac{\pi L_{\omega}}{4b}\right)^{0.3}}{1 + \left(\frac{4b\omega}{\pi V}\right)^2} \tag{45}$$

Here,L_{ω} represents the turbulence scale length and σis the turbulence intensity. The corresponding transfer function used in Simulink is:

$$\psi_{lo} = \frac{\sigma_u \sqrt{\frac{2}{\pi}\frac{L_v}{V}}\left(1 + 0.25\frac{L_v}{V}s\right)}{1 + 1.357\frac{L_v}{V}s + 0.1987\left(\frac{L_v}{V}s\right)^2 s^2} \tag{46}$$

For the lateral speed, the turbulence spectrum is defined as:

$$\psi_{la} = \frac{\mp\left(\frac{\omega}{V}\right)^2}{1 + \left(\frac{3b\omega}{\pi V}\right)^2} \cdot \varphi_v(\omega) \tag{47}$$

and the corresponding transfer function can be expressed as :

$$\psi_{la} = \frac{\mp\left(\frac{s}{V}\right)^1}{1+\left(\frac{3b}{\pi V}s\right)^1}.H_v(s) \tag{48}$$

Finally, the vertical turbulence spectrum is expressed as follows:

$$\psi_v = \frac{\mp\left(\frac{\omega}{V}\right)^2}{1+\left(\frac{4b\omega}{\pi V}\right)^2}.\varphi_\omega(\omega) \tag{49}$$

and the corresponding transfer function is expressed as follows:

$$\psi_v = \frac{\mp\left(\frac{s}{V}\right)^1}{1+\left(\frac{4b}{\pi V}s\right)^1}.H_\omega(s) \tag{50}$$

The Aerodynamic Forces and Moments block computes the aerodynamic forces and moments around the center of gravity. The net rotation from body to wind axes is expressed as:

$$C_{\omega\leftarrow b} = \begin{bmatrix} \cos(\alpha)\cos(\beta) & \sin(\beta) & \sin(\alpha)\cos(\beta) \\ -\cos(\alpha)\sin(\beta) & \cos(\beta) & -\sin(\alpha)\sin(\beta) \\ -\sin(\alpha) & 0 & \cos(\alpha) \end{bmatrix} \tag{51}$$

On the other hand, the fluid structure interaction to model aerodynamic flutter was made using ANSYS multi domain (MFX). As previously mentioned, the drawback of the ANSYS model is that it is very time and memory consuming. However, it provides a very good option to compare and validate simplified model results and understand the intrinsic theories of flutter modelling. On one hand, the aerodynamics of the application is modelled using the fluid module CFX and on the other side, the dynamic structural part is modelled using ANSYS structural module. An iterative exchange of data between the two modules to simulate the flutter phenomenon is done using the Workbench interface.

4.3.3. Lumped model results

We will first present the results obtained by modeling AoA for configuration # 2 of reference [35] (also, discussed in the divergence section 4.2) for an initial AoA of 0°. As soon as divergence is triggered, within 1 second the blade oscillates in a very spectacular and dangerous manner. This happens at a dynamic pressure of 5,59lb/pi^2 (268 N/m^2). Configuration #2 uses, on the airfoil, 20 elements, unity as the normalized element size and unity as the normalized airfoil length. Similarly, the number of elements in the wake is 360 and the corresponding normalized element size is unity and the normalized wake length is equal to 2. The results obtained in [35] are illustrated in Figure 28:

http://dx.doi.org/10.5772/52281

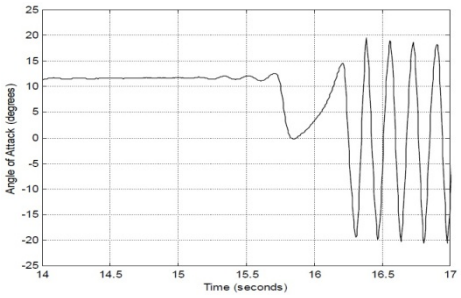

Figure 28. Flutter response- an excerpt from [23]

We notice that at the beginning there is a non-established instability, followed by a recurrent oscillation. The peak to peak distance corresponds to around 2.5 seconds that is a frequency of 0.4 Hz. The oscillation can be defined approximately by an amplitude of $0^0 \pm 17^0$. . The same modelling was performed using the Simulink model and the result for the AoA variation and the plunge displacement is shown below:

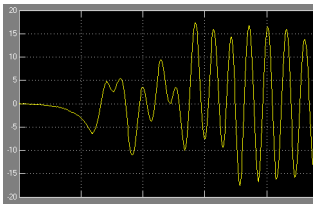

Figure 29. Flutter response obtained from Matlab Aerospace blockset

We note that for the AoA variation, the aerospace blockset based model provides very similar results with Heeg's results [35]. The amplitude is, also, around $0^0 \pm 17^0$ and the frequency is 0.45 Hz. Furthermore, we notice that the variation is very similar. We can conclude that the aerospace model does represent the flutter in a proper manner. It is important to note that this is a special type of flutter. The frequency of the beat is zero and, hence, represents divergence of "zero frequency flutter". Using Simulink, we will vary the angular velocity of the blade until the eigenmode tends to a negative damping coefficient. The damping coefficient, ζ is obtained as: $\zeta = \frac{c}{2m\omega}$, ω is measured as the Laplace integral in Simulink, c is the viscous damping and $\omega = \sqrt{\frac{k}{m}}$. Figure 30 illustrates the results obtained for the variation of the damping coefficient against rotational speed and flutter frequency against rotor speed. We can note that as the rotation speed increases, the damping becomes negative, such that the aerodynamic instability which contributes to an oscillation of the airfoil is amplified. We also notice that the frequency diminishes and becomes closer to the natural frequency of the system. This explains the reason for which flutter is usually very similar to resonance as it occurs due to a coalescing of dynamic modes close to the natural vibrating mode of the system.

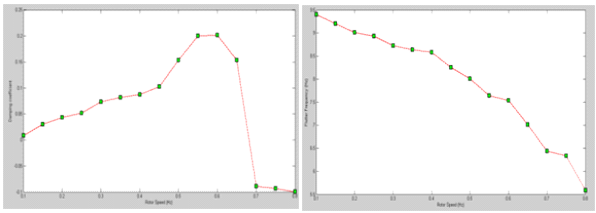

Figure 30. Damping coefficient against rotational speed and flutter frequency against rotor speed

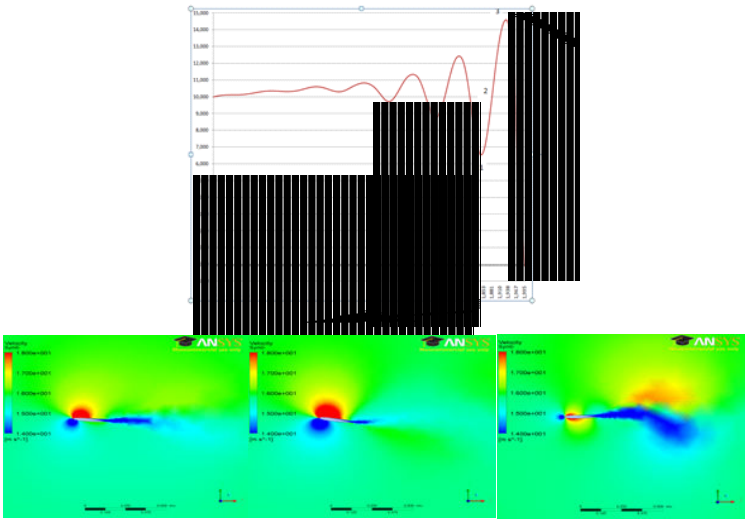

Figure 31. Flutter simulation with ANSYS-CFX at 1) 1.8449 s, 2) 1.88822 s and 1.93154s

We present here the results obtained for the same case study using ANSYS-CFX. The frequency of the movement using Matlab is 6.5 Hz while that using the ANSYS-CFX model is 6.325 Hz compared with the experimental value of 7.1Hz [35]. Furthermore, the amplitudes of vibration are very close as well as the trend of the oscillations. For the points identified as 1, 2 and 3 on the flutter illustration, we illustrate the relevant flow over the airfoil. The maximum air speed at moment noted 1 is 26.95 m/s. We note such a velocity difference over the airfoil that an anticlockwise moment will be created which will cause an increase in the angle of attack. Since the velocity, hence, pressure difference, is very large, we note from the flutter curve, that we have an overshoot. The velocity profile at moment 2, i.e., at 1.88822s shows a similar velocity disparity, but of lower intensity. This is visible as a reduction in the gradient of the flutter curve as the moment on the airfoil is reduced. Finally at moment 3, we note that the velocity profile is, more or less, symmetric over the airfoil such that the moment is momentarily zero. This corresponds to a maximum stationary point on the flutter

http://dx.doi.org/10.5772/52281

curve. After this point, the velocity disparity will change position such that angle of attack will again increase and the flutter oscillation trend maintained, but in opposite direction. This cyclic condition repeats and intensifies as we have previously proved that the damping coefficient tends to a negative value.

Author details

Drishtysingh Ramdenee[1,2], Adrian Ilinca[1] and Ion Sorin Minea[1]

1 Wind Energy Research Laboratory, Université du Québec à Rimouski, Rimouski, Canada

2 Institut Technologique de la Maintenance Industrielle, Sept Îles, Canada

References

[1] J. Scheibert et al. " Stress field at a sliding frictional contact: Experiments and calculations" Journal of the Mechanics and Physics of Solids 57 (2009) 1921–1933

[2] P. Destuynder, Aéroélasticité et Aéroacoustique, 85, 2007

[3] www.nrel.gov/docs/fy06osti/39066.pdf

[4] Gunner et al. Validation of an aeroelastic model of Vestas V39. Risoe Publication, DK 180 91486

[5] Gabriel Saiz. Turbomachinery Aeroelasticity using a Time-Linearized Multi-Blade Row Approach. Ph.D thesis Imperial College, London, 2008

[6] Christophe Pierre et al. Localization of Aeroelastic Modes in High Energy Turbines, Journal of Propulsion and Power. Vol 10, June 1994

[7] Ivan McBean et al. Prediction of Flutter of Turbine Blades in a Transonic Annular Cascade. Journal of Fluids Engineering, ASME 2006

[8] Srinivasan. A. V. Flutter and Resonant Vibration Characteristics of Engine Blades, ASME 1997, page 774-775

[9] Liu. F et al. Calibration of Wing Flutter by a Coupled Fluid Structure Method, Journal of Aeroelasticity, 38121, 2001

[10] K. Rao. V. Kaza. Aeroelastic Response of Metallic & Composite Propfan models in Yawned Flow. NASA Technical Memorandum 100964 AIAA-88-3154

[11] C. Wieseman et al. Transonic Small Disturbance and Linear Analyses for the Active Aeroelastic Wing Program

[12] Todd O'Neil. Non Linear Aeroelastic Response Analyses and Experiments AIAA-1996

[13] R. Bisplinghoff, H. Ashley, R. Halfman, « Aeroelasticity »Dover Editions, 1996

[14] Bisplinghoff R.L.Aeroelasticity. Dover Publications: New York, 1955

[15] Fung, Y.C., 1993. An Introduction to the Theory of Aeroelasticity. Dover Publications Inc., New York

[16] Leishman, J.G., 2000. Principles of Helicopter Aerodynamics. Cambridge University Press, Cambridge

[17] J.W. Larsen et al. / Journal of Fluids and Structures 23 (2007) 959–982

[18] VISCWIND, 1999. Viscous effects on wind turbine blades, final report on the JOR3 CT95-0007, Joule III project, Technical Report, ET-AFM-9902, Technical University of Denmark

[19] D.Ramdenee et A.Ilinca « An insight to Aeroelastic Modelling » Internal Report, UQAR, 2011

[20] Spalart PR and Allmaras SR ''One equation turbulence model for aerodynamic flows''Jan 1993

[21] Davison and Rizzi A''Navier Stokes computation of Airfoil in Stall algebraic stresses model, Jan 1992''

[22] Eppler R airfoil design and data, NY springs Veng 1990. R. Michel et al. ''Stability calculations and transition criteria on 2D and 3D flows'' Laminar and turbulent Novosibirski, USSR,1984

[23] D. Ramdenee, A. Ilinca. An insight into computational fluid dynamics.Rapport Technique, UQAR/LREE

[24] T. Tardif d'Hamonville, A. Ilinca Modélisation et Analyse des Phénomènes Aéroélastiques pour une pale d'Éolienne Masters Thesis, UQAR/LREE

[25] T. Tardif d'Hamonville, A. Ilinca. Modélisation de l'écoulement d'air autour d'un proil de pale d'éolienne,Phase 1: Domaine étude et Maillage. Rapport Technique, UQAR/LREE-05, Décembre 2008

[26] Raymond L.Bisphlinghoff, Holt Ashley and Robert L.Halfman, Aeroelasticity, Dover 1988

[27] www.ltas.mct.ulg.ac.be/who/stainier/docs/aeroelastcite.pdf

[28] Theodorsen, T., General theory of aerodynamic instability and the mechanism of flutter, NACA Report 496, 1935.

[29] Fung, Y. C., An Introduction to the Theory of Aeroelasticity. Dover Publications Inc.: New York, 1969; 210-216

http://dx.doi.org/10.5772/52281

[30] Dowell, E. E. (Editor), A Modern Course in Aeroelasticity. Kluwer Academic Publishers: Dordrecht, 1995; 217-227

[31] Somers, D.M. "Design and Experimental Results for the S809 Airfoil". NREL/SR-440-6918, 1997

[32] Reuss Ramsay R., Hoffman M. J., Gregorek G. M. "Effects of Grit Roughness and Pitch Oscillations on the S809 Airfoil." Master thesis, NREL Ohio State University, Ohio, NREL/TP-442-7817, December 1995.

[33] ANSYS CFX, Release 11.0

[34] Nweland, D.E (1984) Random Vibrations and Spectral Analysis, Longman, UK

[35] Jennifer Heeg, "Dynamic Investigation of Static Divergence: Analysis and Testing", Langley Research Center, Hampton, Virginia, National Aeronautics and Space Administration

[36] Matlab-Simulink documentations. Release 8b

Chapter 5

Structural Analysis of Complex Wind Turbine Blades: Flexo-Torsional Vibrational Modes

Alejandro D. Otero, Fernando L. Ponta and
Lucas I. Lago

Additional information is available at the end of the chapter

http://dx.doi.org/10.5772/51142

1. Introduction

Limitations in the current blade technology constitute a technological barrier that needs to be broken in order to continue the improvement in wind-energy cost. Blade manufacturing is mostly based on composite laminates, which is labor-intensive and requires highly-qualified manpower. It constitutes a bottleneck to turbine upscaling that reflects into the increasing share of the cost of the rotor, within the total cost of the turbine, as turbine size increases. Figure 1 shows a compilation of data by NREL-DOE [26] on the proportional cost of each subsystem for different sizes of wind-turbines, where the systematic increase of the rotor cost share is clearly reflected.

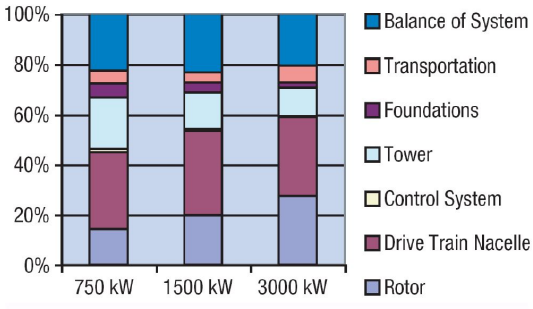

Figure 1. Evolution of the proportional cost for the different wind-turbine subsystems, as size increases (data compilation from [26]).

Moreover, while the rest of the wind turbine subsystems are highly developed technological products, the blades are unique. There is no other technological application that uses such a device, so practical experience in blade manufacturing is relatively new. Blades also operate under a complex combination of fluctuating loads, and huge size differences complicate extrapolation of experimental data from the wind-tunnel to the prototype scale. Hence, computer models of fluid-structure interaction phenomena are particularly relevant to the design and optimization of wind-turbines. The wind-turbine industry is increasingly using computer models for blade structural design and for the optimization of its aerodynamics. Nevertheless, several features of the complex interaction of physical processes that characterize the coupled aeroelastic problem still exceed the capacities of existing commercial simulation codes. Changes in structural response due to the development of new techniques in blade construction and/or the use of new materials would also represent a major factor to take into account if the development of a new prototype blade is considered.

Hence, a key factor for a breakthrough in wind-turbine technology is to reduce the uncertainties related to blade dynamics, by the improvement of the quality of numerical simulations of the fluid-structure interaction process, and by a better understanding of the underlying physics. The current state-of-the-art is to solve the aeroelastic equations in a fully non-linear coupled mode using Bernoulli or Timoshenko beam models (see [11], where a thorough coverage of the topic is presented). The goal is to provide the industry with a tool that helps them to introduce new technological solutions to improve the economics of blade design, manufacturing and transport logistics, without compromising reliability. A fundamental step in that direction is the implementation of structural models capable of capturing the complex features of innovative prototype blades, so they can be tested at realistic full-scale conditions with a reasonable computational cost. To this end, we developed a *generalized Timoshenko* code [27] based on a modified implementation the Variational-Asymptotic Beam Sectional technique (VABS) proposed by Hodges et al. (see [13] and references therein). The ultimate goal is to combine this code with an advanced non-linear adaptive model of the unsteady flow, based on the vorticity-velocity formulation of the Navier-Stokes equations, called the KLE model [32,33], which would offer performance advantages over the present fluid-structure solvers.

In this chapter we present a set of tools for the design and full-scale analysis of the dynamics of composite laminate wind-turbine blades. The geometric design is carried on by means of a novel interpolation technique and the behavior of the blades is then simulated under normal operational conditions. We obtained results for the displacements and rotations of the blade sections along the span, section stresses, and fundamental vibrational modes of the blades.

http://dx.doi.org/10.5772/51142

2. Fluid--Structure Interaction Model

2.1. Structural model

Even though a wind turbine blade is a slender structure that may be studied as a beam, they are usually not simple to model due to the inhomogeneous distribution of material properties and the complexity of their cross section (see Fig. 2. The *ad hoc* kinematic assumptions made in classical theories (like the Bernoulli or the standard Timoshenko approaches) may introduce significant errors, especially when the blade is vibrating with a wavelength shorter than its length. Complex blade geometry due to reasons of aerodynamic/mechanical design, new techniques of blade construction, and the use of new materials combine themselves to give a new dimension to the problem. In order t0 obtain a fluid-structure interaction model capable of dealing with the complex features of new-generation blades, we developed a code [27] based on a modified implementation of the Variational-Asymptotic Beam Sectional (VABS) model. Proposed and developed by Prof. Hodges and his collaborators [see 13, 39, and references therein], VABS is a model for curved and twisted composite beams that uses the same variables as classical Timoshenko beam theory, but the hypothesis of beam sections remaining planar after deformation is abandoned. Instead, the real warping of the deformed section is interpolated by a 2-D finite-element mesh and its contribution to the strain energy is put in terms of the classical 1-D Timoshenko''s variables by means of a pre-resolution. The geometrical complexity of the blade section and/or its material inhomogeneousness are reduced into a stiffness matrix for the 1-D beam. The reduced 1-D strain energy is equivalent to the actual 3-D strain energy in an asymptotic sense. Elimination of the *ad hoc* kinematic assumptions produces a fully populated 6×6 symmetric matrix for the 1-D beam, with as many as 21 stiffnesses, instead of the six fundamental stiffnesses of the original Timoshenko theory. That is why VABS is referred to as a *generalized Timoshenko theory*.

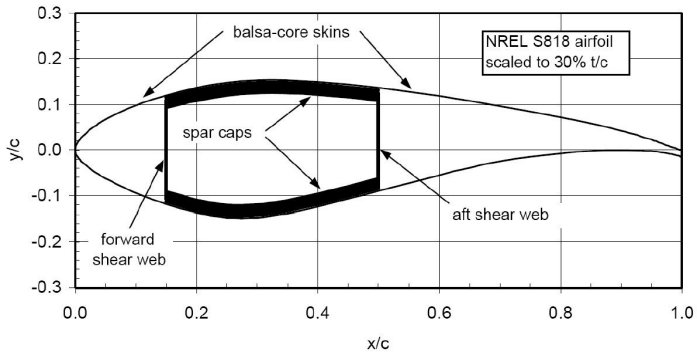

Figure 2. Example of blade-section structural architecture representative of current commercial blade designs. The primary structural member is a box-spar, with a substantial build-up of spar cap material between the webs. The exterior skins and internal shear webs are both sandwich construction with triaxial fiberglass laminate separated by balsa core (from [9]).

Even for the case of large displacements and rotations of the beam sections, our model allows for accurate modeling of the bending and transverse shear in two directions, extension and torsion of the blade structure as a 1-D finite-element problem. Thus, this way we are able to decouple a general 3-D nonlinear anisotropic elasticity problem into a linear, 2-D, cross-sectional analysis (that may be solved *a priori*), and a nonlinear, 1-D, beam analysis for the global problem, which is what we would solve at each time step of a fluid-structure interaction analysis. This translates into substantial savings in computational cost as the structural problem is solved along many timesteps. The cross-sectional 2-D analysis (that may be performed in parallel for the many cross sections along the blade) calculates the 3-D warping functions asymptotically and finds the constitutive model for the 1-D nonlinear beam analysis of the blade. After one obtains the global deformation from the 1-D beam analysis, the original 3-D fields (displacements, stresses, and strains) can be recovered *a posteriori* using the already-calculated 3-D warping functions.

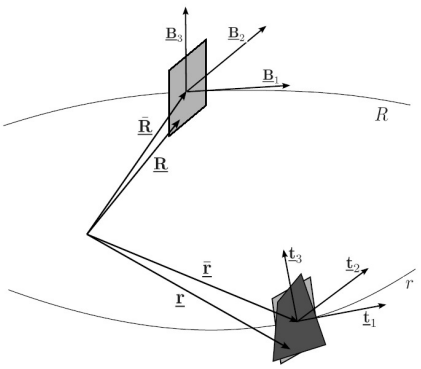

Figure 3. Generalized Timoshenko theory: Schematic of the reference line, orthogonal triads, and beam sections before and after deformation (adapted from [39])

In order to make this chapter self-contained, we shall see a brief outline of the theoretical basis of the dimensional reduction technique. More details can be found in [27, 13, 39] and references therein. Referring to Fig. 3, we have a reference line R drawn along the axis of the beam in the undeformed configuration. R could be twisted and/or curved according to the initial geometry of the beam. Section planes are normal to R at every point along its length. At the point where R intersects the section, an associated orthogonal triad $\underline{\mathbf{B}}_1, \underline{\mathbf{B}}_2, \underline{\mathbf{B}}_3$, is defined in such a way that $\underline{\mathbf{B}}_1$ is tangent to R and $\underline{\mathbf{B}}_2, \underline{\mathbf{B}}_3$ are contained into the section plane; with a correspondent coordinate system (X^1, X^2, X^3) where X^1 is the coordinate along R and X^2, X^3 are the Cartesian coordinates on the section plane. The position of a generic point on each section may be written as

http://dx.doi.org/10.5772/51142

$$\underline{\mathbf{R}}(X^i) = \bar{\underline{\mathbf{R}}}(X^1) + X^\alpha \underline{\mathbf{B}}_\alpha(X^1) \tag{1}$$

where $\underline{\mathbf{R}}$ denotes the position of the center of the tern along R, and the index α assumes values 2 and 3.

When the structure is deformed due to loading, the original reference line R adopts a new geometry r, and we have a new triad $\underline{\mathbf{t}}_1, \underline{\mathbf{t}}_2, \underline{\mathbf{t}}_3$ associated to each point, where $\underline{\mathbf{t}}_1$ is tangent to r and $\underline{\mathbf{t}}_2, \underline{\mathbf{t}}_3$ are contained into the normal plane. The material point whose original position was given by $\underline{\mathbf{R}}$ has now the position vector

$$\underline{\mathbf{r}}(X^i) = \bar{\underline{\mathbf{R}}} + \underline{\mathbf{u}} + X^\alpha \underline{\mathbf{t}}_\alpha + w_i \underline{\mathbf{t}}_i, \tag{2}$$

where w_i are the contribution to the displacement due to warping. Now, we are able to compute the components of the gradient-of-deformation tensor as $F_{ij} = \underline{\mathbf{t}}_i \cdot \mathbf{g}_k \underline{\mathbf{G}}^k \cdot \underline{\mathbf{B}}_j$, where $\mathbf{g}_k$ and $\underline{\mathbf{G}}^k$ are respectively the covariant base vectors for the deformed configuration and the contravariant base vectors in the undeformed configuration, obtained from the kinematic description of equations (1) and (2). The Jaumann-Biot-Cauchy strain tensor is $\Gamma_{ij} = \frac{1}{2}(F_{ij} + F_{ji}) - \delta_{ij}$, which provides a suitable measure of the 3-D strain field in terms of the beam strain measures and arbitrary warping functions. Γ is then used to compute the strain energy density function as

$$2U = \langle\langle \boldsymbol{\Gamma}^T \mid \mathbf{S}\, \boldsymbol{\Gamma} \rangle\rangle, \tag{3}$$

were, $\boldsymbol{S}$ is the matrix of the characteristics of the material expressed in the $\underline{\mathbf{B}}_i$ coordinates, and $\langle\langle \cdot \rangle\rangle = \int_S \cdot \sqrt{G}\, dX^2 dX^3$, where s indicates the 2-D domain of the cross-section.

The next step is to find a strain energy expression asymptotically correct up to the second order of h/l and h/R_0, where h is the characteristic size of the section, l the characteristic wavelength of deformation along the beam axis, and R_0 the characteristic radii of initial curvatures and twist of the beam. A complete second-order strain energy is sufficient for the purpose of constructing a generalized Timoshenko model because it is generally accepted that the transverse shear strain measures are one order less than classical beam strain measures (extension, torsion and bending in two directions) [38]. A strain energy expression that asymptotically approximates the 3-D energy up to the second order is achieved using the Variational Asymptotic Method proposed in [4]. The complete derivation of this procedure is presented in [13], resulting in the following expression for the asymptotically correct strain energy:

$$2U = \varepsilon^T \boldsymbol{A} \varepsilon + \varepsilon^T 2\boldsymbol{B} \varepsilon' + \varepsilon'^T \boldsymbol{C} \varepsilon' + \varepsilon^T 2\boldsymbol{D} \varepsilon'', \tag{4}$$

where **A**, **B**, **C**, **D** are matrices that carry information on both the geometry and the material properties of the cross section, $()''$ indicates the partial derivative with respect to the axial coordinate X^1, and $\varepsilon = [\bar{\gamma}_{11} \; \bar{\kappa}_1 \; \bar{\kappa}_2 \; \bar{\kappa}_3]^T$, are the strain measures defined in the classical Bernoulli beam theory: $\bar{\gamma}_{11}$ the extension of the beam reference line, $\bar{k}_1$ its torsion, and $\bar{k}_2$ and $\bar{k}_3$ the bending of the reference line in axes 2 and 3 due to the deformation.

The variational asymptotic procedure to get the matrices in equation (4) involves the discretization by finite-element techniques of the warping functions w_i defined in expression (2).

During this procedure, a set of four constraints must be applied on w_i. These restrictions, defined as $\langle w_i \rangle = 0$ and $\langle X^2 w_3 - X^3 w_2 \rangle = 0$, where $\langle \bullet \rangle = \int_s \bullet \, dX^2 dX^3$, are intended to eliminate four rigid modes of displacement of the warped section (i.e. the three linear displacements plus the turn around $\underline{\mathbf{t}}1$), which are already included in the Bernoulli strain measures ε. Previous implementations of VABS (e.g. [39,13]) use the technique described by Cesnik *et al.* [6] to impose these constraints. In Cesnik et al.'s method, the rigid modes of displacement are suppressed explicitly. Then, the eigenvectors associated with the rigid modes in the matrix of the linear system that needs to be solved are computed, and used to get a reduced system. Instead of that, in our implementation of VABS, we use the Lagrangian-multiplier technique in its classical way to impose the constraints, solving the expanded system for the constrained variational formulation itself. This simplifies the procedure by basically combining the whole solution in a single step. This simplification produces by itself a certain reduction in the overall computational cost, but most important, it has the advantage of allowing the use of the internal-node condensation technique in the finite-element discretization. As we shall see later, internal-node condensation allows us to substantially improve the efficiency of our solution by the tri-quadrilateral finite-element technique.

Expression (4) for the strain energy is asymptotically correct. Nevertheless, it is difficult to use in practice because it contains derivatives of the classical strain measures, which requires complicated boundary conditions. But, the well known Timoshenko beam theory is free from such drawbacks. Hence, the next step is to fit the strain energy in (4), into a generalized Timoshenko model of the form

$$2U = \begin{bmatrix} \varepsilon^T & \gamma_s^T \end{bmatrix} \begin{bmatrix} \mathbf{X} & \mathbf{Y} \\ \mathbf{Y}^T & \mathbf{G} \end{bmatrix} \begin{bmatrix} \varepsilon \\ \gamma_s \end{bmatrix} = \varepsilon^T \mathbf{X} \varepsilon + 2\varepsilon^T \mathbf{Y} \gamma_s + \gamma_s^T \mathbf{G} \gamma_s, \tag{5}$$

where $= [\gamma_{11} \quad \kappa_1 \quad \kappa_2 \quad \kappa_3]^T$ are the classical Timoshenko strain measures due to extension, torsion and bending, and $\gamma = [2\gamma_{12} \quad 2\gamma_{13}]^T$ the transverse shear strains.

What we need to find is **X**, **Y** and **G** in such a way that the strain energy in (4) and (5) would be equivalent up to at least second order. There is an identity that relates both the Bernoulli and the Timoshenko measures of deformation

$$\varepsilon = \varepsilon + \mathbf{Q}_\gamma \gamma'_s + \mathbf{P}_\gamma \gamma_s, \tag{6}$$

where

$$\mathbf{Q}_\gamma^T = \begin{bmatrix} 0 & 0 & 0 & 1 \\ 0 & 0 & -1 & 0 \end{bmatrix}, \quad \text{y} \quad \mathbf{P}_\gamma^T = \begin{bmatrix} 0 & K_2 & -K_1 & 0 \\ 0 & K_3 & 0 & -K_1 \end{bmatrix}, \tag{7}$$

being K_1 the twist, and K_2 and K_3 the curvatures of the original reference line R. Thus, using (6), we may rewrite expression (4) in terms of the generalized Timoshenko strain measures using the 1-D equilibrium equations. This provides a way to relate the derivatives of strain measures with the strain measures themselves, to fit the resulting expression into the generalized Timoshenko form (5). Then, an asymptotic method is used to get approximations to **X**, **Y** and **G**; using as input the already computed matrices **A**, **B**, **C**, **D** (see [39] for details). Finally, a stiffness matrix for the 1-D beam problem $\bar{\mathbb{S}}$ is formed as a simple reordering of the matrix $\begin{bmatrix} \mathbf{X} & \mathbf{Y} \\ \mathbf{Y}^T & \mathbf{G} \end{bmatrix}$}, in such a way as to get a functional for the strain energy density of expression~(5)

$$2U = \bar{\gamma}^T \, \bar{\mathbb{S}} \, \bar{\gamma} \tag{8}$$

where $\bar{\gamma} = \begin{bmatrix} \gamma \\ \kappa \end{bmatrix}$ is the array of Timoshenko measures of deformation regrouped in a more convenient way, $\gamma^T = [\gamma_{11} \quad 2\gamma_{12} \quad 2\gamma_{13}]$ and $\kappa^T = [\kappa_1 \quad \kappa_2 \quad \kappa_3]$.

For the discretization of the 2-D sections, we adopted the tri-quadrilateral finite-element technique, which is based on the use of nine-node biquadratic isoparametric finite elements that possess a high convergence rate and, due their biquadratic interpolation of the geometric coordinates, provide the additional ability of reducing the so-called skin-error on curvilinear boundaries when compared to linear elements. For a detailed description of the isoparametric-element technique and its corresponding interpolation functions see Bathe [3].

In order to combine the advantages of the nine-node quadrilateral isoparametric element with the geometrical ability of a triangular grid to create suitable non-structured meshes with gradual and smooth changes of mesh density, we implemented what we called tri-quadrilateral isoparametric elements. The tri-quadrilateral elements consist of an assembling of three quadrilateral nine-node isoparametric elements in which each triangle of a standard unstructured mesh is divided into. By static condensation of the nodes that lie inside the triangle, we can significantly reduce the number of nodes to solve in the final system, subsequently recovering the values for the internal nodes from the solution on the non-condensable nodes. The internal nodes may be expressed in terms of nodes which lay on the elemental boundary following the classical procedure for elemental condensation (see [3]).

This process of condensation allows us to reduce the size of the new system to solve to approximately a 40% of the original system. The use of the static condensation procedure is attractive not only because it reduces the size of the stiffness matrices arising in finite-element and spectral-element methods but also because it improves the condition number of the final condensed system. This is related with the properties of the Schur-complement technique. The condensed system is essentially the Schur complement of the interior-node submatrix in the non-condensed original system. A detailed description of the tri-quadrilateral technique may be found in Ponta [33]; including a schematic example of a mesh of tri-quadrilateral finite elements obtained from the original triangular discretization, and a description of the internal topology of the tri-quadrilateral element.

To solve the one-dimensional problem for the equivalent beam, we use a formulation based on the intrinsic equations for the beam obtained from variational principles [12], and weighted in an energy-consistent way according to Patil et al. [30], which produces the following variational formulation:

$$\int_0^{\ell}\Big[\underbrace{\delta\bar{\mathbf{V}}^T\,\bar{\mathbb{I}}\,\dot{\bar{\mathbf{V}}}}_{1}+\underbrace{\delta\bar{\mathbf{F}}^T\,\bar{\mathbb{S}}^{-1}\,\dot{\bar{\mathbf{F}}}}_{2}\Big]dX^1=\int_0^{\ell}\Big[\underbrace{\delta\bar{\mathbf{V}}^T\,\bar{\mathbf{F}}'}_{3}+\underbrace{\delta\bar{\mathbf{V}}^T\,\hat{\bar{\mathbf{K}}}\,\bar{\mathbf{F}}}_{4}+\underbrace{\delta\bar{\mathbf{V}}^T\,\hat{\bar{\gamma}}\,\bar{\mathbf{F}}}_{5}+$$
$$\underbrace{\delta\bar{\mathbf{V}}^T\,\bar{\mathbf{f}}}_{6}-\underbrace{\delta\bar{\mathbf{V}}^T\,\hat{\bar{\mathbf{V}}}\,\bar{\mathbb{I}}\,\bar{\mathbf{V}}}_{7}+\underbrace{\delta\bar{\mathbf{F}}^T\,\bar{\mathbf{V}}'}_{8}-\underbrace{\delta\bar{\mathbf{F}}^T\,\hat{\bar{\mathbf{K}}}^T\,\bar{\mathbf{V}}}_{9}-\underbrace{\delta\bar{\mathbf{F}}^T\,\hat{\bar{\gamma}}^T\,\bar{\mathbf{V}}}_{10}\Big]dX^1, \tag{9}$$

where

$$\mathbf{F}=\begin{bmatrix}\mathbf{F}\\ \mathbf{M}\end{bmatrix},\quad \bar{\mathbf{V}}=\begin{bmatrix}\mathbf{V}\\ \boldsymbol{\Omega}\end{bmatrix},\quad \bar{\mathbf{f}}=\begin{bmatrix}\mathbf{f}\\ \mathbf{m}\end{bmatrix},$$
$$\hat{\bar{\boldsymbol{\gamma}}}=\begin{bmatrix}\tilde{\boldsymbol{\kappa}} & \mathbf{0}\\ \hat{\gamma} & \tilde{\boldsymbol{\kappa}}\end{bmatrix},\quad \hat{\bar{\mathbf{V}}}=\begin{bmatrix}\tilde{\boldsymbol{\Omega}} & 0\\ \tilde{\mathbf{V}} & \tilde{\boldsymbol{\Omega}}\end{bmatrix},\quad \hat{\bar{\mathbf{K}}}=\begin{bmatrix}\tilde{\mathbf{K}} & 0\\ \tilde{\mathbf{e}}_1 & \tilde{\mathbf{K}}\end{bmatrix}.$$

Tilde indicates the skew-symmetric matrix associated to a vector magnitude in such a way that, for example, if we have any pair of vectors **A** and **B**, the matrix--vector product $\tilde{\mathbf{A}}\,\mathbf{B}$ is equivalent to the cross product $\mathbf{A}\times\mathbf{B}$. Thus, $\tilde{\gamma}$ is associated with $\tilde{\kappa}$ with κ, $\tilde{\mathbf{V}}$ with **V**, and so forth. Hence, matrix $\tilde{\gamma}$ is a rearrangement of the components of the strain-measures vector $\bar{\gamma}$ defined above, the generalized-velocities vector $\bar{\mathbf{V}}$ and matrix $\tilde{\mathbf{V}}$ represent the components of the linear and angular velocities, and matrix $\tilde{\mathbf{K}}$ represents the initial torsion and curvatures of the beam (matrix $\tilde{\mathbf{e}}_1$ is the skew-symmetric matrix associated to $\mathbf{e}_1^T=[1\quad 0\quad 0]$, the unit vector along X^1). The generalized-forces vector $\bar{\mathbf{F}}$ represents the forces and moments related with the strain measures $(\bar{\gamma}=\bar{\mathbb{S}}^{-1}\bar{\mathbf{F}})$, and the generalized-distributed-loads vector $\bar{\mathbf{f}}$ represents the forces and moments distributed along the axis of the beam. Here, $\bar{\mathbb{S}}$ is the same stiffness matrix for the 1-D model, see equation (8); and $\bar{\mathbf{I}}$ is the inertia matrix of each section. The upper dot indicates a time derivative, and the prime a derivative with respect to the longitudinal coordinate of the beam X^1.

http://dx.doi.org/10.5772/51142

This variational formulation was discretized by the spectral-element method (see [20,29]). The magnitudes in (9) where replaced by their interpolated counterparts: $\bar{\mathbf{V}}=\mathbf{H}^e_{\bar{\mathbf{V}}}\,\mathbf{Q}^e$, and $\bar{\mathbf{F}}=\mathbf{H}^e_{\bar{\mathbf{F}}}\,\mathbf{Q}^e$, where $\mathbf{H}^e_{\bar{\mathbf{V}}}$ and $\mathbf{H}^e_{\bar{\mathbf{F}}}$ are the interpolation-function arrays, and $\mathbf{Q}^e$ is a vector containing the nodal values of both the generalized velocities and the generalized forces. Superscript *e* indicates discretization of the terms at the elemental level, which will disappear after the final assembly of the terms into the global matrix for the whole beam. The axial derivatives of the magnitudes were interpolated in a similar way: $\bar{\mathbf{V}}'=\mathbf{B}^e_{\bar{\mathbf{V}}}\,\mathbf{Q}^e$, and $\bar{\mathbf{F}}'=\mathbf{B}^e_{\bar{\mathbf{F}}}\,\mathbf{Q}^e$, where $\mathbf{B}^e_{\bar{\mathbf{V}}}$ and $\mathbf{B}^e_{\bar{\mathbf{F}}}$ are the arrays for the interpolation-function derivatives. Then, we arrived to the discretized version of (9):

$$\delta\boldsymbol{Q}^{e\,T}\boldsymbol{M}_{\mathbf{1}}^{e}\dot{\boldsymbol{Q}}^{e}=\delta\boldsymbol{Q}^{e\,T}\left(\boldsymbol{K}_{\mathbf{1}}^{e}+\boldsymbol{K}_{\mathbf{2}}^{e}\right)\boldsymbol{Q}^{e}+\delta\boldsymbol{Q}^{e\,T}\boldsymbol{K}_{\boldsymbol{q}}^{e}\boldsymbol{q}^{-e}+\delta\boldsymbol{Q}^{e\,T}\boldsymbol{B}_{\mathbf{Q}}^{e}\left(\boldsymbol{Q}^{e}\right), \tag{10}$$

where

$$\mathbf{M}_{\mathbf{1}}^{e}=\int_{-1}^{1}\left[\mathbf{H}_{\bar{\mathbf{V}}}^{e\,T}\,\bar{\mathbb{I}}\,\mathbf{H}_{\bar{\mathbf{V}}}^{e}+\mathbf{H}_{\bar{\mathbf{F}}}^{e\,T}\,\bar{\mathbb{S}}^{-1}\,\mathbf{H}_{\bar{\mathbf{F}}}^{e}\right]J\,dt.$$

$$\mathbf{K}_{\mathbf{1}}^{e}=\int_{-1}^{1}\left[\mathbf{H}_{\bar{\mathbf{V}}}^{e\,T}\,\mathbf{B}_{\bar{\mathbf{F}}}^{e}+\mathbf{H}_{\bar{\mathbf{F}}}^{e\,T}\,\mathbf{B}_{\bar{\mathbf{V}}}^{e}\right]J\,dt\,\mathbf{Q}^{e},$$

$$\mathbf{K}_{\mathbf{2}}^{e}=\int_{-1}^{1}\left[\mathbf{H}_{\bar{\mathbf{V}}}^{e\,T}\,\hat{\mathbf{K}}\,\mathbf{H}_{\bar{\mathbf{F}}}^{e}-\mathbf{H}_{\bar{\mathbf{F}}}^{e\,T}\,\hat{\mathbf{K}}^{T}\,\mathbf{H}_{\bar{\mathbf{V}}}^{e}\right]J\,dt$$

$$\mathbf{K}_{\mathbf{q}}^{e}=\int_{-1}^{1}\mathbf{H}_{\bar{\mathbf{V}}}^{e\,T}\,\mathbf{H}_{\bar{\mathbf{F}}}^{e}\,J\,dt.$$

$\mathbf{M}_{\mathbf{1}}^{e}$ corresponds to the discretization of terms 1 and 2 giving the equivalent of a mass matrix. $\mathbf{K}_{\mathbf{1}}^{e}$, corresponding to terms 3 and 8, is the stiffness matrix of the 1-D problem. $\mathbf{K}_{\mathbf{2}}^{e}$, corresponding to terms 4 and 9, is the additional stiffness related with the twist and curvature of the undeformed configuration. $\mathbf{K}_{\mathbf{q}}^{e}$ corresponds to the evaluation of term 6, the contribution of the distributed loads; and $\bar{\mathbf{q}}^{e}$ is an array containing the nodal values of the generalized distributed loads. *t* is the natural coordinate in the elements and *J* is the Jacobian of the mapping from the problem coordinate X^1 to *t* (see [3]). The discretized version of the terms in (9) related to non-linear interactions, i.e. terms 5, 7 and 10, gives

$$\mathbf{B}_{\mathrm{Q}}^{e}\left(\mathbf{Q}^{e}\right)=\int_{-1}^{1}\left[\mathbf{H}_{\bar{\mathbf{V}}}^{e\,T}\,\hat{\gamma}\,\mathbf{H}_{\bar{\mathbf{F}}}^{e}-\mathbf{H}_{\bar{\mathbf{V}}}^{e\,T}\,\hat{\mathbf{V}}\,\bar{\mathbb{I}}\,\mathbf{H}_{\bar{\mathbf{V}}}^{e}-\mathbf{H}_{\bar{\mathbf{F}}}^{e\,T}\,\hat{\gamma}^{T}\,\mathbf{H}_{\bar{\mathbf{V}}}^{e}\right]\mathbf{Q}^{e}\,J\,dt$$

A linearization of $\mathbf{B}_{\mathbf{Q}}^{e}(\mathbf{Q}^{e})$ around any given configuration $\mathbf{Q}_1^e$ gives the matrix

$$\mathbf{K}_{\mathbf{N}}^{e}(\mathbf{Q}_1^e) = \int_{-1}^{1} \left\{ \mathbf{H}_{\bar{\mathbf{V}}}^{e\,T} \left[\hat{\gamma}_1\, \mathbf{H}_{\bar{\mathbf{F}}}^{e} - \hat{\mathbf{V}}_1\, \bar{\mathbb{I}}\, \mathbf{H}_{\bar{\mathbf{V}}}^{e} - \hat{\mathbf{F}}_1\, \bar{\mathbb{S}}^{-1}\, \mathbf{H}_{\bar{\mathbf{F}}}^{e} + \hat{\mathbf{P}}_1\, \mathbf{H}_{\bar{\mathbf{V}}}^{e} \right] + \mathbf{H}_{\bar{\mathbf{F}}}^{e\,T} \left[\hat{\mathbf{V}}_1^{T}\, \bar{\mathbb{S}}^{-1}\, \mathbf{H}_{\bar{\mathbf{F}}}^{e} - \hat{\gamma}_1^{T}\, \mathbf{H}_{\bar{\mathbf{V}}}^{e} \right] \right\} J\, dt,$$

where

$$\hat{\mathbf{F}} = \begin{bmatrix} \mathbf{0} & \tilde{\mathbf{F}} \\ \tilde{\mathbf{F}} & \tilde{\mathbf{M}} \end{bmatrix}, \quad \hat{\mathbf{P}} = \begin{bmatrix} \mathbf{0} & \tilde{\mathbf{P}}_v \\ \tilde{\mathbf{P}}_v & \tilde{\mathbf{P}}_\omega \end{bmatrix}$$

Matrix $\bar{\mathbf{F}}$ is a rearrangement of the components of the generalized-forces vector $\bar{\mathbf{F}}$ defined above. Matrix $\bar{\mathbf{P}}$ is a rearrangement of the components of the generalized-momentum vector $\mathbf{P} = \begin{bmatrix} \mathbf{P}_v \\ \mathbf{P}_\omega \end{bmatrix}$, which represents the linear and angular momenta related with the generalized-velocities $(\bar{\mathbf{P}} = \bar{\mathbb{I}}\, \bar{\mathbf{V}})$. Tilde operates in the same way defined before, and the subscript 1 indicates the value of the magnitudes at a given state $\mathbf{Q}_1^e$.

Finally, after the assembly of the elemental terms into the global system, the solution for the nonlinear problem (9) in its steady state was obtained by solving iteratively for $\Delta\mathbf{Q}$ the discretized expression

$$\left[\mathbf{K_1} + \mathbf{K_2} + \mathbf{K_N}\left(\mathbf{Q}^{(i)}\right) \right] \Delta\mathbf{Q} = -\mathbf{K_q}\bar{\mathbf{q}} - (\mathbf{K_1} + \mathbf{K_2})\, \mathbf{Q}^{(i)} - \mathbf{B}_{\mathbf{Q}}\left(\mathbf{Q}^{(i)}\right), \tag{11}$$

and updating the global vector of nodal values of the generalized velocities and forces as $\mathbf{Q}^{(i+1)} = \mathbf{Q}^{(i)} + \Delta\mathbf{Q}$.

From the steady-state solution we also obtained the vibrational modes of the blade structure and their corresponding frequencies by solving the eigenvalue problem

$$\mathbf{M_1}\dot{\mathbf{Q}} + \left[\mathbf{K_1} + \mathbf{K_2} + \mathbf{K_N}\left(\mathbf{Q}^{(i)}\right) \right] \mathbf{Q} = \mathbf{0}. \tag{12}$$

From these results for the intrinsic equations we recovered the displacements and rotations of the blade sections by solving the kinematic equations for the beam (see [13])

$$\mathbf{u}' - \mathbf{C}_{rR}^{T}(\boldsymbol{\gamma} + \mathbf{e}_1) + \mathbf{e}_1 + \tilde{\mathbf{K}}\, \mathbf{u} = \mathbf{0}, \tag{13}$$

http://dx.doi.org/10.5772/51142

$$\tilde{\mathbf{K}} + \tilde{\boldsymbol{\kappa}} + \mathbf{C}'_{rR}\,\mathbf{C}^T_{rR} - \mathbf{C}_{rR}\,\tilde{\mathbf{K}}\,\mathbf{C}^T_{rR} = \mathbf{0}, \tag{14}$$

where $\mathbf{u}$ is the vector of displacements of each point along the reference line from its position in the reference configuration to the one in the deformed configuration, and $\mathbf{C}_{rR}$ is the orthogonal matrix that rotates the local triad from its original orientation in the reference configuration to the one in the deformed configuration (both are defined in function of the longitudinal coordinate X^1). The strains γ and κ were computed from the generalized forces and the stiffness of the corresponding blade section. Equations (13) and (14) were also linearized, and like the other expressions, discretized by the spectral-element method.

2.2. Aerodynamic model

The flow model that interacts with the structural counterpart presented in section 2.1, called *Large Sectional Rotation BEM (LSR-BEM)*, is responsible to provide the aerodynamic loads along the rotor blades, and is sensitive enough to take into account all the complex deformation modes that the structural model is able to solve. The basis for our aerodynamic model is the well known Blade Element Momentum theory (BEM). Nevertheless, due to the high level of detail that our structural model can provide, a complete reformulation was needed in the aerodynamic model to get a compatible level of description.

The tendency in the wind-turbine industry to increase the size of the state-of-the-art machine [17] drives not only to bigger, but also to more flexible blades which are relatively lighter. It is observed for this type of wind turbine blades that big deformations, either due to blade flexibility or to pre-conforming processes, produces high rotations of the blade sections. Moreover, blades could be pre-conformed with specific curvatures given to any of their axis *(i.e. conning/sweeping)*. This tendency puts in evidence one of the most important limitations of the current BEM theory. While the basics of this theory keeps being perfectly valid, the actual mathematical formulation implies the assumption of blade sections remaining perpendicular to an outwards radial line contained in the plane of the actuator disk coincident with the rotor's plane. That is, even though the basics of the BEM theory (i.e. the equation of the aerodynamic loads and the change of momentum in the streamtubes) keeps being valid, the mathematical formulation cannot represent large rotations of the blade sections. This basically leads to a misrepresentation of the effects of the large deformation associated to flexible blades on the computation of the aerodynamic loads. Hence, a new mathematical formulation is required to project the velocities obtained from momentum theory onto the blade element's plane and then re-project backwards the resulting forces from Blade Element theory onto the plane of the stream tube actuator disk. When analyzing BEM theory for this cases, the principle of equating the forces obtained by Blade Element theory with the ones coming from the the changing of momentum in the stream tube is still valid.

In what follows we will describe the main characteristics of our model, and refer to [25] and [5] for details on the classical *BEM theory*.We start by defining a set of orthogonal matrices that perform the rotation of the physical magnitudes involved (velocities, forces, etc.) The

interaction with external control modules will require a constant update of this projection matrices. For example, the rotor azimuth matrix, besides the instantaneous position of the blade along its rotation, can reflect control actions on the dynamics of the Electro-Mechanical train that define the rotor's angular speed, Ω .

For instance, we could write the wind velocity vector $\mathbf{W_h}$ facing the differential annulus of our actuator disk, affecting its components, according to BEM theory, by the axial induction factor a and the rotational induction factor a'. The h subscript here indicates that the wind velocity vector is described in the *hub* coordinate system according to standards from the International Electrotechnical Commission (IEC) [15].

$$\mathbf{W}_h = \begin{bmatrix} W_{wh_{(1)}}(1-a) \\ W_{wh_{(2)}} + \Omega r_h (1+a') \\ W_{wh_{(3)}} \end{bmatrix}, \tag{15}$$

where $\mathbf{W}_{wh}$ is the incoming wind velocity projected into the h coordinate system, Ω is the angular velocity of the rotor and r_h is the radial distance of the airfoil section in the h coordinate system.

Then, to compute the relative velocity affecting a blade element, we will project $\mathbf{W_h}$ going through the different coordinate systems, from the hub, until reaching the blade's section coordinate system. Let's see first which rotations we shall go through, and which matrices will transform our velocity vector from one coordinate system to the other.

Thus, the conning rotation matrix $\mathbf{C}_{\theta_{cn}}$ is a linear operator with a basic rotation taking into account the conning angle for the rotor, and the Pitching rotation matrix $\mathbf{C}_{\theta_p}$, represents a rotation around the pitch of the blade.

$$\mathbf{C}_{\theta_p} = \begin{bmatrix} \cos(\theta_p) & -\sin(\theta_p) & 0 \\ \sin(\theta_p) & \cos(\theta_p) & 0 \\ 0 & 0 & 1 \end{bmatrix}, \tag{16}$$

where θ_p is the pitch angle.

Two more re-orientations are needed in order to get to the instantaneous coordinate system of the blade sections, associated with the deformed reference line r of section 2.1. The first of this matrices contains information on blade section's geometry at the time the blade was designed and manufactured. As it was mentioned previously, the blade could have pre-conformed curvatures along its longitudinal axis *(i.e. the blade axis is no longer rectilinear)*. This curvatures can reflect either an initial twist along the longitudinal axis or a combination of twist plus pre-bending on the other two axes *(i.e. conning/sweeping)*. To this end, we compute during the blade design stage a set of transformation matrices which contain the information of the three dimensional orientation of the blade''s sections for each posi-

http://dx.doi.org/10.5772/51142

tion on the longitudinal axis as we move along the span. To this end, we compute the Frenet-Serret formulas that define the curvature of the (now curvilinear) longitudinal axis. These differential formulas provide the means to describe the *tangent*, *normal* and *binormal* unit vectors on a given curve. Due to this unit vectors, the Frenet-Serret coordinate system is also known as the *TNB frame*. More information about the calculation of the TNB unit vectors, their properties and other applications can be found in [37]. Around the tangential axis of the TNB, there is a further rotation of each blade section to orient it accordingly to the particular twist specified on the blade's aerodynamic design. Combining these rotations we then create a transformation matrix for every blade section at different span positions. We call this matrix the $\mathbf{C}_{Rb}$, as it relates the global coordinate system of the blade *b*, with the system of coordinates of the blade sections in the undeformed configuration defined by line *R*, as in section 2.1.

After applying the $\mathbf{C}_{Rb}$, one more projection is needed to get to the instantaneous coordinate system associated with *r*. This last transformation is given by the $\mathbf{C}_{rR}$ matrix, computed by the 1D structural model, see equation 14. It contains information to transform vectors from the *R* to the *r* systems after structural deformations had occurred. Note that this matrix is updated at every timestep of the 1D model during dynamic simulations, being one of the key variables transporting information between the structural and aerodynamic models.

After all these projections of the $\mathbf{W}_{\mathbf{h}}$ vector, we have the relative wind velocity expressed in the blade''s section coordinate system. The expression for the flow velocity relative to the blade section, $\mathbf{W}_{rel}$:

$$\mathbf{W}_{rel} = \left(\mathbf{C}_{rR}\mathbf{C}_{Rb}\mathbf{C}_{\theta_p}\mathbf{C}_{\theta_{cn}}\mathbf{W}_h\right) + \mathbf{v}_{str} \tag{17}$$

where the addition of $\mathbf{v}_{str}$ corresponds to the blade section structural deformation velocities, coming from the structural model.

Then, the magnitude $|\mathbf{W}_{rel}|$ and the angle of attack α are used to compute the forces on the airfoil section through the aerodynamic coefficients C_l, C_d. Another innovation of our model is that the data tables from static wind-tunnel are corrected at each timestep to consider either rotational-augmentation or dynamic-stall effects, or both.

The aerodynamic loads acting on the blade element is then projected back onto the *h* coordinate system,

$$\mathbf{dF}_h = \mathbf{C}^T_{\theta_{cn}}\mathbf{C}^T_{\theta_p}\mathbf{C}^T_{Rb}\mathbf{C}^T_{rR}\mathbf{C}_{Lthal}\mathbf{dF}_r \tag{18}$$

where $\mathbf{C}_{Lthal}$ is the matrix which projects the lift and drag forces onto the chord-wise and chord-normal directions, which are aligned with the coordinates of *r*. Finally, as in the classical BEM theory, $\mathbf{dF}_h$ is equated to the rate of change of momentum in the annular streamtube corresponding to the blade element. The component normal to the rotor's disk, is

equated to the change in axial momentum, while the tangential component, is equated to the change of angular momentum.

In order to apply this theory to HAWT rotors, we must introduce some corrective factors into the calculation process. BEM theory does not account for the influence of vortices being shed from the blade tips into the wake on the induced velocity field. These tip vortices create multiple helical structures in the wake which play a major role in the induced velocity distribution at the rotor. To compensate for this deficiency in BEM theory, a tip-loss model originally developed by Prandtl is implemented as a correction factor to the induced velocity field [8]. In the same way, a hub-loss model serves to correct the induced velocity resulting from a vortex being shed near the hub of the rotor (see [25], [5].) Another modification needed in the BEM theory is the one developed by Glauert [7] to correct the rotor thrust coefficient in the "turbulent-wake" state. This correction plays a key role when the turbine operates at high tip speed ratios and the induction factor is greater than about 0.45.

BEM theory was originally conceived for axisymmetric flow. Often, however, wind turbines operate at yaw angles relative to the incoming wind, which produces a skewed wake behind the rotor. For this reason, the BEM model needs also to be corrected to account for this skewed wake effect [31,22]. The influence of the wind turbine tower on the blade aerodynamics must also be modeled. We implemented the models developed by Bak et al. [2] and Powles [34] which provide the influence of the tower on the local velocity field at all points around the tower. This model contemplate increases in wind speed around the sides of the tower and the cross-stream velocity component in the tower near flow field.

Our model also incorporates the possibility to add multiple data tables for the different airfoils, and use them in real-time according to the instantaneous aerodynamic situations on the rotor. It also uses the Viterna's extrapolation method [36] to ensure the data availability for a range of angles of attack ± 180 .

3. Numerical Experimentation

In this section, we report some recent results of the application of our model to the analysis of a set of rotor blades based on the *5-MW Reference Wind Turbine (RWT)* proposed by NREL [17]. We will start describing the structural features of the blade, its general aerodynamic properties, the blade internal structure, and the finite element meshes associated to the structural computations.

3.1. NREL Reference Wind Turbine

Based on the REpower 5MW wind turbine, NREL RWT was conceived for both onshore and offshore installations and is well representative of typical utility-scale multi megawatt commercial wind turbines. Although full specific technical data is not available for the REpower 5MW rotor blades, a baseline from a prototype blade was originally released by LM Glassfiber in 2001 for the *Dutch Offshore Wind Energy Converter (DOWEC) 6MW* wind turbine

http://dx.doi.org/10.5772/51142

project~[21,23] and later re-adapted by NREL. In addition, the NREL 5-MW RWT project has been adopted as a reference model by the integrated European Union UpWind research program~[1] and the International Energy Agency (IEA) Wind Annex XXIII Subtask 2 Offshore Code Comparison Collaboration (OC3)~[14,18,28].

As stated in the NREL"s RWT project, the length of our rotor blade is set to be 61.5m. All basic aerodynamic properties as blade section chords, twist angles and basic spanwise stations distribution, correspond to the original data (see [17]). These aerodynamic properties, as well as the denomination of the basic airfoils at the design stations are included in table 1. Complementing the information in this table, figure 4 shows the blade section chords distribution along the span.

Station	Location [m]	Twist angle [°]	Chord length [m]	Airfoil type
1	0	13.3080	3.5420	Cylinder
2	1.3653	13.3080	3.5420	Cylinder
3	4.1020	13.3080	3.8540	Ellipsoid-1
4	6.8327	13.3080	4.1670	Ellipsoid-2
5	10.2520	13.3080	4.5570	DU 00-W-401
6	14.3480	11.4800	4.6520	DU 00-W-350
7	18.4500	10.1620	4.4580	DU 00-W-350
8	22.5521	9.0110	4.2490	DU 97-W-300
9	26.6480	7.7950	4.0070	DU 91-W-250
10	30.7500	6.5440	3.7480	DU 91-W-250
11	34.8520	5.3610	3.5020	DU 93-W-210
12	38.9479	4.1880	3.2560	DU 93-W-210
13	43.0500	3.1250	3.0100	NACA 64-618
14	47.1521	2.3190	2.7640	NACA 64-618
15	51.2480	1.5260	2.5180	NACA 64-618
16	54.6673	0.8630	2.3130	NACA 64-618
17	57.3980	0.3700	2.0860	NACA 64-618
18	60.1347	0.1060	1.4190	NACA 64-618
19	60.5898	0.0903	1.1395	NACA 64-618
20	61.0449	0.0783	0.7787	NACA 64-618

Table 1. Distributed blade aerodynamic properties.

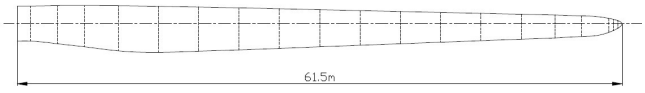

Figure 4. Chord distribution along the blade.

The blade structure is a combination of two external aerodynamic shells, mounted on a box-beam spar which provides the main structural component to the aerodynamic forces. Analysing a blade section (see figure 2) we can see the aerodynamic shells plus two spar caps which, together with two shear webs, form the box-beam spar. Constructive characteristics as thickness as well as number and orientation of fiberglass layers for the different structural components of the blade sections are covered in detail in reports published by SANDIA National Labs. [35,9]. According to these reports, the aerodynamic shells are mainly composed by ±45 layers, plus a small amount of randomly oriented fibers, gelcoat and filling resin. Shear webs, the the box-beam lateral walls, are made up of ±45 layers with a balsa wood core which provides the needed buckling resistance. Shear webs are usually located at the 15% and 45% of the airfoil's chord but, for sections closer to the blade's root, the positions are modified in order to increase the section's stiffness. Focusing now on the spar caps, these are made of 0 layers and are the most important structural element as they give support to the bending loads on the blade. Finally, the blade sections has a reinforcement at its rear part, i.e. the trailing edge spline, also made up of 0 oriented fibers which supports the bending loads in the chord-wise direction. Reports [35,9] also provide a comprehensive description of lamination sequences and material properties.

Material properties within the subregions corresponding to each of the blade section components were assumed homogeneous and equal to those of an equivalent material. The properties of this equivalent material, a 6×6 symmetric matrix with 21 independent coefficients, were computed by a weighted average of the actual laminates properties. Since the thicknesses of the region layers are very small compared to the actual size of the blade section, this assumption does not introduce significant errors. Besides, if more detail is required, our computational codes allow for independent meshing of every single layer of material separately using the exact properties.

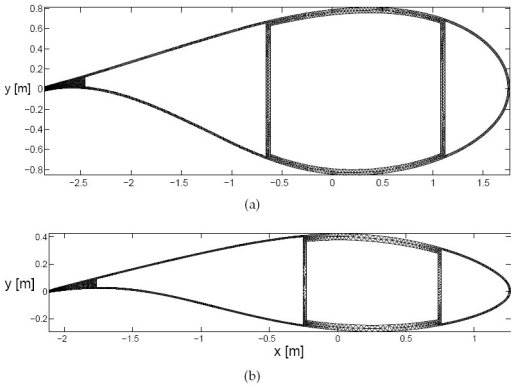

Figure 5. Finite element meshes for morphed sections.]{Finite element meshes for morphed sections corresponding to: (a) 20% of the blade span, and (b) 60% of the blade span.

http://dx.doi.org/10.5772/51142

After the internal regions and materials were defined, a triquadrilateral mesh was generated for a number of blade sections along the span. The preset master sections in table 1 served as the basis for an innovative 3D-morphing technique based on variational cubic-spline interpolation which allows us to obtain smooth transitions between the known 2D airfoil sections along the span of the blade. This way one can divide the blade into any number of sections larger than the known ones and generate finite element meshes for a more refined study of the structural features. As an example, figure 5 shows the finite element meshes of two morphed airfoil sections located at the 20% and 60% of the blade span.

Using the technique described for the internal blade structure components, we refined 46 blade sections along the span to match the structural properties of the ones reported by NREL [17]. The main targeted properties to refine were edgewise, flapwise and torsional stiffness as well as mass density for every blade section. The pitch axis centering and the location of the aerodynamic coefficients reference points were also computed according to information in reference [17].

The general specifications of the turbine also match the ones on NREL's report. Thus, the rotor has an upwind orientation and is composed of three blades. The hub diameter is 3m and is located at 90m from the ground level. Total rotor diameter is 126m. It has a precone of 2.5 and an overhang distance of 5m from the tower axis. The rated wind speed for this turbine is 11.4m/s.

3.2. Aeroelastic Steady State

After computing stiffness and inertia matrices for a discrete number of cross-sections along the span of the blade as described in section 2.1, the calculation of the aeroelastic steady state of the NREL RWT blades working under nominal conditions was solved by fully-coupling the structural and aerodynamic models presented in sections 2.1 and 2.2. Tip speed ratio for the nominal operational condition is $\lambda=7$, so the tangential velocity at the tip of the blade is 80m/s. For this nominal working condition, the power output computed for our rotor is 5.455MW which, taking into account that as in any BEM approach the interference of the tower and the nacelle is computed only approximately, is in very good agreement with the reported power for the NREL-5MW reference turbine rated at 5.296MW according to [17].

Figure 6 shows the displacement of the blade's reference-line (blade axis) $\mathbf{U}_h$ when it is subjected to the aerodynamic steady load in normal operational conditions. Figure 7, shows the corresponding rotations of the blade sections θ_h. These geometrical magnitudes were referred to a coordinate system, h from *hub*, aligned with the rotor's plane, according to standards from the International Electrotechnical Commission (IEC) [15]. Hence, the first unit vector is normal to the rotor's plane (i.e. axial) pointing downwind, the second is in the rotor's tangential direction pointing to the blade's trailing edge, and the third unit vector is in the radial direction pointing to the blade tip.

From figure 6 we can see that the displacement U_{h_1} of the blade's tip, normal to the rotor's plane, is 5.73m. This is perfectly consistent with results shown in [17]. Added to this, the tan-

gential displacement U_{h_2} is 0.78m in the negative direction, meaning that aerodynamic forces are bending the blade in the direction towards its rotation as the rotor is producing a positive driving torque.

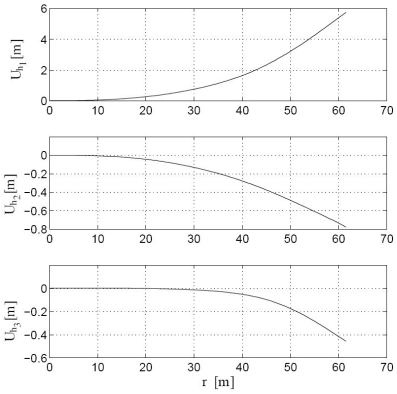

Figure 6. Linear displacements of the reference-line $\mathbf{U_h}$ when the beam is subjected to a steady load in normal operational conditions (referred to a coordinate system aligned with the rotor's plane).

In figure 7, angles $\boldsymbol{\theta}_{\mathbf{h_2}}$ and $\boldsymbol{\theta}_{\mathbf{h_1}}$ are directly associated with blade bending in the normal and tangential directions to the rotor plane, that correspond to displacements U_{h_1} and U_{h_2} respectively. It is important to note that angle $\boldsymbol{\theta}_{\mathbf{h_2}}$ represents the angular displacements which takes the blade's axis out of the rotor's plane.

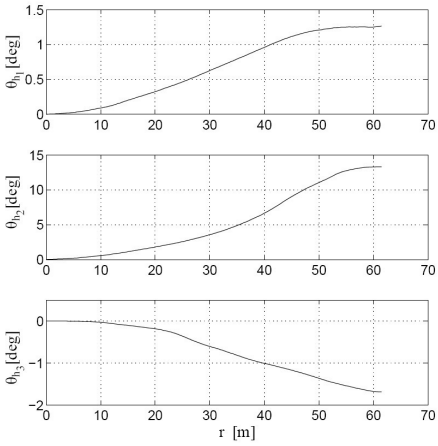

Figure 7. Rotations of the beam sections θ_h when the beam is subjected to a steady load in normal operational conditions (referred to a coordinate system aligned with the rotor's plane).

http://dx.doi.org/10.5772/51142

3.3. Natural frequencies & Linear Modes

Vibrational modes around the aeroelastic steady-state are obtained from the solution of an eigenvalue problem as described in section 2.1. The resulting eigenvalues are complex conjugate, their imaginary part represent frequencies while their non-zero real part correspond to aerodynamic damping effects coming from non-conservative force fields in the 1D functional.

Mode	frequency [Hz]	Dominant U	Dominant θ
1	0.7066	U_{h1}	θ_{h2}
2	1.0188	U_{h2}	θ_{h1}
3	1.8175	U_{h1}	θ_{h2}
4	3.3403	U_{h2}	θ_{h3}
5	3.9493	U_{h1}	θ_{h2}
6	6.4682	U_{h2}	θ_{h3}
7	6.6851	U_{h1}	θ_{h3}
8	8.0129	U_{h2}	θ_{h3}
9	8.2403	U_{h1}	θ_{h2}
10	9.7819	U_{h1}	θ_{h2}

Table 2. List of frequencies and dominant components of $\mathbf{U_h}$ and θ_h for the first ten modes of vibration.

Vibrational mode analysis provides relevant information about both the natural vibrational frequencies of the blade around a steady-state condition, and for the modes of deformation along the blade span. Table 2 summarizes the first 10 modes obtained showing the frequencies together with the corresponding dominant component for the displacements and the rotations of the blade section.

Table 3 shows a comparison of the frequencies obtained for the first 3 modes with the values reported by NREL in [17] using FAST [19] and ADAMS [16] software. FAST and ADAMS are considered today state-of-the-art softwares for structural blades analysis. From this comparison we see that the frequencies computed with our model match previous studies with a difference of 1% for the first mode and a maximum difference of 5% for the second and third modes. This difference is not surprising as the level of detail and richness of information that our computational tools can register is not present in the previous software like FAST or ADAMS.

Mode	frequency [Hz]	FAST	ADAMS
1	0.7066	0.6993	0.7019
2	1.0188	1.0793	1.0740
3	1.8175	1.9223	1.8558

Table 3. Frequencies comparison for the first three modes according to NREL report [17].

Figures 8 and 9 show the amplitude of the deformation along the span for the three components of $\mathbf{U_h}$ and θ_h, normalized by the dominant component, for some of the deformation modes. Every mode shown includes displacements and rotations of the blade sections normalized by the value of the dominant component.

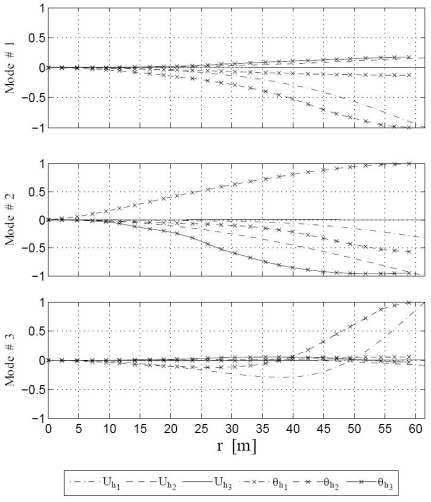

Figure 8. Amplitude of $\mathbf{U}_h$ and θ_h for three vibrational modes around the aeroelastic steady-state configuration (normalized by the dominant component). From top to bottom modes # 1, 2 and 3.

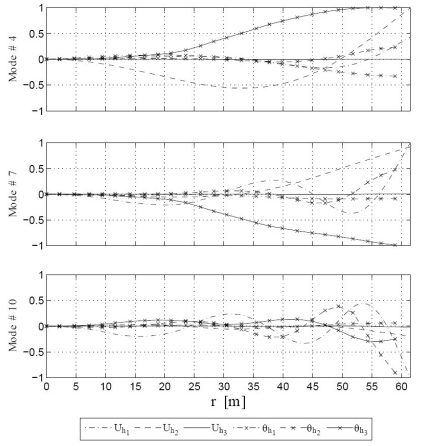

Figure 9. Amplitude of $\mathbf{U}_h$ and θ_h for three vibrational modes around the aeroelastic steady-state configuration (normalized by the dominant component). From top to bottom modes # 4, 7 and 10.

http://dx.doi.org/10.5772/51142

3.4. Recovery of 3-D fields

After computing the global deformation from the 1-D beam analysis, we recovered the corresponding 3-D fields (displacements, strains and stresses) using the 3-D warping functions previously calculated with our model. The knowledge of the stress state of every layer is of utter importance in the analysis of wind turbine blades in order to improve life-time and reliability of the design. Our model can provide the full six tensorial components of the stress tensor. Besides it can provide the 3 components of the displacement and 6 components of the strain.

For the previously solved aeroelastic steady-state, we present in figure 11 and 11 the six components of the Jaumann-Biot-Cauchy stress tensor $\mathbf{Z=S\Gamma}$ for the section located at 40% of the blade span. This region is particularly interesting as it combines energy production and structurally supports significant stress accumulation compared to other regions along the blade span. The dominant stress component, $\mathbf{Z}_{11}$, at the top of figure 10 is the one primarily associated with the out of rotor-plane bending loads. Note here how the lower spar-cap is subjected to tensile stress while the upper one is under compression stress.

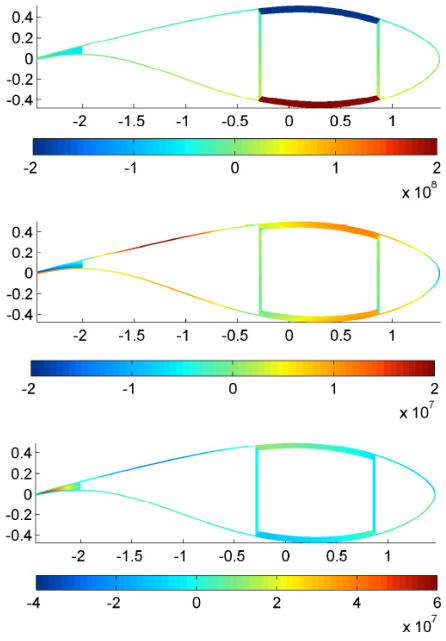

Figure 10. Components of the Jaumann-Biot-Cauchy stress tensor $\mathbf{Z = S\,\Gamma}$ for the section located at 40% of the blade span (referred to the undeformed coordinate system (X^1,X^2,X^3) in Pa). From top to bottom: Z_{11}, Z_{12} and Z_{13}.

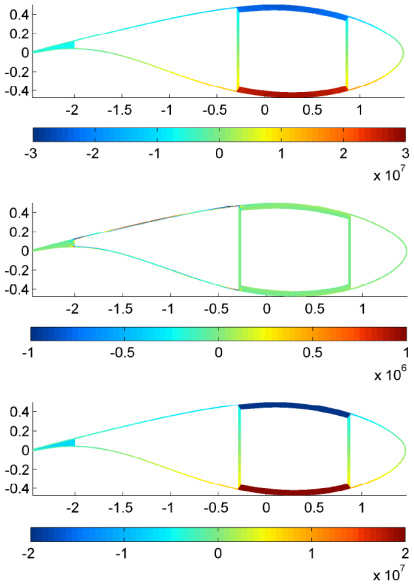

Fig. 11. Components of the Jaumann-Biot-Cauchy stress tensor $\mathbf{Z} = \boldsymbol{S\Gamma}$ for the section located at 40% of the blade span (referred to the undeformed coordinate system (X^1, X^2, X^3) in Pa). From top to bottom: Z_{22}, Z_{23} and Z_{33}.

4. Conclusions

With the method presented in this work we are able to model the structural behavior of wind turbine blades with the simplicity and economy of a one-dimensional model but with a level of description equivalent to a much more costly three-dimensional approach. The one-dimensional model is used to compute a fast, but accurate, solution for the deformed state of the blade when subjected to a steady load in normal operational conditions, and an analysis of the vibrational modes around this steady configuration. This provides a valuable tool to use during the design process. In that sense, the capacity of the Generalized-Timoshenko theory to capture the bending-twisting coupled modes in its fully populated 6×6 stiffness matrix for the 1-D beam problem plays a fundamental role.

Due to the geometrical complexity and material inhomogeneousness in the section, all the deformation modes of the blade are combined modes, i.e. there are no pure-flexural or pure-torsional modes. Plots of the vibrational modes may serve to identify eventual unstable states in the dynamic behavior of innovative prototype blades. Figures 8 and 9 show that, for certain modes, in some portions of the span, bending due to lift force occurs simultaneously with twisting in the sense that increases the angle of attack, and then, the lift force. A complete dynamic analysis of the fluid-structure interaction process would be needed to de-

http://dx.doi.org/10.5772/51142

termine if those particular modes would be activated or not during the blade operation. Nevertheless, having the possibility of quickly identifying those modes (and their associated frequencies) at an early stage of the design process seems very helpful.

Regarding the linear vibrational modes depicted in figure 8, the first mode shows mainly out-of-plane curvature corresponding to the fundamental frequency of the blade but as the blade is initially twisted and has complex inhomogeneous sections, it is not a pure bending mode. Therefore, as a result of the non conventional couplings, curvature deformation in the rotor plane and also torsion appears in this mode. The second mode is also commanded by out-of-plane curvature but it has an important torsion component, while mode number three is similar to the first one with a higher wave number.

Regarding the modes presented in figure 9, the fourth and seventh modes are mainly commanded by torsion and hence they could be responsible for fluttering of the blade in case they are excited by the interaction with the surrounding fluid. The tenth mode is also principally a flap-wise curvature mode but with higher wave number than the first and third. It shows a more complex behavior arising from complicated couplings among different deformations. The frequencies of the first three modes presented in table 3 are in good agreement with published results obtained by other models.

The above-mentioned flexo-torsional characteristic also gives this model the ability to simulate the dynamic performance of *adaptive blades*, at an affordable computational cost. In the Adaptive-Blade concept (see [10,24], among others), tailoring of the flexo-torsional modes of the blade is used to reduce aerodynamic loads by controlling the coupling between bending and twisting. As the blade bends under load, the angle of attack of the airfoil sections changes, reducing the lift force. Limiting extreme loads and improving fatigue performance, this added passive control reduces the intensity of the actuation of the active control system. Plots like figure 6 and figure 7 provide valuable information about the simultaneous deformation of twisting and bending under a given load.

Recovering of the stress tensor components for the different zones of the blade section helps in the prediction of stress concentration in the basic design that may ultimately lead to eventual material failure. More exhaustive fatigue studies can be conducted analyzing the stress both in the steady state or in time-marching solutions of the problem. The capability of computing the whole 6 components of the stress tensor makes it possible to apply sophisticated failure theories.

Our aeroelastic model may also be used to simulate the dynamic response of the wind turbine tower. In that case, the structural model would be applied to the tower to obtain the stiffness matrices of the equivalent beam as it is done with the blades. The aerodynamic loads would be computed from the aerodynamic coefficients of the cylindrical sections of the tower using basically the same subroutines. As in the case of the blades, all the complex flexo-torsional modes of deformation of the tower would be taken into account, and the associated vibrational effects included in the general analysis of the whole turbine.

We plan to continue our work with a dynamic simulation of the fluid-structure problem. In a first stage, we will couple the phenomena by feeding back changes in geometry due to

blade deformation in our aerodynamic model and recomputing the forces. At this stage, we also plan to include statistically-generated perturbations to represent fluctuations in wind speed and direction based on anemometry data for wind resource in several representative locations. Besides providing us with a fast model for a quick analysis, this model will serve as an intermediate step before the ultimate goal of coupling the structural model with the velocity-vorticity KLE approach mentioned above.

Acknowledgements

The authors are very grateful for the financial support made available by the National Science Foundation through grants CEBET-0933058 and CEBET-0952218 and University of Buenos Aires through grant 20020100100536 UBACyT 2011/14.

Author details

Alejandro D. Otero[1,2], Fernando L. Ponta[1*] and Lucas I. Lago[1]

*Address all correspondence to: flponta@mtu.edu

1 Department of Mechanical Engineering - Engineering Mechanics, Michigan Technological University, Houghton, USA

2 CONICET & College of Engineering, University of Buenos Aires, Argentina

References

[1] project [internet]. (May 2012). http://www.upwind.eu/.

[2] Bak, C., Madsen, H. Aagaard, & Johansen, J. (2001). Influence from blade-tower interaction on fatigue loads and dynamic (poster). *Wind energy for the new millennium. Proceedings. 2001 European wind energy conference and exhibition (EWEC''01)*, 2-6.

[3] Bathe, K. J. (1996). Finite element procedures. Prentice Hall, Englewood Cliffs, New Jersey, USA.

[4] Berdichevsky, V. L. (1979). Variational--asymptotic method of constructing a theory of shells. *J. App. Math. and Mech.*, 43, 664-687.

[5] Burton, T., Sharpe, D., Jenkins, N., & Bossanyi, E. (2001). Wind Energy Handbook. Wiley, Chichester, UK.

[6] Cesnik, C. E. S., Sutyrin, V. G., & Hodges, D. H. (1996). Refined theory of composite beams: The role of short-wavelength extrapolation. *Int. J. Sol. and Struct.*, 33, 1387-1407.

[7] Glauert, H. (1926). A general theory of the autogyro. *British ARC*, 1111.

[8] Glauert, H. (1935). Airplane propellers. *Aerodynamic theory*, 4, 169-360.

[9] Griffin, D. A. (2002). Blade system design studies volume I: Composite technologies for large wind turbine blades. Report SAND2002-1879, Sandia National Laboratories.

[10] Griffin, D. A. (2002). Evaluation of design concepts for adaptive wind turbine blades. Report SAND2002-2424, Sandia National Laboratories.

[11] Hansen, M. O. L., Sorensen, J. N., Vousitas, S., Sorensen, N., & Madsen, H. Aa. (2006). State of the art in wind turbine aerodynamics and aeroelasticity. *Prog. in Aerospace Sciences*, 42, 285-330.

[12] Hodges, D. H. (2003). Geometrically exact, intrinsic theory for dynamics of curved and twisted anisotropic beams. *AIAA Journal*, 41, 1131-1137.

[13] Hodges, D. H. (2006). Nonlinear Composite Beam Theory. AIAA, Reston, Virginia.

[14] subtask 2: Research for deeper waters [internet]. (December 2011). http://www.ieawind.org/AnnexXXIII/Subtask2.html.

[15] IEC. Wind turbine generator systems -- part 13: Measurement of mechanical loads. Report IEC/TS 61400--13, International Electrotechnical Commission (IEC). (2001).

[16] Laino, D. J., & Jonkman, J. (May 2012). NWTC design codes ADAMS2AD [internet]. http://wind.nrel.gov/designcodes/simulators/adams2ad/.

[17] Jonkman, J., Butterfield, S., Musial, W., & Scott, G. (2009). Definition of a 5-MW reference wind turbine for offshore system development. Technical Report NREL/TP-500-38060, National Renewable Energy Laboratory.

[18] Jonkman, J., Butterfield, S., Passon, P., Larsen, T., Camp, T., Nichols, J., Azcona, J., & Martinez, A. (4--6 December 2007). Offshore code comparison collaboration within IEA Wind Annex XXIII: Phase II results regarding monopile foundation modeling. *2007 European Offshore Wind Conference & Exhibition*, Berlin, Germany, 2007.

[19] Jonkman, J. M., & Buhl, M. L. Jr. (2005). Fast user's guide. Technical Report NREL/EL-500-38230, National Renewable Energy Laboratory (NREL). Golden, Colorado, USA.

[20] Karniadakis, G. E., Bullister, E. T., & Patera, A. T. (1985). A spectral element method for solution of two- and three-dimensional time-dependent incompressible navier-stokes equations. *Finite Element Methods for Nonlinear Problems*, 803, New York/Berlin, Springer-Verlag.

[21] Kooijman, H. J. T., Lindenburg, C., Winkelaar, D., & Hooft, E. L. van der. (2003). Dowec 6 MW pre-design. Technical report, ECN-CX-01-135, Energy Research Center of the Netherlands, Petten.

[22] Leishman, J. G. (2006). Principles of helicopter aerodynamics. Cambridge University Press, Cambridge, UK.

[23] Lindenburg, C. (2002). Aeroelastic modelling of the LMH64-5 blade. *ECN, Petten, December*.

[24] Locke, J., & Hidalgo, I. Contreras. (2002). The implementation of braided composite materials in the design of a bend-twist coupled blade. Report SAND2002-2425, Sandia National Laboratories.

[25] Manwell, J. F., McGowan, J. G, & Rogers, A. L. (2002). Wind energy explained: Theory, design and application. Wiley, Chichester, UK.

[26] Wind power today. Report DOE/GO-102005-2115, U.S. Department of Energy. (2005).

[27] Otero, A. D., & Ponta, F. L. (2010). Structural analysis of wind-turbine blades by a generalized Timoshenko beam model. *Journal of Solar Energy Engineering*, 132(011015).

[28] Passon, P., Kühn, M., Butterfield, S., Jonkman, J., Camp, T., & Larsen, T.J. (2007). OC3--Benchmark exercise of aero-elastic offshore wind turbine codes. *Journal of Physics: Conference Series*, 75, 012071, IOP Publishing.

[29] Patera, A. T. (1984). A spectral element method for fluid dynamics: laminar flow in a channel expansion. *J. Comput. Phys.*, 54, 468-488.

[30] Patil, M. J., & Althoff, M. (2006). Energy--consistent, Galerkin approach for the nonlinear dynamics of beams using mixed, intrinsic equations. *AIAA/ASME/ASCE/AHE/ASC Structures, Structural Dynamics and Material Conference, Reston, Virginia, USA*, 1-9, AIAA.

[31] Pitt, D. M., & Peters, D. A. (1981). Theoretical prediction of dynamic-inflow derivatives. *Vertica*, 5(1), 21-34.

[32] Ponta, F. L. (2005). The kinematic Laplacian equation method. *J. Comput. Phys.*, 207, 405-426.

[33] Ponta, F. L. (2006). The KLE method: a velocity-vorticity formulation for the Navier-Stokes equations. *J. Applied Mechanics*, 73, 1031-1038.

[34] Powles, S. R. J. (1983). The effects of tower shadow on the dynamics of a horizontal-axis wind turbine. *Wind Engineering*, 7, 26-42.

[35] Parametric study for large wind turbine blades. Report SAND2002-2519, Sandia National Laboratories. (2002).

http://dx.doi.org/10.5772/51142

[36] Viterna, L. A., & Janetzke, D. C. (1982). Theoretical and experimental power from large horizontal-axis wind turbines. Technical report, National Aeronautics and Space Administration, Cleveland, OH (USA). Lewis Research Center.

[37] Yamaguchi, F. (1988). Curves and surfaces in computer aided geometric design. Springer-Verlag, Berlin.

[38] Yu, W., & Hodges, D. H. (2005). Generalized Timoshenko theory of the variational asymptotic beam sectional analysis. *J. American Helicopter Society*, 50, 46-55.

[39] Yu, W., Hodges, D. H., Volovoi, V., & Cesnik, C. E. S. (2002). On Timoshenko-like modeling of initially curved and twisted composite beams. *Int. J. Sol. and Struct.*, 39, 5101-5121.

Section 3

Power Conversion, Control, and Integration

Chapter 6

Recent Advances in Converters and Control Systems for Grid-Connected Small Wind Turbines

Mohamed Aner, Edwin Nowicki and David Wood

Additional information is available at the end of the chapter

http://dx.doi.org/10.5772/51148

1. Introduction

In response to the introduction of feed-in tariffs around the world, an increasing number of small wind turbines are being grid connected [1]. Variable speed wind turbines, though initially more costly, have several advantages over fixed speed systems: (i) average power production is typically 10% higher since the turbine operates more frequently near its ideal tip-speed-ratio, (ii) the turbine and mechanical transmission operate with reduced stresses, (iii) turbine and generator torque pulsations are reduced, and (iv) noise is reduced [2-4]. Variable speed operation in general has only become possible over the last twenty years or so because of major developments in power electronics and associated cost reductions [5]. This reference indicates that power electronic devices are reducing in cost at about 1-5% per year. This chapter will discuss the impact of these developments on small turbine design and operation along with some important aerodynamics issues related to turbine starting.

The blades of most small horizontal-axis wind turbines (HAWTs) have no pitch adjustment. This reduces their cost but makes starting and low wind speed performance a major challenge. In order to extract the maximum possible energy available from the wind, power extraction should begin at the smallest possible wind speed in the shortest possible time. Few researchers have examined wind turbine starting. Ebert and Wood [6] and Mayer et al. [7] measured starting sequences from separate 5 kW HAWTs. Kjellin and Bernhoff [8] developed a scheme for starting a small vertical axis wind turbine (VAWT) using auxiliary generator windings that are not used for power production. Hill et al. [9] discuss the aerodynamic starting of Darrieus VAWTs which have problems similar to, or worse than, those for HAWTs. The remainder of this chapter considers only HAWTs with fixed-pitch blades configured with an AC generator and power converter that delivers fixed frequency electrical power while allowing the turbine to operate at variable rotational speeds.

The lack of pitch adjustment in small wind turbines (considered here to have a rated power output of 50 kW or less) means the blades experience high angles of attack during starting and, hence, low lift to drag ratios. Moreover, most small wind turbines employ permanent magnet synchronous generators (PMSGs) whose cogging torque[1] can have a significant impact on starting. Wood [13] showed that the cogging torque must be less than 1% of the rated torque to be unimportant. Partly because of high cogging torque, the blades of the 500 W HAWT studied by Wright & Wood [11] did not start for a wind speed below 5 m/s approximately, whereas the conventionally-measured cut-in wind speed was 3.5 m/s. The difference was due to the blades' ability to keep rotating as the wind speed decreased below 5 m/s. In other words, the "stopping" wind speed of a HAWT is significantly lower than the aerodynamic "starting" speed and the cut-in speed is some average of the two. It is also noted that 5 m/s is a typical average wind speed for locations where a small turbine is likely to be employed. Wood [10] described the multi-dimensional optimization of blade design including the minimization of starting time. Subsequent tests on 2.5 m long 5 kW blades designed for good aerodynamic starting are described below. From rest, they take about 13 s to reach the power-extracting angular velocity at a wind speed of 10 m/s and about 40 s at 3 m/s. These times can result in a significant loss of output energy compared to operation with much faster starting times.

As modern small wind turbine systems evolve, several issues are emerging that may be effectively and economically dealt with by the use of modern power electronics. While many small turbines operate with variable rotor speed, it is uncommon for their power electronics to allow power flow to and from the grid. In fact, many small turbines are sold with only a diode rectifier or battery charger. The diode rectifier configuration (either a four diode full-bridge for a single-phase generator or a six diode full-bridge for a three-phase generator) is often used because of its simplicity, reliability and economy. A battery charger may be added, in the form of a single-transistor based buck converter or boost converter. Both the diode rectifier and the battery charger allow power flow in one direction only (from generator to a DC capacitor or battery), which to date has been satisfactory, but as suggested below, bi-directional converters may be used in the near future to extract more energy from small wind turbines.

With the conventional diode rectifier based system, small wind turbines normally require a third party inverter for grid connection. This inverter often has to provide the maximum power point tracking (MPPT) for optimal power extraction. In turn, many such inverters are based on photovoltaic inverters for which the "perturb and observe" (P & O) strategy for MPPT is effective [12]. P & O does not work well for wind turbines because of the (usually) rapidly changing wind speed and most sophisticated small turbines with integral inverters base their MPPT on some form of look table for maximum power as a function of generator frequency. Thus the basic operation of small wind turbine inverters needs to be fundamentally different from those used for photovoltaics.

1 By "cogging torque" we mean the maximum value of the phase-dependent cogging torque. The value is independent of the direction of rotation.

http://dx.doi.org/10.5772/51148

Another particular issue is the need to have high rectifier efficiency and high inverter efficiency over a very wide range of power levels. In principle, this is also a requirement for large turbines, but the lower average wind speeds seen by small turbines makes the low power performance especially important. Many commercial small inverters now have efficiencies of over 95% at rated power but drop off alarmingly at lower power levels due to losses in filter, transformer, and controller components (such losses are much more significant in small power converters than in high power converters). The development of modern semiconductor switching devices and advances in high frequency switching control continue to be crucial to the extension of high efficiency operation in low wind speed (i.e. low power) regimes.

Another power electronics issue of rapidly increasing importance is that of AC power quality. At very small power levels (below 500W), where economy is a driving market requirement, the inverter operates with a simple controller that produces a modified square-wave AC output voltage (i.e. a square wave modified by the addition a zero voltage step between negative and positive voltage levels). Such inverter operation is reliable, with low switching losses (since the transistors are switched at the power frequency of 50Hz or 60Hz) and without any need for filter components. The total harmonic distortion (THD) is a measure of deviation from a sinusoidal waveform; for a typical modified square wave the THD is about 30%. However with increasing use of renewable energy sources, it is very possible that in the near future national electronic equipment standards will require manufacturers of small inverters to produce AC voltage (or AC current in the case of grid-connection) having a THD on the order of 5% or even lower. Since about 1990, inverters with a power output above 2kW have increasingly been manufactured with pulse width modulation (PWM) that rapidly (in the range of 1kHz to 10kHz) switches transistors such that the transistor bridge output can be filtered with low cost inductor and/or capacitor components to produce AC output current with low THD for grid connection. It is expected that PWM will become more commonly used even at the very low power levels of a few hundred Watts.

One problem with PWM operation is the issue of increased cost and reduced reliability resulting from the use of the required filter components (without filtering the THD would be well above 100%). A trend that is in its infancy for high power inverters may one day be applied to lower power inverters is the multilevel inverter, which produces a stair-stepped approximation of a sinusoidal voltage or current and requires little filtering (or even no filter if PWM is not used at all and there are a sufficient number of levels). A significant disadvantage of the multilevel inverter is an increase in the number semiconductor power transistors, and hence decreased reliability and increased cost. However with rapidly evolving power semiconductor switching technology, multilevel inverters may one day become economical even at lower power levels.

In this chapter, the focus is on the issue of bi-directional power flow in the power converter of a small wind turbine system. Bi-directionality of power flow is an example of what is now available (and quickly becoming more economical) using modern power electronics. This chapter presents one such system and explores its use in motor-starting a small wind turbine to reduce the starting time. The ideal case of turbine starting after the wind speed

makes a step change from zero to a constant value, U, within the turbine operating range is considered, and any issues regarding the measuring of U is ignored. It is also assumed that power extraction takes over instantaneously from starting at a nominated rotor angular velocity. The justification is that if motor-starting for this case results in an energy gain, it is worth pursuing. If it does not, then it is to be discarded. We show that motor-starting is worth pursuing

The following sections present the electrical system in which motoring and generating modes are controlled by field oriented control (FOC) through a bi-directional very sparse matrix converter (VSMC) which is connected in a backward configuration (i.e. the "rectifier" portion of the VSMC is connected to the grid and the "inverter" portion is connected to the generator). This allows a sufficient DC-link voltage for grid connection at any wind speed while the system is in the generating mode, and also permits straightforward grid synchronization where power is regulated by current control, depending on grid voltage to avoid voltage flicker. In addition, by using a small filter, sinusoidal current can be injected into the grid at unity power factor (or slightly leading or lagging power factor as desired) to improve power quality [13]. An alternative to the VSMC is the well known back-to-back converter (where the rectifier is implemented with a conventional inverter structure). However, the back-to-back converter requires some form of DC-link storage such as a capacitor, which is not the case for the a VSMC.

One particular recent power electronics development of interest for matrix converters is the emergence of the Reverse Blocking IGBT (RB-IGBT) which has become commercially available and tested for matrix converter implementations. It has been shown [14] that the conduction losses, switching losses, and conduction voltage of RB-IGBTs are lower than the current generation IGBTs which should lead to higher converter efficiencies. Another recent power electronics development is the commercialization of the Bi-directional Reverse Blocking IGBT (BRB-IGBT) for use in high power converters which may one day be used in lower power converters. A prime candidate for such switching technology is the matrix converter and its derivatives. Matrix converters (having the ability for extremely flexible bi-directional control of power in three-phase systems) in their conventional (non-sparse) form have long been criticized because of the high cost and high power losses associated with a high transistor and diode count (e.g. 18 transistors and 18 diodes in one particular form). The use of bi-directional reverse blocking devices would remove the need for external reverse voltage blocking diodes, and reduce the control requirements of a full matrix converter (only nine devices to be controlled), as well as reduce power losses in the converter. Thus, BRB-IGBT devices may lead to economical matrix-based or other converter configurations with lower power losses and simplified gate drive requirements [15, 16]. The study discussed below, uses an established implementation of bi-directional power flow in a power switch, namely, a conventional IGBT transistor within a four-diode bridge as shown in Fig.1 (the diodes provide both reverse voltage blocking capability and bi-directional power flow control). This configuration has the advantage of a simplified switch drive circuit (only one IGBT needs to be controlled regardless of power flow) but the disadvantage of increased conduction losses in two conducting diodes. An alternative bi-directional power switch configuration consists

http://dx.doi.org/10.5772/51148

of two anti-parallel IGBT (or other transistor) devices, each with a reverse blocking diode, which would reduce the losses (only one conducting diode) but require a more complicated transistor driver (two transistors need to be controlled for each bi-directional switch). Figure 2 shows the configuration of VSMC built with BRB-IGBT switching devices.

Section 3 describes a 5 kW wind turbine and its starting performance. An expression for the energy gain (i.e. harvested and delivered to the grid) is derived using the proposed motoring approach verses aerodynamic starting. Section 4 presents the model and operation of the PMSG and the VSMC in the backward configuration, including a space vector modulation approach. Then in Section 5, the simulation results for a 5.6 kW wind turbine are presented, including a plot of energy gain as a function of wind speed which compares well with the analytical result presented in Section 4. Conclusions are presented in Section 6.

2. Small wind turbine system configuration with VSMC

Figure 1 illustrates the proposed HAWT, including a PMSG connected to the grid through a backward very sparse matrix converter (where the rectifier side is connected to the grid and the inverter side is connected to the generator). Fig. 1 also shows the maximum power point tracking (MPPT) controller. The current flowing to or from the generator is controlled by field oriented control (FOC). The system operates as follows. Once blade rotation is detected, the generator is operated as a motor with the rated electromagnetic torque in the same direction as the aerodynamic torque until it reaches the nominated speed for power extraction where the MPPT unit takes control to keep the turbine operating at the optimal tip speed ratio (λ_{opt}). The reference torque is converted to a reference generator current through the FOC unit and compared to the actual current to generate the appropriate generator voltage. Then the reference voltage based on space vector modulation forms the switching signals to the VSMC.

The turbine power output, P_m, is expressed in conventional form as:

$$P_m = 0.5\rho A C_P U^3 \tag{1}$$

where ρ is the air density, A is the rotor swept area, U is the wind speed and C_P is the turbine power coefficient which is related to the torque coefficient, C_T, by

$$C_P = C_T \lambda \tag{2}$$

where λ is the tip speed ratio. C_T is approximated by [17]:

$$C_T = a_6\lambda^6 + a_5\lambda^5 + a_4\lambda^4 + a_3\lambda^3 + a_2\lambda^2 + a_1\lambda + a_0 \tag{3}$$

where a_6 to a_0 are turbine coefficients defined in the Appendix.

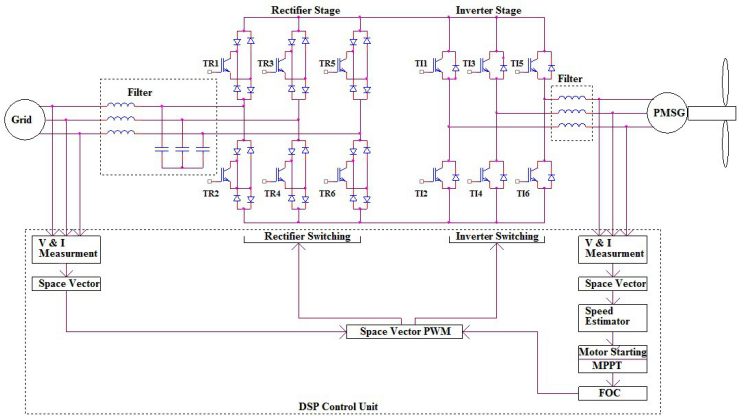

Figure 1. Proposed grid connected HAWT system using backward VSMC.

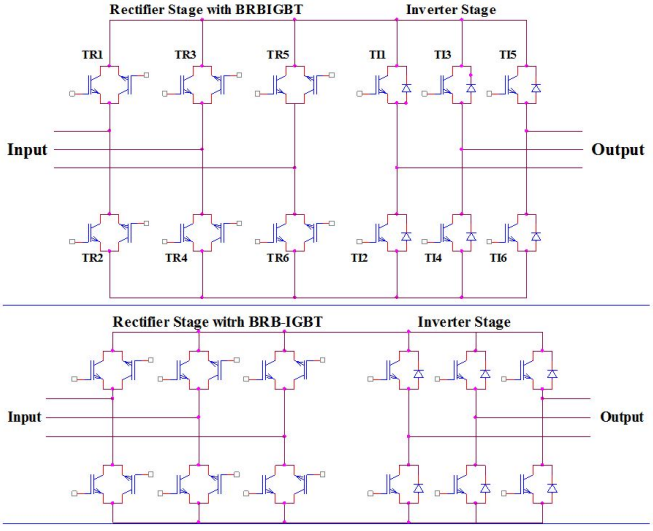

Figure 2. Alternative implementation of the backward VSMC using BRB-IGBT devices.

Figure 3 shows the variation of C_T form Equation (3) versus λ for a 5.6 kW wind turbine whose other parameters, taken to be typical of a wind turbines of that output, are given in the Appendix. Also shown is the measured starting performance of a 5.0 kW turbine whose blades were designed for rapid starting using the methods described by Wood [10]. In Figure 3, a 5th order curve is fitted to the measured starting data, but more important, a linear approximation is also determined and used for simulation of motoring. It is important to

http://dx.doi.org/10.5772/51148

note that the C_T from Equation (3) applies only when power is being extracted. The starting turbine does not extract power so the wind speed does not decrease through the rotor, and the blade aerodynamics is fundamentally different. The starting line and the curve from Equation (3), intersect close to $\lambda \approx 7$ which is approximately the optimum tip speed ratio. This allows the controller to employ the linear plot for motoring and then switch to the steady aerodynamic curve from Equation (3) for power generation.

3. The aerodynamic of starting and energy gain by motoring

Figure 4 shows starting data of a 5.0 kW wind turbine, in terms of wind speed and tip speed ratio as a function of time. The 5 m diameter, two-bladed 5.0 kW turbine had fixed-pitch blades designed for good aerodynamic starting (without motoring). Even at a high wind speed of around 10 m/s the blades take about 13 s to reach the minimum angular velocity for power extraction.

Starting can be analyzed using standard blade element theory with no axial or azimuthal induction, Wood [10]. With all lengths normalized by the blade tip radius, *R*, and all velocities normalized by *U*, the aerodynamic torque, *Ta*, acting on the starting rotor, is given by

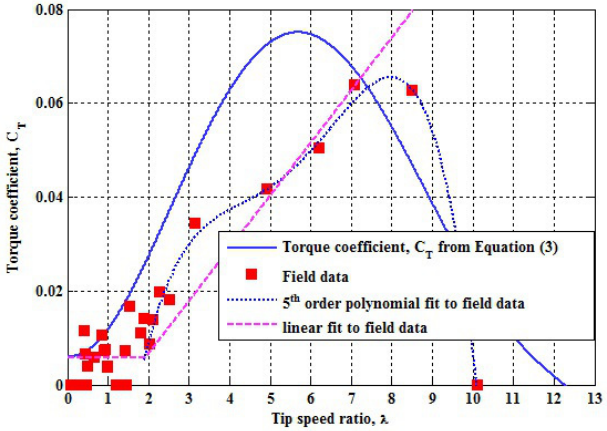

Figure 3. Measured starting torque for a 5 kW wind turbine and assumed power-extracting torque for a 5.6 kW wind turbine.

$$T_a = N\rho U^2 R^3 \int_{r_h}^{1} (1+\lambda^2 r^2)^{1/2} r \sin\theta_p (\cos\theta_p - \lambda r \sin\theta_p) dr \tag{4}$$

where N is the number of blades, c is the blade chord which depends on radius r, and θ_p is the pitch. The integration is from the normalized hub radius, r_{hv} to the tip. Equation (5) is derived in [10] where the assumptions behind it are justified in detail. In particular, it is assumed that the angular acceleration is small enough to allow a quasi-steady analysis and the lift and drag on any airfoil are given by the "flat plate" equations:

$$C_l = 2\sin\alpha\cos\alpha \quad \text{and} \quad C_d = 2\sin^2\alpha \tag{5}$$

which are valid for angles of attack, $\alpha > °30$ approximately. As no power is extracted the rotor torque T_a acts only to accelerate the blades. Thus:

$$d\Omega / dt = (T_a - T_r) / J \text{ or } d\lambda / dt = (T_a - T_r) / (JU) \tag{6}$$

where J is the total rotational inertia and T_r is the resistive torque due to cogging torque or resistance in the gearbox which may or may not depend on Ω. For the start shown in Figure 3 and 4, T_r was negligible and the torque was inferred from Equation (6) and the turbine inertia. It is shown in [10] that for wind turbines of any size, $J \, NJ_b$ where J_b is the inertia of each blade. In words, the turbine inertia is dominated by the blades as can be seen in The Appendix. When T_r can be ignored, starting is independent of N. Equations (4) and (6) were solved by the Adams-Moulton method –a standard numerical technique for ordinary differential equations - to obtain the solid line in Fig. 4, which accurately predicts the initial, 11 s period of slow, approximately constant acceleration. The calculations then become inaccurate because (5) is no longer valid. However, it is clear that starting is dominated by the long period of slow acceleration followed by a much shorter period of rapid acceleration during which the turbine reaches the rotor speed for power production. An important consequence of (4) and (6) which is independent of the form for blade lift and drag, comes from the scaling outside the integral: if T_s is the time required to reach a particular Ω for power extraction to commence, which is the most common strategy for small turbines, then $T_s \sim U^{-2}$. Alternatively, if power extraction starts at a fixed λ, $T_s \sim U^{-1}$. Thus the minimum starting time from Fig. 4 is approximately 40 s at the desirable cut-in wind speed of 3m/s. It is noted that this turbine is believed to be the first whose blades were designed for rapid starting

Knowing T_s as a function of U allows a simple determination of $E_g(U)$, the energy gained by motor-starting when compared to aerodynamic starting, on the basis of the following assumptions:

1. there is no resistive or cogging torque in the drive train and generator
2. motor/generator efficiency =100%
3. all grid power goes to accelerate the rotor
4. the motoring power is the turbine maximum (rated) power
5. $T_a << T_m$ during motoring and can be ignored, where T_m is the motoring torque

6. the turbine switches instantaneously from motoring to generating when $\lambda=\lambda_{opt}$

The energy gain is the product of the difference between the motor-starting and aerodynamic-starting times and the power output at wind speed U minus the energy required to accelerate the rotor. Thus

$$E_g(U)=P(U)[T_a(U)-T_m]-\frac{1}{2}J\Omega_s^2 \tag{7}$$

where T_m is independent of U from assumption 5. From 3 and 4:

$$P(U_r)T_m=\frac{1}{2}J\Omega_s^2 \tag{8}$$

Therefore

$$E_g(U)=P(U)T_a(U)-\frac{1}{2}J\Omega_s^2[1+P(U)/P(U_r)] \tag{9}$$

Assume $P(U) = k_1 U^3$ as in Equation (1) with $k_1 = 5.6$ to give 5.6 kW at $U_r = 10$ m/s. Also $T_a = k_2/U$, where $k_2 = 132$ to fit the starting data. If Ω_s corresponds to λ_{opt}, then

$$\frac{1}{2}J\Omega_s^2=\frac{J\lambda_{opt}^2U^2}{2R^2} \tag{10}$$

and

$$E_g(U)=\left[k_1k_2-\frac{J\lambda_{opt}^2}{2R^2}\{1+(U/U_r)^3\}\right]U^2 \tag{11}$$

For the 5.6 kW turbine documented in the Appendix, J = 18 kgm^2, $\lambda_{opt} = 7$, and $R = 2.5$ m. Thus

$$E_g(U)=70.56[10.48-\{1+(U/U_r)^3\}]U^2 \tag{12}$$

It will be shown below that (12) is a good approximation for $E_g(U)$. Since $(U/U_r)^3 \le 1$, $E_g(U)$ is positive for all values of U. It is this result that makes motor-starting attractive provided the turbine power electronics allows bi-directional power flow.

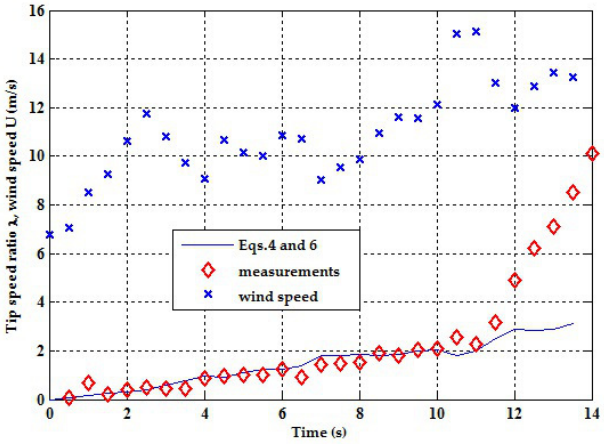

Figure 4. Measured starting sequence of a 5.0 kW two bladed wind turbine which corresponds to the starting torque of Figure 2.

4. Description of the generator and converter

4.1. Permanent magnet synchronous generator

The PMSG model is developed in the *d-q* reference frame to eliminate the time varying inductances assuming a sinusoidal distribution of the permanent magnet flux in the stator and surface mounted round rotor [18]:

$$V_q = -(R_s + pL_q)I_q - \Omega L_d I_d + \Omega \lambda_m \tag{13}$$

$$V_d = -(R_s + pL_d)I_d - \Omega L_q I_q \tag{14}$$

$$T_g = -1.5P\lambda_m I_q \tag{15}$$

$$T_a - T_g = J\,d\Omega / dt \tag{16}$$

where Equation (16) is Equation (6) restated for completeness. L_d and L_q are the *d* and *q*-axis inductances, respectively; R_s is the stator winding resistance; I_d, I_q, V_d and V_q are the *d* and *q* axis currents and voltage respectively; λ_m is the amplitude of the flux induced by the permanent magnets of the rotor in the stator phases; *P* is the number of pole pairs; T_e is the electromagnetic torque. Equation (16) is a basic representation of rotor dynamics which governs the rotor acceleration, neglecting friction and other losses.

http://dx.doi.org/10.5772/51148

The PMSG operation mode depends on the direction of T_g: positive for generating and negative for motoring. T_g is controlled through the backward VSMC. The parameters of the 5.6 kW PMSG used in simulation are shown in the Appendix. These parameters are close to those of the 5 kW PMSG in [19] with the exception of the rated speed which has been altered to be closer to the experimental turbine which used induction generator instead of PMSG.

4.2. Very Sparse Matrix Converter

The VSMC has high efficiency, compact size, a long life span, low input current harmonics, and excellent input and output power quality control without commutation problems [20]. The VSMC provides a continuous transformation from AC-to-AC with adjustable voltage and frequency. The converter can operate in four quadrants and has the ability to shape current to be nearly sinusoidal at both the converter input and at the output using small AC filtering components. The displacement factor can be adjusted to unity by proper pulse width modulation (PWM) control [21]. The very sparse matrix converter is considered a high power density converter due to the lack of DC-link capacitors and has fewer bi-directional switches than the conventional matrix converter which also reduces the system cost [22, 23]. Moreover, the rectifier stage is commutated at zero current providing increased efficiency of the converter by reducing switching losses [24]. Note that the sophisticated control algorithms that we propose for the backward connected VSMC can be implemented at low production cost due to the advances is digital signal processor technology in recent years. At the turn of the century industry preferred the use integer digital signal processors to reduce controller cost. Today (2012), floating point digital signal processors are now quite economical and thus allow the use of sophisticated control in small wind power systems.

4.2.1. Rectifier stage of the VSMC

Many aspects must be taken into consideration in synthesizing the rectifier switching signals [13]. Figure 5 shows the modulation strategy of the rectifier PWM switching signal generation. Each grid cycle is divided to six sectors; in each sector, two of the grid side terminals are connected to either the positive or negative bus of the DC-link while the third terminal is connected to the opposite DC-link. In order to produce the maximum DC-link voltage, the maximum positive input voltage is connected to the positive bus of the DC-link for a complete 60^o while the other phases are modulated to the negative DC-link bus and vice versa. So, the DC-link voltage is formed from the line to line voltage of the supply. Assuming a balanced symmetrical AC grid:

$$\begin{aligned} U_a &= U_m \cos(\omega_i t) \\ U_b &= U_m \cos(\omega_i t - 2\pi/3) \\ U_c &= U_m \cos(\omega_i t - 4\pi/3) \end{aligned} \tag{17}$$

where U_m is the maximum grid input voltage and ω_i is the grid frequency in rad/s. The DC-link voltage varies as the supply varies:

$$U_{dc} = \frac{3U_m}{2\cos(\omega_i t)} \tag{18}$$

Figure 6 shows the space vector of the grid voltage and current. If the phase angle between the space vector of the voltage and current is set to zero, unity displacement factor is achieved. The input current space vector I_i is generated by the projection to the adjacent space vectors I_α and I_β following the grid sinusoidal voltages. The duty cycles of I_α and I_β are calculated as follows:

$$d_{\alpha r} = m_i \sin(\pi/3 - \theta_i) \tag{19}$$

and

$$d_{\beta r} = m_i \sin\theta_i \tag{20}$$

where m_i is the current modulation index which is adjusted to unity to provide the maximum injected current into the grid and maximize the DC-link voltage. In order to commutate the rectifier at zero current, the inverter space vector and switching pattern should be determined and matched with the rectifier space vector to ensure that the rectifier can be switched during the period of inverter zero voltage.

4.2.2. Inverter stage of the VSMC

Switching signals of the inverter stage are generated by FOC based space vector modulation which allows use of a zero voltage vector between the transitions from negative to positive bus. It also provides a chance to distribute the vectors symmetrically to reduce the current distortion and commutate the rectifier stage at zero current to reduce the switching losses [13, 24]. The error between the actual and reference current is compensated by a proportional plus integral (PI) controller to form the generator voltage and frequency to match the operating point which is considered the reference voltage. The reference voltage is transformed to a reference space vector. The amplitude of the vector and its angle determine the active vectors which are used to form the switching signal. The amplitude of the output voltage is proportional to the input voltage according to the transfer ratio of the matrix converter:

$$U_o \le \sqrt{3}/2 m_c U_m \tag{21}$$

where U_o is the output maximum voltage and m_c is the VSMC conversion ratio ($0 \le m_c \le 1$). Fig. 7-a presents the inverter space vectors which are used to form the generator or motor voltage. Fig. 7-b shows an example of the switching signals during one sampling period assuming the reference voltage is in sector 1.

http://dx.doi.org/10.5772/51148

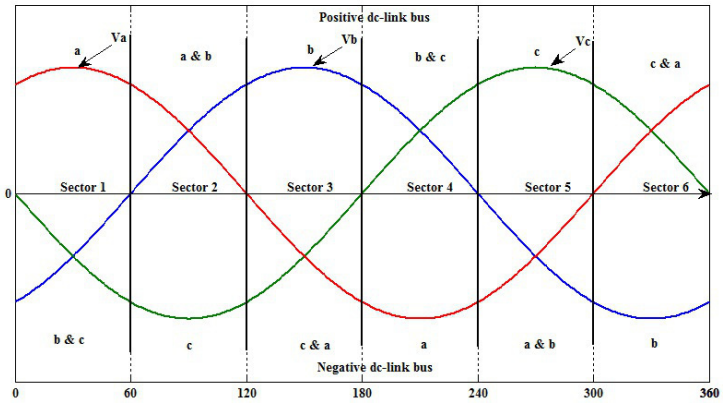

Figure 5. Modulation strategy of the rectifier stage.

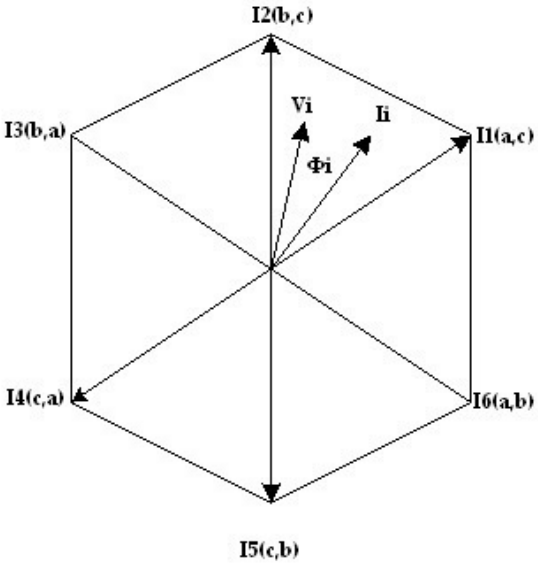

Figure 6. Rectifier stage space vector diagram

Duty cycles of the working vectors are calculated as follows depending on the space vector angle and magnitude.

$$d_{\alpha i} = m_v \sin(\pi/3 - \theta_o) \tag{22}$$

$$d_{\beta i} = m_v \sin(\theta_o) \tag{23}$$

and

$$d_0 = 1 - d_{\alpha i} - d_{\beta i} \tag{24}$$

where $d_{\alpha i}$ and $d_{\beta i}$ represent the duty cycle of the active vectors while d_0 represents the duty cycle of the zero vector.

4.2.3. Backward VSMC

In order to guarantee the transformation of power from the generator to the grid, the DC-link voltage must be held at a fairly constant and sufficiently high average value. Given a variable wind speed and MPPT, the generator operates at variable frequency and variable voltage amplitude which is often less than the corresponding grid voltage. Due to the lack of the DC-link capacitor, the VSMC cannot operate as a boost converter to keep the DC-link voltage at the required minimum value. If employed in its forward configuration, the VSMC can be considered a step down converter according to equation (21) -. So, if the generator is connected in the conventional manner to the rectifier stage and the grid is connected to the inverter stage, (i.e. forward VSMC operation), the converter will operate only when the generator operates at its rated condition, i.e. with the wind speed at or above its rated value (to solve this problem, for a forward configuration of the VSMC, a transformer with a very large step-up ratio would be required for the grid interface) To overcome this problem (i.e. with a lower ratio step-up transformer at the grid interface) a backward connected VSMC system is proposed in [13] where the rectifier stage is connected to the grid and the inverter stage is connected to the generator as shown in Figure 1. In backward operation of the VSMC, the rectifier stage converts the grid AC voltage to a near-constant average DC voltage at the DC-link (variations in the average voltage correspond to variations in the grid voltage) while the inverter steps down the DC-link voltage to variable AC voltage with variable frequency depending on the generator and turbine operating point. In other words, the backward VSMC can be considered a step up converter from the generator side to the grid side. Such operation can be achieved by controlling the modulation index of the inverter stage to boost the generator voltage to the grid voltage depending on the operating speed. This configuration has the merits that control of the DC voltage is not needed, nor is synchronization with the grid required. Voltage flicker is not an issue due to the small filter on the mains side of the converter. The generator voltage and the grid current are synthesized using a space vector PWM technique with the guarantee of injecting current into the grid with or without reactive power to meet the grid power quality requirements as explained in next subsections.

http://dx.doi.org/10.5772/51148

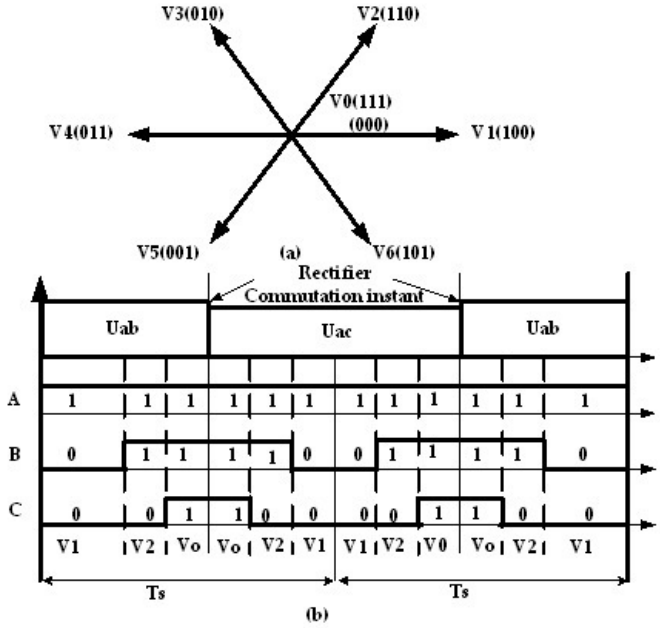

Figure 7. a) Inverter space vector diagram (b) Inverter switching signal for sector 1.

4.3. Motoring-generating mode

Equation (15) shows that the torque direction and hence the generator mode can only be controlled by the quadrature current component direction. In addition the torque is also controlled by the magnitude of I_q to match the wind power at different wind speeds. The amplitude and the direction of the generator quadrature current I_q can be controlled through the inverter stage of the VSMC.

The VSMC can operate the generator as a motor using FOC by controlling the current component which corresponds to the torque limited only by the generator torque rating. Figure 8 shows the flow chart of the starting strategy. The controller produces the reference generator current depending on the mode of operation, either motor starting or generator mode (MPPT control). If in motor starting mode, the actual and reference motor currents are compared to generate the proper machine voltage vector which results in rated torque operation of the machine. Once the turbine reaches the nominated speed, Ω_{ref}, corresponding to λ_{opt}, motoring ceases and generating with MPPT control is enabled. Figure9 shows the proposed control technique for motor starting.

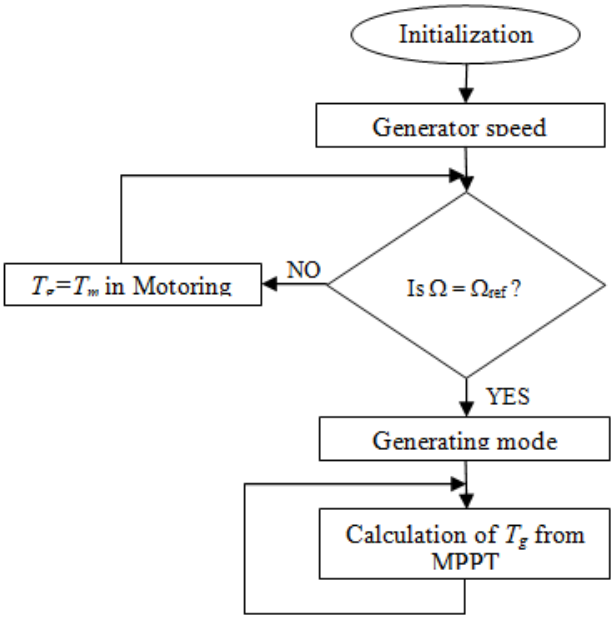

Figure 8. Starting strategy flow chart.

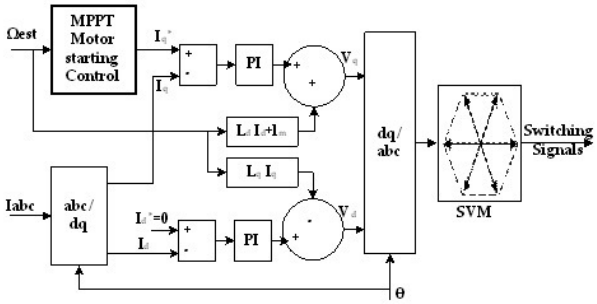

Figure 9. Block diagram of the generator-motor FOC technique.

5. Simulation results and discussion

The system described above was simulated using MATLAB Simulink for the 5.6 kW turbine described in the Appendix, initially for a wind speed is 10 m/s. Figure 10 shows results for

http://dx.doi.org/10.5772/51148

aerodynamic starting where the generator torque is zero up to the λ_{opt}. Then the generator torque closely matches the aerodynamic torque and power production starts. In Figure 11, the turbine is motored to λ_{opt}. The significant reduction in starting time is obvious.

As shown in Figure 11 10, the current is held positive and constant at its rated value during motoring. It is then changed to a negative value corresponding to the wind speed to run as a generator while for aerodynamic starting the current is kept zero then increased in negative direction to the value which matches with the aerodynamic torque. As shown in Figure 10 and 11, the rotor takes 13.29 s to reach λ_{opt} when starting aerodynamically, which is consistent with the field test data in Fig. 4, while it takes 1.9 s for a motored start. The significant difference results in a significant gain in energy harvested.

In both starting cases, the turbine runs at the maximum C_p of 0.476 after λ reaches $\lambda_{opt.}$ The MPPT would re-establish this C_p if U subsequently changes. Whether in motoring or generating mode, the grid current is sinusoidal due to the operating characteristics of the VSMC and its phase angle can be controlled depends on the direction of power flow and if desired unity power factor can be achieved to insure the power quality.

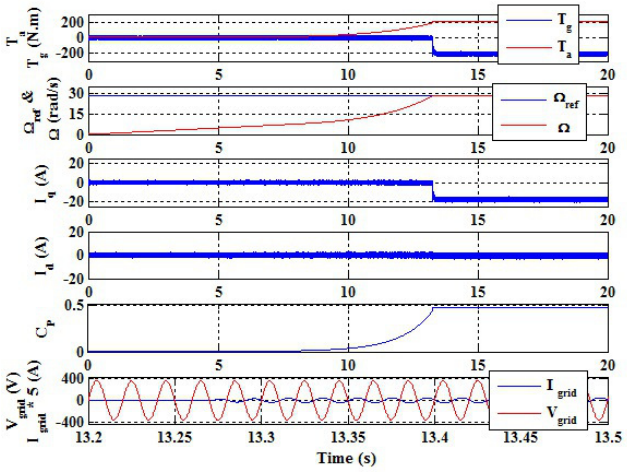

Figure 10. Aerodynamic starting of the 5.6 kW wind turbine for a wind speed of 10 m/s.

As shown in Fig. 12, for all wind speeds, motor starting reduces the starting time. Fig. 12 also shows the starting time when power production commences at a fixed fraction of the rotor maximum speed which is common operational practice for small wind turbines. Fig. 13 indicates that there is a net gain in energy delivered to the grid for motor starting compared to aerodynamic starting. As seen in Fig. 13, provided the turbine is rotating sufficiently fast, the shaft speed at which the controller switches from motor mode to generator mode does not significantly alter the energy gain compared to aerodynamic starting. This is valua-

ble for the practical implementation of the proposed approach since the wind speed does not need to be measured to determine the length of duration of the motoring mode. Motor starting can also reduce the starting wind speed, allowing the turbine to start and then produce power down to 1 m/s.

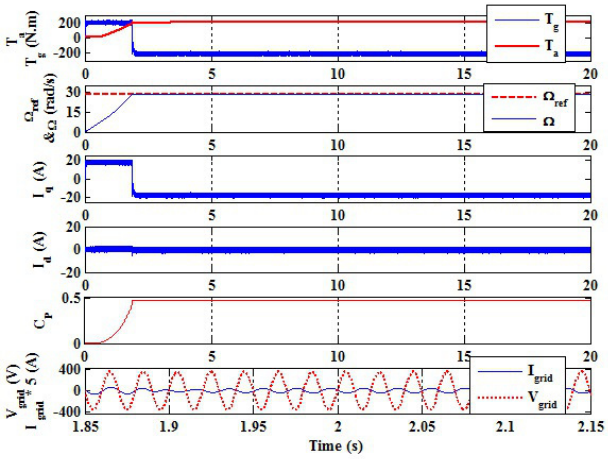

Figure 11. Motor starting of the 5.6 kW wind turbine for a wind speed of 10 m/s.

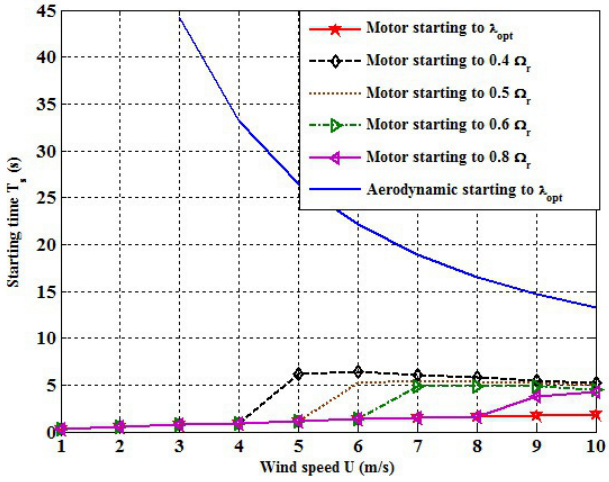

Figure 12. Starting time for aerodynamic and motor starting.

http://dx.doi.org/10.5772/51148

At this point, it is too early to determine the cost effectiveness of the motor starting approach partly because we have not yet done any simulations to test its effectiveness in realistic low-wind conditions. It is also difficult to ascertain the net energy gain over a substantial time (e.g. one year of operation). Nonetheless, as power electronics continue to quickly drop in cost [5], the use of a wind turbine in a variable speed mode of operation with an accompanying power converter seems increasingly attractive, and techniques such as motor starting may be a part of the role that power electronics can serve.

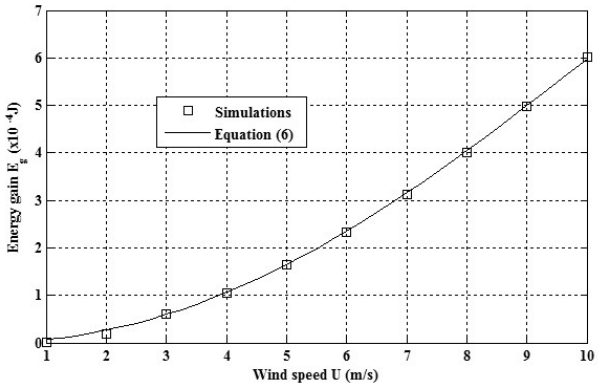

Figure 13. Energy gain by motor-starting to $\lambda_{opt.}$

6. Summary and future developments

Power electronics are developing rapidly and their cost is falling. These trends will continue to be used to reduce the cost of small wind turbines and improve their cost effectiveness. After briefly noting these trends, this Chapter concentrated on a modern converter topology suitable for grid connected small wind turbines: the backward very sparse matrix converter (VSMC). It has the potential to improve conversion efficiency by reducing switching losses. In turn, the ability to switch rapidly in a complex fashion has been made possible by recent improvements in digital signal processing technology. Like many modern topologies, the VSMC allows bi-directional power flow which can be exploited to motor start a small wind turbine and increase the energy extracted, at least for the artificial case of a step increase in the wind speed from zero. The strategy also lowers the cut-in wind speed and shows the importance of considering the whole turbine system when designing the converter.

Motor starting as the wind speed increased was analyzed to compare with conventional aerodynamic starting assessed experimentally for a 5.0 kW wind turbine whose blades were designed to start quickly. Using the scaling outside the integral in Equation (5), the aerodynamic starting at any wind speed was determined. The simple analysis of Section 4 and the

detailed Simulink modeling both show that an energy gain occurs for all wind speeds with motor starting. Moreover, the turbine can contribute energy to the grid at wind speeds below the conventional cut-in speed if motoring is employed. This strongly suggests that motor-starting should be investigated for more typical wind speed variations. The results suggest a good practical strategy is to motor the turbine to 60% of rated rotor speed when the average wind speed is in the range of 4 to 7 m/s [26].

Acknowledgements

This research was funded by the National Science and Engineering Research Council (NSERC) and the ENMAX Corporation under the Industrial Research Chairs programme. Important additional support came from he Schulich endowment to the University of Calgary and the Egyptian Higher Ministry of Education. We thank Heath Raftery for the data in Figure 3.

Appendices

Appendix – Parameter Values used in Simulations

Grid Parameters	
Phase Voltage (rms)	220 (V)
Frequency	60 (Hz)
5.6 kW PMSG Parameters [12]	
Rated phase voltage (rms)	165 (V)
Phase current (rms)	12 (A)
Rated frequency	36 (Hz)
Rated torque	204.2 (Nm)
Rated speed	270 (rpm)
L_d, L_q	0.02047(mH)
R_s	1.5 (ohm)
Magnet flux	0.97 (wb)
pole pairs	8
inertia	0.138 (Kgm^2)
5.6 kW Wind Turbine Parameters [10]	
Rotor diameter, R	5 (m)

Rotor rated speed, Ω_r			270 (rpm)
Cut-in wind speed			2.5 (m/s)
Rated wind speed			10 (m/s)
Inertia, J			18(Kgm^2)
Maximum C_p			0.475
λ_{opt}			7
$a_0 = 0.0061$	$a_1 = -0.0013$	$a_2 = 0.0081$	$a_3 = -9.75\times10^{-4}$
$a_4 = -6.54\times10^{-5}$	$a_5 = 1.30\times10^{-5}$	$a_6 = -4.54\times10^{-7}$	

Author details

Mohamed Aner[1], Edwin Nowicki[1] and David Wood[2*]

*Address all correspondence to: dhwood@ucalgary.ca

1 Dept Electrical and Computer Engineering, Canada

2 Dept Mechanical and Manufacturing Engineering, University of Calgary, Calgary, T2N 1N4, Canada

References

[1] Small Wind Systems UK Market Report. (2011, April). *British Wind Energy Association*, available:, http://www.bwea.com/pdf/small/Small_Wind_Systems_Market _Report_2011.pdf.

[2] Tirumara, R., & Mohan, N. (2000, April 3-7). Dynamic simulation and comparison of slip ring induction generators used for wind energy generation. Paper presented at International Power Electronics Conference, Tokyo. 956-965.

[3] Carlin, P. W., Laxson, A. S., & Muljadi, E. B. (2001, Feb). The history and state of the art of variable-speed wind turbine technology. *National Renewable Energy Laboratory*, 10.2172/776935.

[4] Zaragozaa, J., Poua, J., Ariasa, A., Spiterib, C., Roblesc, E., & Ceballos, S. (2011, May). Study and experimental verification of control tuning strategies in a variable speed wind energy conversion system. *Renewable Energy*, 36(5), 1421-1430.

[5] Ivov, F., & Blaabjerg, F. (2009). Power electronics and control for wind power systems. IEEE Power Electronics and Machines in Wind Applications (PEMWA09) Lincoln, Nebraska, June 24-26 , 1-16.

[6] Ebert, P. R., & Wood, D. H. (1997, Nov). Observation of the start-up behavior of a small horizontal-axis wind turbine. *Renewable Energy*, 12, 245-257.

[7] Mayer, C., Bechly, M. E., Hampsey, M., & Wood, D. H. (2001). The start-up behaviour of a small horizontal-axis wind turbine. Renewable Energy March, 22, 411-417.

[8] Kjellin, J., & Bernhoff, H. (2011). Electrical starter system for an h-rotor type VAWT with PM-generator and auxiliary winding. Journal of Wind Engineering Feb., 35, 85-92.

[9] Hill, N., Dominy, R., Ingram, G., & Dominy, J. (2009). Darrieus turbines: the physics of self-starting. *Proc. IMechE Part A: Journal of Power and Energy*, 223, 21-29.

[10] Wood, D. H. (2011). Small Wind Turbines: Analysis, Design, and Application,. Springer-Verlag, London, 10.1007/978-1-84996-175-2.

[11] Wright, A. K., & Wood, D. H. (2004, Dec). The starting and low wind speed behavior of a small horizontal axis wind turbine. *Journal of Wind Engineering and Industrial Aerodynamics*, 92, 1265-1279.

[12] Qin, S., Wang, M., Chen, T., & Yao, X. (2011, Sept 16-18). Comparative analysis of incremental conductance and perturb-and observation methods to implement MPPT in photovoltaic system. Paper presented at Proc. 2011 International Conference on Electrical and Control Engineering (ICECE),. 5792-5795.

[13] Aner, M., & Nowicki, E. (2011). Two-level backward operation of VSMC for PMSG grid connected variable speed wind turbine systems. in Proc. 2011 IEEE International Electric Machines and Drives Conf., (IEMDC11) Niagara Falls, Canada , 1116-1122.

[14] Motto, E. R., Donlon, J. F., Tabata, M., Takahashi, H., Yu, Y., & Majumdar, G. (2004). Application characteristics of an experimental RB-IGBT (reverse blocking IGBT) module. Paper presented at IEEE Industry Applications Society Annual Meeting, Seattle. 3, 1540-1544.

[15] Takei, M., Odaka, A., & Fujimoto, H. ((2002). Application technologies of reverse-blocking IGBT. Fuji Electric Journal , 75(8)

[16] Itoh, J., Odaka, A., & Sato, I. (2004). High efficiency power conversion using a matrix converter. *Fuji Electric Review*, 50(3), 94-98.

[17] Munteanu, I., Bratcu, A. L., Cutululis, N. A., & Ceanga, E. (2008). Optimal Control of Wind Energy Systems. 1st Ed.Springer-Verlag London , 243.

[18] Tan, K., & Islam, S. (2004). Optimum control strategies in energy conversion of PMSG wind turbine system without mechanical sensors. IEEE Transactions on Energy Conversion June, 19(2), 392-400.

[19] Wu, B., Lang, Y., Zargaria, N., & Kouro, S. (2011). Power Conversion and Control of Wind Energy Systems. Wiley IEEE press, 10.1002/9781118029008.

[20] Itoh, J., Odaka, A., & Sato, I. (2004). High efficiency power conversion using a matrix converter. *Fuji Electric Review*, 5(3), 94-98.

[21] Wheeler, P. W., Rodriguez, J., Clare, J. C., Empringham, L., & Einstein, A. (2002). Matrix converters: a technology review. IEEE Trans. Industrial Electronics April., 49, 276-288.

[22] Kolar, J., Baumann, M., Schafmeister, F., & Ertl, H. (2002). Novel three-phase ac-dc-ac sparse matrix converters- Part I and II. Paper presented at IEEE Applied Power Electronics Conference, Dallas. 777-791.

[23] Kolar, J. W., Schafmeister, F., Round, S. D., & Ertl, H. (2007, Sept). Novel three-phase ac/ac sparse matrix converters,. *IEEE Trans. Power Electronics*, 22, 1649-1661.

[24] Wei, L., & Lipo, T. A. (2001). A novel matrix converter topology with simple commutation,. IEEE Industry Applications Society Annual Meeting Chicago , 1749-1754.

[25] Cha, H. J., & Enjeti, P. N. (2004, July-Aug). Matrix converter-fed ASDs. *IEEE Industry Applications Magazine*, 10, 33-39.

[26] Aner, M., Nowicki, E., Ali, A., & Wood, D. H. (2012). Sensor-less Motor Starting of Grid-Connected Small Wind Turbine. in Proc. RAEPS, April, Alexandria, Egypt.

Chapter 7

Wind Turbine Generator Technologies

Wenping Cao, Ying Xie and Zheng Tan

Additional information is available at the end of the chapter

http://dx.doi.org/10.5772/51780

1. Introduction

Wind energy is playing a critical role in the establishment of an environmentally sustainable low carbon economy. This chapter presents an overview of wind turbine generator technologies and compares their advantages and drawbacks used for wind energy utilization. Traditionally, DC machines, synchronous machines and squirrel-cage induction machines have been used for small scale power generation. For medium and large wind turbines (WTs), the doubly-fed induction generator (DFIG) is currently the dominant technology while permanent-magnet (PM), switched reluctance (SR) and high temperature superconducting (HTS) generators are all extensively researched and developed over the years. In this chapter, the topologies and features of these machines are discussed with special attention given to their practical considerations involved in the design, control and operation. It is hoped that this chapter provides quick reference guidelines for developing wind turbine generation systems.

2. Utilization of wind energy

The utilization of wind energy can be dated back to 5000 B.C. when sail boats were propelled across the river Nile. It was recorded that from 200 B.C. onwards wind was used as an energy source to pump water, grind grain, and drive vehicles and ships in ancient China and Middle East. The first documented windmill was in a book *Pneumatics* written by Hero of Alexandria around the first century B.C. or the first century A.D. [52]. Effectively, these wind mills are used to convert kinetic energy into mechanical energy.

The use of wind energy to generate electricity first appeared in the late 19th century [35] but did not gain ground owing to the then dominance of steam turbines in electricity genera-

tion. The interest in wind energy was renewed in the mid-1970s following the oil crises and increased concerns over resource conservation. Initially, wind energy started to gain popularity in electricity generation to charge batteries [17] in remote power systems, residential scale power systems, isolated or island power systems, and utility networks. These wind turbines themselves are generally small (rated less than 100kW) but could be made up to a large wind farm (rated 5MW or so). It was until the early 1990s when wind projects really took off the ground, primarily driven by the governmental and industrial initiatives. It was also in 1990s there seemed a shift of focus from onshore to offshore development in major wind development countries, especially in Europe.

Offshore wind turbines were first proposed in Germany in 1930s and first installed in Sweden in 1991 and in Denmark in 1992. By July 2010, there were 2.4 GW of offshore wind turbines installed in Europe. Compared to onshore wind energy, offshore wind energy has some appealing attributes such as higher wind speeds, availability of larger sites for development, lower wind sheer and lower intrinsic turbulence intensity. But the drawbacks are associated with harsh working conditions, high installation and maintenance costs. For offshore operation, major components should be marinized with additional anti-corrosion measures and de-humidification capacity [24]. In order to avoid unscheduled maintenance, they should also be equipped with fault-ride-through capacity to improve their reliability.

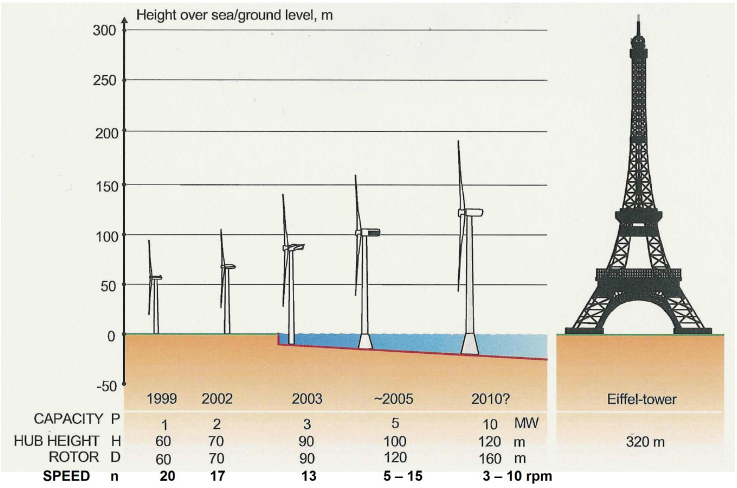

Figure 1. Ever-growing size of horisontal-axis wind turbines [36].

Over the last three decades, wind turbines have significantly evolved as the global wind market grows continuously and rapidly. By the end of 2009, the world capacity reached a total of 160 GW [7]. In the global electricity market, wind energy penetration is projected to rise from 1% in 2008 to 8% in 2035 [45]. This is achieved simply by developing larger wind turbines and employing more in the wind farm. In terms of the size, large wind turbines of

http://dx.doi.org/10.5772/51780

the MW order began to appear in the EU, the US and now in China and India. Typically, the large installed wind turbines in utility grids are between 1.5-5MW whilst 7.5 and 10 MW are under extensive development, as shown in Fig. 1. Nowadays, modern wind turbines are reliable, quiet, cost-effective and commercially competitive while the wind turbine technologies are proven and mature. At present, technical challenges are generally associated with ever-growing wind turbine size, power transmission, energy storage, energy efficiency, system stability and fault tolerance.

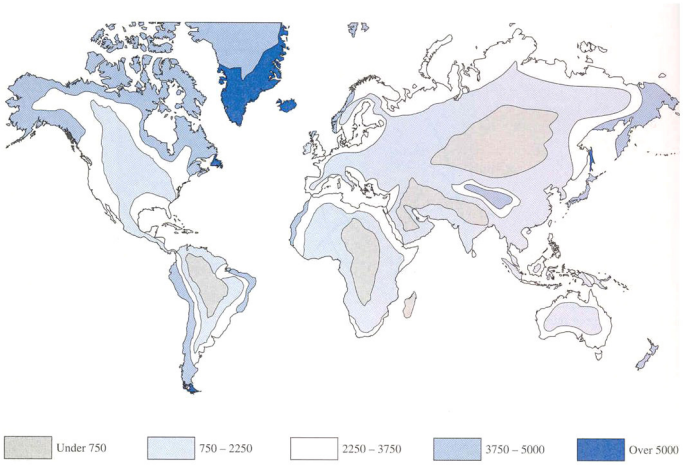

Figure 2. The world's energy potential for land-based wind turbines (estimated energy output in kWh/kW from a wind turbine that is dimensioned for 11 m/s) [36].

Currently, wind power is widely recognized as a main feasible source of renewables which can be utilized economically in large quantity. A world map for wind energy potential is illustrated in Fig. 2. Taking the United Kingdom for example, the usable offshore wind energy alone is enough to provide three times more than the required electricity consumption in the country, given sufficient support. However, wind power fluctuates by its nature and such applications demand high reliability and high availability while the market is still looking to reduce weight, complexity and operational costs.

3. Wind Turbines

Clearly, wind energy is high on the governmental and institutional agenda. However, there are some stumbling blocks in the way of its widespread.

Wind turbines come with different topologies, architectures and design features. The schematic of a wind turbine generation system is shown in Fig. 3. Some options wind turbine topologies are as follows [35],

- Rotor axis orientation: horizontal or vertical;
- Rotor position: upwind or downwind of tower;
- Rotor speed: fixed or variable;
- Hub: rigid, teetering, gimbaled or hinged blades;
- Rigidity: still or flexible;
- Number of blades: one, two, three or even more;
- Power control: stall, pitch, yaw or aerodynamic surfaces;
- Yaw control: active or free.

This chapter focuses only on horizontal-axis wind turbines (HAWTs), which are the prevailing type of wind turbine topology, as is confirmed in Fig. 4.

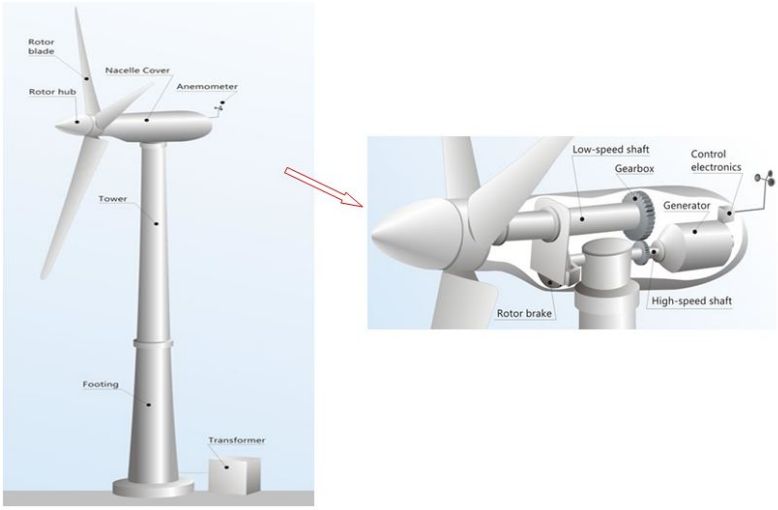

Figure 3. Schematic of a wind turbine generation system [50].

Wind turbines include critical mechanical components such as turbine blades and rotors, drive train and generators. They cost more than 30% of total capital expenditure for offshore wind project [24]. In general, wind turbines are intended for relatively inaccessible sites placing some constraints on the designs in a number of ways. For offshore environments, the site may be realistically accessed for maintenance once per year. As a result, fault tolerance of the wind turbine is of importance for wind farm development.

http://dx.doi.org/10.5772/51780

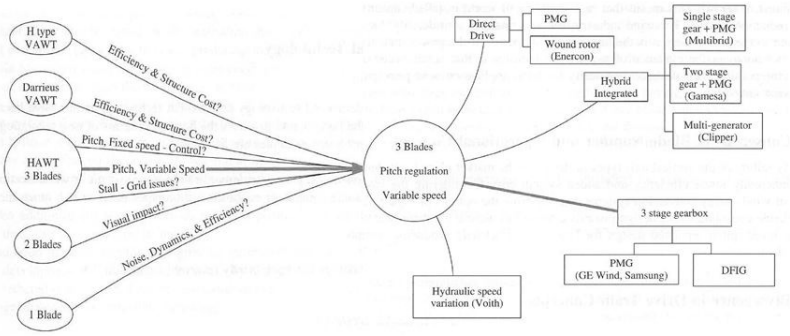

Figure 4. Commonly agreed wind turbine type and its divergence [24].

One of key components in the wind turbine is its drive train, which links aerodynamic rotor and electrical output terminals. Optimization of wind turbine generators can not be realized without considering mechanical, structural, hydraulic and magnetic performance of the drive train. An overview of the drive train technologies is illustrated in Fig. 5 for comparison. Generally, they can be broken down into four types according to their structures [24]:

- Conventional: gearbox and high speed generator with few pole pairs.
- Direct drive: any drive train without a gearbox and low speed generator with many pole pairs.
- Hybrid: any drive train with a gearbox and the generator speed between the above two types.
- Multiple generators: any drive train with more than one generator.

Drive train topologies may raise the issues such as the integration of the rotor and gearbox/bearings, the isolation of gear and generator shafts from mechanical bending loads, the integrity and load paths. Although it may be easier to service separate wind turbine components such as gearboxes, bearings and generators, the industry is increasingly in favor of system design of the integrated drive train components.

4. Wind Turbine Generators

One of limiting factors in wind turbines lies in their generator technology. There is no consensus among academics and industry on the best wind turbine generator technology. Traditionally, there are three main types of wind turbine generators (WTGs) which can be considered for the various wind turbine systems, these being direct current (DC), alternating current (AC) synchronous and AC asynchronous generators. In principle, each can be run at fixed or variable speed. Due to the fluctuating nature of wind power, it is advantageous to

operate the WTG at variable speed which reduces the physical stress on the turbine blades and drive train, and which improves system aerodynamic efficiency and torque transient behaviors.

(a) DC Generator Technologies

In conventional DC machines, the field is on the stator and the armature is on the rotor. The stator comprises a number of poles which are excited either by permanent magnets or by DC field windings. If the machine is electrically excited, it tends to follow the shunt wound DC generator concept.

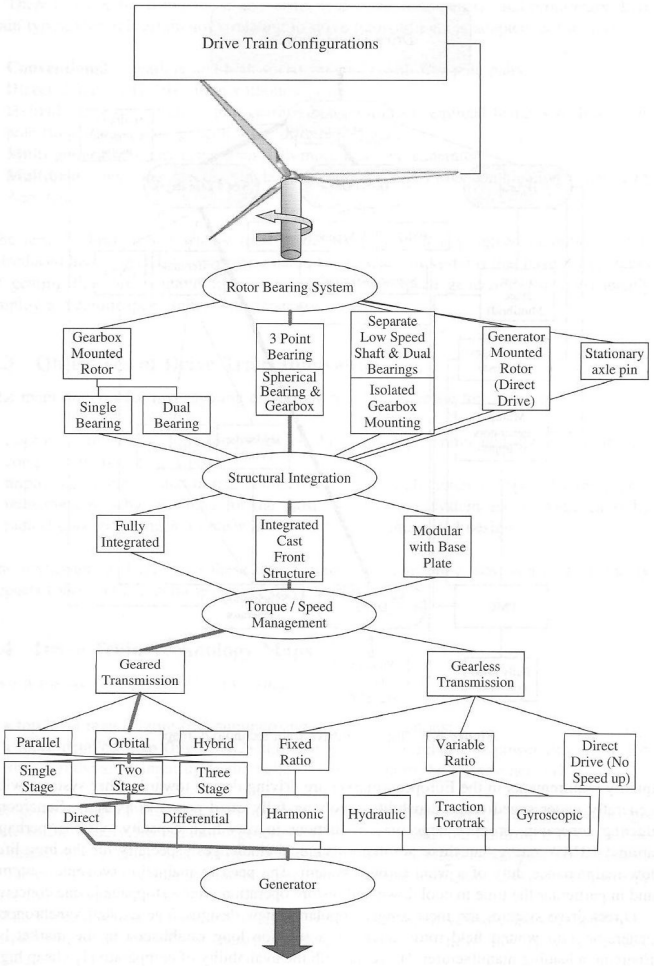

Figure 5. System level drive train technologies [24].

http://dx.doi.org/10.5772/51780

An example of the DC wind generator system is illustrated in Fig. 6. It consists of a wind turbine, a DC generator, an insulated gate bipolar transistor (IGBT) inverter, a controller, a transformer and a power grid. For shunt wound DC generators, the field current (and thus magnetic field) increases with operational speed whilst the actual speed of the wind turbine is determined by the balance between the WT drive torque and the load torque. The rotor includes conductors wound on an armature which are connected to a split-slip ring commentator. Electrical power is extracted through brushes connecting the commentator which is used to rectify the generated AC power into DC output. Clearly, they require regular maintenance and are relatively costly due to the use of commutators and brushes.

In general, these DC WTGs are unusual in wind turbine applications except in low power demand situations [47; 23; 33; 54] where the load is physically close to the wind turbine, in heating applications or in battery charging.

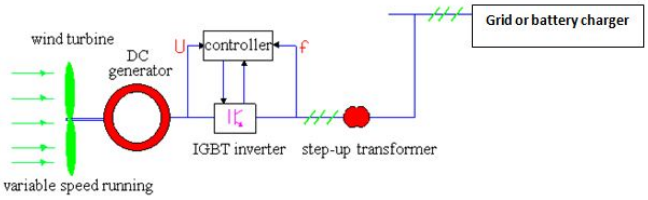

Figure 6. Schematic of a DC generator system [33].

(b) AC Synchronous Generator Technologies

Since the early time of developing wind turbines, considerable efforts have been made to utilize three-phase synchronous machines. AC synchronous WTGs can take constant or DC excitations from either permanent magnets or electromagnets and are thus termed PM synchronous generators (PMSGs) and electrically excited synchronous generators (EESGs), respectively. When the rotor is driven by the wind turbine, a three-phase power is generated in the stator windings which are connected to the grid through transformers and power converters. For fixed speed synchronous generators, the rotor speed must be kept at exactly the synchronous speed. Otherwise synchronism will be lost.

Synchronous generators are a proven machine technology since their performance for power generation has been studied and widely accepted for a long time. A cutaway diagram of a conventional synchronous generator is shown in Fig. 7. In theory, the reactive power characteristics of synchronous WTGs can be easily controlled via the field circuit for electrical excitation. Nevertheless, when using fixed speed synchronous generators, random wind speed fluctuations and periodic disturbances caused by tower-shading effects and natural resonances of components would be passed onto the power grid. Furthermore, synchronous WTGs tend to have low damping effect so that they do not allow drive train transients to be absorbed electrically. As a consequence, they require an additional damping element (e.g. flexible

coupling in the drive train), or the gearbox assembly mounted on springs and dampers. When they are integrated into the power grid, synchronizing their frequency to that of the grid calls for a delicate operation. In addition, they are generally more complex, costly and more prone to failure than induction generators. In the case of using electromagnets in synchronous machines, voltage control takes place in the synchronous machine while in permanent magnet excited machines, voltage control is achieved in the converter circuit.

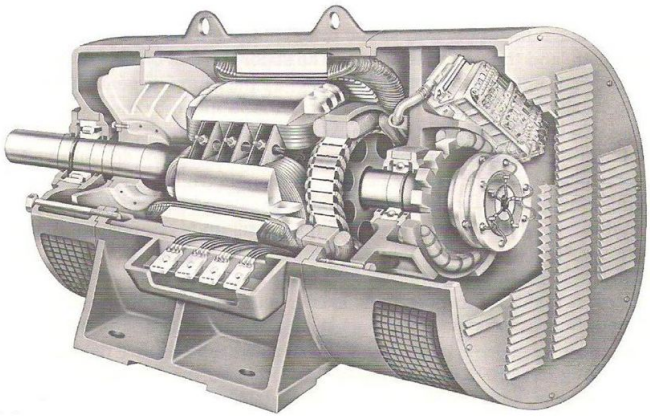

Figure 7. Cutaway of a synchronous generator [22].

In recent decades, PM generators have been gradually used in wind turbine applications due to their high power density and low mass [39]. Often these machines are referred to as the permanent magnet synchronous generators (PMSGs) and are considered as the machine of choice in small wind turbine generators. The structure of the generator is relatively straightforward. As shown in Fig. 8. the rugged PMs are installed on the rotor to produce a constant magnetic field and the generated electricity is taken from the armature (stator) via the use of the commutator, sliprings or brushes. Sometimes the PMs can be integrated into a cylindrical cast aluminum rotor to reduce costs [35]. The principle of operation of PM generators is similar to that of synchronous generators except that PM generators can be operated asynchronously. The advantages of PMSGs include the elimination of commutator, slip rings and brushes so that the machines are rugged, reliable and simple. The use of PMs removes the field winding (and its associated power losses) but makes the field control impossible and the cost of PMs can be prohibitively high for large machines.

Because the actual wind speeds are variable, the PMSGs can not generate electrical power with fixed frequency. As a result, they should be connected to the power grid through AC-DC-AC conversion by power converters. That is, the generated AC power (with variable frequency and magnitude) is first rectified into fixed DC and then converted back into AC power (with fixed frequency and magnitude). It is also very attractive to use these permanent magnet machines for direct drive application. Obviously, in this case, they can elimi-

nate troublesome gearboxes which cause the majority of wind turbine failures. The machines should have large pole numbers and are physically large than a similarly rated geared machine.

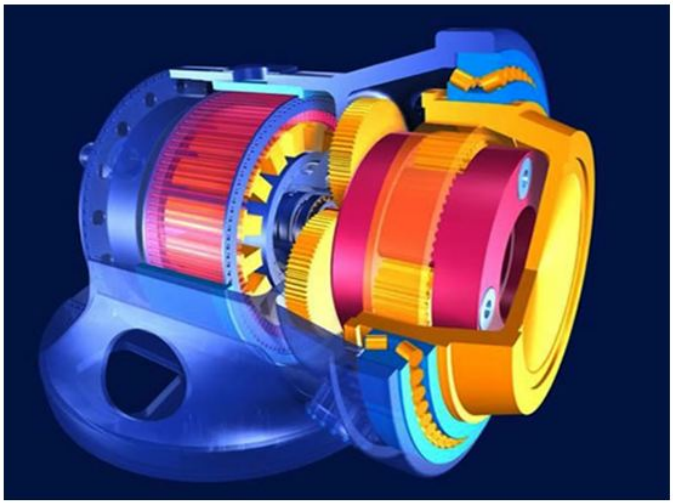

Figure 8. Cutaway of a permanent magnet synchronous generator [18].

A potential variant of synchronous generators is the high-temperature superconducting generator [31; 27; 49; 55]. See Fig. 9 for a multi-MW, low-speed HTS synchronous generator system. The machine comprises the stator back iron, stator copper winding, HTS field coils, rotor core, rotor support structure, rotor cooling system, cryostat and external refrigerator, electromagnetic shield and damper, bearing, shaft and housing. In the machine design, the arrangements of the stator, rotor, cooling and gearbox may pose particular challenges in order to keep HTS coils in the low temperature operational conditions.

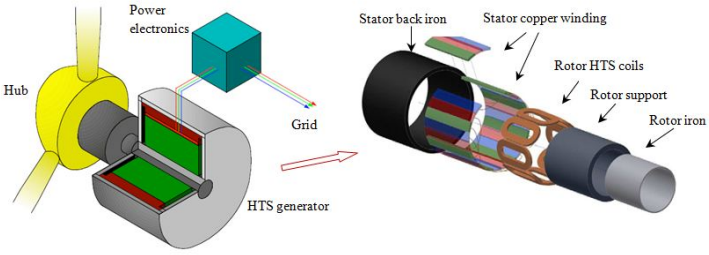

Figure 9. Schematic of a HTS synchronous generator system [11].

Superconducting coils may carry 10 times the current than conventional copper wires with negligible resistance and conductor losses. Without a doubt, the use of superconductors would eliminate all field circuit power loss and the ability of superconductivity to increase current density allows for high magnetic fields, leading to a significant reduction in mass and size for wind turbine generators. Therefore, superconducting generators provide much promise in high capacity and weight reductions, perhaps suited better for wind turbines rated 10 MW or more. In 2005, Siemens successfully launched the world's first superconducting wind turbine generator, which was a 4MW synchronous generator. However, there are many technical challenges to face especially for the long-life, low-maintenance wind turbine systems. For instance, there is always a necessity to maintain cryogenic systems so that the time to cool down and restore operation following a stoppage will be an additional issue.

(c) AC Asynchronous Generators

Whilst conventional power generation utilizes synchronous machines, modern wind power systems use induction machines extensively in wind turbine applications. These induction generators fall into two types: fixed speed induction generators (FSIGs) with squirrel cage rotors (sometimes called squirrel cage induction generators-SQIGs) [40; 1] and doubly-fed induction generators (DFIGs) with wound rotors [9; 29; 19; 32, 43; 13; 34]. Cutaway diagrams of a squirrel-cage induction generator and a doubly-fed induction generator are presented in Fig. 10 and Fig. 11, respectively, and their system topologies are further illustrated in Fig. 12.

When supplied with three-phase AC power to the stator, a rotating magnetic field is established across the airgap. If the rotor rotates at a speed different to synchronous speed, a slip is created and the rotor circuit is energized. Generally speaking, induction machines are simple, reliable, inexpensive and well developed. They have high degree of damping and are capable of absorbing rotor speed fluctuations and drive train transients (i.e. fault tolerant). However, induction machines draw reactive power from the grid and thus some form of reactive power compensation is needed such as the use of capacitors or power converters. For fixed-speed induction generators, the stator is connected to the grid via a transformer and the rotor is connected to the wind turbine through a gearbox. The rotor speed is considered to be fixed (in fact, varying within a narrow range). Up until 1998 most wind turbine manufacturers built fixed-speed induction generators of 1.5 MW and below. These generators normally operated at 1500 revolutions per minute (rpm) for the 50 Hz utility grid [37], with a three-stage gearbox.

http://dx.doi.org/10.5772/51780

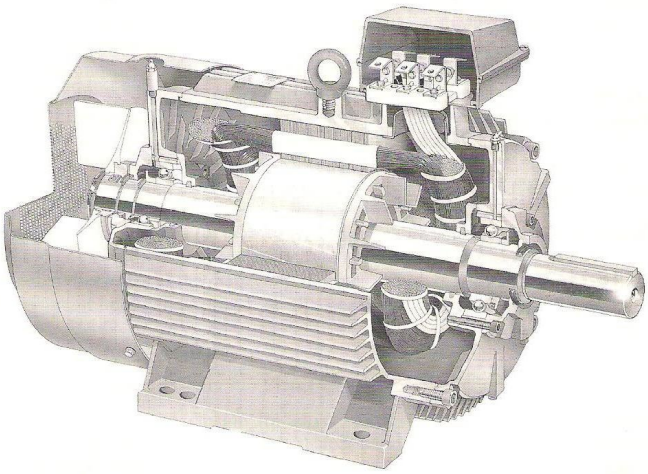

Figure 10. Cutaway of a squirrel-cage induction generator [22].

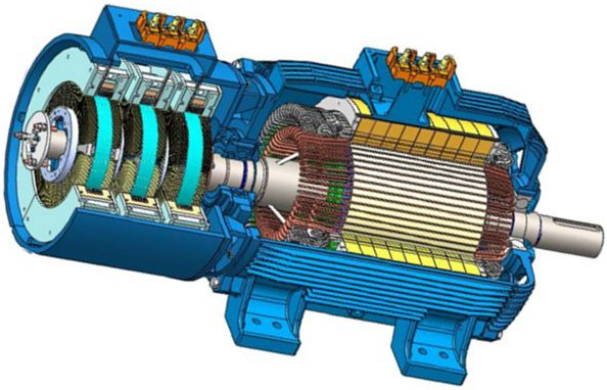

Figure 11. Cutaway of a doubly-fed induction generator with a rotary transformer [43].

SCIGs can be utilized in variable speed wind turbines, as in controlling synchronous machines. However, the output voltage can not be controlled and reactive power needs to be supplied externally. Clearly, fixed speed induction generators are limited to operate only within a very narrow range of discrete speeds. Other disadvantages of the machines are related to the machine size, noise, low efficiency and reliability. These machines have proven to cause tremendous service failures and consequent maintenance.

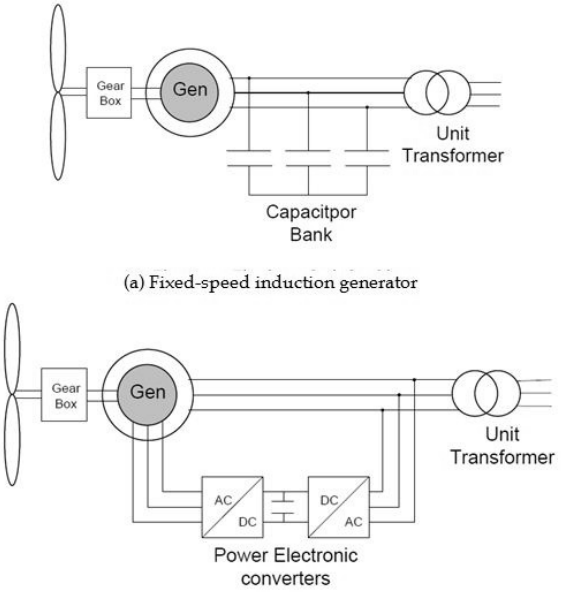

Figure 12. Schematic of two induction generator systems.

SCIGs led the wind turbine market until the last millennium [16; 26], overtaken by the wide adoption of DFIGs. Nowadays, over 85% of the installed wind turbines utilize DFIGs [41] and the largest capacity for the commercial wind turbine product with DFIG has increased towards 5MW in industry. In the DFIG topology, the stator is directly connected to the grid through transformers and the rotor is connected to the grid through PWM power converters. The converters can control the rotor circuit current, frequency and phase angle shifts. Such induction generators are capable of operating at a wide slip range (typically ±30% of synchronous speed). As a result, they offer many advantages such as high energy yield, reduction in mechanical stresses and power fluctuations, and controllability of reactive power.

For induction generators, all the reactive power energizing the magnetic circuits must be supplied by the grid or local capacitors. Induction generators are prone to voltage instability. When capacitors are used to compensate power factor, there is a risk of causing self-excitation. Additionally, damping effect may give rise to power losses in the rotor. There is no direct control over the terminal voltage (thus reactive power), nor sustained fault currents.

As shown in Fig. 12(b), the rotor of the DFIG is mechanically connected to the wind turbine through a drive train system, which may contain high and low speed shafts, bearings and a gearbox. The rotor is fed by the bi-directional voltage-source converters. Thereby, the speed and torque of the DFIG can be regulated by controlling the rotor side converter (RSC). Another feature is that DFIGs can operate both sub-synchronous and super-synchronous conditions. The stator always transfers power to the grid while the rotor can handle power in

http://dx.doi.org/10.5772/51780

both directions. The latter is due to the fact that the PWM converters are capable of supplying voltage and current at different phase angles. In sub-synchronous operation, the rotor-side converter acts as an inverter and the grid-side converter (GSC) as a rectifier. In this case, active power is flowing from the grid to the rotor. Under super-synchronous condition, the RSC operates as a rectifier and the GSC as an inverter. Consequently, active power is flowing from the stator as well as the rotor to the power grid.

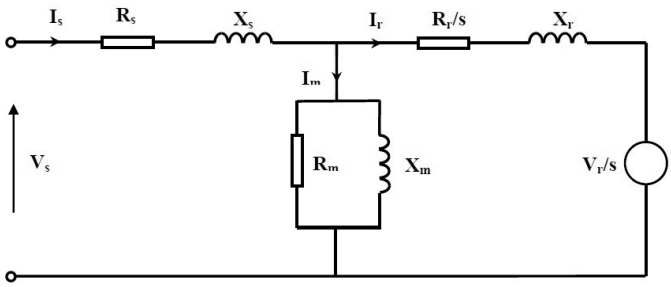

Figure 13. Per-phase equivalent circuit of the DFIG.

To analyze the DFIG's performance, it always needs to adopt its per-phase equivalent circuit, as exampled in Fig. 13. From this figure, it can be seen that the DFIG differs from the conventional induction machine in the rotor circuit where a voltage source is added to inject voltage into the rotor circuit. The actual *d-q* control of the DFIG is similar to the magnitude and phase control of the injected voltage in the circuit.

The matrix form of the equation for this circuit is

$$\begin{bmatrix} V_s \\ V_r / s \end{bmatrix} = \begin{bmatrix} R_s + j(X_s + X_m) & -jX_m \\ -jX_m & R_r / s + j(X_r + X_m) \end{bmatrix} \begin{bmatrix} I_s \\ I_r \end{bmatrix} \tag{1}$$

The input power P_{in} can be summarized from the output power P_{out} and the total loss P_{loss}. The latter includes stator conductor loss P_{cu1}, rotor conductor loss P_{cu2}, core loss P_{core}, windage and friction losses P_{wf} and stray load loss P_{stray}. Among these losses, P_{cu1} is assumed to vary with the square of the stator current I_s while P_{cu2} varies with the square of the rotor current I_r. The stray load loss could be split into two parts: the fundamental component P_{fun} occurring at the stator side and P_{har} at the rotor side. Thus P_{fun} is proportional to I_s^2 while P_{har} is proportional to I_r^2.

The total loss is then given by

$$P_{loss} = 3I_s^2(R_s + R_{fun}) + 3I_r^2(R_r' + R_{har}) + P_{core} + P_{wf} \tag{2}$$

The efficiency of the DFIG is

$$\eta = \frac{P_{out}}{P_{in}} = \frac{3V_{out}\cos\varphi_r}{6I_s(R_s + R_{fun} + R_r{}' + R_{har}) + 3V_{out}\cos\varphi_r} \tag{3}$$

The efficiency can be expressed as a function of the load current I_s and this function is continuous and monotonic. Consequently, the maximum efficiency can be found when

$$\frac{\partial\eta}{\partial I_s} = 0 \tag{4}$$

That is, the condition of maximum efficiency for DFIGs is

$$P_{core} + P_{wf} = P_{cu1} + P_{cu2} + P_{stray} \tag{5}$$

In order to optimize the DFIG machine design, its losses and efficiency need to derive numerically or experimentally. An additional refinement parameter is the machine's operational point. The condition of the maximum efficiency occurrence indicates: when the load-dependent losses equalise the load-invariant losses, the machine efficiency peaks. In the design and operation of DFIGs, it is beneficial to match the generator's characteristics with the site-specific wind speed by moving this maximum efficiency point close to the rated or operational load.

For control purposes, the DFIG mathematical model is based on the synchronous reference frame as follows,

$$\begin{cases} v_{sd} = r_s i_{sd} + \dfrac{d\psi_{sd}}{dt} - \omega_s \psi_{sq} \\ v_{sq} = r_s i_{sq} + \dfrac{d\psi_{sq}}{dt} + \omega_s \psi_{sd} \end{cases} \tag{6}$$

$$\begin{cases} v_{rd} = r_r i_{rd} + \dfrac{d\psi_{rd}}{dt} - (\omega_s - \omega_r)\psi_{rq} \\ v_{rq} = r_r i_{rq} + \dfrac{d\psi_{rq}}{dt} + (\omega_s - \omega_r)\psi_{rd} \end{cases} \tag{7}$$

$$\begin{cases} \psi_{sd} = (L_{ls} + L_m) i_{sd} + L_m i_{rd} \\ \psi_{sq} = (L_{ls} + L_m) i_{sq} + L_m i_{rq} \end{cases} \tag{8}$$

http://dx.doi.org/10.5772/51780

$$\begin{cases} \psi_{rd} = (L_{lr} + L_m) i_{rd} + L_m i_{sd} \\ \psi_{rq} = (L_{lr} + L_m) i_{rq} + L_m i_{sq} \end{cases} \tag{9}$$

wherer_s and r_r are the stator and rotor resistances in Ω, $L_{ls}$and L_{lr} are the stator and rotor leakage inductances in H, $L_m$is the magnetizing inductance in H. $\omega_s$is the synchronous electrical speed in rad/sec. $\omega_r$is the rotor electrical speed of the DFIG and its relation with rotor mechanical speed ω_g is$\omega_r = P\omega_g$, where P is pole pairs.

The electromagnetic torque is given by

$$T_e = \frac{3}{2} P L_m (i_{sq} i_{rd} - i_{sd} i_{rq}) \tag{10}$$

In DFIGs, active power is used to evaluate the power output and reactive power is responsible for its electrical behavior in the power network. The DFIG requires some amounts of reactive power to establish its magnetic field. In case of grid-connected systems, the generator obtains the reactive power from the grid itself [48]. In case of isolated system operation, the reactive power needs to be provided by external sources such as capacitors [4] or batteries [9].

(d) Switched Reluctance Generator Technologies

Switched reluctance WTGs are characterized with salient rotors and stator. As the rotor rotates, the reluctance of the magnetic circuit linking the stator and rotor changes, and in turn, induces currents in the winding on the armature (stator). See Fig. 14 for a schematic of the switched reluctance generator system.

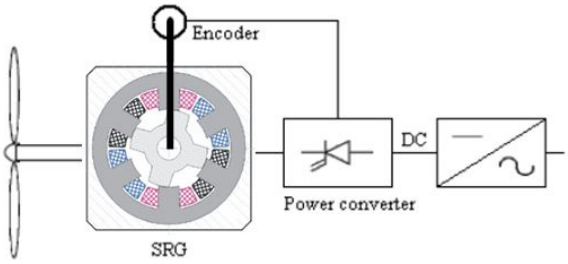

Figure 14. Schematic of a switched reluctance generator system [12].

The reluctance rotor is constructed from laminated steel sheets and has no electrical field windings or permanent magnets. As a result, the reluctance machine is simple, easy to manufacture and assembly. An obvious feature is their high reliability because they can work in

harsh or high-temperature environments. Because the reluctance torque is only a fraction of electrical torque, the rotor of switched reluctance is generally large than other with electrical excitations for a given rated torque. If reluctance machines are combined with direct drive features, the machine would be extremely large and heavy, making them less favorable in wind power applications.

5. Design Considerations and Challenges

Generally speaking, wind turbine generators can be selected from commercially available electrical machines with or without minor modifications. If a wind turbine design is required to match a specific site, some key issues should be taken into account. These include:

- Choice of machines
- Type of drive train
- Brush topology
- Rated and operating speeds
- Rated and operating torques
- Tip speed ratio
- Power and current
- Voltage regulation (synchronous generators)
- Methods of starting
- Starting current (induction generators)
- Synchronizing (synchronous generators)
- Cooling arrangement
- Power factor and reactive power compensation (induction generators)
- Power converter topology
- Weight and size
- Protection (offshore environment)
- Capital cost and maintenance.

Among these design considerations, the choice of operating speed, drive type, brush topology, and power converter are focused and further analyzed in details.

(a) Fixed or Variable Speed?

Clearly, it is beneficial to operate WTGs at variable speed. The reasons are several. When the wind speed is below rated, running the rotor speed with the wind speed and keeping the tip

http://dx.doi.org/10.5772/51780

speed ratio constant ensure that the wind turbine will extract the maximum energy. Variable speed operation helps reduce fluctuating mechanical stresses on the drive train and machine shaft, the likelihood of fatigue and damage as well as aerodynamically generated acoustic noise. The rotor can act as a regenerative storage unit (e.g. flywheel), smoothing out torque and power fluctuations prior to entering the drive train. Direct control of the air-gap torque also aids in minimizing gearbox torque fluctuations. Since there is a frequency converter between the wind turbine generator and the power grid, it becomes possible to decouple the network frequency and the rotor rotational speed. This permits variable speed operation of the rotor and controllability of air-gap torque of the machine. Furthermore, variable speed operation enables separate control of active and reactive power, as well as power factor. In theory, some wind turbine generators may be used to compensate the low power factor caused by neighboring consumers. In economic terms, variable speed wind turbine can produce 8-15% more power than fixed speed counterparts [45]. Nonetheless, the capital costs will be increased arising from the variable speed drive and power converters, as well as increased complicity and control requirements.

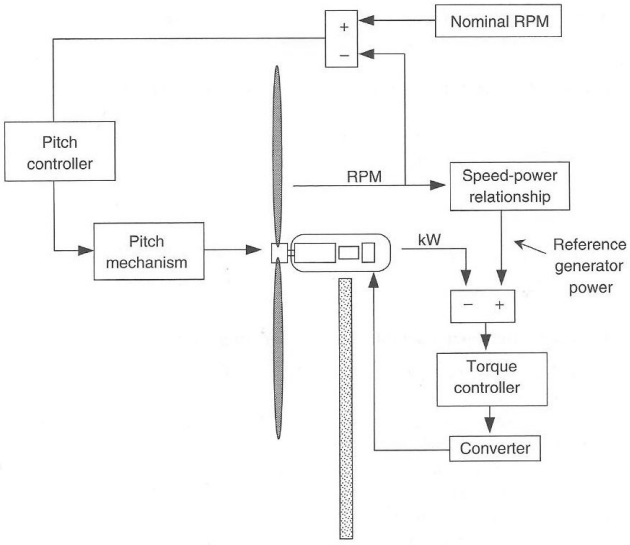

Figure 15. Variable speed control system [35].

In principle, variable speed operation can be achieved mechanically by the use of differential gearboxes or continuously-variable transmission systems [8], based on the control of speed and angular speed of gyroscopes. But the general practice is to achieve this goal by electrical means. There are two major methods in use: broad range and narrow range variable speed [8]. The former refers to a wide operational range from zero to the full rated speed where the latter refers to a narrow operational range between a fraction (up to ±50%) of synchronous speed. In reality, this latter range is practically sufficient and can saving significant

costs on power electronic converters. A closed loop speed control of such a method is demonstrated in Fig. 15.

In the design of variable-speed wind turbines, three control aspects in association with the wind speed need to consider. First, a constant optimized tip speed should be maintained to achieve maximum aerodynamic efficiency by varying the rotor speed with the actual wind speed. Second, the rotor speed should be maintained constant after the rotor has reached its rated speed but the power has not, in the case of moderate winds. When the wind speed is higher, the control is to maintain a constant rated power via the pitch angle control or stall control. Whilst using the pitch angle control, the blade pitch is varied to control the rotor speed together with the generator torque.

(b) Direct or Geared Drive?

In a geared wind turbine, the generator speed increases with the gear ratio so that the reduction in machine weight is offset by the gain in gearbox weight. For instance, the wind turbine operates at a speed of 15 rpm and the generator is designed to operate 1200 rpm (for 60 Hz) [2]. An up-speed gearbox of 1:80 is required to match the speed/torque of the turbine with these of the generator.

However, historically, gearbox failures are major challenges to the operation of wind farms. This is especially true for offshore wind turbines which are situated in harsh and less-accessible environments. Because of this, direct drive systems are increasingly desired in new wind turbine systems. One example is the excited synchronous generator with wound field rotor is a well-established design in the marketplace; and another may be a popular neodymium magnet generator design which also attracts much attention in the marketplace.

Obviously, direct drive configuration removes the necessity for gears and the related reliability problems [46]. Therefore, some wind turbine manufacturers are now moving toward direct-drive generators to improve system reliability. Since wind turbine generators are operated with power electronic converters, direct drive topology can provide some flexibility in the voltage and power requirements of the machines. Nonetheless, a drawback of the direct drive is associated with the low operating speed of the turbine generator. As the nominal speed of the machine reduces, the volume and weight of its rotor would increase approximately in inverse proportion for a given power output. This can be explained in the following equation governing the power output of any rotating electrical machine [28],

$$P = k \times (D^2 L) \times n \tag{11}$$

where k is a constant, n is the rotor rotational speed, D is the rotor diameter and L is the rotor length, in arbitrary units.

Direct drive increases the size of electrical generators which effectively offsets some of the weight savings from removing gearboxes. See Fig. 16 for a direct drive wind turbine generator, which is more than 10 times larger than its equivalent geared machine. Moreover, it typically requires the full rated power converters for grid connection. As a consequence, it is

http://dx.doi.org/10.5772/51780

always needed to strike a balance between the weight of machines and the weight of gearboxes. Hybrid systems use one or two stages of gears rather than three or four required by conventional MW generators. Sometimes, hybrid systems can offer a better compromise in terms of the overall performance of the wind turbine system.

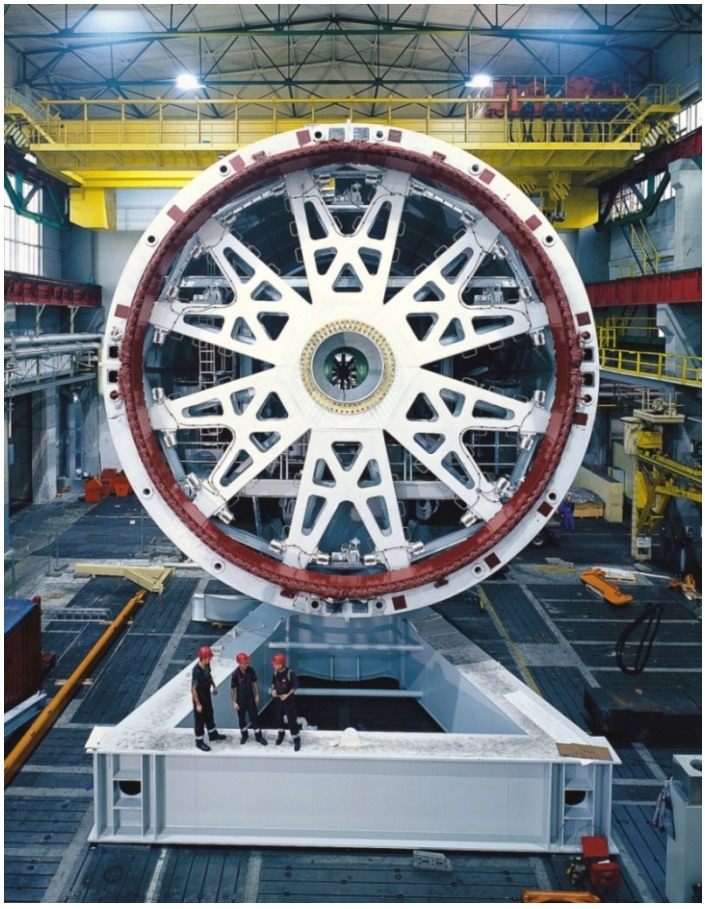

Figure 16. Example of a direct drive MW wind turbine generator.

For direct drive, the popular machine option is the PM synchronous machines. Although considerable effort and investment have been spent on improving reluctance machines [10; 15], they are still not commercially competitive to date. Direct drive brings about some design challenges on the generator and the power converters. For PM direct drive generators, they require a significant amount of costly rare-earth permanent magnets [51; 53; 44]. In addition, it needs to increase the rating of IGBTs in the back-to-back converter, or to integrate machine side converter components with the stator windings. Obviously, the advantage of

direct drive is the removal of gearbox at the expense of increased size and weight of the wind turbine generator. As a rule of thumb, the machine volume is proportional to the torque required and inversely proportional to the operational speed for a given power. The increased mass of the generator can be a limiting factor for offshore installations because the shipping carrying capacity is generally limited to 100 tons so that the direct drive generator may not be greater than 10 MW.

With the hybrid option, the generator size and speed lie in between direct and geared drives. In this case, synchronous machines are more popular than induction machines. It generally involves medium-speed, multi-pole generators which are almost exclusively permanent magnet machines. The hybrid drive train can facilitate more nacelle arrangements and match the size of the generator and gearbox.

(c) Brushed or Brushless Topology?

In general, DC machines, wound rotor synchronous generators, wound rotor induction generators all employ commutators, brushes or sliprings to access the rotating rotor circuits. Consequently, routine maintenance and replacement lead to some difficulties in wind power applications, especially for offshore installations. Clearly it would be particularly desirable to rid of any components physically connected to the rotating parts of wind turbines. There are several ways of achieving this. Taking the DFIG for example, brushless doubly-fed generators (BDFGs) can be a solution. They use two windings on the stator (a power winding and a control winding) with different pole numbers. The rotor can be of squirrel cage type and an indirect coupling of the two stator windings is established through the rotor. It is also possible to use a reluctance rotor in this topology where the machine has become a brushless reluctance generator [6, 14, 25]. By modifying the conventional machines, a higher reliability is achieved due to the absence of the brushes and slip rings. The penalty is the use of two machines in a machine case.

(d) Two-Level, Multi-Level or Matrix Converter?

Power electronics is recognized as being a key and enabling component in wind turbine systems. Broadly, there are three types of converters widely used in the wind market. These are two-level, multi-level and matrix converters.

Two level power converters are commonly called “back-to-back PWM converters”, as shown in Fig. 17(a). They include two voltage source inverters (with PWM control scheme) connected through a DC capacitor. This is a mature technology but suffers from high costs, high switching loss and large DC capacitors. Any power converters having three or more voltage levels are termed “multi-level converters”. These are illustrated in Fig. 17(b). They are particularly favored in multi-MW wind turbines since they offer better voltage and power capacity, lower switching loss and total harmonic distortion. However, the power electronic circuits are more complex and costly.

http://dx.doi.org/10.5772/51780

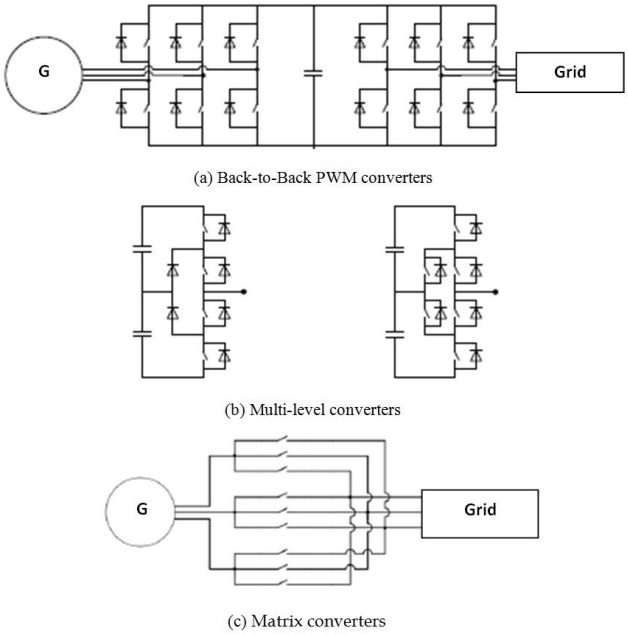

Figure 17. Three types of power converters in wind applications. (a) [21], (b) [42], (c)[5].

On the contrary, matrix converters are different in the way of AC-AC conversion. They remove the necessity of a DC stage and directly synthesize the incoming AC voltage waveform to match the required AC output. As shown in Fig. 17(c), they generally have nine power electronic switches with three in a common leg. The elimination of DC capacitors improves the reliability, size, efficiency and cost of power converters. The downsides are the limited voltage (up to 86% of the input voltage), sensitivity to grid disturbances [26], and high conducting power loss.

5. Performance Comparisons

A quantitative comparison of DFIGs, synchronous and PM generators is listed in Table 1. It can be seen that direct drive wind turbine generators are larger in size but shorter in length compared to geared counterparts. From this limited range of data, three-stage geared DFIGs appear to be lightest; conventional synchronous generators are the heaviest and the mostly costly machines.

In addition, a performance comparison of different wind turbine generators is summarized in Table 2.

Parameter	DFIG		Synchronous generators		
	1-stage geared	3-stage geared	Electro-excited direct drive	PM 1-stage geared	PM direct drive
Air-gap diameter (m)	3.6	0.84	5	3.6	5
Stack length (m)	0.6	0.75	1.2	0.4	1.2
Iron weight (ton)	8.65	4.03	32.5	4.37	18.1
Copper weight (ton)	2.72	1.21	12.6	1.33	4.3
PM weight (ton)				0.41	1.7
Generator active material cost (kEuro)	67	30	287	43	162
Gearbox cost (kEuro)	120	220		120	
Converter cost (kEuro)	40	40	120	120	120
Generator construction cost (kEuro)	60	30	160	50	150
Total generator system cost (kEuro)	287	320	567	333	432
Annual electricity yield (MWh)	7760	7690	7740	7700	7890
Yield/total cost (kWh/Euro)	4.22	4.11	3.67	4.09	3.98

Table 1. Quantitative comparison of three major wind turbine generators [38; 30].

Performance indicator	DC generators	Induction generators		Synchronous generators			
		FSIG	DFIG	Electromagnet	PM	Reluctance	HTS
Speed	variable	fixed	variable	variable	variable	variable	variable
Power supply	directly to the grid	directly to the grid	partially stator-converter	totally via converters	totally via converters	totally via converters	totally via converters
Voltage fluctuation	high	high	low	low	low	medium	very low
Converter scale	100%	0%	app. 30%	100%	100%	100%	100%
Controllability	poor	poor	good	good	good	good	very good
Active-reactive power control	no	dependent	separate	separate	separate	separate	separate
Grid-support capability	low	low	high	medium	very high	medium	high
Efficiency	low	low	high	high	very high	medium	extremely high
Reliability	poor	medium	high	high	high	very high	high

http://dx.doi.org/10.5772/51780

Performance indicator	DC generators	Induction generators		Synchronous generators			
		FSIG	DFIG	Electromagnet	PM	Reluctance	HTS
Fault response	slow	slow	high	high	high	high	very high
Cost	low	low	medium	medium	high	medium	very high
Mass saving	low	low	high	medium	very high	low	extremely high
Suitability	low power, residential application	small wind turbines	medium-large wind turbines	small-medium wind turbines	direct drive; small-medium wind turbines	early stage	large wind turbines; early stage

Table 2. Overall performance comparison of different wind turbine generators (partially, 3; 20).

6. Conclusions

Wind energy has attracted much attention from research and industrial communities. One of growth areas is thought to be in the offshore wind turbine market. The ongoing effort to develop advanced wind turbine generator technologies has already led to increased production, reliability, maintainability and cost-effectiveness. At this stage, the doubly-fed induction generator technology (equipped with fault-ride-through capacity) will continue to be prevalent in medium and large wind turbines while permanent magnet generators may be competitive in small wind turbines. Other types of wind turbine generators have started to penetrate into the wind markets to a differing degree. The analysis suggests a trend moving from fixed-speed, geared and brushed generators towards variable-speed, gearless and brushless generator technologies while still reducing system weight, cost and failure rates.

This paper has provided an overview of different wind turbine generators including DC, synchronous and asynchronous wind turbine generators with a comparison of their relative merits and disadvantages. More in-depth analysis should be carried out in the design, control and operation of the wind turbines primarily using numerical, analytical and experimental methods if wind turbine generators are to be further improved. Despite continued research and development effort, however, there are still numerous technological, environmental and economic challenges in the wind power systems.

In summary, there may not exist the best wind turbine generator technology to tick all the boxes. The choice of complex wind turbine systems is largely dictated by the capital and operational costs because the wind market is fundamentally cost-sensitive. In essence, the decision is always down to a comparison of the material costs between rare-earth permanent magnets, superconductors, copper, steel or other active materials, which may vary remarkably from time to time.

Acknowledgements

The authors gratefully acknowledge the helpful discussions with Prof G. Asher of Nottingham University and Prof B. Mecrow of Newcastle University, UK.

Author details

Wenping Cao[1], Ying Xie[2*] and Zheng Tan[1]

*Address all correspondence to: ying.xie@hust.edu.cn

1 University of Newcastle upon Tyne, United Kingdom

2 Harbin University of Science and Technology, P. R. China

References

[1] Abo-Khalil, A. G. (2011). A new wind turbine simulator using a squirrel-cage motor for wind power generation systems. *IEEE Ninth International Conference on Power Electronics and Drive Systems (PEDS)*, 750-755.

[2] Al-Majed, S. I., & Fujigaki, T. (2010). Wind power generation: An overview. *the International Symposium on Modern Electric Power Systems (MEPS)*, 1-6.

[3] Aly, H. H., & El -Hawary, M. E. (2010). An overview of offshore wind electric energy resources. *23rd Canadian Conference on Electrical and Computer Engineering CCECE*, 1-8.

[4] Bansal, R. C., Zobaa, A. F., & Saket, R. K. (2005). Some issues related to power generation using wind energy conversion systems: an overview. *Int. J. Emerging Electr . Power Syst.*, 3(2), Article 1070.

[5] Barakati, M., Kazerani, M., & Aplevich, D. (2009). Maximum power tracking control for a wind turbine system including a matrix converter". *IEEE Power & Energy Society General Meeting (PES)*, 1.

[6] Betz, R. E., & Jovanovic, M. G. (2000). The brushless doubly fed reluctance machine and the synchronous reluctance machine-a comparison. *IEEE Transactions on Industry Applications*, 36(4), 1103-1110.

[7] BTM Consult ApS. (2010). World market update 2010 forecast 2010-2014. 978-8-79918-698-3.

[8] Burton, T., Sharpe, D., Jenkins, N., & Bossanyi, E. (2001). Wind energy handbook. Wiley & Sons,, England.

[9] Caratozzolo, P., Fossas, E., Pedra, J., & Riera, J. (2000). Dynamic modeling of an isolated system with DFIG. *Eighth IEEE Int. Powe Electronics Congress Conf.*, 287-292.

[10] Cardenas, R., Pena, R., Perez, M., Clare, J., Asher, G., & Wheeler, P. (2005). Control of a switched reluctance generator for variable-speed wind energy applications. *IEEE Transactions on Energy Conversion*, 20(4), 781-791.

[11] Converteam, (2012). High Temperature Superconducting (HTS)- Converteam. online: http://www.converteam.com/converteam/1/doc/Markets/Energy_Wind/HTS_Datasheet.GB.7018.gb.10.07.01.pdf

[12] Darie, E., & Cepisca, C. (2008). The use of switched reluctance generator in wind energy applications. *13th Power Electronics and Motion Control Conference (EPE-PEMC)*, 1963-1966.

[13] Delli, Colli. V., Marignetti, F., & Attaianese, C. (2012). Analytical and multiphysics approach to the optimal design of a 10-MW DFIG for direct-drive wind turbines. *IEEE Transactions on Industrial Electronics*, 59(7), 2791-2799.

[14] Dorrell, D. G., Knight, A. M., & Betz, R. E. (2011). Improvements in brushless doubly fed reluctance generators using high-flux-density steels and selection of the correct pole numbers. *IEEE Transactions on Magnetics*, 47(10), 4092-4095.

[15] Echenique, E., Dixon, J., Cardenas, R., & Pena, R. (2009). Sensorless control for a switched reluctance wind generator, based on current slopes and neural networks. *IEEE Transactions on Industrial Electronics*, 56(3), 817-825.

[16] Gao, G., & Chen, W. (2009, May-June). Design challenges of wind turbine generators. Montreal, Canada. *IEEE Electrical Insulation Conference (EIC)*, 146-152.

[17] Gipe, P. (1995). Wind energy comes of age. Wiley & Sons, USA.

[18] Google image. (2012). Magnetic generators. online:, http://www.google.co.uk/imgres?imgurl=http://magneticgeneratordiy.com/wp-content/uploads/2012/02/permanent-magnet-generator.jpg&imgrefurl=http://magneticgeneratordiy.com/permanent-magnet-generator/&h=426&w=500&sz=52&tbnid=px5NXzuFFZ_FWM:&tbnh=111&tbnw=130&prev=/search%3Fq%3Dpermanent%2Bmagnet%2Bwind%2Bturbine%2Bpicture%26tbm%3Disch%26tbo%3Du&zoom=1&q=permanent+magnet+wind+turbine+picture&usg=__SExjmg6ut-F14p2DVEB6Rkyz70Q=&hl=en&sa=X&ei=EnnoT4_xEOOi0QWPmdSjCQ&ved=0CBYQ9QEwAg.

[19] Guo, J., Yu, X., Wu, T., Chang, X., Li, S., Liu, H., & Sun, Y. (2010). Simulation and experimental analysis of grid-connected doubly-fed induction generators. *International Conference on Electrical and Control Engineering (ICECE)*, 5583-5586.

[20] Hansen, L. H., Helle, L., Blaabjerg, F., Ritchie, E., Munk-Nielsen, S., Bindner, H., Sørensen, P., & Bak-Jensen, B. (2001). Conceptual survey of generators and power electronics for wind turbines. online: http://www.risoe.dk/rispubl/vea/veapdf/risr-1205.pdf

[21] Hansen, L.H, Madsen, P.H, Blaabjerg, F, Christensen, H.C, Lindhard, U, & Eskildsen, K. (2001). Generators and power electronics technology for wind turbines. *The 27th Annual Conference of the IEEE Industrial Electronics Society*, 3, 2000-2005.

[22] Heier, S. (1996). Wind energy conversion systems. Wiley & Sons, England

[23] Hunter, R., & Elliot, G. (1994). Wind-diesel dystems: a guide to the technlogy and its implementation. Cambridge University Press, Cambridge

[24] Jamieson, P. (2011). Innovation in wind turbine design. Wiley, England

[25] Jovanovic, M. (2009). Sensored and sensorless speed control methods for brushless doubly fed reluctance motors. *IET Electric Power Applications*, 3(6), 503-513.

[26] Kim, H. S., & Lu, D. D. C. (2010). Review on wind turbine generators and power electronic converters with the grid-connection issues. *20th Australasian Universities Power Engineering Conference (AUPEC)*, 1-6.

[27] Kim, N., Kim, G. H., Kim, K. M., Park, M., Yu, I. K., Lee, S., Song, E., & Kim, T. W. (2012). Comparative analysis of 10 MW class geared and gearless type superconducting synchronous generators for a wind power generation system. *IEEE Transactions on Applied Superconductivity*, 22(3), 5202004.

[28] Laithwaite, E. R., & Freris, L. L. (1980). Electrical power: its generation, transmission and use. McGraw-Hill,, Maidenhead, UK.

[29] Li, H., & Chen, Z. (2008, October). Design optimization and evaluation of different wind generator systems. Wuhan, China. *International Conference on Electrical Machines and Systems (ICEMS)*, 2396-2401.

[30] Li, H., & Chen, Z. (2008). Overview of different wind generator systems and their comparisons. *IET Renewable Power Generation*, 2(2), 123-138.

[31] Li, X., Zhou, y., Han, l., Zhang, D., Zhang, J., Qiu, Q., Dai, S., Zhang, Z., Xia, D., Zhang, g., Lin, L., Xiao, l., Zhu, S., Bai, H., Bian, B., Li, S., & Gao, W. (2011). Design of a high temperature superconducting generator for wind power applications. *IEEE Transactions on Applied Superconductivity Part: 2*, 21(3), 1155-11580.

[32] Liserre, M., Cardenas, R., Molinas, M., & Rodriguez, J. (2011). Overview of multi-MW wind turbines and wind parks. *IEEE Transactions Industrial Electronics,*, 58(4), 1081-1095.

[33] Ma, H, Chen, L, Ju, P, Liu, H, Jiang, N, & Wang, C. (2009, April). Feasibility research on DC generator based wind power generation system. *International Conference on Sustainable Power Generation and Supply (SUPERGEN)*, 1-5.

[34] Madawala, U. K., Geyer, T., Bradshaw, J. B., & Vilathgamuwa, D. M. (2012). Modeling and analysis of a novel variable-speed cage induction generator. *IEEE Transactions on Industrial Electronics*, 59(2), 1020-1028.

[35] Manwell, J. F., Mc Gowan, J. G., & Rogers, A. L. (2009). Wind energy explained: theroy, design and application. *2nd edition, Wiley, England*.

[36] NTNU, (2012). Renewable energy. Materials, online http://www. ntnu.no

[37] Polinder, H. (2011). Overview and trends in wind turbine generator systems",. *IEEE Power and Energy Society General Meeting*, 1-8.

[38] Polinder, H., van der Pijl, F. F. A., de Vilder, G. J., & Tavner, P. J. (2006). Comparison of direct-drive and geared generator concepts for wind turbines. *IEEE Transactions on Energy Conversion*, 21(3), 725-733.

[39] Potgieter, J. H. J., & Kamper, M. J. (2012). Design of new concept direct grid-connected slip-synchronous permanent-magnet wind generator. *IEEE Transactions on Industry Applications*, 48(3), 913-922.

[40] Quinonez-Varela, G., & Cruden, A. (2008). Modelling and validation of a squirrel cage induction generator wind turbine during connection to the local grid. *IET Generation, Transmission & Distribution,*, 2(2), 301-309.

[41] Rechesteiner, R. (2008). Wind power in context- A clean revolution in the energy sector. online, http://www.energywatchgroup.org/fileadmin/global/pdf/2009-01_Wind_Power_Report.pdf.

[42] Rodriguez, J, Bernet, S, Steimer, P.K, & Lizama, I.E. (2010). A survey on neutral-point-clamped inverters. *IEEE Transactions on Industrial Electronics*, 57(7), 2219-2230.

[43] Ruviaro, M., Runcos, F., Sadowski, N., & Borges, I. M. (2012). Analysis and test results of a brushless doubly fed induction machine with rotary transformer. *IEEE Transactions on Industrial Electronics*, 59(6), 2670-2677.

[44] Semken, R. S., Polikarpova, M., Roytta, P., Alexandrova, J., Pyrhonen, J., Nerg, J., Mikkola, A., & Backman, J. (2012). Direct-drive permanent magnet generators for high-power wind turbines: benefits and limiting factors. *IET Renewable Power Generation*, 6(1), 1-8.

[45] Shanker, T., & Singh, R. K. (2012). Wind energy conversion system: A review. *Students Conference on Engineering and Systems (SCES)*, 1-6.

[46] Shrestha, G., Polinder, H., Bang, D., & Ferreira, J. A. (2010). Structural flexibility: A solution for weight reduction of large direct-drive wind-turbine generators. *IEEE Transactions on Energy Conversion*, 25(3), 732-740.

[47] Suzuki, T., Okitsu, H., & Kawahito, T. (1982). Characteristics of a small wind-power system with dc generator. *IEE Proceedings Electric Power Applications B*, 129(4), 217-220.

[48] Tazil, M., Kumar, V., Bansal, R. C., Kong, S., Dong, Z. Y., Freitas, W., & Mathur, H. D. (2010). Three-phase doubly fed induction generators: an overview. *IET Electric Power Applications*, 4(2), 75-89.

[49] Terao, Y., Sekino, M., & Ohsaki, H. (2012). Electromagnetic design of 10 MW class fully superconducting wind turbine generators. *IEEE Transactions on Applied Superconductivity*, 22(3), 5201904.

[50] Wavege,. (2012). Wind turbine diagram. online:, http://www.google.co.uk/imgres?imgurl=http://www.wavege.com/assets/wind-turbine-diagram-nacelle.jpg&imgrefurl=http://www.wavege.com/wind-turbine-diagram.html&h=266&w=550&sz=22&tbnid=pCbFxrdGh1NQ9M:&tbnh=64&tbnw=133&prev=/search%3Fq%3Dinside%2Ba%2Bwind%2Bturbine%2Bdiagram%26tbm%3Disch%26tbo%3Du&zoom=1&q=inside+a+wind+turbine+diagram&usg=__C8M6im4YQyvtKK1zA-LYF__YLYVs=&hl=en&sa=X&ei=h8jlT8KcCYXc8gOp1sWjCg&ved=0CBoQ9QEwBA.

[51] Westlake, A. J. G., Bumby, J. R., & Spooner, E. (1996). Damping the power-angle oscillations of a permanent-magnet synchronous generator with particular reference to wind turbine applications. *IEE Proceedings Electric Power Applications*, 143(3), 269-280.

[52] Woodcroft, B. (1851). Translation from the Greek "Pneumatics". Taylor Walton & Maberly, London

[53] Ying, F., Chau, K. T., & Ming, C. (2006). A new three-phase doubly salient permanent magnet machine for wind power generation. *IEEE Transactions on Industry Applications*, 42(1), 53-60.

[54] Zhang, M., Wang, W., Chen, Y. R., & Coombs, T. (2012). Design methodology of HTS bulk machine for direct-driven wind generation. *IEEE Transactions on Applied Superconductivity*, 22(3), 5201804.

[55] Zhang, Z., Yan, Y., & Tao, Y. (2012). A new topology of low speed doubly salient brushless DC generator for wind power generation. *IEEE Transactions on Magnetics*, 48(3), 1227-1233.

Chapter 8

A Model for Dynamic Optimization of Pitch-Regulated Wind Turbines with Application

Karam Y. Maalawi

Additional information is available at the end of the chapter

http://dx.doi.org/10.5772/53347

1. Introduction

With the growing demand for cost-effective wind energy, optimization of wind turbine components has been gaining increasing attention for its acknowledged contributions made to design enhancement, especially in early stages of product development. One of the major design goals is the accurate determination of structural dynamics and control, which is directly related to fatigue life and cost of energy production: a major design goal in exploiting wind energy. Modern wind turbines are designed with pitch-regulated rotor blades, which have to be able to turn around their longitudinal axis several times per second in order to face the rapidly changing wind direction. This fact emphasizes the need to improve the design of pitch mechanisms using optimization techniques in order to increase availability of the turbines and reduce their maintenance overheads. (Florin et al., 2004; Jason et al. 2005) demonstrated the different tools for performing the analysis of the interaction between the mechanical system of the wind turbine and the electrical grid as well as the calculation of the dynamic loads on the turbine structure. In case of stronger winds it is necessary to waste part of the excess energy of the wind in order to avoid damaging the wind turbine. All wind turbines are therefore designed with some sort of power control. There are different ways of doing this safely on modern wind turbines: pitch, active stall and passive stall controlled wind turbines.

On a pitch controlled wind turbine (Hansen et al., 2005) the turbine's electronic controller checks the power output of the turbine several times per second. When the power output becomes too high, it sends an order to the blade pitch mechanism which immediately pitches (turns) the rotor blades slightly out of the wind. Conversely, the blades are turned back into the wind whenever the wind drops again. The rotor blades thus have to be able to turn around their longitudinal axis (to pitch) as shown in Fig. 1. The pitch mechanism

is usually operated using hydraulics or electric stepper motors. Fig. 2 shows the optimal operational conditions of a pitch-controlled 2 MW wind turbine. During normal operation the blades will pitch a fraction of a degree at a time, and the rotor will be turning at the same time. The computer will generally pitch the blades a few degrees every time the wind changes in order to keep the rotor blades at the optimum angle to maximize output power for all wind speeds.

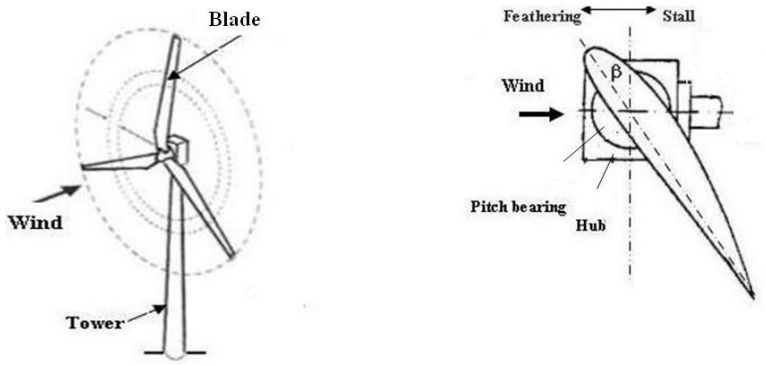

Figure 1. Limiting power output using pitch control.

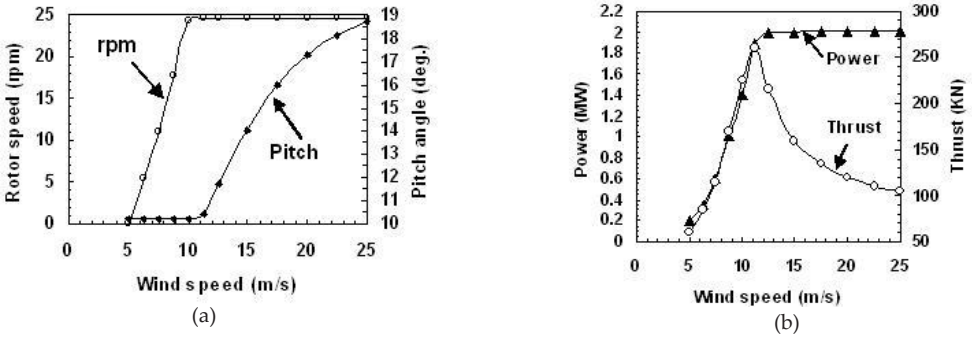

Figure 2. Operational conditions of a pitch-controlled, 2.0 MW wind turbine (Hansen et al., 2005)

On the other hand, passive stall controlled wind turbines (Leithed & Conner, 2002; Hoffmann, 2002) have the rotor blades bolted onto the hub at a fixed angle. The geometry of the rotor blade profile however has been aerodynamically designed to ensure that

http://dx.doi.org/10.5772/53347

the moment the wind speed becomes too high; it creates turbulence on the side of the rotor blade which is not facing the wind. This stall prevents the lifting force of the rotor blade from acting on the rotor. The rotor blade of a stall controlled wind turbine is twisted slightly along its longitudinal axis. This is partly done in order to ensure that the rotor blade stalls gradually rather than abruptly when the wind speed reaches its critical value. The basic advantage of stall control is that one avoids moving parts in the rotor itself, and a complex control system. On the other hand, stall control represents a very complex aerodynamic design problem, and related design challenges in the structural dynamics of the whole wind turbine, e.g. to avoid stall-induced vibrations. Around two thirds of the wind turbines currently being installed in the world are stall controlled machines.

Larger wind turbines (1-MW and up) are being developed with an active stall power control mechanism (Hoffmann, 2002). Technically the active stall machines resemble pitch controlled machines, since they have pitchable blades. In order to get a reasonably large torque at low wind speeds, the machines will usually be programmed to pitch their blades much like a pitch controlled machine at low wind speeds. One of the advantages of active stall is that one can control the power output more accurately than with passive stall, so as to avoid overshooting the rated power of the machine at the beginning of a gust of wind. Another advantage is that the machine can be run almost exactly at rated power at all high wind speeds. A normal passive stall controlled wind turbine will usually have a drop in the electrical power output for higher wind speeds, as the rotor blades go into deeper stall. As with pitch control it is largely an economic question whether it is worthwhile to pay for the added complexity of the machine, when the blade pitch mechanism is added. One of the most cost-effective solutions in reducing the produced vibrations and avoiding pitch-control failures on wind turbines (see Fig.3) is to separate the natural frequencies of the blade structure from the critical exciting pitching frequencies (Bindner et al., 1997). This would avoid resonance where large amplitudes of torsional vibration could severely damage the whole structure. The frequency-placement technique (Pritchard & Adelman, 1990; Maalawi, 2007; Maalawi & Badr, 2010) is based on minimizing an objective function constructed from a weighted sum of the squares of the differences between each important frequency and its desired (target) value. Approximate values of the target frequencies are usually chosen to be within close ranges; sometimes called frequency-windows; of those corresponding to a reference baseline design, which are adjusted to be far away from the critical exciting frequencies. Direct maximization of the system natural frequencies (Shin et al., 1988; Maalawi & EL-Chazly, 2002) is also favorable for increasing the overall stiffness-to-mass ratio level of the blade structure being excited. This may further other design objectives such as higher stability and fatigue life and lower cost and noise levels. (Maalawi & Negm 2002) considered the optimal frequency design of a wind turbine blade in flapping motion. They used an exact power series solution to determine the exact mode shapes and the aeroelastic stability boundaries, where conspicuous design trends were given for optimum blade configurations. Both primal and dual optimization problems were thoroughly examined.

Figure 3. Typical blade failure of a three-bladed, 2 MW wind turbine

The scope of this chapter is not just to apply optimization techniques and find an optimum solution for the problem under study. The main aim, however, is to first; perform the necessary exact dynamical analysis of a pitch-regulated wind turbine blade by solving the exact governing differential equation using analytical Bessel's functions. Secondly, the behavior of the pitching fundamental frequency augmented with the mass equality constraint will be investigated in detail to see how it changes with the selected design variables. The associated optimization problem is formulated by considering two forms of the objective function. The first one is represented by a direct maximization of the fundamental frequency, while the second considers minimization of the square of the difference between the fundamental frequency and its target or desired value. In both strategies, an equality constraint is imposed on the total structural mass in order not to violate other economic and performance requirements. Design variables encompass the tapering ratio, blade chord and skin thickness distributions, which are expressed in dimensionless form, making the formulation valid for a variety of blade configurations. The torsional stiffness simulating the flexibility of the inboard panel near the rotor hub is also included in the whole set of design variables. Case studies include the locked and unlocked conditions of the pitching mechanism, in which the functional behavior of the frequency has been thoroughly examined. The developed exact mathematical model guarantees full separation of the frequency from the undesired range which resonates with the pitching frequencies. In fact, the mathematical procedure implemented, combined with exact Bessel's function solutions, can be beneficial tool, against which the efficiency of approximate methods, such as finite elements, may be judged. Finally, it is demonstrated that global optimality can be

http://dx.doi.org/10.5772/53347

achieved from the proposed model and an accurate method for the exact placement of the system natural frequencies has been deduced.

2. Structural dynamic analysis

The isolated blade structure to be analyzed herein is illustrated in figure 4. The inboard panel having ignored length relative to the outboard one is considered as a flexible segment modeled by an equivalent torsion spring. The blade has a polar moment of area I spinning about its longitudinal axis, x, at an angular displacement $B(x,t)$ relative to the pitch bearing at the rotor hub. The blade is analyzed considering the state of free torsional vibration about its elastic axis. The pitching mechanism and the short segment near the hub are assumed to have a linear torsional spring with stiffness K_s. Applying the classical theory of torsion (Rao, 1994), the governing equation of the motion is cast in the following:

$$\frac{\partial}{\partial x}[GJ(x)\frac{\partial B(x,\,t)}{\partial x}]=\rho I(x)\frac{\partial^2 B(x,\,t)}{\partial t^2} \tag{1}$$

which must be satisfied over the interval $0<x<L$.

The associated boundary conditions are described as follows:

Case (I): Pitch is active

$$\begin{aligned} &\text{at blade root (x=0)} GJ\frac{\partial B}{\partial x}\Big|_{x=0} = 0 && \text{a}\\ &\text{at blade tip (x=L)} GJ\frac{\partial B}{\partial x}\Big|_{x=L} = 0. && \text{b} \end{aligned} \tag{2}$$

Case (II): Pitch is inactive

$$\begin{aligned} &\text{at blade root (x=0)} GJ\frac{\partial B}{\partial x}\Big|_{x=0} = K_s B(0,\,t) && \text{a}\\ &\text{at blade tip (x=L)}|_{x=L} = 0 && \text{b} \end{aligned} \tag{3}$$

where $GJ(x)$ and $\rho I(x)$ represent the torsional stiffness and the mass polar moment of inertia per unit length, respectively. The twisting angle $B(x,t)$ is assumed to be separable in space and time, $B(x,\,t)=\beta(x).q(t)$, where the time dependence $q(t)$ is harmonic with circular frequency ω. Substituting for $\frac{d^2q}{dt^2}=-\omega^2 q$, the associated eigenvalue problem can be written directly in the form

$$\frac{d}{dx}[GJ(x)\frac{d\beta}{dx}]+\rho I(x)\omega^2\beta(x)=0 \tag{4}$$

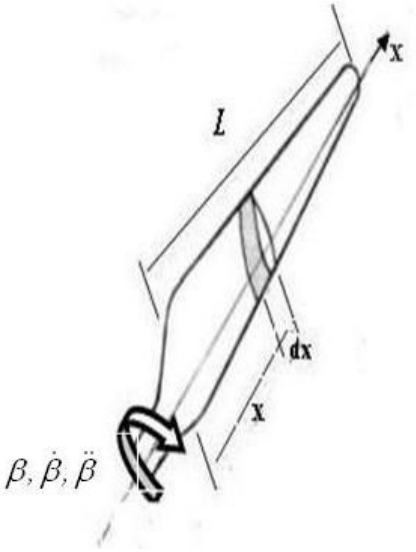

Figure 4. Isolated blade in pitching motion.

The boundary conditions can be obtained from Eqs. (2) and (3). Considering a tapered blade with thin-walled airfoil section (refer to Figures1 & 4), the torsional constant and the second polar moment of area are directly proportional to h and C^3, which are assumed to have the same linear distribution described by the expressions:

$$\begin{aligned} C &= C_o(1-\alpha\hat{x}) \qquad \text{a} \\ h &= h_o(1-\alpha\hat{x}) \qquad \text{b} \end{aligned} \tag{5}$$

$\hat{x}$ and α are dimensionless parameters defined as:

$$\hat{x} = \frac{x}{L},\ \alpha = (1-\Delta),\ \Delta = C_t \Big/ C_0 \tag{6}$$

where Δ is the taper ratio of the wind turbine blade.

3. Solution procedures

For thin-walled, cellular blade construction, the total structural mass M, the torsional constant $J(x)$, and the polar moment of area I(x) can be determined from the expressions:

http://dx.doi.org/10.5772/53347

$$M = f_1 \int_0^L Ch(x)dx \quad \text{a}$$
$$J(x) = f_2 C^3 h(x) \quad \text{b} \tag{7}$$
$$I(x) = f_3 C^3 h(x) \quad \text{c}$$

where f_1, f_2 and f_3 are shape factors depend upon the shape of the airfoil section, number of interior cells and the ratios between the shear web thicknesses and the main wall thickness $h(x)$. It is convenient first to normalize all variables and parameters with respect to a reference design having uniform stiffness and mass distributions with the same material properties, airfoil section, and type of construction as well (see Table 1). The dimensionless expressions for the total mass, torsional constant and polar moment of area are, respectively given by:

$$\text{Mass} \quad \hat{M} = \int_0^1 \hat{C}\hat{h}\, d\hat{x} \quad \text{a}$$
$$\text{Torsion constant} \quad \hat{J} = \hat{C}^3\hat{h} \quad \text{b} \tag{8}$$
$$\text{Polar moment of area} \quad \hat{I} = \hat{C}^3\hat{h} \quad \text{c}$$

Therefore, dividing by the corresponding reference design parameters, the governing differential equation takes the following dimensionless form:

$$\beta'' - \frac{4\alpha}{(1-\alpha\hat{x})}\beta' + \hat{\omega}^2\beta = 0; \quad 0 \le \le 1 \tag{9}$$

Quantity	Notation	Dimensionless expression
Circular frequency	ω	$\hat{\omega} = \omega L\sqrt{\rho I_r / GJ_r}$
Spatial coordinate	x	$\hat{x} = x/L$
Airfoil chord	C	$\hat{C} = C / C_r$
Shear wall thickness	h	$\hat{h} = h / h_r$
Structural mass	M	$\hat{M} = M / M_r$
Torsion constant	J	$\hat{J} = J / J_r \, (= \hat{C}^3\hat{h})$
Polar moment of area.	I	$\hat{I} = I / I_r \, (= \hat{C}^3\hat{h})$
Stiffness coefficient at root	K_s	$\hat{K}_s = \frac{K_s}{(GJ_r / L)}$

Reference parameters: M_r=structural mass, J_r= torsion constant, I_r=2nd polar moment of area, where C_r=Chord length, h_r=wall thickness, blade taper $\Delta=1$.

Table 1. Definition of dimensionless quantities

The boundary conditions to be satisfied are $\beta' = 0$ at both blade root and tip for the unlocked pitching condition and $\beta' = (\frac{\hat{K}_s}{\hat{J}_0})\beta$ at root, $\beta' = 0$ at tip for the locked condition, where the prime denotes here differentiation with respect to $\hat{x}$. Using the transformation $\hat{x} = \frac{1}{\alpha} - \frac{1}{\hat{\omega}} y$ ($\alpha \neq 0$), Eq. (9) takes the form:

$$\frac{d^2\beta}{dy^2} + \frac{4}{y}\frac{d\beta}{dy} + \beta = 0; \quad \delta \le y \le \gamma \tag{10}$$

which can be further transformed to the standard form of Bessel's equation by setting $\beta = \psi / \sqrt{y^3}$, to get

$$y^2 \frac{d^2\psi}{dy^2} + y\frac{d\psi}{dy} + (y^2 - \frac{9}{4})\psi = 0 \tag{11}$$

This has the solution

$$\psi(y) = C_1 J_{3/2} + C_2 J_{-3/2} \tag{12}$$

where C_1 and C_2 are constants of integration and $J_{3/2}$ and $J_{-3/2}$ are Bessel's functions of order $k = \pm 3/2$, given by (Edwards & Penney, 2004):

$$\begin{aligned} J_{3/2}(y) &= \sqrt{\frac{2}{\pi y^3}}(\sin y - y\cos y) && \text{a} \\ J_{-3/2}(y) &= -\sqrt{\frac{2}{\pi y^3}}(\cos y + y\sin y) && \text{b} \end{aligned} \tag{13}$$

The exact analytical solution of the associated eigenvalue problem is:

$$\beta(y) = A[\frac{y\cos y - \sin y}{y^3}] + B[\frac{y\sin y + \cos y}{y^3}] \tag{14}$$

where A and B are constants depend on the imposed boundary conditions. Applying the boundary conditions, given in Eqs. (2) and (3), and considering only nontrivial solution the frequency equation can be directly obtained. The final derived exact frequency equations for both active and inactive pitching motion in appropriate compacted closed forms are summarized in the following:

Baseline design with rectangular planform (D=1) $\hat{\omega}\tan\hat{\omega} = \hat{K}_s / (\hat{h}_o \hat{C}_o^3)$ (15)

http://dx.doi.org/10.5772/53347

$$\text{Active pitching } \tan\hat{\omega} = \frac{3\hat{\omega}(3+\gamma\delta)}{(\gamma\delta)^2 - 3\gamma^2(1+\Delta^2) + 9(1+\gamma\delta)} \tag{16}$$

$$\text{Locked pitching mechanism } \tan\hat{\omega} = \frac{(1-3\theta)(3\hat{\omega} - \gamma\delta^2) - 3\gamma^2\delta\theta}{3\gamma\delta(1-3\theta) + (3-\delta^2)(1-3\theta+\theta\gamma^2)} \tag{17}$$

The definition of the various quantities in Eqs. (15), (16) and (17) is given in Table (1) and the appendix of nomenclature.

4. Optimization problem formulation

Attractive goals of designing efficient structures of wind generators include minimization of structural weight, maximization of the fundamental frequencies (Maalawi & EL-Chazly, 2002; Maalawi & Negm, 2002; Maalawi & Badr, 2010), minimization of total cost per energy produced, and maximization of output power (Maalawi & Badr, 2003). Another important consideration is the reduction or control of the vibration level. Vibration can greatly influence the commercial acceptance of a wind turbine because of its adverse effects on performance, cost, stability, fatigue life and noise. The reduction of vibration can be attained either by a direct maximization of the natural frequencies or by separating the natural frequencies of the blade structure from the harmonics of the exciting torque applied from the pitching mechanism at the hub. This would avoid resonance and large amplitudes of vibration, which may cause severe damage of the blade. Direct maximization of the natural frequencies can ensure a simultaneous balanced improvement in both of the overall stiffness level and the total structural mass. The mass and stiffness distributions are to be tailored in such a way to maximize the overall stiffness/mass ratio of the vibrating blade. The associated optimization problems are usually cast in nonlinear mathematical programming form (Vanderplaats, 1999). The objective is to minimize a function $F(\underline{X})$ of a vector $\underline{X}$ of design variables, subject to certain number of constraints $G_j(\underline{X}) \le 0$, $j=1,2,\ldots m$.

In the present optimization problem, two alternatives of the objective function form are implemented and examined. The first one is represented by a direct maximization of the fundamental frequency, which is expressed mathematically as follows:

$$\text{Maximize } F(\underline{X}) = -\hat{\omega}_1 \tag{18}$$

where $\hat{\omega}_1$ is the normalized fundamental frequency (see Table1) and $\underline{X} = (\hat{C}_o, \hat{h}_o, \Delta)$ is the chosen design variable vector. The second alternative is to minimize the square of the difference between the fundamental frequency $\hat{\omega}_1$ and its target or desired value $\hat{\omega}^*$, i.e.

$$\text{Minimize } F(\underline{X}) = (\hat{\omega} - \hat{\omega}^*)^2 \tag{19}$$

Both objectives are subject to the constraints:

$$\text{Mass constraint: } \hat{M} = \int_0^1 \hat{C}\,\hat{h}\; d\hat{x} = 1 \tag{20}$$

$$\text{Side constraints: } \underline{X}_L \le \underline{X} \le \underline{X}_u \tag{21}$$

where $\underline{X}_L$ and $\underline{X}_U$ are the lower and upper limiting values imposed on the design variables vector $\underline{X}$ in order not to obtain unrealistic odd-shaped designs in the final optimum solutions. Approximate values of the target frequencies are usually chosen to be within close ranges; sometimes called frequency – windows; of those corresponding to an initial baseline design, which are adjusted to be far away from the critical exciting pitching frequencies. Several computer program packages are available now for solving the above design optimization model, which can be coded to interact with structural and eigenvalue analyses software. Extensive computer implementation of the models described by Eqs. (18-21) have revealed the fact that maximization of the fundamental frequency is a much better design criterion. If it happened that the maximum frequency violates frequency windows, which was found to be a rare situation, another value of the frequency can be chosen near the global optima, and the frequency equations (15-17) can be solved for any one of the unknown design variables instead. Considering the frequency-placement criterion, it was found that convergence towards the optimum solution, which is also too sensitive to the selected target frequency, is very slow.

5. Optimization techniques

The above optimization problem described by Eqs.(18-21) may be thought of as a search in an 3-dimensional space for a point corresponding to the minimum value of the objective function and such that it lie within the region bounded by the subspaces representing the constraint functions. Iterative techniques are usually used for solving such optimization problems in which a series of directed design changes (moves) are made between successive points in the design space. The new design $\underline{X}_{i+1}$ is obtained from the old one $\underline{X}_i$ as follows:

$$\underline{X}_{i+1} = \underline{X}_i + a_i \underline{S}_i \tag{22}$$

$$\text{Such that } F(X_{i+1}) < F(X_i) \tag{23}$$

where the vector $\underline{S}_i$ defines the direction of the move and the scalar quantity α_i gives the step length such that $\underline{X}_{i+1}$ does not violate the imposed constraints, $G_j(X)$. Several optimization techniques are classified according to the way of selecting the search direction $\underline{S}_i$. In general, there are two distinct formulations (Vanderplaats, 1999): the constrained formulation and the unconstrained formulation. In the former, the constraints are considered as a limiting

http://dx.doi.org/10.5772/53347

subspace. The method of feasible directions is one of the most powerful methods in this category. In the unconstrained formulation, the constraints are taken into account indirectly by transforming the original problem into a series of unconstrained problems. A method, which has a wide applicability in engineering applications, is the penalty function method.

The *MATLAB* optimization toolbox is a powerful tool that includes many routines for different types of optimization encompassing both unconstrained and constrained minimization algorithms (Vekataraman, 2009). One of its useful routines is named *"fmincon"* which implements the method of feasible directions in finding the constrained minimum of an objective function of several variables starting at an initial design. The search direction $\underline{S}_j$ must satisfy the two conditions $\underline{S}_j.\nabla F < 0$ and $\underline{S}_j.\underline{\nabla} G_j < 0$, where $\underline{\nabla} F$ and $\underline{\nabla} G_j$ are the gradient vectors of the objective and constraint functions, respectively. For checking the constrained minima, the Kuhn-Tucker test (Vanderplaats, 1999) is applied at the design point $\underline{X}_D$, which lies on one or more set of active constraints. The Kuhn-Tucker equations are necessary conditions for optimality for a constrained optimization problem and their solution forms the basis to the method of feasible directions.

6. Results and discussions

The developed mathematical model has been implemented for the proper placement of the frequencies of typical blade structure in free pitching motion. Optimum solutions are obtained by invoking the *MATLAB* routine *"fmincon"* which interacts with the eigenvalue calculation routines. The target frequencies, at which the pitching frequencies needed to be close to, depend on the specific configuration and operating conditions of the wind machine. Various cases of study are examined including, blades with both locked and unlocked pitching conditions. The main features and trends in each case are presented and discussed in the following sections.

6.1. Unlocked pitching mechanism condition

Considering first the case of active pitching, figure 5 shows the variation of the first three resonant frequencies with the tapering ratio. It is seen that the frequencies decrease with increasing taper. Blades having complete triangular planforms shall have the maximum frequencies which is favorable from structural design point of view. However, such configurations violate the requirement of having an efficient aerodynamic surface producing the needed mechanical power. Now, in order to place any frequency at its desired value $\hat{\omega}_i^*$, *i=1,2,3,* the first step is to calculate the dimensionless frequency $\hat{\omega}_i$, *i=1,2,3,* for known properties of the blade material and airfoil section, and then obtain the corresponding value of the taper ratio from the curves presented in figure 5. The next step is to choose appropriate value for the dimensionless thickness $\hat{h}_o$ at the blade root and find the corresponding chord length $\hat{C}_o$ at the determined taper ratio (see figure 6), which should satisfy the equality mass constraint expressed by Eq. (20). It is to be noticed here that the dimensionless wall thickness $\hat{h}_o$ at root shall be constrained to be greater than a preassigned lower bound,

which can either be determined from the minimum available sheet thicknesses or from considerations of wall instability that might happen by local buckling.

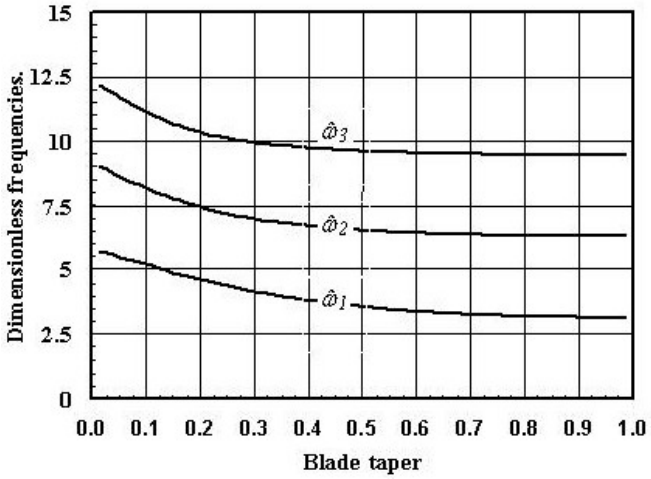

Figure 5. Normalized frequencies of free pitching motion (Unlocked blade)

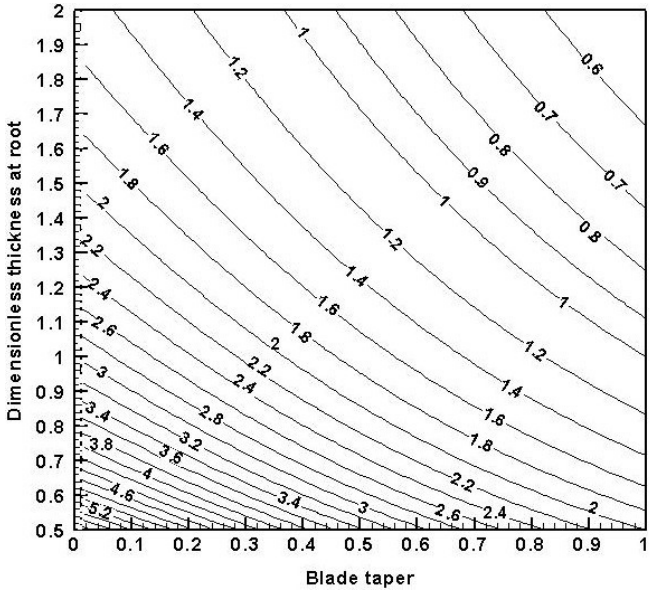

Figure 6. Optimized tapered blades with constant mass ($\hat{C}_o$- Level curves, $\hat{M}$=1)

http://dx.doi.org/10.5772/53347

6.2. Condition of locked pitching mechanism

Extensive computer solutions for the frequency equation (17) have indicated the existence of the frequency level curves in the selected design space. Figures 7, 8 and 9 depicts, respectively, the developed frequency charts for the design cases of locked pitching mechanism with $\hat{K}_s$= *10, 100 and 1000* representing flexible, semi-rigid and rigid blade root. Any other specific case can be easily obtained by following and applying the same procedures outlined before in sections 3 and 4. It is seen from the figures that the frequency function is well behaved and continuous in the selected design space $(\hat{h}_o, \hat{C}_o)$. Actually, these charts represent the fundamental pitching frequency augmented with the equality mass constraint. Therefore, they reveal very clearly how one can place the frequency at its target value without the penalty of increasing the total mass of the main blade structure. Such charts also can be utilized if one is seeking to maximize the frequency under equality mass constraint. Maximization of the natural frequencies has the benefit of improving the overall stiffness/mass ratio of the vibrating structure (Maalawi and Negm, 2002).

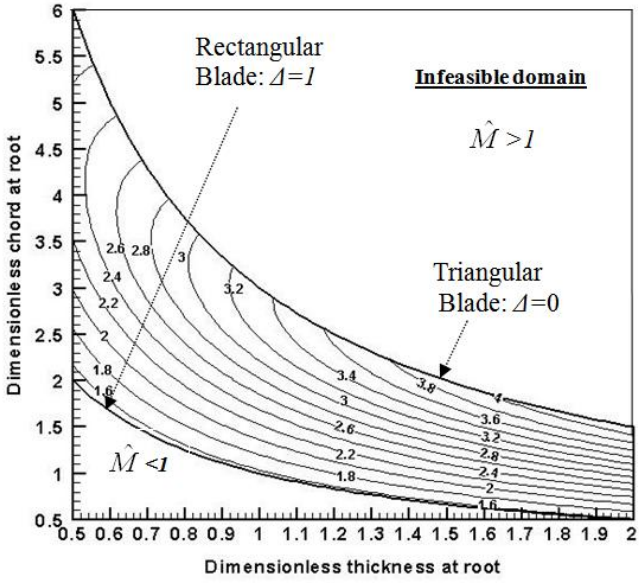

Figure 7. Augmented frequency-mass contours ($\hat{\omega}_1$) for a blade with flexible blade root: $\hat{K}_s$ = 10 ($\hat{M}$ =1)

As seen, the developed contours depicted in figure 7 has a banana- shaped profile bounded by two curved lines; the one from above represents a triangular blade (Δ=*0*) and the other

lower one represents a rectangular blade geometry ($\Delta=1$). It is not allowed to penetrate these two borderlines in order not to violate the imposed mass equality constraints. Each point inside the feasible domain in the middle corresponds to different mass and stiffness distributions along the blade span, but the total structural mass is preserved at a constant value equals to that of the rectangular reference blade. The lower and upper empty regions represent, respectively, infeasible blade designs with structural mass less or greater than that of the baseline design. The global optimal design is too close to the design point $\{\hat{C}_o, \hat{h}_o \Delta\}=\{1.202, 2.011, 0.207\}$ with $\hat{\omega}_{1,max}=2.6472$. If it happened that such global optima violates frequency windows, another value of the frequency can be taken near the optimum point, and an inverse approach is utilized by solving the frequency equation for any one of the unknown design variables instead.

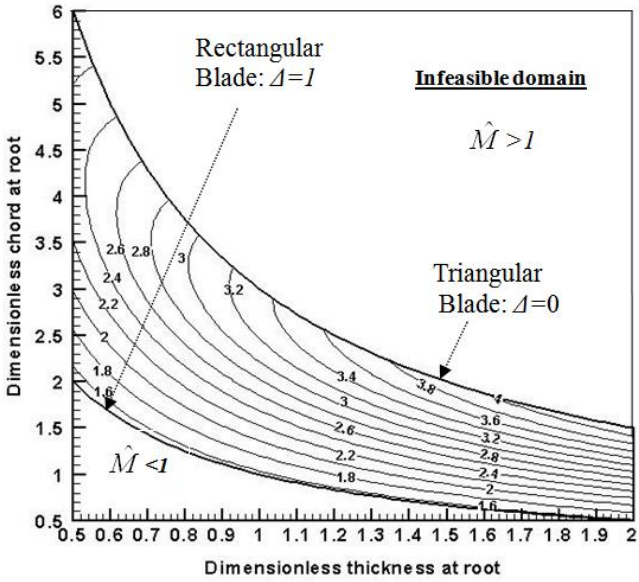

Figure 8. Level curves of $\hat{\omega}_1$ for a semi-rigid blade root; $\hat{K}_s=100$, $\hat{M}=1$.

Other cases for semi-rigid and rigid blade root are shown in figures 8 and 9. It is seen that the contour lines become more flatten and parallel to the two borderlines as the hub stiffness increases. The calculated maximum values of the fundamental pitching frequency are 4.2161 at the design point {1.5, 2, 0} for $\hat{K}_s=100$ and 4.4825 at the same design point for $\hat{K}_s=1000$. Such optimal blade designs having triangular planform are

http://dx.doi.org/10.5772/53347

favorable from structural point of view. However, such configurations violate the requirement of having an efficient aerodynamic surface producing the needed mechanical power. In all, it becomes now possible to choose the desired maximum frequency, which is far away from the excitation frequencies, and obtain the corresponding optimum variables directly from the developed frequency charts. Actually, the charts represent the fundamental frequency function augmented with the imposed mass equality constraint so that the problem may be treated as if it were an unconstrained optimization problem. Table 2 summarizes the final optimum solutions showing that good blade patterns ought to have the lowest possible tapering ratio. This means that the optimum design point is always very close to the lower limiting value imposed on the blade tapering ratio, i.e. 0.25.

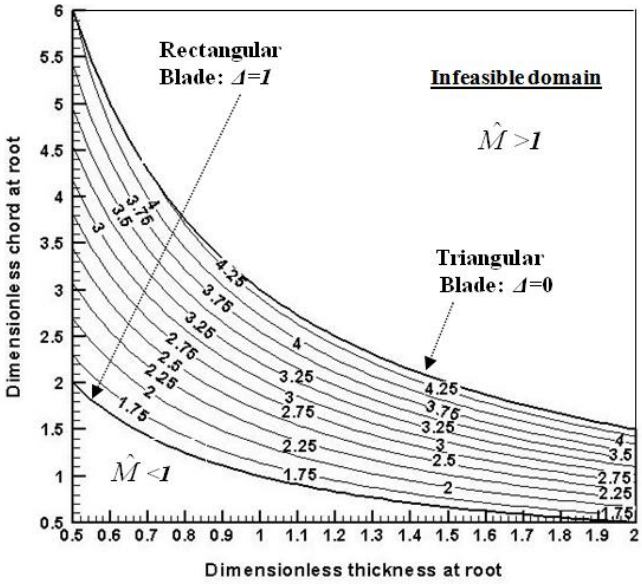

Figure 9. Level curves of $\hat{\omega}_1$ for a rigid blade root; $\hat{K}_s=1000$, $\hat{M}=1$.

Figure 10 depicts the variation of the maximum fundamental frequency with the stiffness at blade root. It is seen that the frequency decreases sharply with increasing the stiffness coefficient up to a value of 10, after which it increases in the interval between $\hat{K}_s$=10 and 100 and then remain approximately constant at the principal values $\pi/2$ and π. The average attained optimization gain reached a value of about 86.95 % as measured from the reference design.

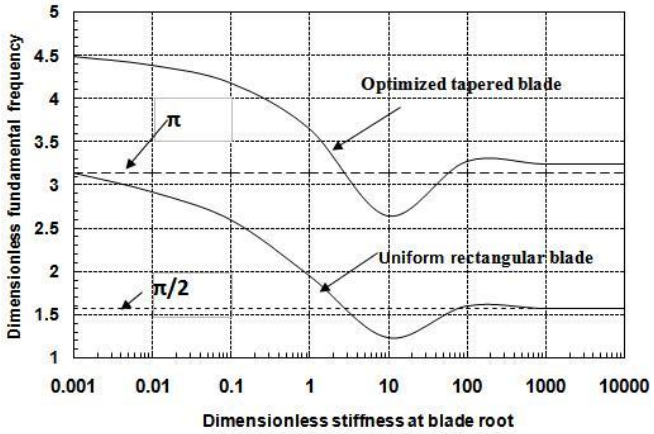

Figure 10. Variation of the constrained maximum fundamental frequency $\hat{\omega}_{1,max}$ with blade root stiffness $\hat{K}_s$, ($\hat{M}$=1)

Stiffness coefficient ($\hat{K}_s$)	Reference rectangular ($\hat{C}_o, \hat{h}_o, \Delta$)=(1, 1, 1)	Optimized tapered blade	
	$\hat{\omega}_1$	$\hat{\omega}_{1,max}$	$(\hat{C}_o, \hat{h}_o, \Delta)_{optimum}$
0.0 (Unlocked pitch)	3.1416 (π)	4.4871	(1.4520, 1.5861, 0.2514)
0.01	2.9235	4.3891	(1.7289, 1.3122, 0.2522)
0.1	2.5987	4.1871	(1.5973, 1.4221, 0.2541)
1	1.9546	3.6542	(1.3794, 1.6583, 0.2527)
10	1.2322	2.6467	(1.1651, 1.9546, 0.2504)
100	1.59811	3.2741	(1.2533, 1.7982, 0.2532)
1000	1.5731	3.2435	(1.4523, 1.5822, 0.2531)
∞ (Perfect rigidity)	1.5708 (π/2)	3.2389	(1.4763, 1.5428, 0.2529)
Equality mass constraint : $\hat{M}=1$ Inequality side constraints: $0.5 \le \hat{C}_o \le 2.0$ $0.25 \le \hat{h}_o \le 2.0$ $0.25 \le \Delta \le 0.75$			

Table 2. Constrained optimal solutions for different blade root flexibility.

http://dx.doi.org/10.5772/53347

6.3. Model validation: Actual operation case

As a part of the ministry of electricity plans for wind energy programs in Egypt, a study is currently performed concerning the design and manufacture of an upwind, two-bladed, pitch-controlled, horizontal-axis wind turbine producing *100 KW* electrical power output. The wind turbine will be erected for testing and experimental investigation in the western coast of the Gulf of Suez near Hurghada, which has the most favorable wind condition with average wind speeds between *7-12 m/s*. The followings are the relevant values of the reference blade design parameters:

- Planform: rectangular *(*taper $\Delta=1)$, chord $C_r=1.0\ m$, Elastic length $L=12.5\ m$.
- Cross section: *NACA 4415* airfoil, single cell construction.
- Wall thickness $h_r=5.0x10^{-3}\ m$.
- Torsion constant $J_r=1.536\ x\ 10^{-4}\ m^4$.
- 2nd moment of area $I_r=7.462\ x\ 10^{-4}\ m^4$.
- Type of material: E-glass/Epoxy composite.
- Equivalent in-plane shear modulus $G=4.7\ GPa$, mass density $\rho=1800\ kg/m^3$
- Total structural mass: $M_r=250.0\ kg$.
- Dimensionless circular frequency:

$\hat{\omega}_r = \pi$ for unlocked pitch

$= \pi/2$ for locked pitch

$\therefore$Dimensional circular frequency $\omega_r = 58.65\ \hat{\omega}_r\ rad/sec$. (refer to Table 1).

Frequency in *HZ:* $f_r=\omega_r/2\pi$

$=29.325\ HZ$ (Unlocked condition)

$= 14.6625\ HZ$ (Locked condition)

- Excitation frequency $f=20.0\ HZ$.

The final attained optimal design for the case of active pitch is (see Table 2 and Figure 5):

- The first three frequencies are $f_{i,max}= 41.8846,\ 67.802,\ 95.548\ HZ$, which corresponds to the optimal chord and thickness distributions:

$C(\hat{x}) = 1.452\ (1-0.7486\ \hat{x})\ m$

$h(\hat{x}) = 7.931x10^{-3}(1-0.7486\ \hat{x})\ m,\ 0 \le \hat{x} \le 1.$

$\Delta=0.2514$.

Other cases with different blade root flexibilities can be obtained using the dimensionless optimal solutions given in Table 2.

7. Conclusions

Efficient model for optimizing frequencies of a wind turbine blade in pitching motion has been presented in this chapter. The mathematical formulation is given with dimensionless quantities so as to make the model valid for a real-world wind turbine blade of any size and configuration. It provides exact solutions to the vibration modes of the blade structure in free pitching motion, against which the efficiency of other numerical methods, such as the finite element method, may be judged. Design variables include the chord length of the airfoil section, shear wall thickness and blade tapering ratio. Useful design charts for either maximizing the natural frequency or placing it at its desired (target) value has been developed for a prescribed total structural mass, and known torsional rigidity near blade root. The fundamental frequency can be shifted sufficiently from the range which resonates with the excitation frequencies. In fact the developed frequency charts given in the paper reveal very clearly how one can place the frequency at its proper value without the penalty of increasing the total structural mass. Each point inside the chart corresponds to different mass and stiffness distribution along the span of constant mass blade structure. The given approach is also implemented to maximize the frequency under equality mass constraint. If it happened that the obtained maximum frequency violates frequency windows, another value of the frequency can be taken near the optimum point, and an inverse approach can be applied by solving the frequency equation for any one of the unknown design variables instead. Other factors under study by the author include the use of material grading concept to enhance the dynamic performance of a wind turbine blade. Exciting frequencies due to the turbulent nature of the wind, especially in large wind turbines with different types of boundary conditions, are also under considerations. Another extension of this work is to optimize the aerodynamic and structural efficiencies of the blade by simultaneously maximizing the power coefficient and minimizing vibration level under mass constraint using a muli-criteria optimization technique.

Appendix

$B(x,t)$ pitch angle about blade elastic axis: $B(x,\ t)=\beta(x).q(t)$,

C chord length of the airfoil section

C_t chord length at blade tip

C_o chord length at blade root

G shear modulus of blade material

h skin thickness of the blade

h_o skin thickness at blade root

I second polar moment of area

http://dx.doi.org/10.5772/53347

J torsion constant of the blade cross section

K_s torsional stiffness coefficient at blade root

L effective blade length

$q(t)$ time dependence of blade pitch angle.

t time variable

X design variables vector.

x distance along blade span measured from chord at root

$\alpha = (1 - \Delta)$

$\beta(x)$ amplitude of the pitch angle

ω circular frequency of pitching motion

$\hat{\omega}$ normalized frequency

$\gamma \quad (=\hat{\omega}/\alpha)$

$\delta \quad (=\gamma\Delta)$

ρ mass density of blade material

Δ blade taper ratio (C_t/C_o)

$\theta\ (=\alpha\hat{h}_o\hat{C}_o^3/\hat{K}_s)$

Author details

Karam Y. Maalawi

National Research Centre, Mechanical Engineering Department, Cairo, Egypt

References

[1] Bindner, H., Rebsdorf A., and Byberg, W., (1997). Experimental investigation of combined variable speed / variable pitch controlled wind turbines. European Union Wind Energy Conference, EWEC97, Dublin, Ireland.

[2] Edwards, C.H. and Penney, D.E. (2004). Elementary differential equations with applications. Prentice-Hall, Inc., Englewood Cliffs, New Jersey.

[3] Florin Iov, Hansen, A.D., Jauch, C., Sorensen, P., & Blaabjerg F. (2004). Advanced tools for modeling, design and optimization of wind turbine systems. Proceedings of

NORDIC Wind Power Conference, Chalmers University of Technology, Goteborg-Sweden, 1-2 March, 2004.

[4] Hansen, M.H., Hansen, A., Larsen, T.J., Oye, S.I., Sorensen, P., & Fuglsang P. (2005). Control design for a pitch regulated, variable speed wind turbine. Riso National Laboratory, Riso-R-1500 (EN), Roskilde, Denmark.

[5] Hoffmann, R. (2002). *A comparison of control concepts for wind turbines in terms of energy capture*. M.Sc. Thesis, Department of Electronic and Information, University of Darmstadt, Germany.

[6] Jason, M. Jonkman, Marshall L. & Buhl, Jr. (2005). FAST User's Guide. Technical Report, NREL/EL-500-38230.

[7] Leithed, W.E. and Conner, B.C., (2002). Control of variable speed wind turbines: Dynamic modeling. *International Journal of Control*, 73(13), 1173-1188.

[8] Maalawi, K.Y. and Negm, H.M. (2002). Optimal frequency design of wind turbine blades. *Journal of Wind Engineering and Industrial Aerodynamics*, 90(8), 961-986.

[9] Maalawi, K.Y. and El-Chazly, N.M. (2002). Global optimization of multi-element beam-type structures. The Second International Conference on *Advances in Structural Engineering and Mechanics*, ASEM'02, Busan, South Korea, August 21-23.

[10] Maalawi, K.Y. and Badr, M.A. (2003). A practical approach for selecting optimum wind rotors. *International Journal of Renewable Energy*, 28, 803-822.

[11] Maalawi, K.Y. (2007). A model for yawing dynamic optimization of a wind turbine structure. *International Journal of Mechanical Sciences*, 49, 1130-1138.

[12] Maalawi, K.Y. and Badr, M.A. (2010). Frequency optimization of a wind turbine blade in pitching motion. *Journal of Power and Energy*, JPE907, Proc. IMechE Vol. 224, Part A, pp. 545-554.

[13] Rao, J.S. (1994). Advanced theory of vibration, Wiley Eastern Limited, New York.

[14] Pritchard, J.I. and Adelman, H.M. (1990). Optimal placement of tuning masses for vibration reduction in helicopter rotor blades, *AIAA Journal*, 28(2), 309-315.

[15] Shin, Y.S., Haftka, R.T., Plaut, R.H. (1988). Simultaneous analysis and design of eigenvalue maximization, *AIAA Journal*, 26(6), 738-744.

[16] Vanderplaats, G.N. (1999). Numerical optimization techniques for engineering design with applications. McGraw Hill, New York

[17] Vekataraman, P. (2009). Applied optimization with *MATLAB* programming. 2nd Edition, Wiley, New York.

Chapter 9

Comparative Analysis of DFIG Based Wind Farms Control Mode on Long-Term Voltage Stability

Rafael Rorato Londero, João Paulo A. Vieira and Carolina de M. Affonso

Additional information is available at the end of the chapter

http://dx.doi.org/10.5772/52690

1. Introduction

The wind energy industry is experiencing a strong growth in most countries in the last years. Several technical, economic and environmental benefits can be attained by connecting wind energy to distribution systems such as power loss reduction, the use of clean energy, postponement of system upgrades and increasing reliability. The doubly fed induction generator (DFIG) is currently the most commonly installed wind turbine in power systems. DFIG can be operated in two different control modes: constant power factor and voltage control. In the power factor control mode, the reactive power from the turbine is controlled to match the active power production at a fixed ratio. When terminal voltage control is employed, the reactive power production is controlled to achieve a target voltage at a specified bus. Many wind operators currently prefer the unity power factor mode since it is the active power production that is rewarded [1].

The integration of wind turbine in electricity networks still face major challenges with respect to various operational problems that may occur, especially under high penetration level [2,3]. Among many problems, it can be highlighted the voltage instability phenomenon, a constant concern for modern power systems operation [4,5]. Voltage stability refers to system ability to keep voltage at all buses in acceptable ranges after a disturbance. This phenomenon is local and non-linear, characterized by a progressive decline in voltage magnitudes, and occurs basically due to system inability to meet a growing demand for reactive power at certain buses in stressed situations [6,7]. The phenomena involved in voltage stability is usually of slow nature (minutes or hours), being driven by the action of discrete type devices and load variations [7].

Some papers have analyzed the impacts caused by the connection of wind generation on voltage stability using static models [8,9]. However, the exclusive use of static models is insufficient to fully describe voltage instability phenomenon, especially considering the actuation of dynamics equipments. Also, few papers have explored the differences in DFIG mode of operation [10,11,12]. Until now, no work has presented a study analyzing the impacts of different DFIG control modes on long-term voltage stability analysis, especially considering the dynamics aspects and interaction of equipments installed in the network, such as Over Excitation Limiters (OEL) and On Load Tap Changers (OLTC).

This chapter presents a study comparing the impacts caused by different control modes of DFIG wind turbine on long-term power system voltage stability. The study uses time domain simulations and also includes the representation of Over Excitation Limiter (OEL) and On Load Tap Changers (OLTC). The analysis focuses on the two DFIG excitation control modes: constant voltage control and constant power factor control (unity power factor and leading power factor) with a 20% load increase. The impact of each control strategy is studied and the resulting change in long-term system stability is quantified, as well as the interaction between OLTC and OEL equipments.

2. Doubly Fed Induction Generators (DFIGs)

Doubly-fed induction generators are gaining popularity these days for several reasons. The primary reason for this is their ability to vary their operating speed, typically +/- 30% around the synchronous speed. The stator is directly connected to the grid and the rotor is fed from a back-to-back AC/DC/AC converter set as shows Fig. 1. The rotor side converter (RSC) controls the wind turbine output power and the voltage measured at the grid side. The grid side converter (GSC) regulates the DC bus voltage and interchange reactive power with the grid, allowing the production or consumption of reactive power. Then, DFIG can operate on voltage control mode (PV) or power factor control mode (PQ).

PV mode refers to DFIG generating or absorbing reactive power (MVAr) to/from the distribution network in order to maintain the terminal voltage at a specified value. The minimum and maximum MVAr have to be specified in order to operate at a power factor between 0.9 leading and 0.85 lagging, otherwise the plant operators will be charged for violating the operational limit. In load flow studies DFIG is represented as a PV bus for voltage control mode [13].

PQ mode refers to the DFIG generation at a fixed MW and a fixed MVAr. When DFIG real power generation varies, the reactive power will also vary to maintain a fixed power factor. This mode usually employs unity power factor operation (zero reactive power output). However, other power factor values can be specified (e.g., from 0.95 leading to 0.95 lagging) according to the system operator requirements. In load flow studies DFIG is represented as a PQ bus for power factor control mode. In this study both control modes are considered.

http://dx.doi.org/10.5772/52690

3. System modelling

3.1. Wind turbine model

The wind turbine mechanical power may be calculated as:

$$P_{mec} = 0.5 C_P \rho \, r^2 U_W^3 \tag{1}$$

Where r is the radius of the wind turbine rotor, U_w is the average wind speed (m/s), $\rho$is the air-specific mass (kg m3) and C_P is the wind turbine power coefficient [12]. C_P is a function of the tip speed ratio λ and the blade pitch angle β, and can be expressed as:

$$C_p(\lambda,\beta) = 0.73\left(\frac{115}{\lambda_i} - 0.58\beta^{2.14} - 13.2\right)e^{\frac{-18.4}{\lambda_i}} \tag{2}$$

$$\lambda = \frac{1}{\frac{1}{\lambda} - 0.02\beta + \frac{0.003}{\beta^3 + 1}} \tag{3}$$

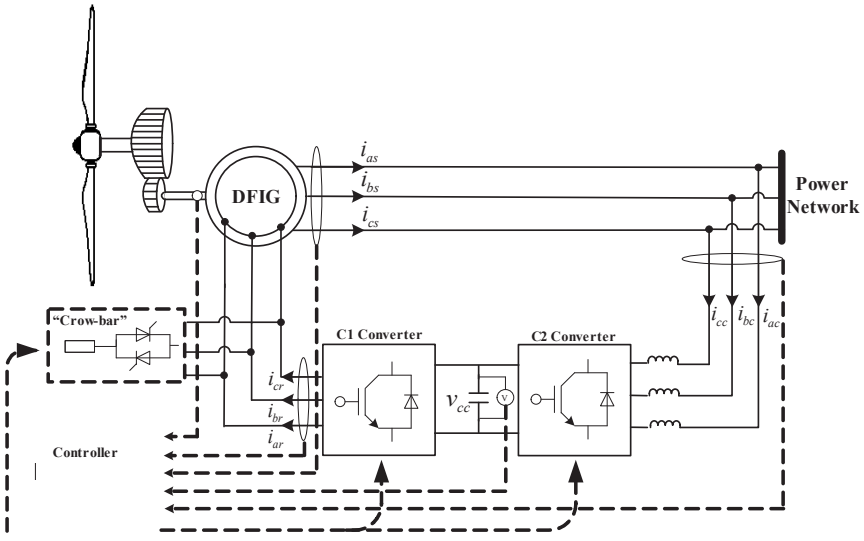

Figure 1. DFIGs Scheme

To represent the electrical and mechanical interaction between the electrical generator and wind turbine in transient stability studies, the global mass model is presented:

$$\frac{d\overline{\omega}_r}{dt} = \frac{1}{2H_T}\left(T_m - \overline{T}_e - \overline{D}\overline{\omega}_r\right) \tag{4}$$

Where $\overline{D}$ is the damping coefficient; and H_T is the inertia constant, in seconds.

3.2. The DFIG model

For power system stability studies, the generator may be modeled as an equivalent voltage source behind a transient impedance. Since the stator dynamic are very fast, when compared with the rotor ones, it is possible to neglect them. The differential equations of the induction generator rotor circuits with equivalent voltage behind transient impedance as state variables can be given in a d-q reference frame rotating at synchronous speed. For adequately representing the DFIG dynamics the second order model of the induction generator is used in the following per-unit form [14,15]:

$$\overline{v}_{ds} = -\overline{R}_s\overline{i}_{ds} + \overline{X}'\overline{i}_{qs} + \overline{e}_d' \tag{5}$$

$$\overline{v}_{qs} = -\overline{R}_s\overline{i}_{qs} - \overline{X}'\overline{i}_{ds} + \overline{e}_q' \tag{6}$$

$$\frac{d\overline{e}_d'}{dt} = -\frac{1}{T_o'}\cdot\left[\overline{e}_d' - \left(\overline{X} - \overline{X}'\right)\overline{i}_{qs}\right] + s\omega_s\overline{e}_q' - \omega_s\frac{\overline{L}_m}{\overline{L}_{rr}}\overline{v}_{qr} \tag{7}$$

$$\frac{d\overline{e}_q'}{dt} = -\frac{1}{T_o'}\cdot\left[\overline{e}_q' + \left(\overline{X} - \overline{X}'\right)\overline{i}_{ds}\right] - s\omega_s\overline{e}_d' + \omega_s\frac{\overline{L}_m}{\overline{L}_{rr}}\overline{v}_{dr} \tag{8}$$

Where:

V_{ds}, V_{qs}: d and q axis stator voltages;

R_s: stator resistance;

X′, X: transient reactance and the open circuit reactance;

i_{ds}, i_{qs}: d and q axis stator currents;
e_d',e_q': d-axis and q-axis components of the internal voltage; T_o': open circuit time constant in seconds;

ω_S: synchronous speed;

L_m: mutual inductance;

L_{rr}: rotor inductance;

V_{dr}, V_{qr}: d and q axis rotor voltages;

http://dx.doi.org/10.5772/52690

The components of the internal voltage behind the transient reactance are defined as:

$$\bar{e}_d^{'} = -\frac{\bar{\omega}_s \bar{L}_m}{\bar{L}_{rr}} \cdot \bar{\lambda}_{qr} \tag{9}$$

$$\bar{e}_q^{'} = \frac{\bar{\omega}_s \times \bar{L}_m}{\bar{L}_{rr}} \cdot \bar{\lambda}_{dr} \tag{10}$$

where λ_{qr} and λ_{dr} are d and q rotor fluxes. The reactances and transients open-circuit time constant are given:

$$\bar{X}^{'} = \bar{\omega}_s \left(\bar{L}_{ss} - \frac{\bar{L}_m^2}{\bar{L}_{rr}} \right) = \bar{X}_s + \frac{\bar{X}_r \bar{X}_m}{\bar{X}_r + \bar{X}_m} \tag{11}$$

$$\bar{T}_o^{'} = \frac{\bar{L}_r + \bar{L}_m}{\bar{R}_r} = \frac{\bar{L}_{rr}}{\bar{R}_r} \tag{12}$$

$$\bar{X} = \bar{\omega}_s \bar{L}_{ss} \tag{13}$$

$$T_o^{'} = \frac{\bar{L}_{rr}}{2\pi f_{base} \bar{R}_r} \tag{14}$$

3.3. DFIG converter model

In this study the converters are modeled according to reference [16], as show the diagrams presented in Figs. 2 and 3. The V_{d1} component is used to the capacitor voltage and V_{q1} is used to fix at zero the reactive power absorbed by the rotor side converter. This component may be used to provide additional reactive power support to the system.

The component I_{q2} of the rotor current is used to control the rotor speed and as a consequence, the active power supplied by the machine. The component I_{d2} of the rotor current is used to control the generator terminal voltage or power factor.

3.4. OEL model

The objective of the over excitation limiter is to protect the generator from thermal overload. The OEL model adopted in this study is the same of reference [14] and the model is presented in Fig. 4. The OEL detects the over-current condition, and after a time delay, acts reducing the excitation by reducing the field current to a value of 100% to 110% of the nominal value. Once the OEL acts, the field current no longer increases, limiting the reactive power supplied by the machine to a minimum value, overloading the other generators, contributing significantly to the voltage instability.

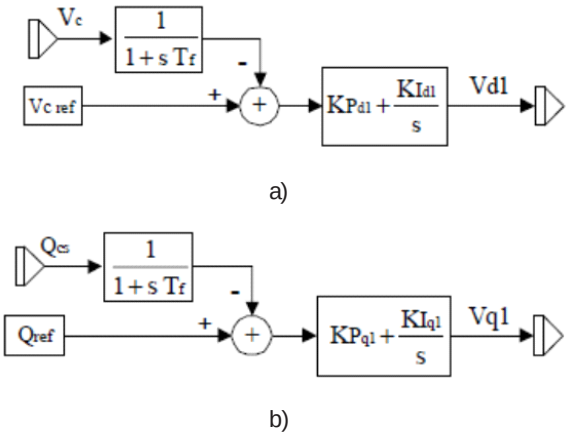

Figure 2. Control loop of the stator side converter (SSC) a) Component V_{d1} b) Component V_{q1}.

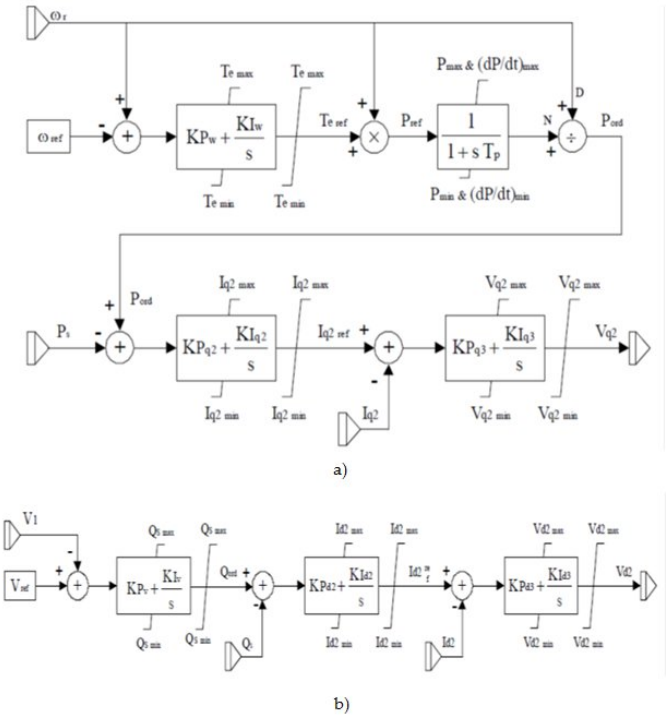

Figure 3. Control loop of the rotor side converter (RSC) a) Component I_{q2} b) Component I_{d2}.

http://dx.doi.org/10.5772/52690

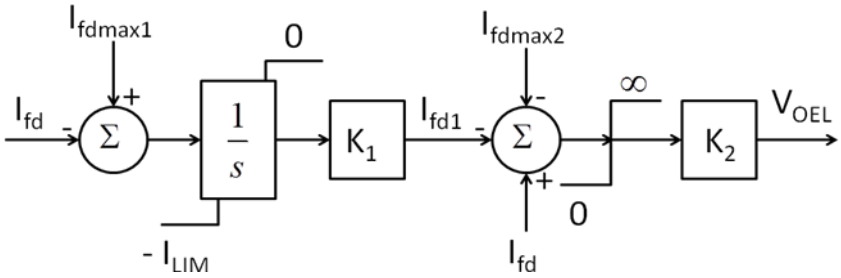

Figure 4. OEL model.

4. Test system

The test system used in this study is shown in Fig. 5 and is based on the system developed in [14] for voltage stability analysis. To conduct this study the original system was modified, adding a transformer between buses 8 and 12 to connect a 212.5 MW wind farm at bus 12, consisting of 250 turbines of 850kW. Four generation sources are modeled: G1, G2 and G3 are synchronous generators and the wind farm is based on DFIG. The OEL device is installed in generator G3 and the OLTC between buses 10 and 11. The OLTC model used is presented in reference [17].

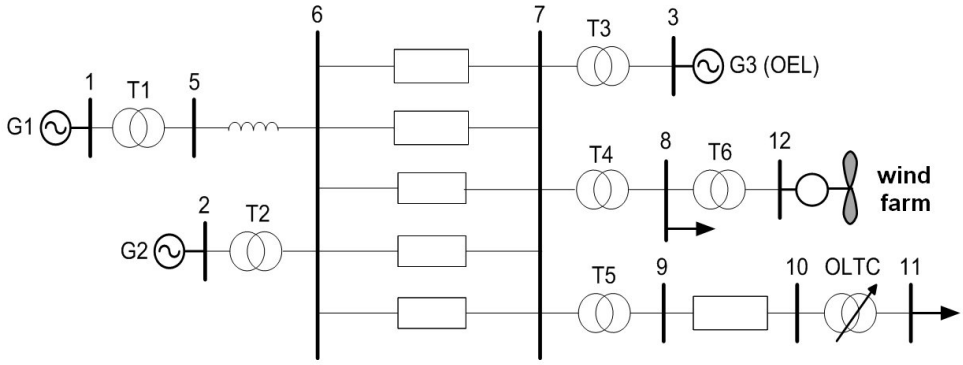

Figure 5. Test system diagram.

Table 1 shows the generation and load scenarios considered. The penetration level of the wind farm is 17.6%. Scenario 1 considers the load at bus 8 modeled as constant impedance for both active and reactive components and the load at bus 11 modeled as 50% constant impedance and 50% constant current for both active and reactive components. Scenario 2 considers the active power component of load at bus 8 represented as an equivalent of 450

induction motors which parameters are presented in the Appendix, and all other components are modeled as in scenario 1.

Scenarios	Load at bus 8		Load at bus 11	
	P(MW)	Q(Mvar)	P(MW)	Q(Mvar)
Scenario 1	3,271.0	1,015.0	3,385.0	971.3
Scenario 2	1,660.0	1,050.2	3,388.4	972.3

Table 1. Load Scenarios

Scenarios	Generator 1 (MW)	Generator 2 (MW)	Generator 3 (MW)	DFIG (PV mode) (MW/Mvar)	DFIG (PQ mode) (MW/Mvar)
Scenario 1	2,747.0	1,736.0	1,154.0	1,200.0 / -364.0	1,200.0 / 100.0
Scenario 2	1,115.5	1,736.0	1,154.0	1,200.0 / -14.3	1,200.0 / 200.0

Table 2. Generation Scenarios

The intermittent characteristic of wind generation is considered following the wind regime presented on Fig. 6, with the initial wind speed of 12 m/s.

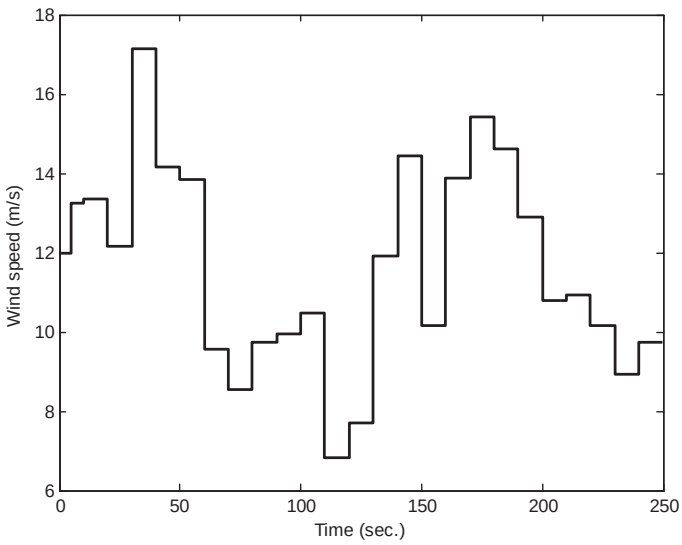

Figure 6. Wind speed regime.

http://dx.doi.org/10.5772/52690

5. Simulation and results

To evaluate the different impacts caused by DFIG control modes on long-term voltage stability, two cases are analyzed:

- Case A: Static load model (scenario 1): This scenario considers the load at buses 8 and 11 represented by the commom ZIP model.
- Case B: Static and dynamic load model (scenario 2): This scenario considers the load at bus 11 represented by the common ZIP model and the active power component of load at bus 8 represented by an equivalent induction motor.

All simulations considered both DFIG control modes alternatively: power factor control mode (0.99 leading) and voltage control mode. The results and analysis are presented next in the following sections. The simulations were conducted using the softwares ANAREDE for load flow calculations and ANATEM for transient stability simulations [18,19].

5.1. Case A: Static load model (Scenario 1)

This case considers the successive increase on system total demand, with increments of 0.1% every second in respect with the initial load from scenario 1 as presented in tables 1 and 2. The load increases up to 200 seconds and the simulation time is 250 seconds.

As load increases, the voltage at bus 11 decreases, causing OLTC to operate in order to maintain voltage close to the reference level for both control modes as shows Fig. 7. However, while OLTC improves voltage level at bus 11, it progressively depresses voltage at bus 8 with each tap-changing operation, mainly when power factor control mode is employed in wind generation as shows Fig. 8. In voltage control mode, DFIG maintain the voltage level at bus 8 with its capacity to supply reactive power support. Fig. 9 presents the reactive power injected and absorbed by DFIG. Note that when OLTC starts to operate close to 60 seconds, the DFIG starts to inject more reactive power in the system until it reaches its maximum limit.

The voltage reductions at load buses 8 and 11 are directly reflected in the field current of generator 3, because with the load increase, the generator AVR (Automatic Voltage Regulator) would quickly restore terminal voltage by increasing excitation, which results in additional reactive power flow through the inductances of transformers and lines, causing increased losses and voltage drops. At this stage, generator G3 tends to reach its field current limit with the load ramp increase as shows Fig. 10. In this scenario 1, generator 3 does not suffer over-excitation (the OEL is not activated), and the long-term power system voltage stability is maintained in both reactive power control modes, at least apparently. However, as can be seen in Fig. 10, the DFIG's voltage control mode has a positive effect in the power system voltage stability since it tends to delay the OEL operation because the field current level is smallest from 110 s up to 250 s, providing less risk of protection interventions and system security degradation.

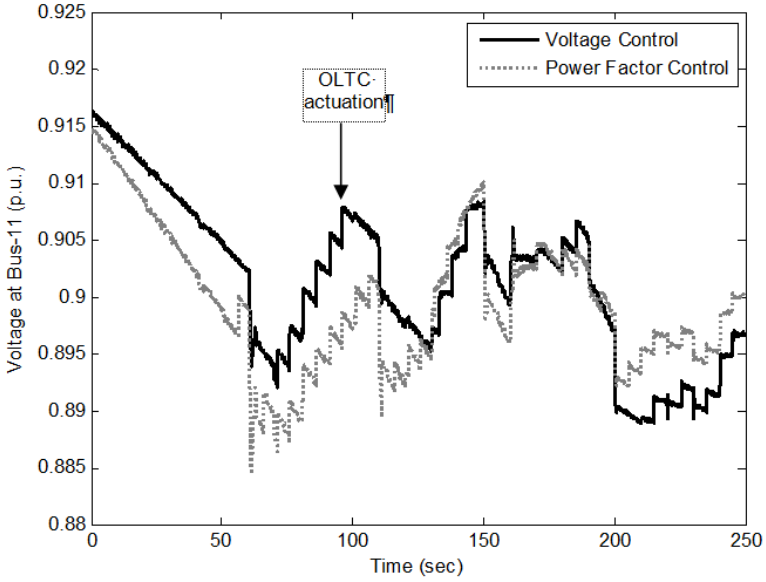

Figure 7. Voltage at bus 11

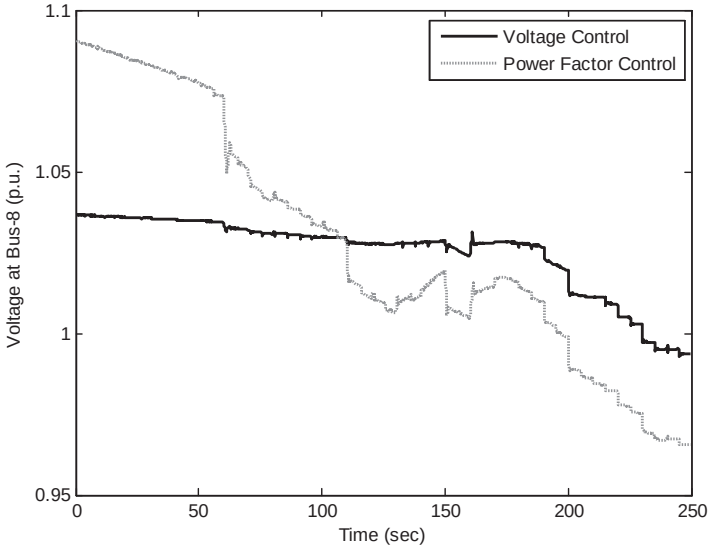

Figure 8. Voltage at bus 8

http://dx.doi.org/10.5772/52690

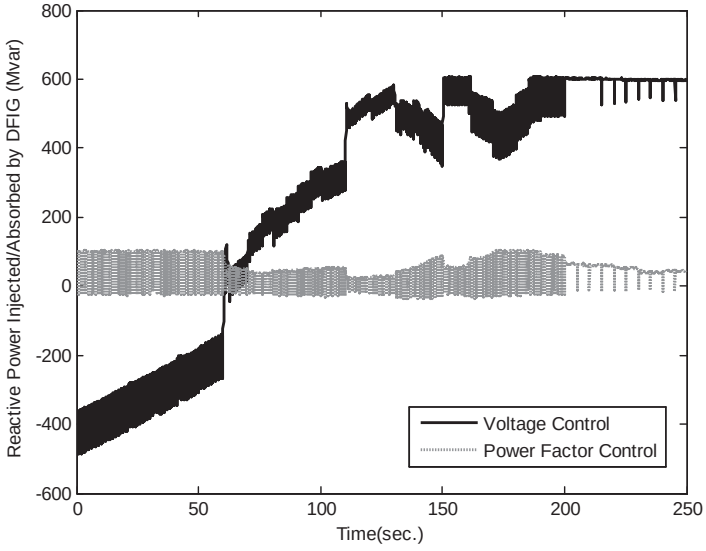

Figure 9. Reactive power injected / absorbed by DFIG.

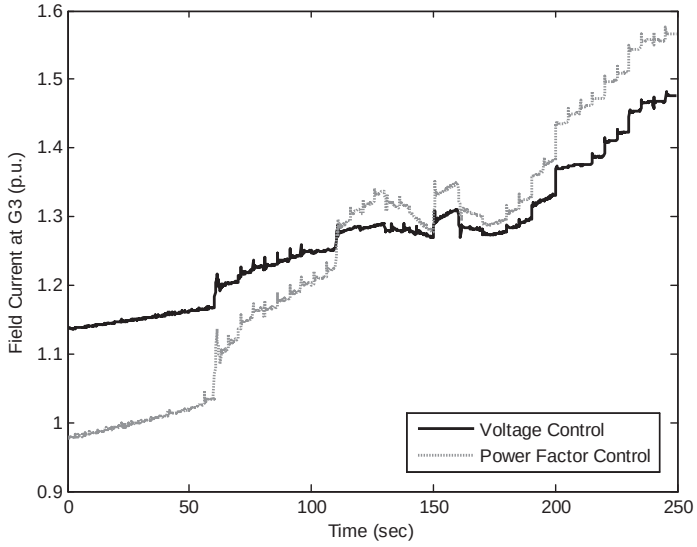

Figure 10. Field current at G3.

Fig. 11 shows the OLTC behavior during the load ramp increase. The results show that the OLTC reaches its upper limit when the DFIG wind generators are configured to control the power factor, and in this case the wind turbines cannot provide reactive power to support the voltages in the system. On the other hand, when the voltage control mode is used, the OLTC does not reach the upper tap limit, increasing the long term voltage stability margin.

Fig. 12 shows the system PV curve when DFIG is operating in both power factor and voltage control modes. These curves were obtained by increasing the load and plotting the voltage at bus 8 considering the dynamic aspect of the equipments in the system. This curve indicates the maximum loadability point, which is the maximum power the system can provide. The results show that when DFIG is operating in voltage control mode it increases significantly the maximum loadability point (nose point), since this equipment can supply reactive power to the system through voltage control. It is important to mention that the PV curves contours are irregular since they represent the discrete actuation of OEL and OLTC.

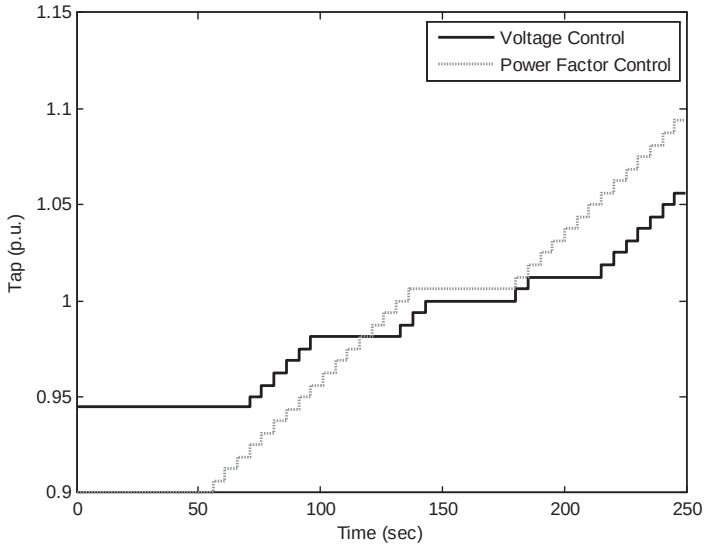

Figure 11. Tap position.

http://dx.doi.org/10.5772/52690

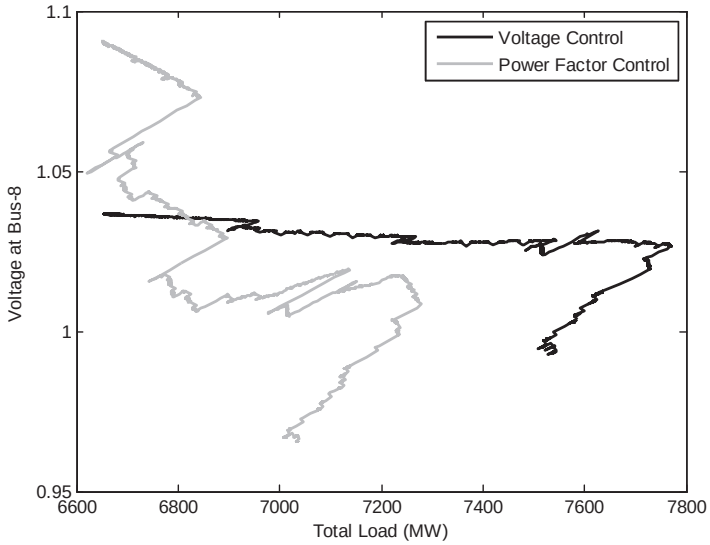

Figure 12. PV curve at bus 8.

5.2. Case B: Static and dynamic load models (Scenario 2)

This case considers the successive increase on system demand from bus 11, with increments of 0.1% every second in respect to the initial load from scenario 2 as presented in tables 1 and 2. The load increases up to 200 seconds and the simulation time is 250 seconds.

As seen in Figs. 13 and 14, the power factor control mode results in a heavy reactive power demand from the power system, leading to a very low voltage profile at load buses 11 and 8. In this case, constant power factor strategy decreases the long-term voltage stability margin, resulting in the voltage deterioration at load buses caused by relevant effect of the OEL combined with the OLTC action. In voltage control mode, the DFIG maintain the voltage level at bus 8 with its capacity to supply reactive power to the grid, as shows Fig. 15.

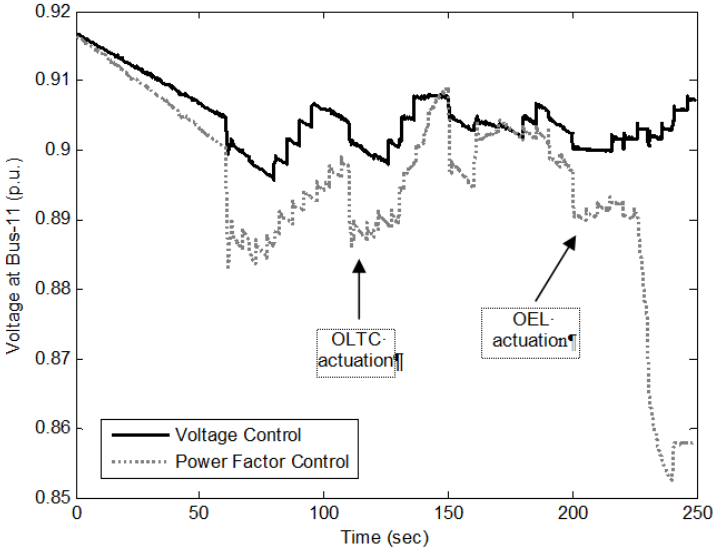

Figure 13. Voltage at Bus 11.

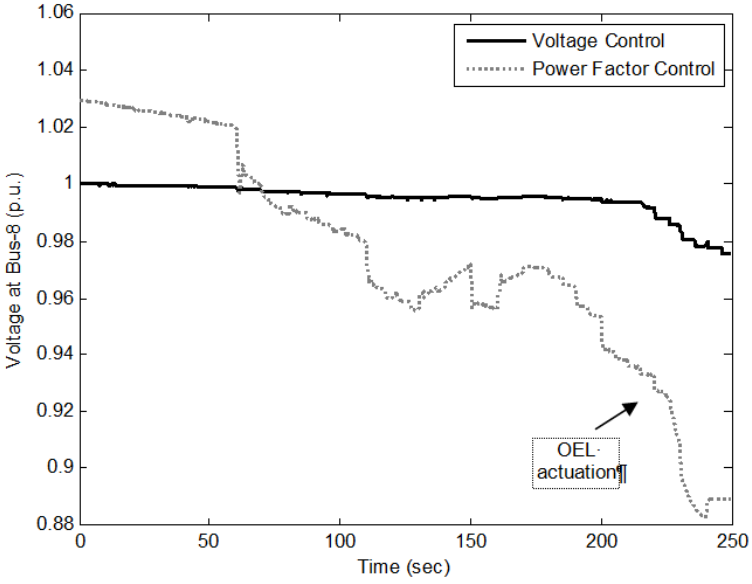

Figure 14. Voltage at Bus 8.

http://dx.doi.org/10.5772/52690

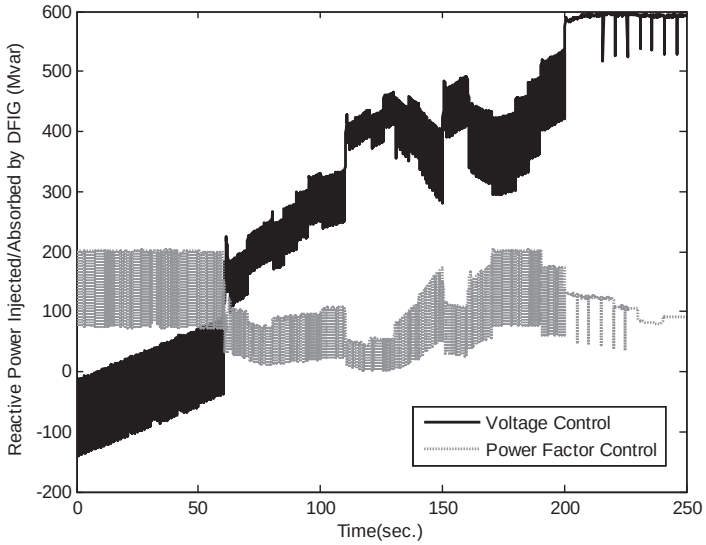

Figure 15. Reactive power injected / absorbed by DFIG.

Fig. 16 shows the field current behavior from generator 3. The DFIG's power factor control mode increases the field current demand and the OEL begins to operate at 225 s reducing the current, and as a consequence, the reactive power injected by G3 decreases.

On the other hand, when the DFIG is operating with voltage control mode the OEL is not activated, increasing the voltage stability margin. The DFIG's voltage control mode demonstrates that can be utilized in order to improve the long-term voltage stability in a system with a high wind penetration. From these results, one can conclude that the DFIG's voltage control mode has a beneficial effect in the voltage stability when the power system is submitted to load increase, considering the dynamic aspects of the OEL and OLTC combined with the load characteristics adopted. It is important to highlight that load characteristics and power system voltage control devices are among key factors influencing voltage stability.

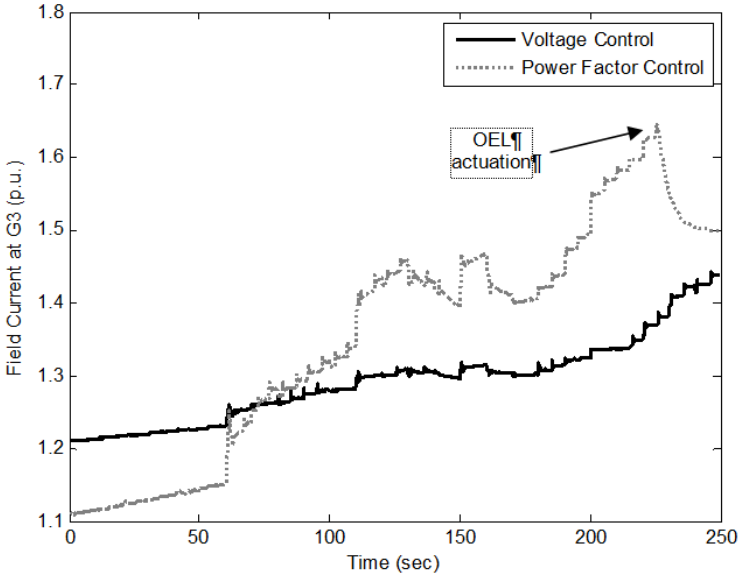

Figure 16. Field Current from G3.

Fig. 17 shows the OLTC behavior during the load ramp increase. It is observed that the minimum and maximum tap positions are reached when the DFIG wind turbines are configured to control the power factor, in order to support the voltage at bus 11. This is a great disadvantage of power factor control mode. The reactive power system reserves are insufficient and the OLTC tap changing is detrimental to voltage profile, increasing the risk of long-term voltage instability.

On the other hand, the voltage control strategy provides a delay on the OLTC actuation. Besides, the OLTC does not even reach the upper tap limit. When the OLTC is not changing its tap position, the reactive power absorbed decreases as well as the transmission line losses, causing a smallest drop in voltages. In this case, the power system is much more prone to maintain the voltage stability.

http://dx.doi.org/10.5772/52690

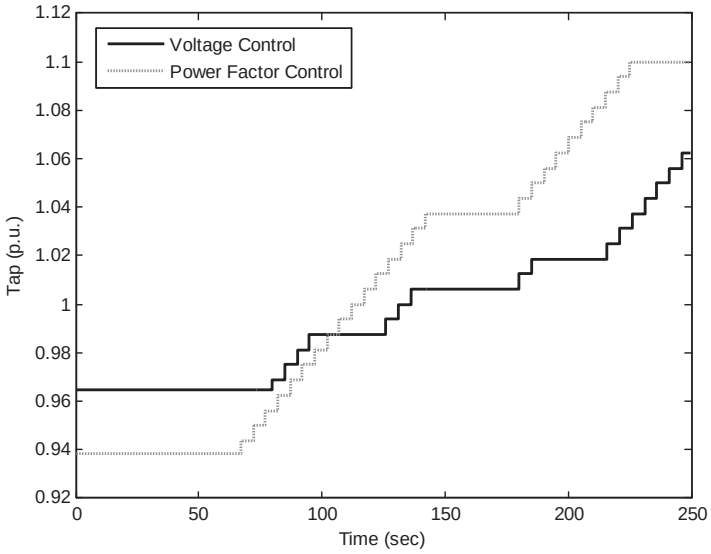

Figure 17. Tap position.

The DFIG's terminal voltage control mode based on the rotor excitation current allows the maintenance of reactive power consumed by the motor as shows Fig. 18. In this case, there are no extra static or dynamic reactive compensation demands for maintaining the power system long-term voltage stability. On the other hand, the DFIG's power factor control mode causes an increase in the reactive power drawn by the motor, which is necessary to maintain the power system reactive power balance. In this case, the motor is subject to a sudden stall that can cause a voltage collapse manifested as a slow decay of voltage in a significant part of the power system.

Fig. 19 shows the system PV curve for both DFIG control modes. In this case, the maximum loadability points for voltage and power factor control modes don't show much difference between each other as the previous case (static load). This occurs since in this case the load is incremented only at bus 11, which is controlled by the OLTC. Then, the active power absorbed at bus 8 shows only a small drop, which is reflected to the PV curve. The load at bus 8 (motors) was not incremented because the motor would consume too much reactive power from the system.

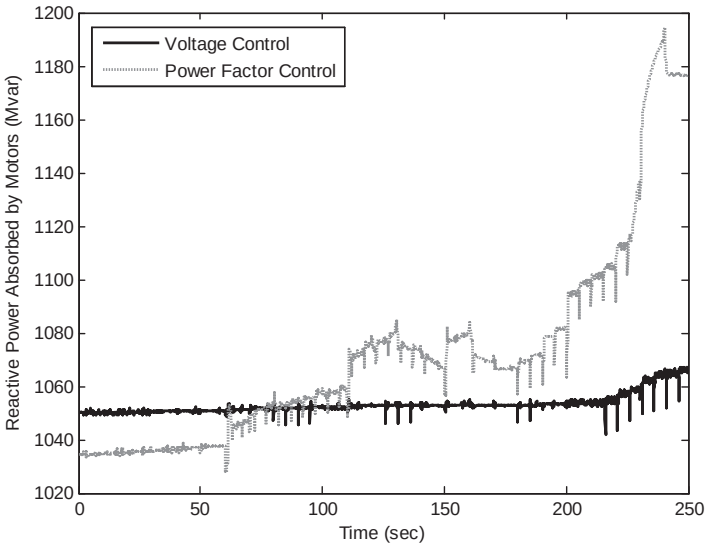

Figure 18. Reactive power absorbed by the motors.

http://dx.doi.org/10.5772/52690

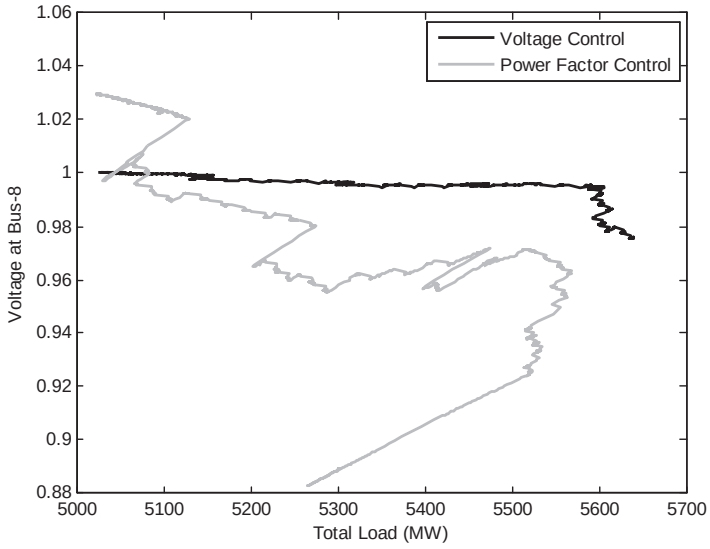

Figure 19. PV curve at bus 8.

6. Conclusion

This paper presented studies analyzing the impacts of different control strategies from DFIG wind turbines on power system long-term voltage stability by time domain simulations. The study considered the dynamic models of generator OEL and OLTC transformer combined with static and dynamic load representations. The simulation results confirm the expectation that when DFIG operates in power factor control mode the voltage stability margin is poor, mainly when the motor model is used to represent a part of the load. The results clearly show that DFIG's voltage control mode enhances voltage stability margin. The voltage control is more robust than power factor control when the power system is subjected to a slow load increase, a process that involves the OEL and OLTC actions and interactions. The use of DFIG in voltage control mode also increased the maximum loading point as well as delayed the OEL and OLTC actuation, helping to avoid problems of voltage collapse in the power system. As part of the ancillary services, the voltage control mode may have an increasing market ahead. This is an important feature that must be considered in the choice of the control strategy to be used on DFIG wind turbines.

Appendix

Generators 1, 2 and 3 parameters (p.u. on base of machine rating):

$R_a = 0.0046 X_d = 2.07 X'_d = 0.28 X''_d = 0.215$

$X_q = 1.99 X'_q = 0.49 X''_q = 0.215 X_l = 0.155$

$T'_{d0} = 4.10\ s T'_{q0} = 0.56\ s$

$T''_{d0} = 0.033 s T''_{q0} = 0.0062\ s$

G2: H = 2.09s, S_b = 2200 MVA

G3: H = 2.33s, S_b = 1400 MVA

SCIG and DFIG parameters (on base of machine rating):

$r_s = 0.85\% X_s = 5.776\% X_m = 505.9\%$

$r_r = 0.712\% X_r = 8.094\% H = 3.5\ s$

Poles = 2Power = 1140 HP

DFIG wind turbine parameters:

Rotor diameter = 58 mGear ratio = 74.5

DFIG power curve:

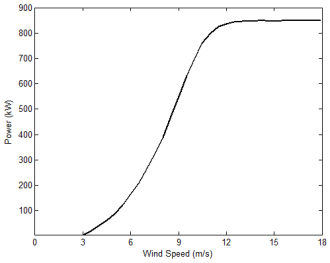

OLTC parameters:

Time delay for the first tap movement = 30 s

Time delay for subsequent tap movement = 5 s

Dead band = ±1% bus voltage

Tap range = ±16 steps

Step size = 5/8% (0.00625 pu)

Induction Motor parameters (p.u. on base of machine rating):

$X_m = 3.3\ R_s = 0.01 X_s = 0.145$

$R_r = 0.008 X_r = 0.145$

H = 0.6s, 4,826.0 HP

Generic network parameters (p.u. on base S_b = 100MVA):

Line 5-6:R = 0.0 X = 0.0040B = 0.0

Line 6-7:R = 0.0015 X = 0.0288B = 1.173

Line 9-10: R = 0.0010X = 0.0030B = 0.0

T1:R = 0.0X = 0.0020Ratio = 0.8857

T2: R = 0.0X = 0.0045Ratio = 0.8857

T3:R = 0.0 X = 0.0125Ratio = 0.9024

T4:R = 0.0 X = 0.0030Ratio = 1.0664

T5:R = 0.0 X = 0.0026Ratio = 1.0800

http://dx.doi.org/10.5772/52690

Author details

Rafael Rorato Londero, João Paulo A. Vieira and Carolina de M. Affonso

Faculty of Electrical Engineering, Federal University of Pará, Belém, PA, Brazil

References

[1] Standard interconnection agreements for wind energy and other alternative technologies, Washington, DC: Federal Energy Regulatory Commission (FERC) 661-A, Dec. 2005.

[2] Jenkins N, Allan R, Crossley P, Kirschen D, Strabac G (2000) Embedded Generation, The Institution of Electrical Engineers, London, United Kingdom.

[3] Trichakis P, Taylor P C, Lyons P F, Hair R (2008). Predicting the technical impacts of high levels of small-scale embedded generators on low-voltage networks, IET Renewable Power Generation, vol. 2, no. 4, pp. 249–262.

[4] Vournas C D, Nikolaidis V C, Tassoulis A (2005). Experience from the Athens Blackout of July 12, 2004, in Proceedings of the IEEE Power Tech Conference, St Petersburg, Russia, pp. 1-7.

[5] Corsi S, Sabelli C (2004). General Blackout in Italy Sunday September 28, 2003, h. 03:28:00, in Proc. IEEE Power Engineering Society General Meeting, vol. 2, pp. 1691-1702.

[6] Taylor C (1994). Power System Voltage Stability, New York: McGraw-Hill Inc.

[7] IEEE/CIGRE Joint Task Force on Stability Terms and Definitions (2004). Definition and Classification of Power System Stability, IEEE Trans. on Power Systems, vol. 19, no. 2, pp. 1387-1401.

[8] Tapia A, Tapia G, Ostolaza J X, Saenz J R (2003). Modeling and control of a wind turbine driven doubly fed induction generator, IEEE Trans. Energy Conversion, vol. 18, no. 2, pp. 194–204.

[9] Cartwright P, Holdsworth L, Ekanayake J B, Jenkins N (2004). Coordinated voltage control strategy for a doubly-fed induction generator (DFIG)-based wind farm, in Proceedings of the IEE Generat. Transmiss. Distribution, vol. 151, no. 4, pp. 495–502.

[10] Kayıkçi M, Milanović J V (2007). Reactive Power Control Strategies for DFIG-Based Plants, IEEE Trans. on Energy Conversion, vol. 22, no. 2, pp. 389-396.

[11] Muñoz J C, Cañizares C A (2011). Comparative Stability Analysis of DFIG-based Wind Farms and Conventional Synchronous Generators, IEEE Power Systems Conference and Exposition, Phoenix, pp. 1-7.

[12] Ackermann T (2005). Wind Power in Power Systems, John Wiley & Sons Ltd..

[13] Koon L C, Abdul Majid A A (2007). Technical issues on Distributed Generation (DG) connection and guidelines, 19th International Conference on Electricity Distribution (CIRED), Vienna, pp. 1-4.

[14] Kundur P (1994). Power System Stability and Control, New York: McGraw-Hill.

[15] Anaya-Lara O, Jenkins N, Ekanayake J, Cartwright P, Hughes M (2009). Wind Energy Generation Modelling and Control, John Wiley & Sons.

[16] Ekanayaka J B, Holdsworth L, Wu X G, Jenkins N (2003). Dynamic Modeling of Doubly Fed Induction Generator Wind Turbine, IEEE Transactions on Power Systems, vol.18, no.2, pp.803-809.

[17] Rangel R D, Guimarães C H C (2007). Modelagem de Transformadores com Dispositivos de Comutação em Carga para Utilização em Programas de Simulação Dinâmica, in Proceedings of XIX Seminário Nacional de Produção e Transmissão de Energia Elétrica - SNPTEE.

[18] CEPEL, Centro de Pesquisas de Energia Elétrica (1999). ANAREDE: Programa de Análise de Redes, Manual Guide, 9.5 Version.

[19] CEPEL, Centro de Pesquisas de Energia Elétrica (2002). ANATEM: Análise de Transitórios Eletromecânicos, Manual Guide, 10 Version.

Design of a Mean Power Wind Conversion Chain with a Magnetic Speed Multiplier

Daniel Matt, Julien Jac and Nicolas Ziegler

Additional information is available at the end of the chapter

http://dx.doi.org/10.5772/51949

1. Introduction

When designing a wind turbine for power generation there are two methods of linking the wind sensor to the generator, as seen in figure 1.

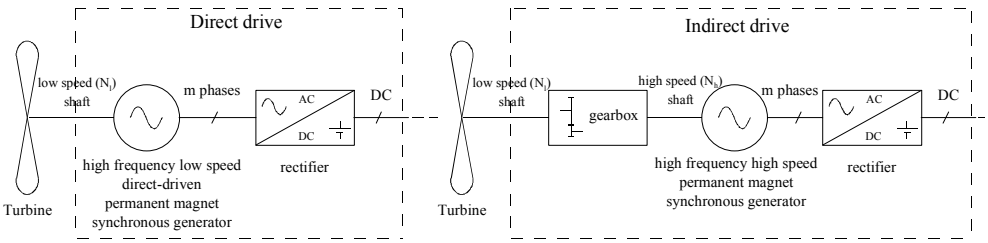

Figure 1. Linking the wind turbine to the generator

The first, the most common, links the turbine to the generator via a mechanical speed multiplier. In this configuration, the mechanical power is transmitted at high speed to the electrical machine. The size of the latter may then be easily reduced. This method has the major advantage of allowing the use of simply designed synchronous or asynchronous generators, which are readily available and inexpensive.

This first method is mainly used for high power wind turbines (above a few tens of kilowatts, to establish an order of magnitude) because at this power level, the large size of the generator becomes a problem, it becomes difficult to do without the speed multiplier.

The second, more recent, alternative is to link the generator directly to the turbine without a mechanical intermediary [8]. This method is known as "direct drive" and has become economically viable in recent years thanks to the progress made on permanent magnets. The cost of permanent magnets has dropped significantly while their performance has continued to improve. They have enabled the design of high performance, high power density, synchronous machines, well suited to the low speed operation imposed by the wind sensor, at reasonable cost.

The direct-drive method is attractive because it eliminates the weak element of the conversion chain: the speed multiplier gearbox. This is indeed a frequent source of failure, an additional noise source and may also require regular maintenance, resulting in high operating costs [8,9]. Finally, the multiplier can be the source of chemical pollution due to the lubricant oil. This explains why the latter option is widely preferred in the installation of small and medium size wind turbines for domestic applications, which are intended for operation over a long time without maintenance.

Above a certain power level, typically 10 kW, both methods become competitive in terms of cost; only a fine techno-economic study would tip the balance one way or the other.

As part of a medium-power design, there is a third method which offers an interesting alternative to the mechanical speed multiplier: the use of a magnetic gear [3-7]. This chapter, then, is devoted to the description of this device and shows the utility and feasibility of such a wind conversion chain. The different magnetic multiplier structures are presented and the design of this device will allow comparison with traditional solutions.

The advantage of the magnetic speed multiplier over its mechanical counterpart is clearly the contact-free force transmission that enables operation without any maintenance. We also show that the size and efficiency of magnetic speed multiplier are not prohibitive for the intended application.

2. Presentation of the magnetic speed multiplier

The principle of the magnetic speed reducer or multiplier is now well known, but the use of this type of converter is uncommon and usually reserved for low power [3-6]. We will show why the transmission of substantial power with very low wind turbine operating speed is useful.

The operation of the speed multiplier is based, firstly, on the principle of a Vernier type teeth coupling [1,2,10] between a series of alternating permanent magnets and a series of magnetic teeth. The following diagram, which represents a cylindrical or discoid developed structure, demonstrates the principle used in the calculation of the magnetic field in the air gap. In this device, a series of $2.N_r$ alternating permanent magnets, configured around a rotor, moves before a series of N_s magnetic teeth around a stator. The number N_s is different to N_r.

http://dx.doi.org/10.5772/51949

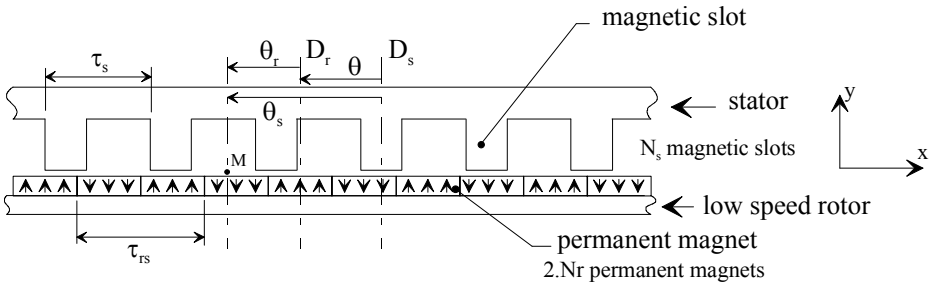

Figure 2. Cross-section of a Vernier machine with distributed windings

The calculation of the magnetic field at a point M, anywhere in the air gap, requires the azimuthal coordinates, θ_s and θ_r, identified respectively relative to the axis D_s, linked to the stator, and D_r, linked to the rotor. The angle, θ, between the two axes is a function of time.

The wave of flux density in the air gap, $b_a(\theta_s, \theta)$, created by the permanent magnets, is deduced from the following equation:

$$b_a(\theta_s,\theta) = P(\theta_s)\cdot\varepsilon_a(\theta_s,\theta) \tag{1}$$

where $\varepsilon_a(\theta_s, \theta)$ represents the scalar magnetic potential associated with the permanent magnets and $P(\theta_s)$ represents the density of the air gap permeance modulated by the magnetic teeth. We retain only the initial harmonics of these waves.

$$\varepsilon_a(\theta_s,\theta) = \varepsilon_1\cdot\cos N_r(\theta_s - \theta) \tag{2}$$

$$P = P_0 + P_{1s}\cdot\cos(N_s\theta_s) \tag{3}$$

The multiplication leads to:

$$b_a(\theta_s,\theta) = \tfrac{1}{2}\cdot\varepsilon_1\cdot P_{1s}\cdot\cos\left(\left(N_s - N_r\right)\cdot\theta_s + N_r\theta\right) + \tfrac{1}{2}\cdot\varepsilon_1\cdot P_{1s}\cdot\cos\left(\left(N_s + N_r\right)\cdot\theta_s - N_r\theta\right) + \varepsilon_1\cdot P_0\cdot\cos Nr(\theta_s - \theta) \tag{4}$$

The second term is without practical interest, its periodicity, $2\pi/|N_s+N_r|$, is too small for its implementation in a synchronous coupling with another magnetic field.

The third term, of a periodicity of $2\pi/N_r$, is quite simply linked to the distribution of the permanent magnets, and thus holds no interest for us in the mode of Vernier coupling as defined here.

We shall consider, then, only the first term, which is in fact the fundamental. Its periodicity, $2\pi/|N_s-N_r|$, is characteristic of the Vernier effect:

$$b_a(\theta_s,\theta) = b_{a1}\cdot\cos\left(\left(N_s - N_r\right)\cdot\theta_s + N_r\theta\right), \text{ with } b_{a1} = \tfrac{1}{2}\cdot\varepsilon_1\cdot P_{1s} \quad (5)$$

Taking $\theta = \Omega_r.t$, the term appears as a wave rotating at a speed of $N_r.\Omega_r/|N_s\text{-}N_r| = k_v.\ \Omega_r$, the coefficient k_v is known as the Vernier ratio.

With small sized permanent magnets (N_r large) it is possible to have a high speed ratio between the magnetic field rotation speed and the rotor rotation speed. It is this phenomenon which is used to design the speed multiplier. The main physical limitation of the process is that the smaller the magnets, the smaller the field b_{a1}, as a result of not being able to reduce the air gap sufficiently.

In the Vernier structure, provided that the number of magnetic teeth or permanent magnets is large, the pitch τ_s, seems to be little different from pitch τ_{rs}, it is then possible to isolate a pseudo repeat pattern, characteristic of the magnetic interaction between a tooth and two magnets. This pattern is fully defined by four adimensional parameters, α, Λ, s, ε, as shown in the figure 3.

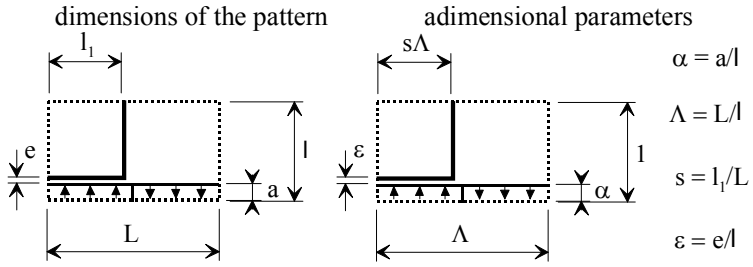

Figure 3. Elementary domain; tooth coupling

A parametric study conducted on the elementary pattern [1,10] allows us to quantify the amplitude of the first harmonic of the flux density, b_{a1}.

It is thus demonstrated, in [1], that b_{a1} that can be expressed as:

$$b_{a1} = \frac{\alpha\cdot\Lambda}{\left(\varepsilon+\alpha\right)^2}\cdot\frac{k_s}{\pi}\cdot B_{ar} \quad (6)$$

where B_{ar} represents the remanent magnetization of the permanent magnet.

A first approximation of the teeth coupling coefficient, k_s, obtained through numerical calculation of the magnetic fields, depends only on the adimensional parameters (α, Λ), and is given in the figure 4.

http://dx.doi.org/10.5772/51949

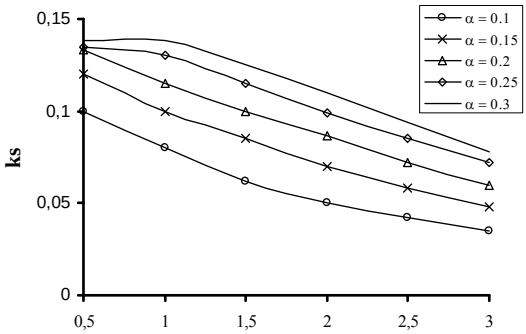

Figure 4. Variation of the coupling coefficient in terms of α and Λ

Taking the following typical values: $\Lambda = 1$, $\alpha = 0.2$, $\varepsilon = 0.05$, $B_{ar} = 1$ T, we obtain $k_s \approx 0.12$, i.e. $b_{a1} \approx 0.12$ T. It would appear that the magnetic field, b_a, is always weak, but in fact the field varies with time to a high frequency, becoming higher as N_r becomes greater. It is precisely this phenomenon which will be advantageously exploited in the transmission of mechanical force within the converter that we will describe.

The second principle used in the design of a magnetic speed multiplier is that of the magnetic coupler. This device combines two rotors through the magnetic field produced by permanent magnets.

In a magnetic speed multiplier, as shown in the figure below, an intermediate stator allows the decoupling of the velocity of the two rotors using the principle of teeth coupling as seen in the Vernier structure.

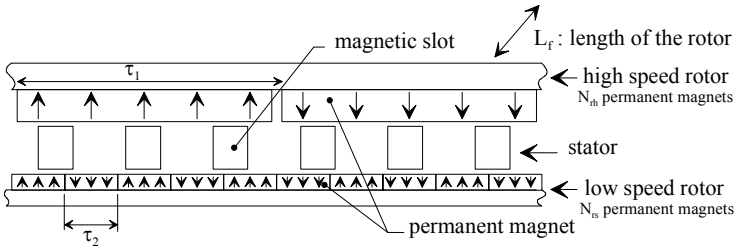

Figure 5. Magnetic gear: operating principle

The number of pairs of magnetic poles, p, of this structure, is defined by the number of pairs of permanent magnets linked to the high speed rotor, N_{rh}. This must correspond to the number of poles created by the coupling between the N_{rs} number of permanent magnet pairs on the low speed rotor, and the N_s stator teeth. The following formula must then be verified:

$$\left|N_s - N_{rs}\right| = p = N_{rh} \tag{7}$$

Operation is possible with $N_s > N_r$: the high speed rotor will then move in the opposite direction to the low speed rotor; or $N_r > N_s$: the two rotors will rotate in the same direction. Previous studies of Vernier structures [2] show however that the first configuration, $N_s > N_r$, is far better, giving higher force in relation to the air gap surface.

When the low speed rotor is displaced to the value of one small magnet pitch, τ_2, the high speed rotor will displace to the value of one large permanent magnet pitch, τ_1. The gear ratio is simply obtained by calculating the ratio of τ_1 and τ_2:

$$k_m = \left|N_{high} / N_{low}\right| = \tau_1 / \tau_2 = N_{rs} / N_{rh} = k_v \tag{8}$$

Operation in synchronous mode, characterized by the above equation, is possible only if the torque on the output shaft does not exceed a maximum value. We also show the consequences of a possible stall.

3. Intrinsic performance of magnetic speed multiplier

In a traditional speed multiplier gearbox, which transmits force via the intermediary of a mechanical contact, the sizing, in terms of transmissible torque, is dictated by considerations of wear and material strength. This is a good solution which allows compact structures, but the design must take into account many safety factors to reduce the risk of breakage, which is ultimately quite high [9].

The level of transmissible force without contact, via the intermediary of a magnetic field coupling within a magnetic gear, is obviously much weaker than with a traditional mechanical solution. On the other hand, it is not necessary to introduce safety factors that penalize the design, because there is no risk of breakage.

In order to quantify the performance level of the magnetic speed multiplier, we shall introduce tangential magnetic force density, defined by the following equation:

$$F_{st} = \frac{F_{\max}}{S_e} \tag{9}$$

Maximum force on the low speed rotor, F_{max}, is obtained when the flux density fields created by the permanent magnets of both rotors are phase shifted at an electric angle of $\pi/2$, as shown in the figure 6.

The tangential force density can be calculated from the elementary domain of width τ_1 and depth L_f. The air gap surface, S_e, is equal to $\tau_1.L_f$.

http://dx.doi.org/10.5772/51949

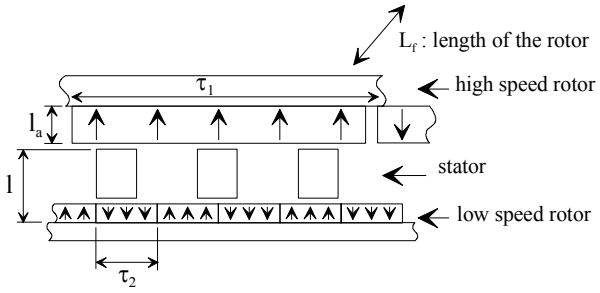

Figure 6. Position at maximum force

The calculation of F_{st} is made using a magnetic field, finite element, calculation software. Parameters are defined from the relative thickness of the main permanent magnet, $\beta = l_a/l$, and the multiplication ratio, k_v. The adimensional parameters of the magnetic pattern, relative to the low speed rotor, are arbitrarily assigned using the following values:

$\Lambda = 1$, $\alpha = 0.2$, $\varepsilon = 0.05$

These values generally give a good result in the Vernier machines design [1,10].

The air gap on the high speed rotor is defined as equal to one tenth of the thickness of the main magnet. This dimension, however, has less importance.

The following figure shows the flux lines within a configuration similar to that in figure 6, for a value of k_v equal to 5 and β equal to 1/2.

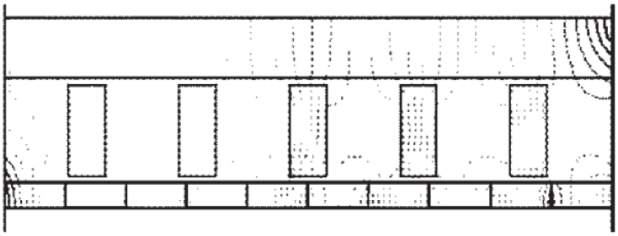

Figure 7. Flux lines in maximum force position

The tangential force density, F_{st}, is represented in figure 8 versus the relative thickness, β. These are trend curves in linear mode.

It is important to note that the tangential force density level reached in the speed multiplier, from 40 to 50.10^3 N/m², is significantly higher than that obtained in a conventional electromechanical converter, which is closer from 10 to 20.10^3 N/m², at steady state and with air cooling [10]. This complex phenomenon is created by the fact that in an electromechanical converter, one of the magnetic field components, that interact to create the torque, is created

by currents, with less efficiency than with permanent magnets, as is the case in the speed multiplier. This is a general principle observed in all converters using magnets.

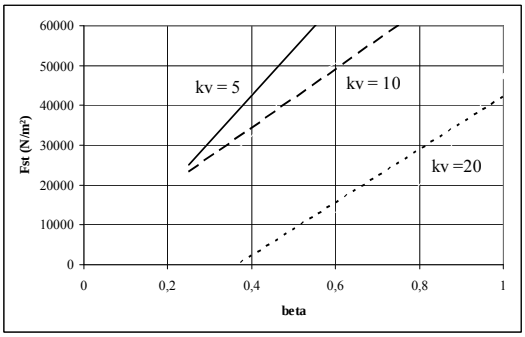

Figure 8. Tangential force density for different values of k_v (B_{ar} = 1.2 T)

Figure 9 shows, on the same basis, the evolution of the normal force density, $F_{sn} = F/S_e$, versus , for a value of k_v equal to 10.

The force F is perpendicular to the surfaces of the air gap; it produces no motive force but tends to introduce constraints on the bearings, as we shall see later. The normal force density is calculated for the low speed rotor and for the high speed rotor. It is much higher on the low speed rotor side, making it impossible to balance the force on the stator.

The normal force density level, which comes from the following relationship for flux density B, is, in most cases, still well above the level of tangential force density.

$$F_{sn} = \frac{B^2}{2 \cdot \mu_0} \tag{10}$$

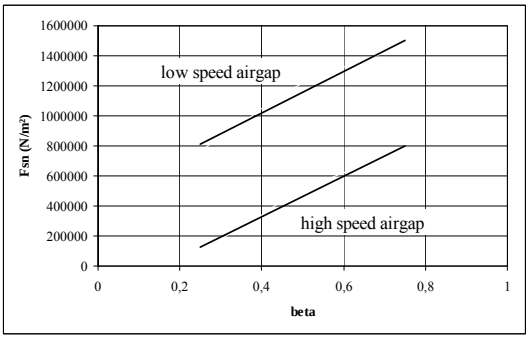

Figure 9. Normal force density (k_v = 10)

http://dx.doi.org/10.5772/51949

4. Different configurations of magnetic speed multiplier systems

The device described above can be applied in numerous ways within a wind conversion chain.

It must be noted that Vernier-type interaction, of the magnetic teeth with small permanent magnets, can be achieved directly in an electric motor [1,8], which has the double advantage of being of a relatively simple design, with high performance at low speeds, for the given reasons (electromechanical conversion at high frequency). This shows its potential for direct drive use, without multiplier.

Figure 10 shows the design of such a machine, with $N_s = 12$, $N_r = 10$, $p = 2$, $k_v = 5$. This configuration will be a base to compare performance, in the next paragraph, for sizing at 10kW, corresponding to a medium power wind turbine/conversion system.

Despite its main problem, which is that it operates naturally with a low power factor (typically 0.4 to 0.7), this configuration lends itself admirably to wind turbine generator design because its mass power ratio is unrivalled in this kind of application [8].

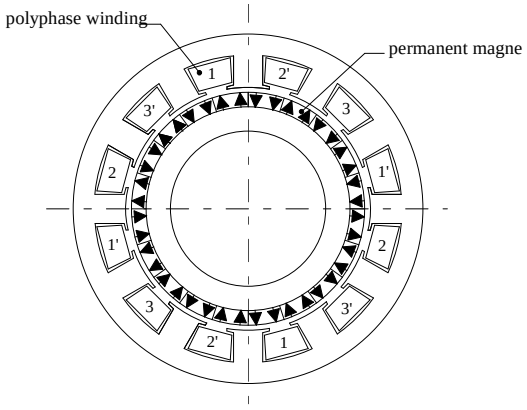

Figure 10. Vernier permanent magnet synchronous generator

The design of the magnetic speed multiplier conversion chain has the major advantage of allowing de-coupling between the electric problems (overheating, power factor …) and the problems arising from the Vernier effect in speed conversion.

We will also show that, given the high level of tangential force density attained in the multiplier, this solution may be more efficient in terms of weight and size than the more direct solution shown in Fig. 10.

The design generally adopted for the multiplier, based entirely on the principle described in figure 5, is thus the following:

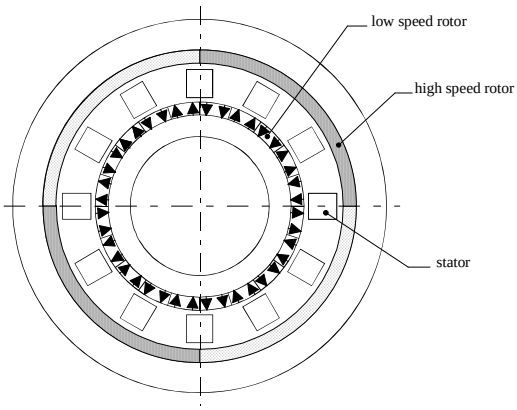

Figure 11. Magnetic speed multiplier with cylinder design

This figure immediately brings out a major difficulty in designing this type of device. This architecture is based on the overlap of three concentric cylinders, the two rotors and the stator, all rotating in relation to each other, the rotational guidance of the two rotors is necessarily delicate [3].

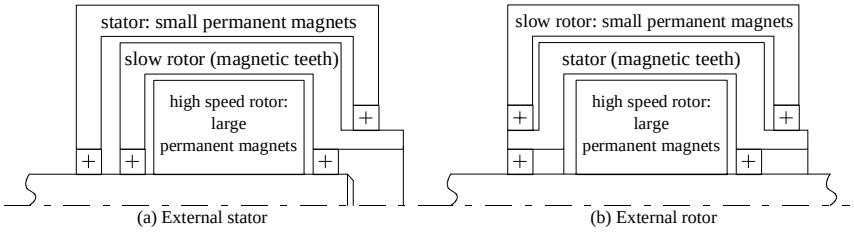

Figure 12. Arrangement of the bearings in cylindrical structure

The figure 12 shows two examples of bearing arrangement to solve the problem mentioned, but in all cases the additional constraints on by the bearings will be a source of accelerated aging of the structure.

In the first alternative arrangement (a), it is the magnetic teeth which act as low speed rotor. The small permanent magnets are on the stator. In the second arrangement (b), the magnetic teeth are fixed; the small permanent magnets are on the low speed rotor, which is external.

It should also be noted that the assembly consisting of alternating magnetic and nonmagnetic teeth is not easy to achieve because the magnetic teeth should be laminated or made with SMC material. The achievement of this complex, highly heterogeneous, structure, is still problematic.

The following photographs show an example of such a design. The magnetic teeth are secured using epoxy resin, the resulting assembly is reinforced by threaded rods visible in Figure 13(c).

http://dx.doi.org/10.5772/51949

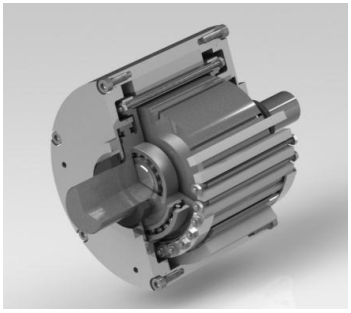

(a) Virtual photography

(b) Stator

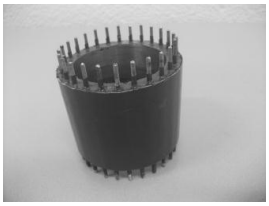

(c) Low speed rotor (magnetic teeth)

(d) High speed rotor

Figure 13. Prototype of a magnetic gear

An alternative solution to figures 10 and 11, described in [5,7], consists of combining the high-speed generator and the speed multiplier within the same structure, by inserting a polyphase winding between the magnetic teeth, in accordance with the following figure:

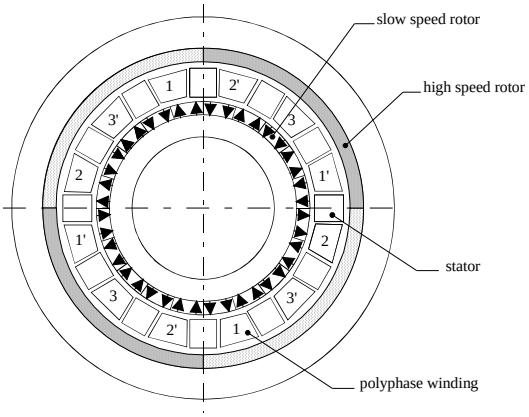

Figure 14. Combining the high-speed generator and the speed multiplier

This solution is attractive, but the technological design difficulties lead to sub-optimization (e.g. increase of air gap...), so it is highly unlikely that the result would be better than with the simplified solution seen in Figure 10.

The principle we have just described can be advantageously implemented in discoid structures, such as that in the figure 15, performing one or more multiplier stages.

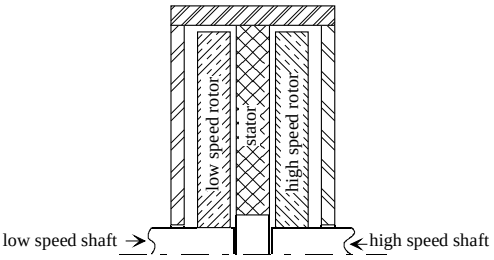

Figure 15. Magnetic speed multiplier: one stage discoid structure

This magnetic gear design has the advantage of being more compact than the cylindrical design for a higher level of torque, because it allows better use of the maximum radius. Above all, it has the advantage of being mechanically simpler; the rotors can be maintained by a simple bearing on each side of the stator.

On the other hand, in the structure shown in Figure 15, the rotors are subjected to huge axial forces that we will quantify, which will also constrain the bearings. This is typical of discoid structures and can be tricky to control. It is the main design problem.

5. Design of a magnetic gear

In order to clarify the potential uses of magnetic multipliers in the design of a wind conversion chain, we will size the electro mechanic device for an electric output power of 10 kW. This power output corresponds to an average power installation, for example for a small farm or a small group of isolated houses. This type of turbine has grown significantly.

To quantify the level of performance, we will compare the combination of multiplier and high-speed generator to a direct drive, low speed generator: a Vernier configuration like that in Figure 10. A study carried out in [1,8] shows that the power density of this configuration is significantly better than that obtained using a more conventional configuration with a large number of poles.

The nominal speed, N_{low}, of the wind turbine used for this study, is 150 RPM.

The following table presents the principal characteristics obtained with a Vernier generator operating in association with an active rectifier.

http://dx.doi.org/10.5772/51949

Characteristics	Values
N_s / N_r	108 / 90
Number of pole-pairs, armature winding	18
Nominal rotation speed (rpm)	150
f_e at nominal rotation speed (Hz)	225
Output power (kW)	10
E at nominal rotation speed (steady state) (V)	166
r (steady state) (Ω)	0,44
L_s (mH)	2,2
Joule losses (W)	650
Iron losses (W)	720
Torque ripple without load (cogging torque) (%)	0
Efficiency (%)	88

Table 1. Electrical characteristics of a 10 kW Vernier generator

The main dimensions of this generator are shown in Table 2.

Dimensions	Values
External diameter (mm)	500
Airgap diameter (mm)	468
Stator length (mm)	187
Rotor length (mm)	127
Internal diameter of the rotor (mm)	454
Mass, rotor and stator (kg)	26

Table 2. Principal dimensions of the Vernier generator

We observe that the high operating frequency, 225Hz, at low speed, 150 RPM, leads to a mass-power ratio of about 400 W/kg, taking into account only the weight of the active parts. The mass-power ratio of a conventional machine, with a large number of poles, would be in the order of 200W/kg. The efficiency of the Vernier machine is comparable to a conventional machine, under the same operating conditions, with more iron losses, but with less Joule loss. This is also a direct consequence of increased frequency.

The speed multiplier, which will be linked to a high speed machine, will be sized in operating conditions similar to that of the Vernier machine, in particular for the operating frequency of the low speed rotor, f_{rs}, which will be of the order of 225 Hz.

The low-speed rotor has N_{rs} permanent magnet pairs, the operating frequency, f_{rs}, is then equal to:

$$f_{rs} = \frac{N_{rs} \cdot N_{slow}}{60} \tag{11}$$

With f_{rs} = 225 Hz, we obtain N_{rs} = 90 pairs of permanent magnets for the entire low-speed rotor.

The choice of the multiplication ratio is an important parameter for optimizing the system; the higher the ratio the lower the size of the generator. On the other hand, in accordance with the results of Figure 8, the higher the ratio the lower the tangential force density within the multiplier, resulting in an increase of the size of the multiplier.

It is not within the scope of this chapter to optimize this system; we find simply that beyond k_v = 10, according to the results shown in Figure 8, the tangential force density decreases rapidly, so we will take k_v = 10 as the multiplication ratio, which leads to a nominal speed rotation of the generator, N_{high}, of 1500 RPM.

From this value we deduce the number of pole pairs, p:

$$p = \frac{N_{rs}}{k_v} = 9 \tag{12}$$

These selected values of p and N_{rs} will allow us to calculate the main dimensions of the multiplier as defined in the figure 16:

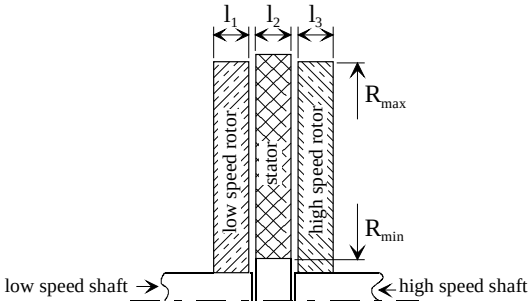

Figure 16. Main dimensions of the speed multiplier

The torque on the low-speed rotor is calculated from the discoid air gap surface and the tangential force density, F_{st}, as follows:

$$T_{low} = \frac{2}{3} \cdot \pi \leq \cdot (R_{\max}^3 - R_{\min}^3) \cdot F_{st} \tag{13}$$

http://dx.doi.org/10.5772/51949

The generator should deliver an electrical power of 10 kW with 90% efficiency. The generator input power, P_m, is then equal to 11.1 kW. Ignoring the efficiency of the speed multiplier, we get a torque, T_{low}, equal to:

$$T_{low} = \frac{60 \cdot P_m}{2 \cdot \pi \cdot N_{low}} \approx 700 \text{ Nm} \tag{14}$$

The tangential force density, F_{st}, being fixed to an average value of 40.10^3 N/m² in accordance with the results of Figure 8, the radius R_{max} and R_{min} can be deduced from the above formulae. Taking a value for R_{max} that is slightly lower than the outer radius of the Vernier machine, R_{max} = 210 mm, the radius, R_{min}, is equal to 100 mm.

The thicknesses of the speed multiplier discs, l_1, l_2, l_3, can be deduced from the dimensions of the small permanent magnets in the elementary domain defined in Figure 3, by adopting the following values for the adimensional parameters: $\Lambda = 1$, $\alpha = 0.2$, $\varepsilon = 0.05$. The calculation is lengthy but not difficult. The following table summarizes the dimensions of the (speed) multiplier:

Dimensions (mm)	Values
Thickness of the small permanent magnets	3
Thickness of the low speed magnetic yoke	20
l_1	23
Low speed air gap	0,75
Thickness of the high speed permanent magnets	7,5
Thickness of the high speed magnetic yoke	20
l_3	27,5
High speed air gap	0,75
Thickness of the magnetic teeth, l_2	11
Total lenght	63
Weight of active parts (kg)	**50**

Table 3. Dimensions of the magnetic speed multiplier

The obtained result shows that the mass of the magnetic gear is substantially greater than that of the Vernier machine, counting only the active parts. The structure of the Vernier machine being hollow, unlike that of the speed multiplier, the addition of structural elements gives us the same result, i.e. about 50 kg (for the entire device). The technologies used being similar, this result is to be expected.

On the other hand, the extremely compact structure of the discoid multiplier gives a smaller size than the direct drive Vernier machine, the external diameter being slightly smaller, the length is reduced by almost a third.

The associated generator works at a nominal speed of 1500 RPM. It is driven with a torque equal to one tenth of the low-speed torque, i.e. 70 Nm. Designed on the principle of a permanent magnet synchronous machine, for which a torque per unit mass of 2 Nm/kg is possible [10], the mass of the associated generator would be about 30 to 40 kg. This leads to a total mass of less than 100 kg for the multiplier and generator combined.

The specific power of the system is then equal to 100 W/kg.

The efficiency of the magnetic gear is essentially related to losses in the small permanent magnets from the low-speed rotor, and to losses in the magnetic teeth, which are subject to a highly variable magnetic field. So efficiency will be calculated on the basis of these losses, ignoring the iron losses in the magnetic yokes.

The figure 17 shows the spatial evolution of the magnetic flux density in the permanent magnets of the low-speed rotor (configuration of Figure 7).

In a Vernier structure, the temporal evolution of the magnetic field is similar to the spatial evolution, therefore, we note from the figure that the amplitude, ΔB, of the temporal component, is approximately equal to 0.4 T, with a magnetic field of 1.2 T when the permanent magnets are polarized in the forward direction, and 0.4 T when they are polarized in the opposite direction.

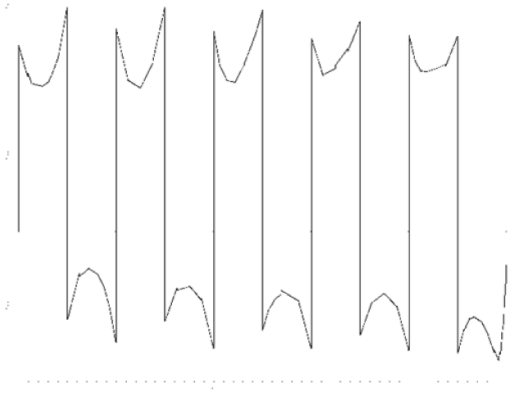

Figure 17. Flux density in the low-speed permanent magnets.

The permanent magnets are parallelepipeds 3 mm thick (in the direction of magnetization), 110 mm high and 5.4 mm wide on average; the volume, V_a, is equal to 1782 mm3. The following equation then allows the calculation of losses in a permanent magnet:

$$P_f = \frac{\pi^2 \cdot f^2 \cdot \Delta B^2 \cdot t_a^2}{6 \cdot \rho} \cdot V_a \tag{15}$$

http://dx.doi.org/10.5772/51949

Total losses in the permanent magnets are equal to $2\ N_{rs}\ P_f = 156$ W.

The figure 18 shows the spatial evolution of the magnetic field in the magnetic teeth (configuration of Figure 7).

The amplitude of variation of the magnetic field in the teeth is 1 T. The calculation of losses depends on the nature of the material used to make the teeth, and on the thickness of the lamination, if these teeth are made of stacked plates, so it is not possible to quantify the level of loss. However, taking an average value of specific loss, at 225 Hz and 1T, i.e. 15W/kg for a common material, with 2.75 kg of magnetic teeth, the losses are in the order of 40 W.

The efficiency of the magnetic gear, which follows from the previous calculation of losses, is close to 98%. Taking into account the additional iron losses and mechanical losses induced by stress on the bearings, efficiency remains well above 90%.

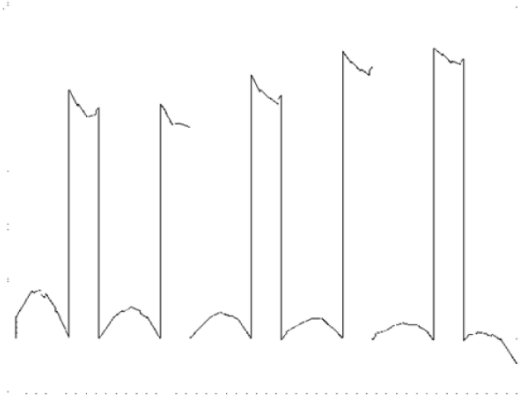

Figure 18. Flux density in the magnetic teeth

The final problem to consider in the design of the device lies in taking into account normal forces, F_1 and F_2, which act on the discs. These forces are calculated from the air gap surface and from the results of Figure 9. They are shown in Figure 19.

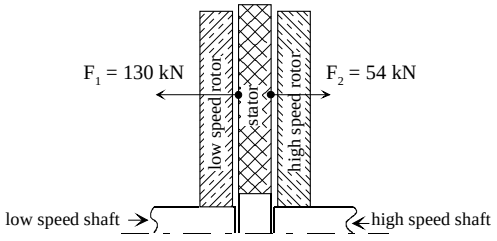

Figure 19. Normal forces

These forces are very high and are a major problem in bearing design. The axial force on the bearings is equal to the resultant force exerted on the stator, i.e. 76 kN. This problem exists in most discoid machines and hampers their development.

6. Stability in operation

The operation of the speed multiplier is of synchronous type, with no possibility of direct control, so there is a risk of stalling one rotor relative to the other. A precise study of this phenomenon is yet to be done (because, oddly, there is nothing definite on this subject in the bibliography). It goes without saying that this issue is delicate.

In the absence of a comprehensive study, the main solution to this problem in the design of the wind system is to monitor the electrical angle, ψ, between the magnetic fields from the two rotors through position sensors placed on the two shafts, or by indirect measurement through the voltage produced by a detection coil placed at the magnetic teeth.

When ψ tends to become greater than 90°, especially during rapid changes in the mechanical power from the wind turbine due to gusts, it is possible to influence the level of electrical power delivered by the generator in order to act on the dynamics of the driven load, allowing it to follow more easily the variations in speed.

However, the system becomes more stable as the maximum torque level transmitted by the multiplier is distanced from the maximum torque absorbed by the generator. This necessarily leads to oversizing of the speed multiplier.

The consequences of a possible stall are not really problematic for the intended application, provided that there is an electrical method of slowing down the wind turbine to allow mechanical braking or pitch control of the blades.

The addition of electrical conductors at the high speed rotor, intended to act as electrical shock absorbers and allowing the transmission of high asynchronous torque, makes the operation safer.

7. Conclusion

It has been shown that a system combining a magnetic speed multiplier and a high-speed generator is an interesting alternative to the use of a direct drive generator. The high performance level of the magnetic gear discoid structure allows the design of a more compact system with better efficiency.

In this context, despite its limited capacity in the transmission of torque, the magnetic speed multiplier has many advantages over its mechanical counterpart, but the cost will inevitably be higher because of the use of expensive materials.

http://dx.doi.org/10.5772/51949

The absence of maintenance of the magnetic device could nevertheless tip the economic balance towards the latter.

The magnetic gear discoid structure is particularly suitable for power levels of tens of kilowatts. The design made in paragraph 5, for a 10 kW wind turbine, confirms this. The same calculations show that a speed multiplier for a wind turbine of 40 kW (approx. 4000 Nm at 100 RPM), would have an external diameter of 800 mm, which is reasonable considering the mechanical structure.

For significantly higher powers, above 100 kilowatts, the design of a large diameter discoid structure becomes difficult, particularly because of the axial forces acting on the discs, according to what was discussed in Section 5. The solution is no longer economically viable.

At the opposite side of the power scale, for a wind turbine of a few hundred watts to several kilowatts, the use of a multiplier, mechanical or magnetic, is unwise. A structure of direct-drive generator, like that of Figure 10, for example, allows a more economical and more reliable design.

Magnetic gear technology is not yet fully developed and many of the mechanical problems in cylindrical or discoid design are yet to be resolved.

Author details

Daniel Matt[1], Julien Jac[2] and Nicolas Ziegler[2]

1 Institut d'Electronique du Sud - Université Montpellier 2, Montpellier, France

2 Société ERNEO SAS, Cap Alpha, Clapiers, France

References

[1] Matt D., Llibre J.F. Performances comparées des machines à aimants et à réluctance variable, J. Phys. III France 5, october 1995, 1621-1641.

[2] Toba A., Lipo T.A. Generic Torque-Maximizing Design Methodology of Surface Permanent-Magnet Vernier Machine. IEEE transactions on industry applications, vol. 36 n°6, November-December 2000, 1539-1545.

[3] Atallah K., Calverley S.D., Howe D. Design, analysis and realisation of a high performance magnetic gear, IEE Proc. Electr. Power Appl., Vol. 151, No. 2, March 2004, 135-143.

[4] Mezani S., Atallah K., Howe, D. A high-performance axial-field magnetic gear, Journal of applied physics 99, 1, 2006.

[5] Atallah K., Rens J.J. Patent WO2007/125284 A1, PCT/GB2007/001456.

[6] Brönn L., Wang R.J., Kamper M.J. Development of a shutter type magnetic gear, Proceedings of the 19th Southern African Universities Power Engineering Conference, SAUPEC 2010, University of the Witwatersrand, Johannesburg, 78-82.

[7] Jian L., Xu G., Gong Y., Song J., Liang J., Chang M. Electromagnetic Design and Analysis of a Novel Magnetic-Gear-Integrated Wind Power Generator Using Time-Stepping Finite Element Method, Progress In Electromagnetics Research, 113, 2011, 351-367.

[8] Matt D., Enrici P., Dumas F., Jac J. Optimisation of the association of electric generator and static converter for a medium power wind turbine, "Wind Power", InTech, http://www.intechopen.com/books/fundamental-and-advanced-topics-in-wind-power/optimisation-of-the-association-of-electric-generator-and-static-converter-for-a-medium-power-wind-t.

[9] Ragheb A.M., Ragheb M. Wind Turbine Gearbox Technologies, "Wind Power", InTech, http://www.intechopen.com/books/fundamental-and-advanced-topics-in-wind-power/wind-turbine-gearbox-technologies.

[10] Matt D., Tounzi A., Zaïm M.E. Low speed teeth coupling machines. In: Non-conventional Electrical Machines, ISTE (UK) and WILEY (USA), 2012, 39-116.

Chapter 11

Low Speed Wind Turbine Design

Horizon Gitano-Briggs

Additional information is available at the end of the chapter

http://dx.doi.org/10.5772/53141

1. Introduction

The use of wind turbines for electrical power generation has been around for over one hundred years. Recent concerns over the price and environmental impacts of fossil fuels have spurred the proliferation of wind turbines in a wide range of powers. Today there is a wide variety of commercial wind power systems commercially available. Even the lower power rated turbines, however, are generally designed for relatively high wind speeds, typically around 10 to 15 m/s [4]. At lower wind speeds typical of many inland sites in South East Asia the commercially available wind power systems do not produce a significant amount of power. This either excludes them from use, or results in very inefficient power extraction in lower wind speed regions. With careful design of the turbine and generator, power production greatly in excess of commercial turbines is possible at lower wind speeds. This will allow the use of wind power in applications in remote areas of South East Asia and around the world where low wind speeds prevail. This would include power for remote meteorological telemetry stations, radio repeaters, rural habitations and schools as well as applications requiring spark free power supplies, such as in the proximity of petroleum extraction, refining, refuelling and transportation sites and military outposts. This chapter is dedicated specifically to the design of low wind speed turbine systems. As the available power in the wind is significantly lower at low wind speeds we will be focusing on smaller turbines in the sub 1kW range.

2. Wind Power

The wind power captured by a turbine is commonly expressed as a function of the turbine's swept area and a coefficient of performance, the air density and the wind speed [8]

$$P_{turb} = \frac{1}{2} C_p \rho A V^3 \quad (1)$$

Where:

P_{turb} is the mechanical power of the turbine in Watts

C_p is the dimensionless coefficient of performance

ϱ is the air density in kg/m^3

A is the swept area of the turbine in m^2

V is the speed of the wind in m/s

For wind sites near sea level the atmospheric pressure is approximately 1.18 kg/m^3 and decreases with altitude. The coefficient of performance is related to the turbine design, and has a theoretical upper limit of 0.593, referred to as the Betz limit [5]. Most sub 10kW wind turbines are rated for speeds from 8 to 12m/s. The coefficient of performance of commercial small turbines generally falls in the range of 0.25 to 0.45 based on manufacturers rated powers, speeds and diameters. The power of a turbine is directly proportional to the swept area, thus it is proportional to the blade length squared. The factor with the largest influence on turbine power, however, is the wind speed. From the turbine cut-in speed to the rated speed a turbine's power is proportional to the cube of the wind speed. That means that a 10m/s wind will deliver eight times the power of a 5m/s wind. This is why most turbines have a fairly high rates wind speed: it is the easiest way to achieve a high power output.

3. Small Turbines

Small turbines are of a limited variety of designs due to cost and performance constraints. The most common design is a stall regulated, variable speed, horizontal axis, fixed pitch 3-blade, direct drive permanent magnet machine [3]. Blade pitch control would be difficult to justify economically, so the blades are given a fixed pitch, and optimized for power production at the rated speed. This results in poorer performance at lower speeds than could be achieved by a turbine with active pitch control. The ultimate speed of the turbine is determined by the wind speed and the applied load. Usually a power controller is still required to prevent turbine over speed, and over charging of the batteries. This power controller may also incorporate power matching circuitry allowing optimized power extraction from the wind turbine at various wind speeds [6]. Turbine over-speed is avoided by applying a low resistance dump load to the generator, increasing the load torque to the turbine, slowing the blades, and resulting in aerodynamic stall.

http://dx.doi.org/10.5772/53141

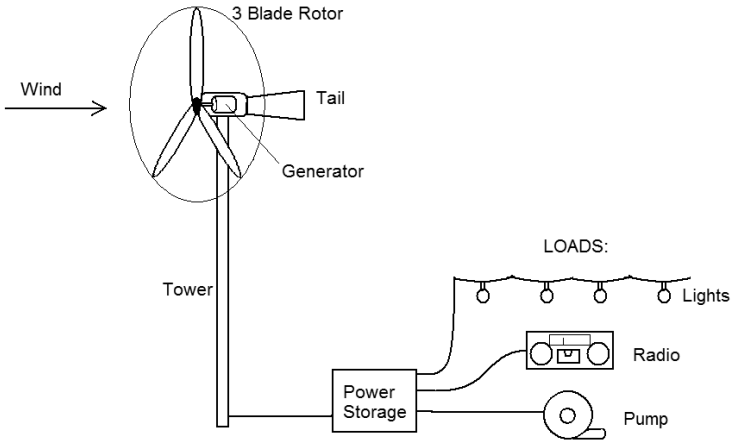

Figure 1. Schematic of typical small wind power system including wind turbine, storage system and loads

3.1. Commercial Small Turbines

There are significant differences between how various manufacturers state turbine specifications, however it is generally understood that the turbine will produce the rated power at the rated wind speed. Based on a survey of data published for small wind turbines we have selected the following typical commercial turbine specifications:

Turbine Diameter	m	1.6	2.7	5.5
Rated Wind Speed	m/s	10	10	10
Rated Power	W	300	1000	5000
Rated Turbine Speed	rpm	400	300	200
Predicted Power at 3 m/s	W	8	27	135
Coeficient of Performance		0.25	0.30	0.36

Table 1. Typical commercial turbine specifications

When these turbines are installed in a lower wind region the actual power produced will be significantly less than the rated power. In much of South-East Asia, for example, the average wind speed is only 3m/s. While this may be below the turbines cut in speed (the lowest speed at which it can produce power) assuming power is proportional to the cube of the wind speed we can calculate the theoretical power production at 3m/s, as enumerated in the table. It can be seen that the power production of these machines is far below the rated power, underscoring the need for turbine optimization for low wind speed regions.

3.2. Analysis of speed, power and Cp

One of the biggest factors affecting the performance of a turbine is the blade pitch angle. The pitch angle is the angle between the blade and the plane of rotation. The attack angle is the angle between the chord of the airfoil and the relative wind, as shown in figure 2.

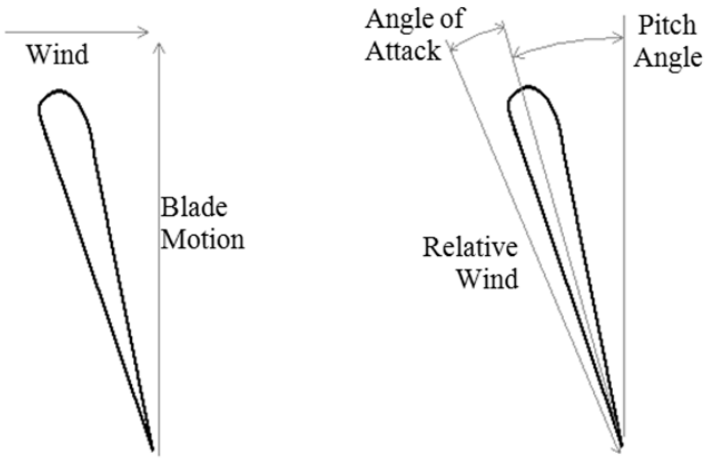

Figure 2. Wind vector, blade motion, pitch angle and angle of attack.

For most airfoils lift is maximized at an attack angle between 10 and 15 degrees. Obviously the angle of attack will depend on the wind speed and the turbine speed. A convenient parameter in the analysis of turbine performance is the Tip Speed Ratio (TSR) which is defined as the linear speed of the tip of the turbine blade divided by the prevailing wind speed. For a given wind speed, a lower pitch angle will result in a higher TSR at the maximum lift. A larger pitch angle will tend to give the maximum lift, and thus greater torque, at a lower TRS [11]. In the end higher coefficients of performance are achieved by blades with lower pitch angles and higher TRS, however at the expense of low speed torque which results in higher cut in speeds.

At very low wind speeds the turbine produces too little torque to overcome friction. Once the wind speed is sufficient to allow the turbine to rotate, the output power is approximately proportional to the cube of the wind speed. This remains true up to the rated speed. Above this speed the power production levels off, and with stall regulated turbines actually drops as wind speeds are increased. Finally at an even higher wind speed, the furling speed, the turbine is shut down to avoid damage to the machine. A typical turbine power curve is shown in figure 4.

http://dx.doi.org/10.5772/53141

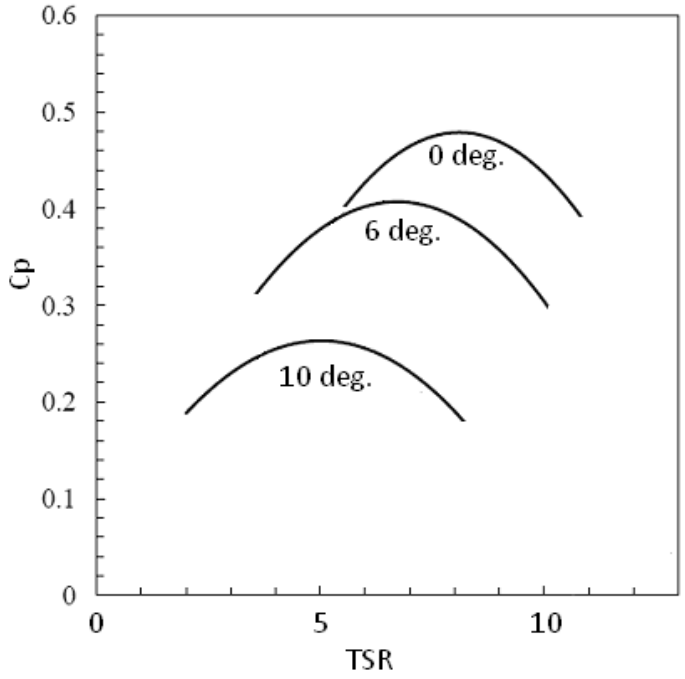

Figure 3. Coefficient of Performance variation with angle of attack versus TSR.

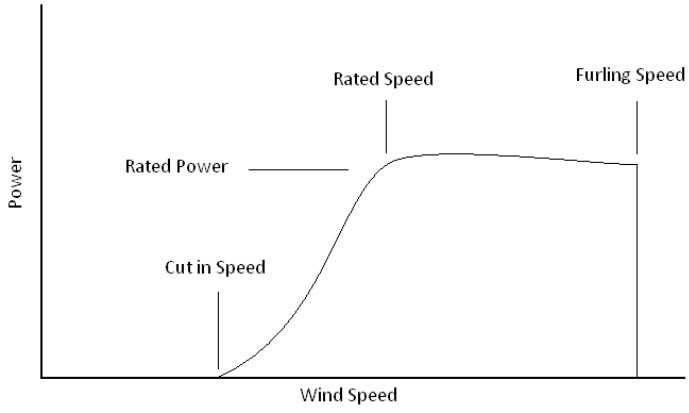

Figure 4. Turbine power versus wind speed.

Stresses in the turbine are related to the wind load, causing a bending of the blade in the direction of the wind, centrifugal forces, pulling the blades radialy outward, and various dy-

namic stresses. The centrifugal forces are proportional to the blade weight, blade length and square of the turbine speed, and limit the maximum speed of the turbine. Assuming similar materials and blade design, in order to achieve the same level of stress a larger, heavier, blade will have to spin at a lower speed than a smaller blade. This maximum speed of turbine operation becomes one of the limiting factors in the wind turbine, requiring either an extremely robust design or an active speed control system. Stall control systems are mechanically simple to implement, and thus common on small turbine systems. As the wind speed increases above the rated speed, a large electrical load, generally a high power resistor bank, is applied to the output of the generator. This increases the torque load on the turbine, slowing it. As the TSR is reduced, the angle of attack is raised above the optimum, and lift drops off as the blade begins to stall. This subsequently reduces the turbine's torque, slowing it further. This technique has been shown effective at preventing over speed in small turbines.

4. Design of Slow Wind Speed Wind Turbines

As previously stated, the problem of concern here is that existing commercial turbines are generally designed for wind speeds greatly in excess of typical wind speeds for major portions of the planet. Rather than simply exclude wind power from the potential energy scenario for these regions, we would like to design a small wind turbine especially for low wind speed regions [9]. Most of South East Asia (SEA) lies in a region of relatively low wind speeds. Wind speed data form a test site in Malaysia is shown in figure 5. Wind power probability is derived by multiplying the wind speed probability by the cube of the wind speed. The highest wind power probability is at approximately 3 m/s. At this wind speed commercial turbines will produce very little power.

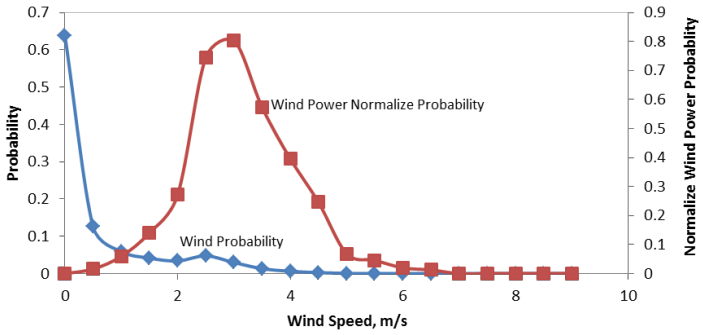

Figure 5. Wind and normalized wind power probability from a low wind speed test site

In order to improve power extraction the wind turbine requires a fundamental redesign. Equation 1 provides us the first indication of how to proceed. For a given wind speed we are left with modifying the turbine area, and optimizing the coefficient of performance. Control over the ambient air density is beyond the scope of this text. Lengthening the blades will

http://dx.doi.org/10.5772/53141

increase the cross sectional area of the turbine, increasing the power of the turbine. This will, however, also increase the load on the turbine and tend to result in a slower rate of rotation. Electrical power production from a generator is proportional to the square of the rotational speed, so it may be advantageous to adjust the pitch angle in order to maximize the TRS, and thus increase the generator speed. For low wind speeds both the turbine hub and generator will need re-optimization for the larger blades required to achieve a reasonable level of power production.

4.1. Overall Turbine Design

As a starting point for the design we will chose a system capable of providing power for a model rural dwelling typical of the remote regions of SEA. Such dwellings generally use rechargeable automotive lead acid batteries to power electrical lights, radios and televisions. These batteries are transported weekly to a diesel powered generator station for recharging. Transporting the batteries weekly is a significant burden to the rural residents which can be alleviated with the use of a wind power system. With improved access to electrical power the electrical power consumption will probably increase significantly. Additional power is likely to go to improved lighting, and additional appliances such as fans and even refrigerators. The actual power required will vary widely, but we will assume here that the typical house will consume approximately 1kWh per day.

The wind power system should have sufficient storage capacity for at lease one week with no power generation, thus we require at least 7kWh of electrical storage. As in most small off grid electrical power applications power will be stored in 12V automotive batteries. To minimize power transmission losses we will chose the highest system voltage considered safe for such applications. An operating voltage of 48V can be achieved with 4 batteries in series, and the constraint of 7kWh of energy storage then translates into a battery capacity of about 150Ah, similar to common truck batteries.

With good turbine sighting on a hill top, peak power probabilities of around 5m/s are possible in some costal regions of SEA. From long term measurements we can determine that the wind may achieve this target speed about 20% of the time, or 4.8 hours per day. Assuming that the turbine needs to generate about 1/3 more than the daily required power to compensate for loses in the system, we'll require about 1.3kWh per day of electrical power production. At 4.8 hours of power production per day the system will have to produce approximately 270W in the 5m/s wind. Assuming a generator efficiency of 80% and a Cp of 0.29, from equation 1 we can determine the area of the turbine to be 15.9m^2, yielding a blade length of approximately 2.25m. If we accept a conventional TSR of around 8, the turbine will be spinning at 170 rpm. Based on some initial measurements it was determined that a conventional generator design would require a much higher rotational speed to achieve the desired power output, so we will target twice this speed, or 340rpm. The operational TSR will be optimized via turbine blade pitch adjustment during field testing of the system, but we will target a TSR of 16, twice the conventional ratio. The operating current of the generator at this point will be approximately 5.8A.

Leveraging off of existing small turbine designs [1] the generator is to be a 3-phase, axial flux synchronous permanent magnet generator. We have selected a 12 pole design with 25 x 50mm, 11mm thick nickel plated NdFeB magnets. The generator is based around an automotive wheel bearing and disk brake, thereby defining the rotor diameters. The initial specifications for the turbine are listed in table 2.

Wind Speed	m/s	5
Power	W	272
Balde Legnth	m	2.25
Cp		0.29
Generator speed	rpm	340
Generator Efficiency	%	80
Voltage	V	48
Current	A	5.8
Poles		12
Phases		3
Rotor ID	mm	125
Rotor OD	mm	360

Table 2. Wind turbine and generator initial specifications

5. Experimental Results

Taking the well publicized small turbine design of Hugh Piggot as the starting point, we studied several generator and turbine parameters in order to optimize the design for the lower speed wind [10]. Generator measurements were performed on an electric motor driven dynamometer allowing simultaneous measurements of both mechanical and electrical power. The final generator was then placed in service on a turbine with adjustable pitch blades. The turbine power output was measured along with the wind speed for turbine optimization.

5.1. Generator Optimization

Initially a basic study of open circuit voltage was performed. Several coils with varying numbers of turns were prepared from 1mm diameter enamel coated magnet wire. In each case the coils were wrapped on a 20 x 40mm oval shaped core, slightly smaller than the rotor magnets. The thickness of the coil in the axial direction, which defines the thickness of the stator, was kept constant at 10mm. As the coils grow larger, the space between adjacent coils decreases, resulting in a maximum coil size of approximately 150 x 100mm. As can be seen in figure 6 the open circuit voltage increases linearly with the number of turns.

http://dx.doi.org/10.5772/53141

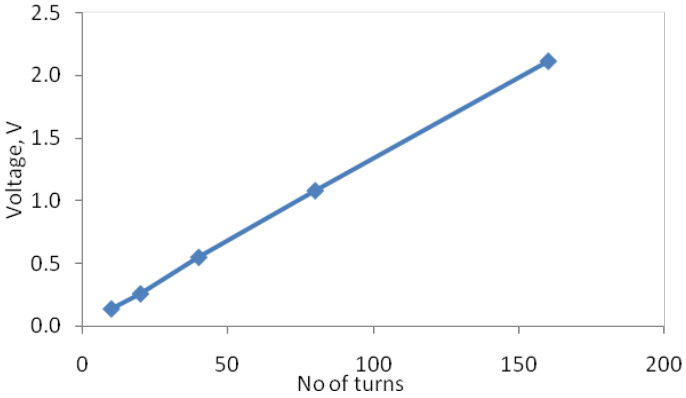

Figure 6. Individual coil open circuit voltage vs. number of turns at 50 rpm

If the coils were allowed to grow larger eventually contradictory flux from adjacent magnet pairs could enter the larger coils reducing the net flux and thus the voltage. With the current design the largest coils possible for a given stator thickness will deliver the maximum power.

For maximum flux transfer through the coils of motors and generators the coils have cores of laminated soft iron, or other magnetically conductive materials in an electrically insulating design (to reduce eddy currents). These soft iron cores provide a low resistance path for magnetic flux to pass through the coils. This however will also cause a significant "cogging" torque as the magnets tend to stick in positions over the cores [10]. High cogging torque will raise the turbine cut in speed, thus most low speed turbines are produced without magnetic materials in the cores, resulting in "core less" or "air core" coils. While the utility of this is appreciated, we decided to test both an air core coil and an identical coil with a core of steel baring epoxy. This epoxy was found to have very high electrical resistance, and significant magnetic susceptibility. The cores were tested on the generator dynamometer rotating at 125 rpm yielding the results in table 3. As only a single coil was installed, the resulting power extraction and efficiencies are very low. Both the electrical and mechanical power increase with the use of the epoxy in the coil's core as expected from the greater flux transfer. The efficiency of the epoxy core coil is also slightly higher than the air core coil. The cogging torque was measured to be significantly smaller than the rotor's bearing friction, thus the epoxy core coils were selected for the final configuration generator.

	Torque (Nm)	Mechanical Power (W)	Voltage (V)	Current (A)	Electrical power (W)	Efficiency
Epoxy Coil	1.13	14.2	2.3	0.98	2.25	0.16
Air Coil	0.91	11.4	1.9	0.81	1.54	0.14

Table 3. Comparison between air core and metal filled epoxy core coils

Another important optimization was the stator axial thickness. A thicker stator will allow more turns of wire, increasing the output voltage, however it will also require a greater rotor spacing distance. As the rotors are spaced further apart, more flux from the magnets will tend to "short circuit" to the adjacent magnets, rather than traverse the stator to the magnet on the opposite stator [3]. This situation is shown in figure 7

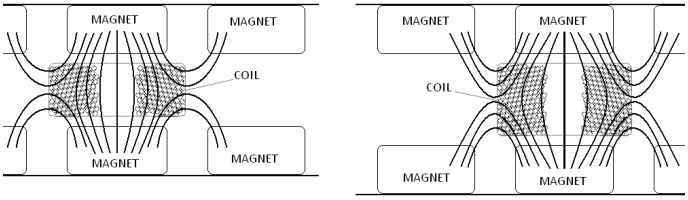

Figure 7. Lateral flux short circuiting to adjacent magnets increases (right) with increased rotor separation distance.

The induced voltage per turn can be seen to drop rapidly as the rotors are spaced further apart in figure 8.

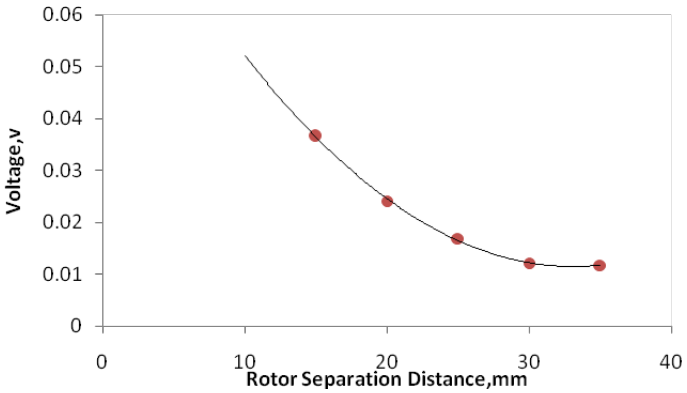

Figure 8. Voltage per turn versus rotor separation distance at 125 rpm

For a given rotor separation distance there is a maximum number of coil turns which will fit between the rotors. A margin of 2.5 mm is provided between the magnet surfaces and the stator to avoid physical contact, and allow air flow to cool the stator coils. Thus for a 10mm rotor separation, the stator is limited to a 5mm thickness which will allow about 50 turns per coil.

Coils of 5, 10 and 15mm thicknesses were prepared for 10, 15 and 20mm rotor separations respectively. These coils were then tested on the generator dynamometer at 125 rpm yielding the data of table 4.

http://dx.doi.org/10.5772/53141

Rotors Separation Distance (mm)	10	15	20
No. of Coil Turns	50	100	150
Total Open Circuit Voltage (v)	2.25	3.7	3.6
Coil Thickness (mm)	5	10	15

Table 4. Open circuit voltage and coil parameters for various rotor separation distances.

As the rotors are moved closer together, the magnetic flux passing through the coil increases producing a higher open circuit voltage per coil turn. However the smaller separation distance results in a smaller number of turns per coil. To achieve maximum open circuit voltage, there is a compromise between number of turns and rotors separation distance. As shown in the Table 4 the 15mm rotor separation distance will give the maximum open circuit voltage.

A generator was fabricated with the largest coils possible in a 10mm stator, and the cores were filled with metal bearing epoxy. The generator was then tested on the dynamometer with various loads. Figure 9 shows the results of electrical power measurements with the generator connected to various resistance loads.

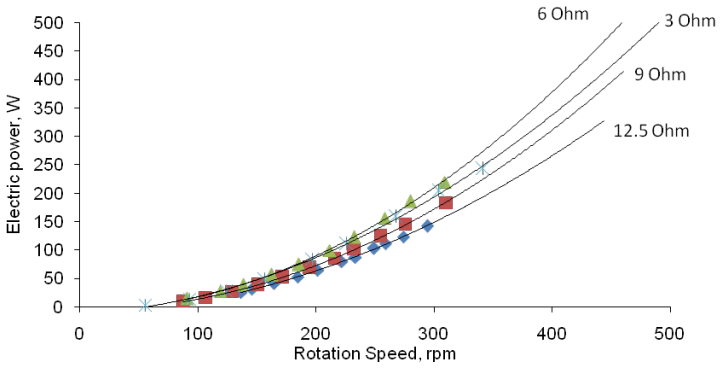

Figure 9. Power versus rotational speed for various loads

The maximum power of the system was produced with the 6 ohm load which is approximately equal to the internal resistance of the stator as the resistance per coil is 0.67ohm and there are 9 coils in series. Our initial design required approximately 270W of power production at 340 rpm. This power was above the capabilities of the relatively low power dynamometer, but falls within the range of power production predicted based on the square of the speed (black trend line) for the 6 ohm load.

5.1. Turbine Optimization

The generator was then placed in service on the roof of the mechanical engineering building as shown in figure 10. The 2.25 meter long wooden blades were fabricated with a NACA 4412 profile commonly used for low speed turbines. During testing the turbine blades were set to a given pitch angle and the generator was connected to a fixed resistance load. Wind speed and electrical power production data was then continuously logged. After several weeks of testing the turbine would then be adjusted to a new angle of attack and/or the load resistance would be changed.

Due to inconsistencies in the wind, not all configurations were tested at the same speeds for the same durations. Overall trends, however, were readily apparent. During the period of field testing the maximum instantaneous wind speed recorded was 8m/s while the maximum sustained wind speed was around 4 to 5m/s.

Figure 10. Wind turbine with optimized generator during turbine evaluation. Notice the anemometer in the background to the left.

The data generated during testing at the 9 degree attack angle shown in figure 11 was typical of the testing. The turbine's cut in speed is around 2m/s, and power output increases rapidly with wind speed for all load resistances. Data for the 3 and 6 ohm loads show the 3 ohm load having slightly higher power output below 3 m/s and the 6 ohm load giving greater power above 3 m/s. Theoretically the 6 ohm load should give the greatest power extraction as the load is well matched to the generator. In general the 6 ohm load gave the best power extraction, and was selected for further analysis.

http://dx.doi.org/10.5772/53141

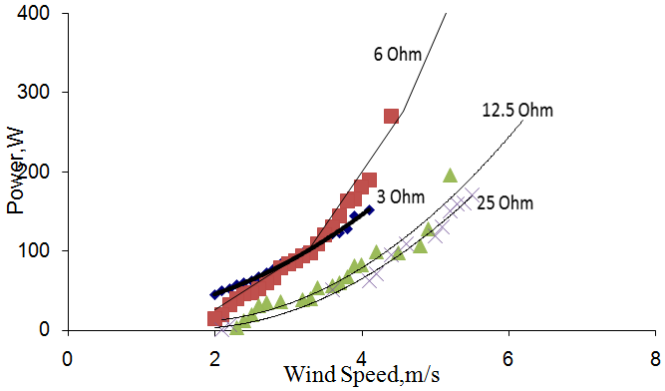

Figure 11. Electrical power versus wind speed at various loads for 9 degree angle of attack

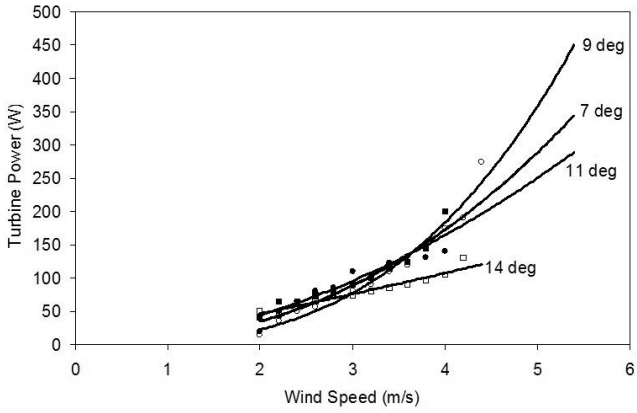

Figure 12. Electrical power vs wind speed at various angles of attack for the 6 ohm load

The power production was not a strong function of angle of attack in the 7 to 11 degree range, but dropped significantly at 14 degrees. Based on extrapolation of the data to higher speeds, the 9 degree angle of attack is expected to give the highest power production in the 3.5 to 5 m/s wind speed range.

Taking the best fit curve to the 9 degree angle of attack blade pitch with the 6 ohm load (figure 13) we can calculate that the turbine should produce about 200W at a 4.2 m/s wind speed. Taking this with the known turbine blade length of 2.25 meters and an assumed generator efficiency of 80% [7], we can use equation 1 to calculate the coefficient of performance to be 0.36, somewhat better than the assumed value of 0.29.

Additional measurements made on the turbine bearings indicated frictional losses account for 23W at 300 rpm. This is approximately 10% of the electrical power produced. The use of automotive bearings is perhaps not optimal from a friction stand point, thus with improvements in the bearings it may be possible to improve the turbine output by something on the order of perhaps 5% or so.

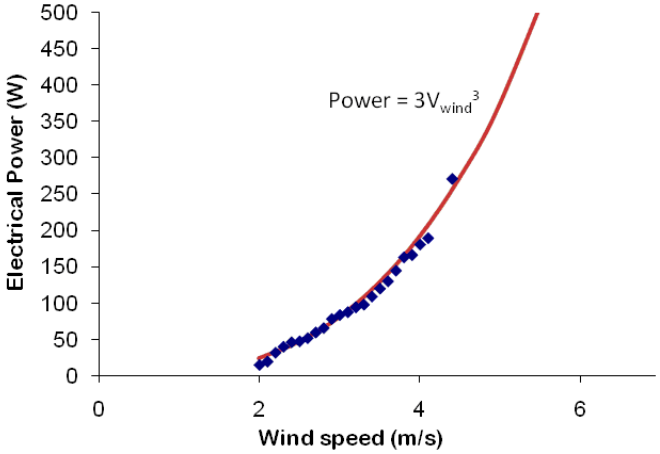

Figure 13. Electrical power versus wind speed at 9 degree attack angle with 6 ohm load

Looking back at figure 9 we can see that a 200W output should occur at approximately 300rpm with the 6 ohm load. Using this to calculate the TSR at a 4.2m/s wind speed we come up with a TRS of 17, close to our assumed value of 16, and significantly higher than the conventional value of 8.

6. Performance Comparison

Taking the measured turbine performance we can predict the power production versus wind speed. Based on manufacturers published performance curved our turbine can be compared to existing commercial turbines. Wind data was recorded at a proposed turbine test site on a costal facing ridge at an altitude of 400m at Banjaran Relau in Kedah, Malaysia. This gave slightly higher wind speeds than the turbine test site atop the mechanical engineering building. A sample of the wind data is shown in figure 14.

The wind speed data exhibits a diurnal pattern with some marine layer pumping associated with the proximity to the coast with the highest winds speeds in the afternoon. Additionally is can be seen that there can be several days, eg. day 13 to 18 in figure 14, with very little wind underscoring the need for significant storage capacity.

http://dx.doi.org/10.5772/53141

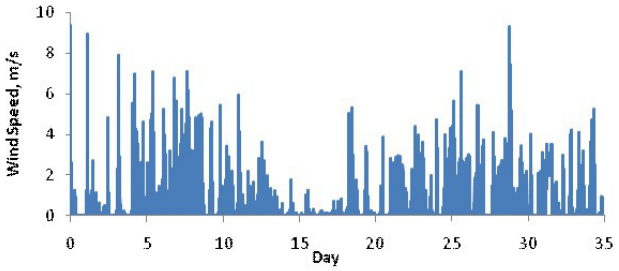

Figure 14. Wind speed the Banjaran Relau turbine test site in Kedah, Malaysia

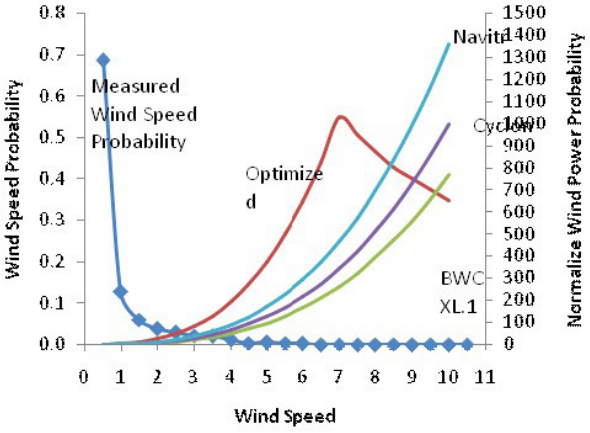

Figure 15. Wind probability and predicted electrical power production versus wind speed for several commercial turbines, and the turbine developed in this study.

Figure 15 shows the power produced by three small commercial turbines, and the one developed in this study versus wind speed, as well as the wind probability at the turbine test site. As the optimized turbine will be spinning at a higher rotational speed than the other turbines, the controller will begin electrical breaking at wind speeds above 7m/s, effectively negating the turbine's output above this speed. This is not overly restrictive as the wind rarely blows at speeds above 7m/s for more than a few minutes per month.

It can be seen that the optimized turbine produces significantly more power than the commercial turbines at the lower wind speeds, and of course significantly less power at the higher speeds the other turbines are rated for. This is expected as the optimized turbine has a larger swept area, and has been tuned for low wind speed operation.

Multiplying the generator's power times the wind speed probability at each wind speed, we can derive the normalized power production curves of figure 16. Peak power probability for this data set is at 3m/s, with a lower peak in the power probability curve at 4.5m/s. As the wind speed at the test site never exceeded 7m/s for any significant amount of time the optimized turbine is shown to generate 3 to 4 times more power than the commercial turbines over the whole available wind speed range. There is a dip in the wind probability data at around 4m/s in the data over the period sampled due to the limited amount of data. In general we would expect a fairly smooth wind probability profile with a peak between 3.5 and 4.5m/s at this wind site.

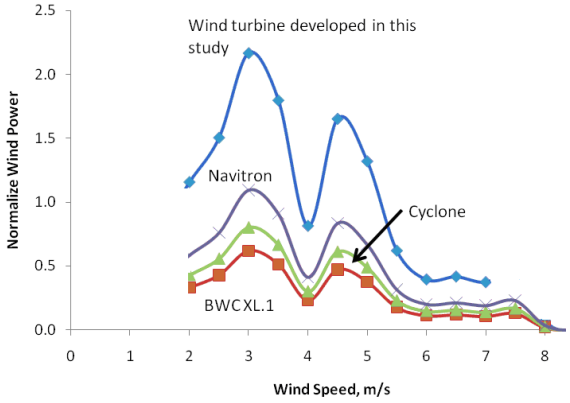

Figure 16. Comparison of normalize wind power for various wind turbines

Power production in a 5 m/s wind is expected to be around 350W, and in a region producing this wind for 4.8 hours of production per day, should result in 1.68 kWh of energy production per day. Assuming storage losses of 30% associated with charge/discharge of batteries and power transmission this will result in about 1.2kWh of usable energy per day, close to our initial estimate of 1.3kWh per day required for a rural dwelling. Thus it is expected that a purpose designed 2.25m radius wind turbine of relatively simple construction is sufficient to power a single rural dwelling in the windier parts of SEA.

7. Conclusion

Most commercial turbines are designed for relatively high wind speeds, around 10m/s, produce insignificant amounts of power below 5m/s. Taking a conventional axial flux, direct drive horizontal axis 3-blade wind turbine as the starting point we were able to optimize the turbine and generator for lower wind speed operation and achieve a significantly higher power output than existing commercial turbines at lower wind speeds. Further optimization of the turbine is possible and should focus on airfoil shape, blade weight and construction

http://dx.doi.org/10.5772/53141

and bearing friction. While the use of larger blades will increase the cost and weight of the turbine and tower it is still believed that wind power can be a viable alternative even in regions of relatively low winds.

Author details

Horizon Gitano-Briggs*

Address all correspondence to: horizonusm@yahoo.com

University Kuala Lumpur – MSI, Malaysia

References

[1] Aydin, M., Huang, S., & Lipo, T. A. (2004). Axial Flux Permanent Magnet Disc Machines: A Review.

[2] Chalmers, B. J., & Wu, W. (1999). An Axial Flux Permanent Magnet Generator for a Gearless Wind Energy System. *IEEE Transactions on Energy Conversion*, 14(2), June, pg., 610-616.

[3] Chan, T. F., & Lai, L. L. (2007). An Axial-Flux Permanent-Magnet Synchronous Generator for a Direct-Coupled Wind Turbine System. Journal of IEEE Transactions on Energy Conversion March, 22(1)

[4] Chen, Y. C., Pillay, P., & Khan, A. (2005). PM Wind Generator Topologies. *IEEE Transactions on Industry Applications*, 41(6), November/December.

[5] Dwinnell, J. H. (1949). Principles of Aerodynamics McGraw-Hill, New York.

[6] Gitano-Briggs, H. (2010). Wind Power. 9-78953-761-9.

[7] Grauers, A. (1996). Efficiency of Three Wind Energy Generator Systems. *Journal of IEEE Transactions on Energy Conversion*, 11(3), September.

[8] Johnson, G. (1985). Wind Energy Systems Prentice-Hall. *Engelwood Cliffs NJ*, 013957754801.

[9] Li, H., & Chen, Z. (2009). Design Optimization and Site Matching of Direct-Drive Permanent Magent Wind Power Generator Systems. *Journal of Renewable Energy*, 34, 1175-1184.

[10] Piggot, H. (2012). www.scoraigwind.com, accessed 30-07-2012.

[11] Sathyajith, Mathew. (2006). Wind Energy, Fundamentals, Resource Analysis and Economics. *Springer*, 103540309055.

Chapter 12

Wind Power Variability and Singular Events

Sergio Martin-Martínez,
Antonio Vigueras-Rodríguez, Emilio Gómez-Lázaro,
Angel Molina-García, Eduard Muljadi and
Michael Milligan

Additional information is available at the end of the chapter

http://dx.doi.org/10.5772/52654

1. Introduction

There are several sources of wind power variability, including short-term (seconds to minutes) and long-term (hours of the day, or seasonal). The type of wind turbine, the control algorithm, and wind speed fluctuations all affect the short-term power fluctuation at each turbine. The blade of a Type 1 induction generator wind turbine experiences the tower shadow effect every time a blade passes the tower; the output of the Type 1 turbine commonly fluctuates because of this. Wind turbines Type 3 and Type 4 are equipped with power electronics and have a reasonable range of speed variation; thus, the impact of the tower shadow effect is masked by the power converter control. Because of wind speed fluctuations and wind turbulence, the power output also influences the output of the wind turbine generator.

However, in the big picture, the power fluctuation at a single turbine is not as important as the total power output of a wind power plant. The interface between the wind power plant and the power system grid is called the point of interconnection (POI). All the meters to calculate revenue, measure voltage and frequency, and measure other power quality attributes are installed at the POI. At the POI, all the output power from individual turbines is injected into the power grid. A wind power plant covers a very large area; thus, there are various diversities within each plant (e.g., wind speed, line impedance, and instantaneous terminal voltage at each turbine). The power measurement from a single wind turbine usually shows a large fluctuation of output power; however, because many turbines are connected in a wind power plant, the power fluctuation from one turbine may cancel that of another, which effectively rectifies the power fluctuation of the overall plant.

Additionally, many wind power plants are co-located in the same region where wind resources are excellent; thus, the spatial diversity among wind power plants contributes to a smoother output power of the region than the output power of an individual wind power plant.

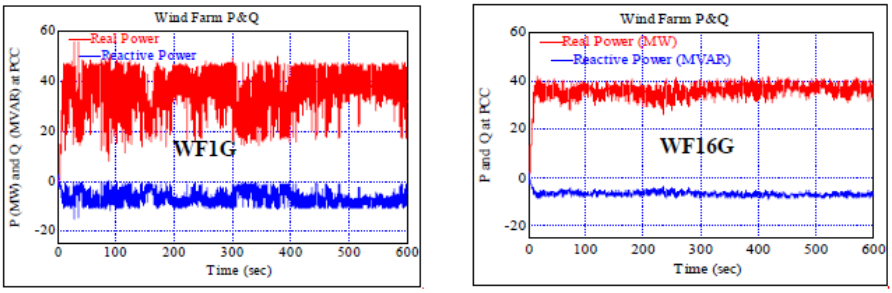

Figure 1. Real and reactive power output of a wind power plant; (a) Single turbine representation (b) Sixteen turbines representation

Figure 1(a) shows the fluctuation in the output power when the wind power plant is represented by a single turbine. Figure 1(b) illustrates the real and reactive power output when the wind power plant is represented by sixteen turbines. With greater wind diversity, as shown in Figure 1(b), the power fluctuation is smoother than that with less wind turbine representation, as shown in Figure 1(a) [1].

2. Wind speed variability

Overall wind variability consists of different fluctuating terms with different periods, depending on the sources. For instance, fluctuating term can be caused by day-night effects (e.g., the effects of sea breeze), because there are "quick" fluctuations in some minute periods.

Figure 2 shows a typical power curve of a variable speed wind turbine generator. In general, the operating wind speed is divided into different regions. In Region 1 and Region 2 (low to rated wind speed), a wind turbine is operated in variable speed at a constant pitch angle (typically 0^{o}). The output power of the generator is low to rated power. The operation is optimum because the turbine is operated at the maximum performance coefficient Cp. When wind speed varies, the output power varies as the cube of wind speed variations. Once wind reaches its rated speed, the rotational speed also reaches the rated speed. This rotational speed must be limited by the pitch control to keep the rotor speed from a runaway condition and to limit the mechanical stresses of the wind turbine structure (tower, blades, and gearbox). The output power is limited to its rated value.

Thus, wind power output varies only when wind speeds are below rated value. Below rated wind speed, the rate of change of the output power $\left(\frac{dP}{dt}\right)$ is either positive or negative, de-

http://dx.doi.org/10.5772/52654

pending on the direction of wind speed change. Above rated wind speeds, any fluctuations will be capped at rated by the pitch action, or $\frac{dP}{dt}=0$.

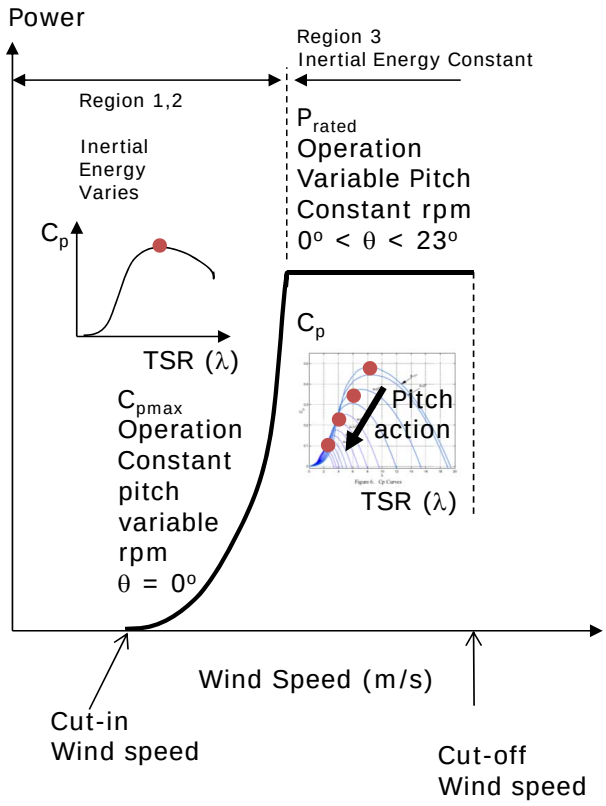

Figure 2. Power curve of a typical wind turbine generator

If the power controller is not properly designed, wind fluctuations may excite the mechanical resonance of the structure or gearbox, which may lead to mechanical failures of the wind turbine [2]–[3].

Spectral tools are often used to analyze wind speed variability because they make it possible to study different frequency fluctuation terms. The most popular one used for this purpose is the Power Spectral Density (PSD).

The PSD of a function is defined by the Fourier transform of its autocorrelation. PSD is therefore expressed in frequency domain. Its physical meaning is related to fluctuating kinetic energy on a certain frequency.

Van der Hoven [4] analyzed the PSD of horizontal wind speed, based mainly on measurements done at Brookhaven National Laboratory. Figure 3 shows such spectra, with two main peaks and a spectral gap between them. The first peak occurred at a period of around four days and was caused by migratory pressure systems of a synoptic weather map scale. The second peak occurred at a period of 1 minute because of a mechanical and/or convective type of turbulence. Van der Hoven's observations also showed some relation between the spectral gap shape and surface roughness under some circumstances. Additional analysis shows more complex spectra, especially over the ocean or in smooth terrains [5]–[9]; where there is an important contribution of mesoscale fluctuations combined with various phenomena such as convective longitudinal rolls [11] or cumulus clouds [12] that may contain considerable spectral density in the frequency range. At some other places, the gap was verified by experimental data [4], [13]–[14].

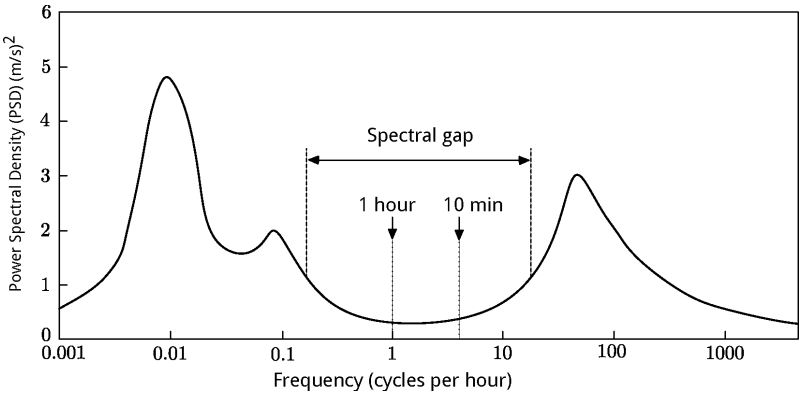

Figure 3. Spectrum estimated by Van der Hoven [4]

PSD spectrum is usually calculated by using short segments of data with similar atmospheric characteristics. The reduction or removal of the spectral gap introduces some difficulties on the analysis because microscale and macroscale are no longer separated. This limits the findings of particular atmospheric regimes lasting long enough to calculate a meaningful spectrum. Thus, some researchers are considering the use of more complex spectral tools based on time and frequency domain. For instance, the Hilbert-Huang transform has been used for analyzing wind fluctuations over the North Sea [8].

Wind speed variability is important with regard to power system management. An example of the significance of these power fluctuations is in Energinet.dk (the Danish Transmission System Operator). According to [15], Energinet.dk has observed that power fluctuations from the 160-MW offshore wind power plant at Horns Rev in West Denmark introduce several challenges to reliable operation of the local power system. The power fluctuations also contribute to deviations from the planned power exchange with the Central European Power System. Moreover, it was observed that the timescale of the power fluctuations was from tens of minutes to several hours.

http://dx.doi.org/10.5772/52654

Figure 4 shows the relation between time and geographical scales and the impacts affecting power system operation. Depending on the level of the wind power penetration, power fluctuations due to wind speed variability may influence the frequency regulation; transmission and distribution efficiency, and load flow; or even efficiency of the thermal and hydro power plants connected to the same grid.

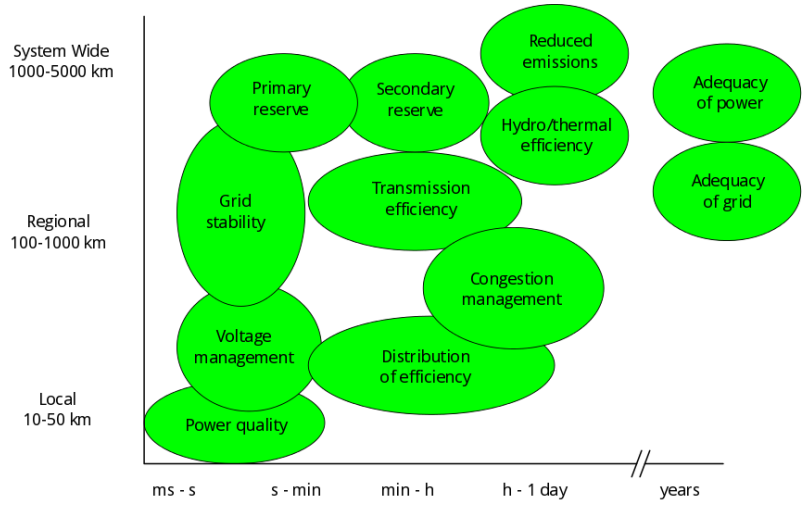

Figure 4. Time and geographical scales of power system issues [16]

3. From wind speed variability to regional wind power fluctuations

As highlighted above, from the point of view of power systems, it is important to analyze wind power fluctuations from tens of minutes to several hours. Therefore, it is important to study the relation between wind speed variability and wind power fluctuations.

Different operating regions give different rates of power fluctuations. The first stage in the conversion of wind power to electrical power is the smoothing and sampling effect produced by the size of the wind turbine rotor. In fact, some variations in wind speed at a single point within the rotor swept area are smoothed out when considering the entire blade length. Particularly, uncorrelated oscillations of wind speed are attenuated when considering several points within the rotor swept area. To analyze the correlation between such oscillations, spectral coherence is usually considered. Studies have been done of spectral coherence between the horizontal wind speeds within the rotor disk, showing a large smoothing of the (high-frequency) quickest variations [17]. To illustrate these effects, Figure 5 compares wind speed at a single point within the rotor swept area, with an equivalent wind speed over the rotor disk [18].

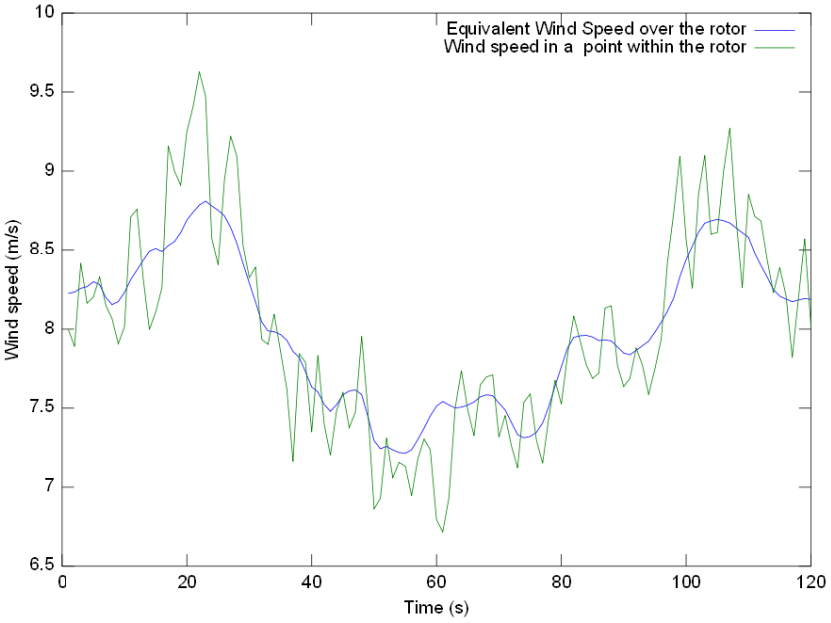

Figure 5. Comparison between wind speed in a single point of the rotor disk and the equivalent wind over the rotor disk

Moreover, the conversion of wind energy into electrical power is not linear. In a typical power curve (Fig. 2), there are wind speed ranges with different impacts on the conversion from wind speed variations to wind power fluctuations. Between cut-in wind speed and nominal wind speed, variability in power tends to amplify wind speed variability because of the "near" cubic dependence between power and wind speed. On the other hand, for wind speeds below cut-in wind speed or between nominal and cut-out wind speed, power fluctuations are smoothed considerably. However, if wind speed crosses cut-out speed or oscillates around it, fluctuations can be significantly increased as power varies from 100% (rated output power) to 0% (when the wind power plant is disconnected above cut out wind speeds). Figure 6 shows two different series of power: the reduction or increasing of variability depending on the wind speed range within the wind turbine power curve.

The second stage considers the reduction of the power fluctuations when aggregating several wind turbines within a wind power plant and even aggregating wind power plants in a large region. Aggregated power fluctuations are reduced by the diversity of the wind speeds within a large area. Analogously to the effect mentioned above, with regard to the rotor disk effect, spectral coherence can also be studied in wind power plants or even larger regions, analyzing which parts of the power fluctuations are not correlated or even which parts are delayed between wind turbines or power plants [19]–[20]. Studies on spectral coherence in wind power plants or regions can be found in the literature [21]–[23]. Examples

http://dx.doi.org/10.5772/52654

of those effects are illustrated in Figure 7 and Figure 8, where power in a single turbine is compared with the aggregated power of a wind power plant and a set of wind power plants, respectively.

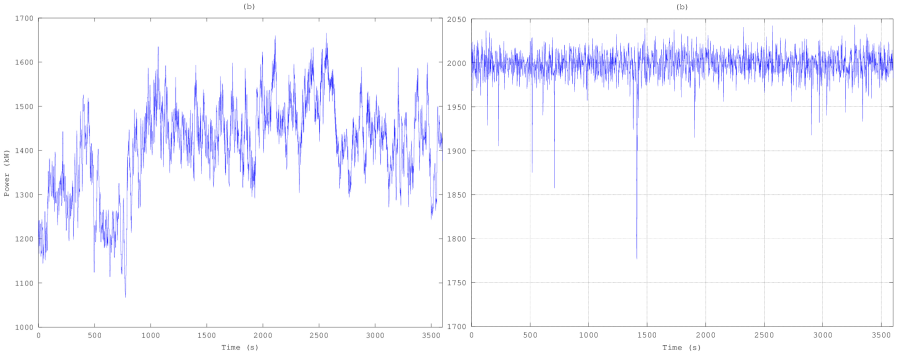

Figure 6. The figure on the left shows the power generated from a single wind turbine when wind is between cut-in and nominal speed; whereas the figure on the right shows wind speed between nominal and cut-out speed [23]

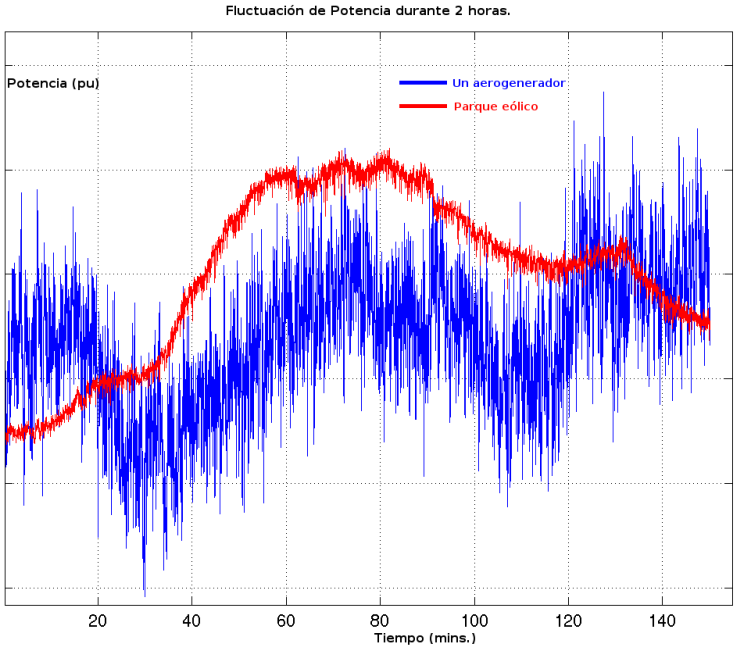

Figure 7. Comparison between a single wind turbine in an offshore wind power plant and the aggregated production of the whole wind power plant

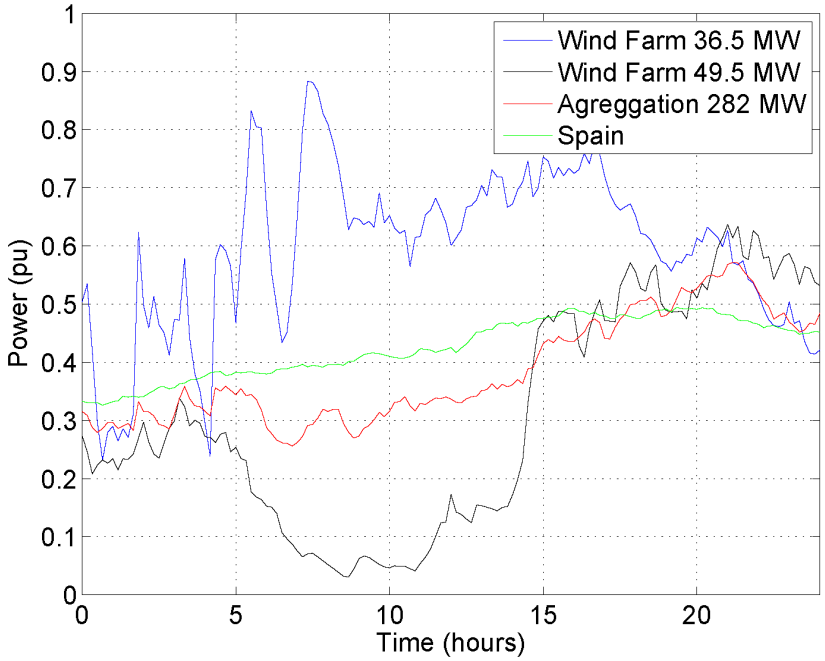

Figure 8. Comparison between the power produced by two wind power plants with the aggregation of nine wind power plants (including the previous ones) and the whole of Spanish wind power output

Finally, when aggregation includes different types of wind turbines, with different nominal wind speeds and different cut-out speeds, extreme aggregated fluctuations are also reduced significantly.In short, temporal diversities and spatial diversities reduces the peak-to-peak magnitudes of power fluctuations.

On the other hand, some regions wind power fluctuations are not related wind speed variability. Instead, the power fluctuations are caused by technical and operational challenges rather than by meteorological phenomena.Particularly, these include:

- Voltage sags. Voltage sags produce a sudden drop of wind power generation. This drop is usually recovered is quickly.
- Wind power curtailment. This is due to integration issues in the power system, such as limitations on the transmission or distribution networks, inability to ramp up or ramp down other generation sources, lack of enough reserves, etc.

Another classification is laid down. Attending to their ramping characteristics, wind power fluctuations events can be classified in:

- Wind power die-out. A wind power die-out refers to a persistent drop in wind power.

- Wind power rise. A wind power rise consists in a sustained rise in wind power that can create a persistent ramp up.
- Wind power lull. Wind die-outs are inevitably followed by wind rises. When both events happen in short succession, they form a wind power lull or a wind power dip.
- Wind power gust. A wind gust is opposite of a wind lull: it starts with a ramp up and ends with a ramp down.

4. Overview of spanish experience dealing with wind power variability: Examples of singular events

In this section, examples of the Spanish experience of singular events produced by either wind speed variability or operational issues are examined.

4.1. Voltage sags

Wind turbine manufacturers are required by transmission system operators (TSOs) to equip their turbines with fault ride-through (FRT) capability as the penetration of wind energy in the electrical systems grows [25]. Spain developed a procedure to measure and to evaluate the response of wind turbines and wind power plants subjected to voltage sags [26].The procedure for verification, validation, and certification of the requirements are described in the PO 12.3. This wind power plant commissioning and validation are based on the response of wind power plants in the event of voltage sags. The result of wind power plant commissioning leads to the certification of its conformity with the response requirements specified in the Spanish grid code [27]. Some aspects related to that grid code are explained in detail in [28]–[29].

On the other hand, because of the growing impact on power grid operations, the recent rapid expansion of wind generation has given rise to widespread interest in field testing and commissioning of wind power plants and wind turbines. Validation of computer dynamic models of wind turbines is not a trivial issue. Validation must ensure that wind turbine models represent with sufficient accuracy the performance of the real turbine, especially during severe transient disturbances [30]. In [32], different field tests for model validation and standards compliance are categorized according to the main input or stimulus in the test—control stimulus and external physical stimulus. Among these tests, the FRT capability of wind turbines can be performed using factory tests, at the individual wind turbine generator terminals, and using short-circuit field measurement data based on operational wind turbines and wind power plants.

Short-circuit field measurement data on operational wind turbines and wind power plants [33]—called opportunistic wind power plant testing in [31]—is performed with measurement equipment installed at the wind power plant site. The equipment records naturally occurring power system disturbances that are then used to validate wind turbine models. Power system modeling during the disturbances must be taken into account in the validation of wind turbine models. Therefore, monitoring wind power plants and wind turbines

can be of interest for turbine manufacturers, wind power plant operators, and TSOs.Both the pre fault and the post fault data and power system network must be represented properly.

An extreme event recorded in Spain related to voltage sags occurred on March 19 and 20, 2007.Within twelve hours, four different disconnections of large amounts of wind power because of voltage sags were recorded. Those voltage sags were located in areas with high penetration wind power and during high wind speed periods. Figure 9 shows the recorded Spanish wind power output during these events.

The amount of wind power generation disconnected during these voltage sags were 553 MW, 454 MW, 989 MW, and 966 MW, respectively.

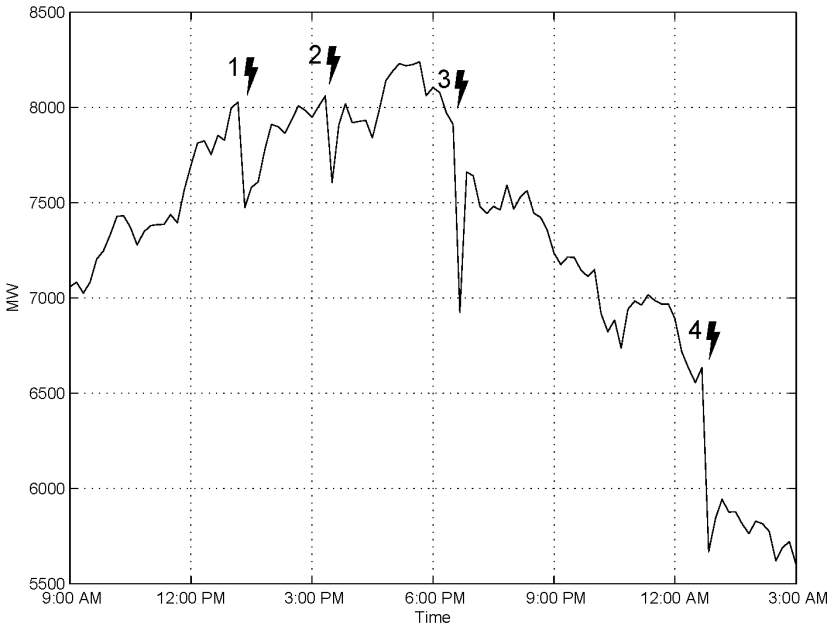

Figure 9. Spanish wind power during the voltage sags on March 19 and 20, 2007

In addition, nine Spanish wind power plants located in different areas were also analyzed during these events. Nominal power of these wind power plants varied from 6.8 MW at Wind Power plant 9 to 49.5 MW at Wind Power plant 4. In Figure 10, the wind power output from these nine wind power plants are presented. Highlights include:

- Wind Power plants 1, 2, and 3 are located in the same area. They were at high fluctuating partial load. These power plants were not affected by voltage sags because they were far away from the faults.
- Voltage Sags 1 and 2 affected only Wind Power plant 4.

http://dx.doi.org/10.5772/52654

- Voltage Sag 3 affected Wind Power plants 5, 6, and 7. These wind power plants are nearby. In these three cases, the responses to the sag were similar.
- Only Wind Power plant 9 was affected by Voltage Sag 4.
- All voltage sags during this period were located in areas with high wind power penetration.

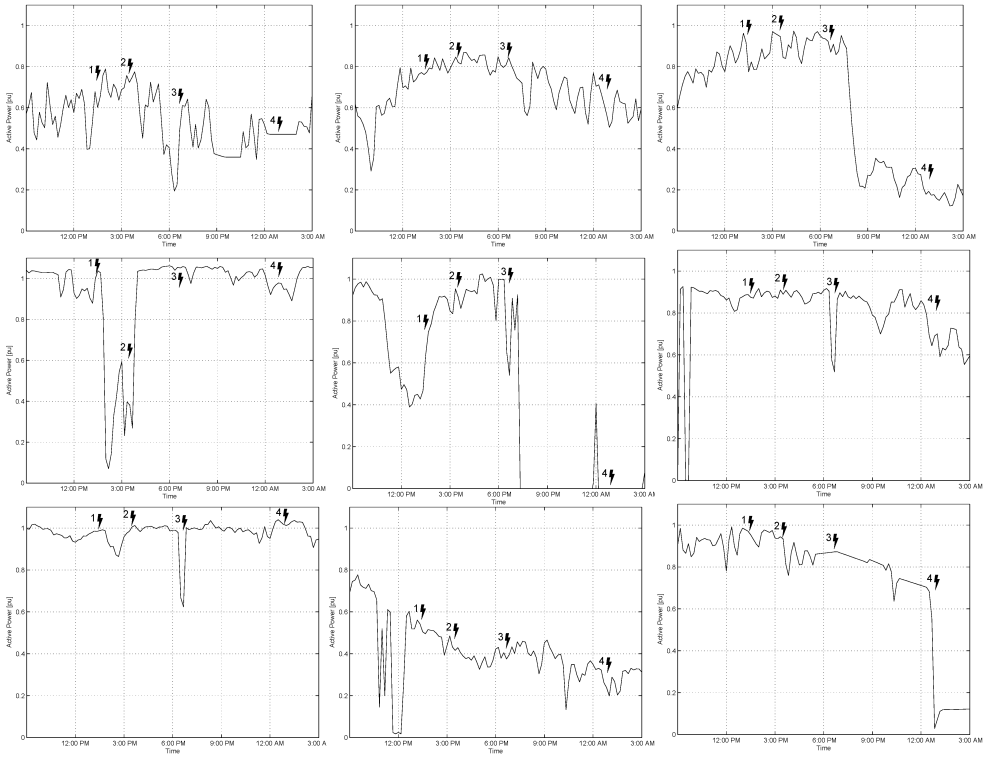

Figure 10. Wind power production of nine wind power plants during voltage sags on March 19 and 20, 2007

The operation of power systems under the effect of voltage sags in wind power has led TSOs to require FRT capability in wind power plants. By the end of 2010, 704 Spanish wind power plants had been certified against FRT capability (19.2 GW and around 95% of the installed capacity). A total of 1 GW wind turbines are excluded because of their missed manufacturers, small size, or because they are prototypes turbines. Figure 11 shows the number of power losses greater than 100 MW from 2005 and the percentage of wind power without FRT. As a result of the FRT implementations, the problem of significant wind generation tripping has been solved; therefore, wind plant curtailments have not been required since 2008.

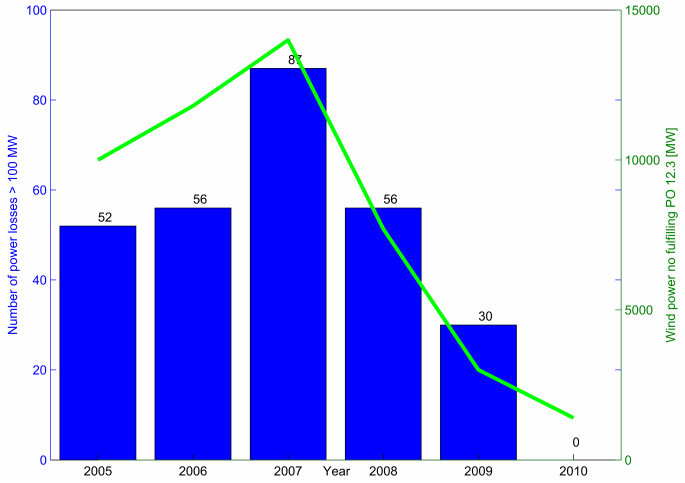

Figure 11. Evolution of wind power with FRT and number of power losses greater or equal to 100 MW by voltage sags in Spain [34]

The implementation of the supervisory control and data acquisition of wind generation in real time have decreased the number and the size of power curtailments, improved the quality and the security of the electricity supply, and maximized renewable energy integration. To further enhance wind energy integration, the Spanish TSO (Red Eléctrica de España, or REE) submitted a proposal of a new grid code (P.O 12.2) to the Ministry, with additional technical requirements for FRT, among others. The main purpose this proposal is to anticipate the expected problems in the Spanish power system between 2016 and 2020, by taking into account the incoming plants and new power plants to be deployed during these years to come. It is expected that P.O. 12.2 can be approved and applied in 2013.

4.2. Klaus Storm (January 23, 24, and 25, 2010)

Meteorological phenomena (e.g., storms or cyclones) are capable of causing large variations in wind power production and very high wind speeds.A storm within this category can affect a large number of wind turbines that have approximately the same cut-out wind speeds. When the cut-out speed is reached, the power generated goes from rated power to zero immediately. If this phenomenon spreads over several wind power plants in a particular area, it can cause a major threat to the power system stability and may lead to a cascading blackout.

The storm Klaus was named after an extra-tropical mid-latitude cyclone that struck between January 23 to January 25, 2009, affecting northern Spain and southern France. Wind speeds of higher than 150 km/h were recorded in the Spanish and French coastlines. The result was the disconnection of many wind power plants in northern areas of Spain, leading to a reduction of about 7,000 MW of wind power in a few hours (refer to Figure 12). Figure 13 shows the impact of the storm on a Spanish wind power plant.The wind power plant consists of 30 NEG Micon 82 Wind Turbines with a nominal power of 49.5 MW.

http://dx.doi.org/10.5772/52654

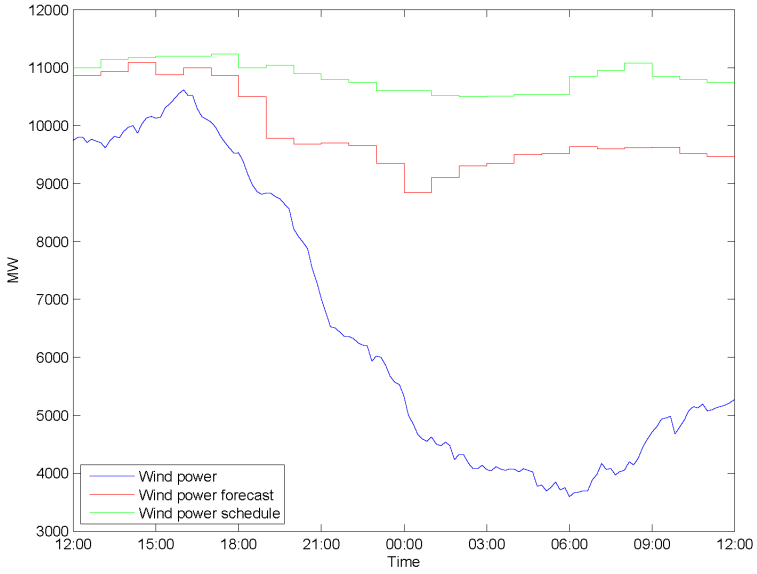

Figure 12. Wind power, forecasting, and schedule during the Klaus storm

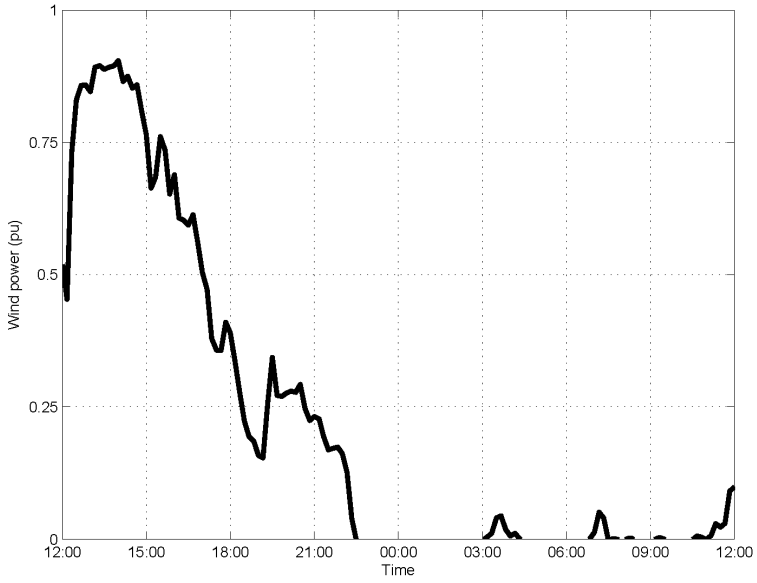

Figure 13. Wind power in a 49.5-MW wind power plant during the Klaus storm

During this emergency situation, the Spanish TSO REE has deployed several thermal power plants to increase the reserve power generation. Despite of the large difference between the forecast and actual wind power production, the power system continued to operate within the normal operating range.

This example shows the difficulties for forecasting wind power during these types of events.Differences between forecast and real wind power generation reached almost 6,000 MW. Furthermore, wind power decrement during the storm happened in the night, thus, it followed the ramping down of the daily load, so the increased reserves generation (6 GW) were sufficient to maintain the system balance.

4.3. Wind power curtailments

Wind energy curtailments because of integration issues in the power system have appeared in the Spanish power system. Until 2009, major curtailments were due to limitations on distribution networks, but since the end of 2009, cuts have been applied in real time to scheduled energy. However, the nature of renewable energy along with the economic and environmental issues, have provoked an interest in adding energy storage (such as pumped hydro storage PHS, a well-known technologies) into the power system mix.Spain accounts for around 5,000 MW (2.75 GW of pure PHS), with 77 GWh capacity. This technology is usually deployed because of the limited transmission capacity for exporting or importing power to neighboring countries.

As an example of wind power curtailment, Table 1 indexes orders delivered by the Spanish TSO on February 28, 2010. The initial and end times for every curtailment period are presented in columns 1 and 2. Column 3 represents Spanish wind power at the beginning of the period. In column 4, the Spanish TSO set point for this period is listed. In column 5, the real increase or reduction experimented by Spanish wind power in this period is shown. Finally, the ratio between the real increase/decrease and the increase/decrease obtained if wind power would match the set point is presented in column 6. In decrease periods, this ratio is equal to or higher than 1; in increase periods, it is equal to or less than 1, 1 being the optimum value.

Initial Time	End Time	Wind Power (MW)	Wind Power Set Point (MW)	Real Increase/Reduction (MW)	Ratio
1:08	2:07	7796	7331	-796	1.71
2:07	3:48	6470	6099	-718	1.93
3:48	6:08	5175	4904	-720	2.66
6:08	8:45	4036	5904	217	0.11
8:45	9:10	3772	6905	420	0.14
9:10	9:43	3807	7905	276	0.07
9:43	–	4209	Installed capacity	–	–

Table 1. Curtailment schedule on February 28, 2010

http://dx.doi.org/10.5772/52654

4.4. Over-response to wind power curtailments

On January 1, 2010, the REE gave instructions for several wind power curtailments considering "Non-Integrable Wind Power Excess" as defined in Operational Procedure 3.7 [35]. During these curtailments, an over-response in the wind power plant power generation was obtained and the reduced power ratio was greater than four times the order required. This kind of event may threaten the power system operation, and from an economical point of view, because reserves generators are used for balancing, increasing costs are produced.

Figure 14 shows the sequence of curtailment instructions provided by the CECRE, the control center of renewable energies, together with the wind power generation in the power system. There were four orders with over-response during these hours, with effective wind power reduction from 2.42 to 4.02 times the commanded reduction.

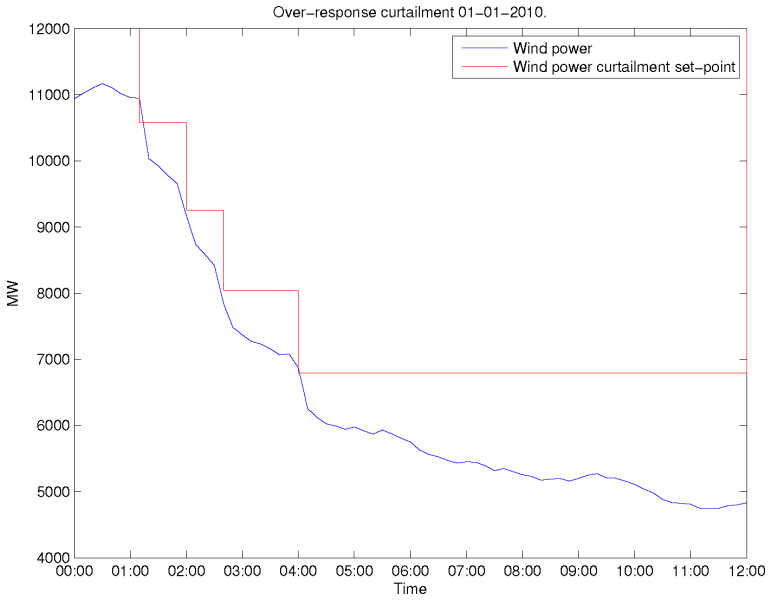

Figure 14. Over-response to curtailments in the entire Spanish wind power generation

The main causes of this over-response were:

- Curtailment is usually performed during low load and high wind penetration periods.
- During these periods, wind power plants often operate in high wind speed conditions and wind power fluctuations are dominant. Many wind power plants were stopped or operates in low output production due to cut-out protection disconnect the wind turbines operating above cut-out wind speeds.
- Curtailment is usually applied by disconnecting the entire wind power plant instead of turning off specific wind turbines (partial disconnections) within the wind power plant.

In Figure 14, an example of over-response to this curtailment is presented for the 49.5-MW wind power plant discussed previously. The TSO set point was ordered during early morning (03:00 to 07:00). When wind speed was above the cut-out wind speed (20 m/s), wind power decreased below the set point, reaching half generation and almost no generation. This additional drop must be replaced by the generation reserves.

The sequence of range of production was as follows:

- From 00:00 to 03:00, no curtailment was ordered. Most wind turbines were near or at 1 pu during this period. At 02:10, a slight wind power lull occurred as wind speed fell.
- From 03:00 to 04:40, a 0.6 pu TSO set point was applied. Then wind speed passed 20 m/s and most of the wind turbines were disconnected by cut-out speed protection. Wind power plant production fell to 0.1 pu, much less than 0.6 pu. Then wind speed went down, and wind power plant production almost reached the TSO set point. Some wind turbines were maintained at maximum available power; whereas others were disconnected, resulting in the TSO set point for the whole wind power plant. Some wind turbines were at maximum available power, and the rest remained disconnected. This kind of regulation involves repeated connections and disconnections during curtailment.
- From 04:40 to 07:40, the TSO set point changed from 0.6 pu to 0.5 pu. More wind turbines were disconnected to achieve this change.
- Finally, at 07:40, the TSO released the set point and the wind power plant recovered normal control.

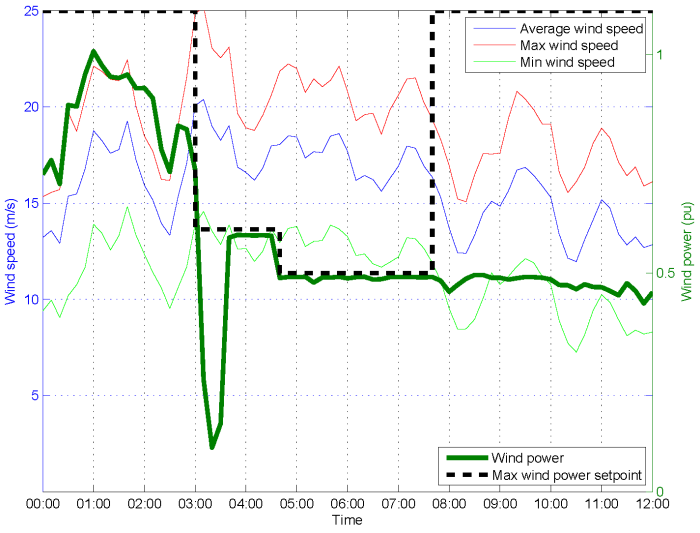

Figure 15. Example of an over-response in a 49.5-MW wind power plant on January 1, 2010

Possible solutions to avoid over-response to wind power curtailments, with the actual capacity of energy storage and transmission to other countries, are:

- The TSO should dispose of real-time wind power generation as well as a wind power forecast during the curtailment period. Maintenance schedules and cut-out shutdowns must be taken into account.
- Performing curtailment orders at the control center level instead of the wind power plant level must be studied.
- Control centers are connected to the CECRE and could improve curtailment management.
- Information about the reasons of curtailment, the application method, and wind power plant response could help toward overall optimization.

5. Conclusions

There are different types of events in which wind power fluctuates significantly. In some cases, fluctuations are produced by variations of wind speed, especially during meteorological events such as storms. Other power fluctuations are not directly linked with wind behavior and have a technical cause related to power system operation issues.

In this chapter, examples of the different events affecting wind power fluctuations were shown.The behaviors and the responses of the Spanish power system and wind power plants experiencing such events were analyzed. Examples presented in this chapter show that some of the wind power integration issues are related to low-voltage ride-through. They are solved through strict grid code enforcement. Other solutions to manage the reserve power generation and the wind power fluctuations are also very important in order to achieve high levels of wind power penetration. In the Spanish case, this could require increasing the availability of dispatchable and fast-start power plants, as well as increasing wind power plant participation on supporting the power system by providing voltage control, inertial emulation, frequency control, oscillation damping, or updated voltage ride-through capabilities.

Acknowledgements

This work was supported in part by the “Ministerio de Ciencia y Innovación” (ENE2009-13106) and in part by the “Junta de Comunidades de Castilla-La Mancha” (PEII10-0171-1803), both projects co-financed with FEDER funds.

This work was also supported by the U.S. Department of Energy under Contract No. DE-AC36-08-GO28308 with the National Renewable Energy Laboratory.

Author details

Sergio Martin-Martínez[1], Antonio Vigueras-Rodríguez[2], Emilio Gómez-Lázaro[1], Angel Molina-García[3], Eduard Muljadi[4] and Michael Milligan[4]

1 Renewable Energy Research Institute, Universidad de Castilla-La Mancha, Albacete, Spain

2 Renewable Energy Research Institute, Albacete Science and Technology Park and Universidad de Castilla-La Mancha, Albacete, Spain

3 Department of Electrical Engineering, Universidad Politécnica de Cartagena, Cartagena, Spain

4 National Renewable Energy Laboratory, Golden, Colorado, USA; Michael Milligan, National Renewable Energy Laboratory, Golden, Colorado, USA

References

[1] Bialasiewicz, J. T., & Muljadi, E. The Wind Farm Aggregation Impact on Power Quality. In: The 32nd Annual Conference of the IEEE Industrial Electronics Society (IECON'06), Paris, France; (2006).

[2] Mandic, G., Gotbi, E., Nasiri, A., Muljadi, E., Oyague, F., Mechanical, Stress., Reduction, in., Variable, Speed., Wind, Turbine., & Drivetrains, . In: Windpower (2011). Anaheim, CA; 2011.

[3] GoranMandic, Adel Nasiri, Eduard Muljadi, EhsanGhotbi and Francisco Oyague.Mechanical Stress Reduction in Variable Speed Wind Turbine Drivetrains. In: IEEE ECCE, Phoenix, AZ; (2011).

[4] Van der Hoven.Power spectrum of horizontal wind speed in the frequency range from 0.0007 to 900 cycles per hour. Journal of Meteorology (1957). , 14, 160-164.

[5] Heggem, T., Lende, R., & Løvseth, J. Analysis of long time series of coastal wind. American Meteorological Society (1998). , 55, 2907-2917.

[6] Fiedler, F., & Panofsky, H. A. Atmospheric scales and spectral gaps. Bulletin of the American Meteorology Society (1970). , 51, 1114-1119.

[7] Agee, E., Chen, T., Dowell, K. A., review, of., mesoscale, cellular., & convection, . Bulletin of the American Meteorology Society (1973). , 54, 1004-1012.

[8] Vincent, C. L., Pinson, P., & Giebela, G. Wind fluctuations over the North Sea, International Journal of Climatology (2011). , 31(11), 1584-1595.

[9] Vigueras-, Rodríguez. A., Sørensen, P., Cutululis, N., Viedma, A., & Donovan, M. H. Wind model for low frequency power fluctuations in offshore wind farms. Wind Energy (2010). , 13(5), 471-482.

[10] Gjerstad, J., Aasen, S. E., Andersson, H. I., Brevik, I., & Lovseth, J. Andersson HI, Brevik I, and Lovseth J. An analysis of low-frequency maritime atmospheric turbulence. Journal of the atmospheric sciences (1995).

[11] Smedman, A. Occurrence of roll circulation in a shallow boundary layer. Boundary-Layer Meteorology (1991). , 57, 343-358.

[12] Stull, R. An Introduction to Boundary Layer Meteorology. Kluwer Academic: Norwell, USA, (1988).

[13] Courtney, M., & Troen, I. Wind speed spectrum from one year of continuous 8 hz measurements. In: Proceedings of the Ninth Symposium on Turbulence and Diffusion; (1990).

[14] Yahaya, S., & Frangi, J. P. Cup anemometer response to the wind turbulence measurement of the horizontal wind variance. AnnalesGeophysicae (2004).

[15] Akhmatov, V., Kjaergaard, J. P., & Abildgaard, H. Announcement of the large offshore wind farm Horns Rev B and experience from prior projects in Denmark. In: European Wind Energy Conference; (2004).

[16] Holttinen, H., Meibom, P., Orths, A., O'Malley, M., Ummels, B., Tande, J. O., Estanqueiro, A., Gomez, E., Smith, J. C., & Ela, E. Impacts of large amounts of wind power on design and operation of power systems, results of IEA. In: 7th International Workshop on Large Scale Integration of Wind Power and on Transmission Networks for Offshore Wind Farms; (2008).

[17] Veers PS. Three-Dimensional Wind Simulation.Sandia National Laboratories Technical Report: New Mexico and California, USA, (1988).

[18] Sørensen, P., Hansen, A. D., & Carvalho-Rosas, P. E. Wind models for simulation of power fluctuations from wind farms. Journal of Wind Engineering and Industrial Aerodynamics (2002). , 90, 1381-1402.

[19] Sørensen, P., Cutululis, N., Vigueras-Rodríguez, A., Jensen, L. E., Hjerrild, J., Donovan, M. H., & Madsen, H. Power Fluctuation from Large Wind Farms IEEE Transactions on Power Systems (2007). , 22(3), 958-965.

[20] Sørensen, P., Cutululis, N., Vigueras-Rodríguez, A., Madsen, H., Pinson, P., Jensen, L. E., Hjerrild, J., & Donovan, M. Modelling of Power Fluctuations from Large Offshore Wind Farms. Wind Energy (2008). , 11, 29-43.

[21] Schlez W, Infield D. Horizontal, two point coherence for separations greater than the measurement height. Boundary-Layer Meteorology 1998; 87: 459-480.

[22] Vigueras-Rodríguez, A., Sørensen, P., Viedma, A., Donovan, M. H., & Gómez-Lázaro, E. Spectral Coherence Model for Power Fluctuations in a Wind Farm. Journal of Wind Engineering and Industrial Aerodynamics (2012). , 102, 14-21.

[23] Woods, M., Davy, R., Russel, C., Coppin, P., & Cross, . Cross-Spectrum of Wind Speed for Meso-Gamma Scales in the Upper Surface Layer over South-Eastern Australia. Boundary Layer Meteorology (2011).

[24] Jensen, N. O., Kristensen, L., Larsen, S. E., (ed., , America, Meteorology., Society, Boston., & , U. S. A. (1990). 301-304.

[25] Characterization and visualization of voltage dips in wind power installations. IEEE Transactions on Power Delivery, , 24(4), 2071-2078.

[26] Spanish Wind Energy Association.Procedure for verification validation and certification of the requirements of the PO 12.3 on the response of wind farms in the event of voltage dips, 4th edition, Spain, (2008).

[27] Red Eléctrica de España. REE. P.O. 12.3 Requisitos de respuesta frente a huecos de tensión de las instalaciones eólicas. Red Eléctrica de España, (2006).

[28] Gómez-Lázaro, E., Fuentes, J. A., Molina-García, A., Ruz, F., & Jimenez, F. Field tests of wind turbines submitted to real voltage dips under the new Spanish grid code requirements. Wind Energy (2007).

[29] Gómez-Lázaro, E., Fuentes-Moreno, J. A., Molina-García, A., Ruz, F., & Jiménez-Buendía, F. Results using different reactive power definitions for wind turbines submitted to voltage dips: Application to the Spanish grid code. In Power Systems Conference (IEEE PES). Atlanta (USA), (2006).

[30] Jimenez, F., Gómez-Lázaro, E., Fuentes, J. A., Molina-García, A., & Vigueras-Rodríguez, A. Validation of a DFIG wind turbine model and wind farm verification following the Spanish grid. Wind Energy (2012).

[31] Coughlan, Y., Smith, P., Mullane, A., & O'Malley, M. Wind turbine modelling for power system stability analysis- a system operator perspective. IEEE Transactions on Power Systems (2007).

[32] Piwko RJ, Miller NW, and MacDowell JM.Field testing and model validation of wind power plants. In IEEE Power and Energy Society General Meeting- Conversion and Delivery of Electrical Energy in the 21st Century, Pittsburgh PA, USA; (2008).

[33] Singh, M., Faria, K., Santoso, S., & Muljadi, E. Validation and analysis of wind power plant models using short-circuit field measurement data. In IEEE Power & Energy Society General Meeting, Calgary, Canada; (2009).

[34] Coronado LM. Huecos de tensión: La visión del operador del sistema.In Huecos de Tensión: Requisitos y Procedimientos en Fotovoltaica, Madrid, Spain; (2011).

[35] Red Eléctrica de España. P.O. 3.7 Programación de la generación de origen renovable no gestionable ;2009.

Chapter 13

Power Electronics in Small Scale Wind Turbine Systems

Mostafa Abarzadeh, Hossein Madadi Kojabadi and Liuchen Chang

Additional information is available at the end of the chapter

http://dx.doi.org/10.5772/51918

1. Introduction

Although fossil fuel is the main energy supplier of the worldwide economy, due to its adverse effects on environment, the scientists look for alternative resources in power generation. Electricity generation using renewable energy has been well recognized as environmentally friendly, socially beneficial, and economically competitive for many applications. Wind turbines, photovoltaic systems, full cells and PATs are main resources for distributed generation systems [1]. Compared with other renewable energy, wind power is more suitable for some applications with relatively low cost [2,3]. Wind turbine system (WTS) technology is still the most suitable renewable energy technology. While most large companies are focusing on large wind turbines of the utility scale, small wind turbines as distributed power generators have attracted a growing interest from the general public, small farms and remote communities [4]. In recent years, the level of interest in small-scale wind turbine generators has been increasing due to growing concerns over the impact of fossil-fuel based electricity generation [5]. According to the American Wind Energy Association (AWEA) annual wind industry report, the U.S. market for small wind turbines (<100kW) grew 78% in 2008 adding 17.3 MW of installed capacity. Over 10,000 small wind turbines were sold in the U.S. in 2008 [6]. UK based consultants Gerrad Hassan also predicts that small wind turbine sales have the potential to increase to well over US$750 million by 2005 [4]. Small-scale wind turbines are particularly advantageous for power generation at a household level [5]. A small-scale wind turbine consists of a generator, a power electronic converter, and a control system. Among different types of small-size wind turbine, permanent magnet (PM) generator is widely used because of its high reliability and simple structure [1,2]. The power electronic converter topology used depends on the required output power and cost of the system. Control systems are used to control the rotational speed of

small-scale wind turbines enabling them to operate with optimum speed to extract maximum power from wind [1,2,4].

For rural and remote areas, the small-scale stand-alone wind power system with a battery bank as the energy storage component is common and essential for providing stable and reliable electricity [2,7-10]. For the stand-alone wind power system, the load is a battery that can be considered as an energy sink with almost constant voltage. The battery can absorb any level of power as long as the charging current does not exceed its limitation. Since the voltage remains almost constant, but the current flows through it can be varied, the battery can be also considered as a load with a various resistance [2,11,12].

There is increasing market for a grid connected small wind generating system (without battery storage) for home owners and small businesses in rural areas. In this case the excess energy form the wind generator is fed to the utility grid. The AC grid can also be a diesel grid or a battery/diesel mini hybrid grid. A grid connected inverter structure which extracts energy even at low wind speeds will assist in reducing capital cost and offer opportunities for interfacing small-scale wind generators with the AC grid. Conventional grid connected wind turbines use a charge controller to charge the batteries and a grid connected inverter to process power from the battery to the utility grid [4].

This chapter presents a power electronic energy conversion system for small-scale stand-alone wind power system with a battery bank as the energy storage component and grid connected power electronic interface for interfacing variable speed small-scale wind generators to a grid. Small-scale wind turbine consist of permanent magnet synchronous generator (PMSG), AC/DC converter, DC/DC converter as the maximum power point tracking controller, inverter and load.

2. Small-scale wind turbine system

A small wind turbine generally consists of the following components: A rotor with a variable number of blades for convert the power from wind to mechanical power, an electric generator, control and protection mechanisms, and power electronic components for feeding electricity into a battery bank, the public grid or, occasionally, into a direct application such as a water-pump[1,13].

The generator is the main part of a small wind turbine. The generator converts the mechanical power into electrical power. The two common types of electrical machines used in small scale wind turbines are self excited induction generators (SEIG) and permanent magnet synchronous generators (PMSG). In these cases, the common way to convert the low-speed mechanical power to electrical power is a utilizing a gearbox and a SEIG with standard speed. The gearbox adapts the low speed of the turbine rotor to the high speed of generators, though the gearbox may not be necessary for multiple-pole generator systems. In the self-excited induction generators, the reactive power necessary to energize the magnetic circuits must be supplied from parallel capacitors bank at the machine terminal. In this case, the ter-

http://dx.doi.org/10.5772/51918

minal voltage or reactive power may not be directly controlled, and the induction generators may suffer from voltage instability problem. There is considerable interest in the application of the multiple-pole Permanent Magnet Synchronous Generators (PMSG) driven by a wind-turbine shaft without gearbox [1]. As described above, the electric generators of modern small wind turbines are generally designed to use permanent magnets and a direct coupling between rotor and generator. The following common topologies can be encountered:

1. Axial flow air-cored generators
2. Axial flow generators with toroidal iron cores
3. Axial flow generators with iron cores and slots
4. Radial flow generators with iron cores and slots
5. Transverse flow generators with slotted iron core

In the topologies above the type of flow refers to the direction of the magnetic flow lines crossing the magnetic gap between the poles with respect to the rotating shaft of the generator [13].

It is important to be able to control and limit the converted mechanical power during higher wind speeds. The power limitation during higher wind speeds in small scale wind turbines may be done by furling control or soft-stall control [1,14]. Furling is a passive mechanism used to limit the rotational frequency and the output power of small-scale wind turbine in strong winds. While other mechanisms, such as passive blade pitching or all-electronic control based on load-induced stall can occasionally be encountered, furling is the most frequently used mechanism [13]. Many small wind turbines use an upwind rotor configuration with a tail vane for passive yaw control. Typically, the tail vane is hinged, allowing the rotor to furl (turn) in high winds, providing both power regulation and over-speed protection. At higher wind speeds, the generated power of the wind turbine can go above the limit of the generator or the wind turbine design. When this occurs, small wind turbines use mechanical control or furling to turn the rotor out of the wind resulting in shedding the aerodynamic power or a steep drop in the power curve [1,13-16]. The basic operating principle of furling system is shown in Figure 1.

Often, small turbine rotors furl abruptly at a wind speed only slightly above their rated wind speed, resulting in a very "peaky" power curve and poor energy capture at higher wind speeds. This energy loss is compounded by the furling hysteresis, in which the wind speed must drop considerably below the rated wind speed before the rotor will unfurl and resume efficient operation. One way to improve the performance of furling wind turbines is to design the rotor to furl progressively, causing the power output to remain at or near rated power as the wind speed increases beyond it's rated value. This approach has two drawbacks: wind turbine rotors operating at high furl angles tend to be very noisy and experience high flap loads. Note that manufactured wind turbines use a damper to reduce the furling loop hysteresis. Damping is necessary to keep the wind turbine from cycling or chattering in and out of furling. The damping plus the gyroscopic effect of turning wind turbine

blades add to the unproductive time of entering and leaving the furling condition creating a hysteresis during transition. All of these delays reduce the wind turbine energy production [1,14-16].

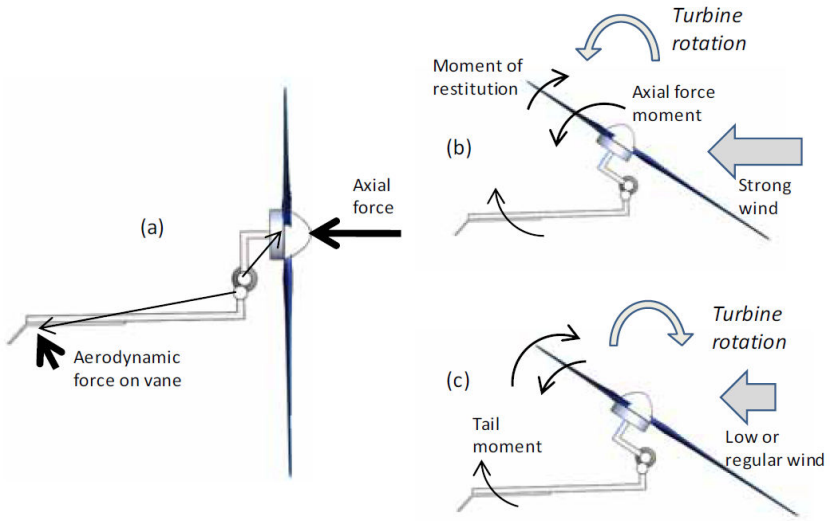

Figure 1. Overview of the operating principles of a furling system. (a) Aerodynamic forces. (b) Furling movement in strong winds. (c) Restitution of normal (aligned) operation upon reduction of the wind speed [13].

The soft-stall concept is to control the generator rotations per minute (rpm) and achieve optimum operation over a wide range of rotor rpm. In order to control the generator rpm, the soft-stall concept regulates the stall mode of the wind turbine, thus furling can be delayed in normal operation. Furling is still used in the soft-stall concept during very high winds and emergency conditions. Potential advantages of soft-stall control are listed as follows:

- Delays furling as long as possible, which increases energy production
- Controls the wind turbine rotational speed to achieve the maximum power coefficient
- Operates the wind turbine at a low tip-speed ratio during high wind speeds to reduce noise and thrust loads [1,14-16].

The only difference between furling and soft-stall control is the addition of the DC-DC converter that allows the power to be controlled. With the DC-DC Converter between the rectifier and load, the transmitted power to the load can be controlled according to prescribed power/rpm schedule.

A variable speed wind turbine configuration with power electronics conversion corresponds to the full variable speed controlled wind turbine, with the generator connected to the load or to the grid through a power converter as shown in Figure 2.

http://dx.doi.org/10.5772/51918

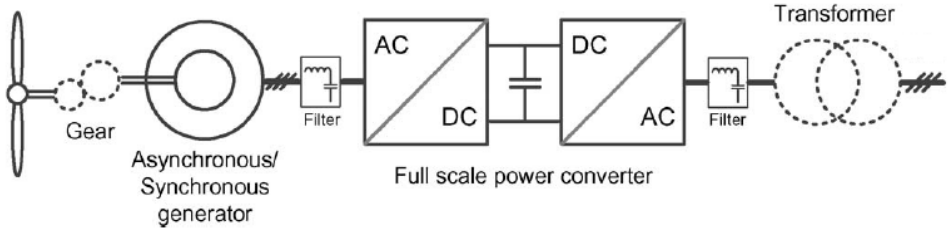

Figure 2. AC/DC/AC power electronic interface for a wind generator.

The grid-connected inverters will inject the active power to the grid with minimum total harmonic distortion (THD) of output current and voltage. The grid voltage and inverter output voltage will be synchronized by zero-crossing circuit. The generator can be self-excited asynchronous generator (SEIG), or permanent magnet synchronous generator (PMSG). The stator windings are connected to the load or to the grid through a full-scale power converter. Some variable speed WTSs are gearless. In these cases, a direct driven multi-pole generator is used.

3. Power electronic converters for wind turbine system

A permanent magnet generator has no excitation control and output voltage is proportional to the rotor speed. Therefore, in control of wind turbine, the rotor speed is obtained via the output voltage measurement. The earliest and still most widely used power electronic circuit for this application uses an AC/DC/AC technology in which the variable frequency, variable voltage from the generator is first rectified to DC and then converted to AC and fed to the grid or load. The continuous variation of wind speed will result in a DC link voltage varying in an uncontrolled manner. In order to get variable speed operation and stable dc bus voltage, a boost dc-dc converter could be inserted in the dc link [17]. As there is active power flows unidirectionally from the PMSG to the dc link through a power converter, only a simple diode rectifier can be applied to the generator side converter in order to obtain a cost-efficient solution [4,5].

3.1. AC/DC/AC converters for power electronic interface

3.1.1. Three-Phase bridge rectifier

A three-phase bridge rectifier is commonly used in wind power applications. This is a full-wave rectifier and gives six-pulse ripples on the output voltage. Each one of six diodes conducts for 120º. The pair of diodes which are connected between that pair of supply lines having the highest amount of instantaneous line-to-line voltage will conduct [18]. The three-phase bridge rectifier is shown in Figure 3.

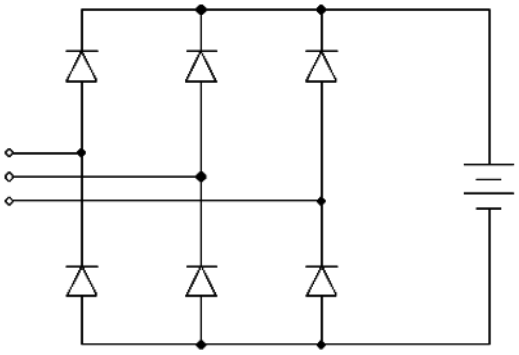

Figure 3. Three-phase bridge rectifier.

If V_m is the peak value of the phase voltage, then the average and rms output voltage is calculate with

$$V_{dc} = \frac{2}{2\pi/6}\int_0^{\pi/6} \sqrt{3}\, V_m \cos \omega t \; d(\omega t) = \frac{3\sqrt{3}}{\pi} V_m = 1.654 V_m \tag{1}$$

$$V_{rms} = \left[\frac{2}{2\pi/6}\int_0^{\pi/6} 3\, V_m{}^2 \cos^2 \omega t \; d(\omega t)\right]^{1/2} = \left(\frac{3}{2} + \frac{9\sqrt{3}}{4\pi}\right)^{1/2} V_m = 1.6554 V_m \tag{2}$$

3.1.2. DC/DC converters

Dc converters can be used as switching-mode regulators to convert to dc voltage, normally unregulated, to a regulated dc output voltage. The regulation is normally achieved by PWM at a fixed frequency and the switching device is normally IGBT or MOSFET. The following range of DC-to-DC converters, in which the input and output share a common return line, are often referred to as "three-terminal switching regulators" [19].

The switching regulators will often replace linear regulators when higher efficiencies are required. They are characterized by the use of a choke rather than a transformer between the input and output lines. The switching regulator differs from its linear counterpart in that switching rather than linear techniques are used for regulation, resulting in higher efficiencies and wider voltage ranges. Further, unlike the linear regulator, in which the output voltage must always be less than the supply. The switching regulator can provide outputs which are equal to, lower than, higher than, or of reversed polarity to the input. There are four basic topologies of switching regulators:

1. *Buck regulators:* In buck regulators, the output voltage will be of the same polarity but always lower than the input voltage. One supply line must be common to both input and output. This may be either the positive or negative line, depending on the regulator design.

http://dx.doi.org/10.5772/51918

2. *Boost regulators:* In boost regulator, the output voltage will be of the same polarity but always higher than the input voltage. One supply line must be common to both input and output. This may be either the positive or negative line, depending on the design. The boost regulator has a right-half-plane zero in the transfer function.

3. *Buck-boost regulators:* Because of a combination of the buck and boost regulators, this type is known as a "buck-boost" regulator. In this type, the output voltage is of opposite polarity to the input, but its value may be higher, equal, or lower than that of the input. One supply line must be common to both input and output, and either polarity is possible by design. The inverting regulator carries the right-half-plane zero of the boost regulator through to its transfer function.

4. *Cuk regulators:* This is a relatively new class of boost-buck-derived regulators, in which the output voltage will be reversed but may be equal, higher, or lower than the input. Again one supply line must be common to both input and output, and either polarity may be provided by design. This regulator, being derived from a combination of the boost and buck regulators, also carries the right-half-plane zero through to its transfer function [18-20].

3.1.2.1. Buck regulators

The step-down dc-dc converter, commonly known as a buck converter, is shown in Figure 4. Its operation can be seen as similar to a mechanical flywheel and a one piston engine. The L-C filter, like the flywheel, stores energy between the power pulses of the driver. The input to the L-C filter (choke input filter) is the chopped input voltage. The L-C filter volt-time averages this duty-cycle modulated input voltage waveform. The L-C filtering function can be approximated by

$$V_{out} = V_{in} \times Duty\ cycle \tag{3}$$

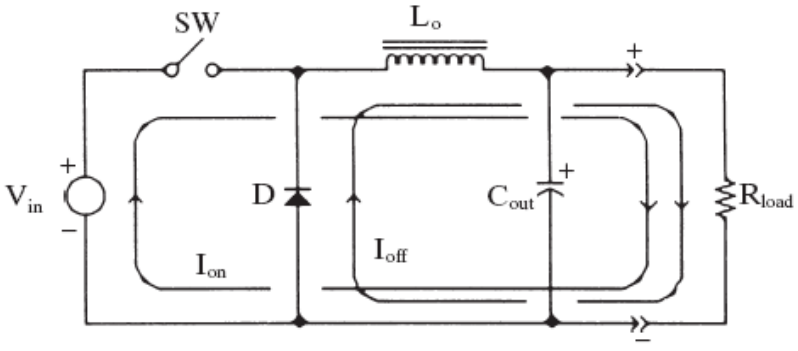

Figure 4. Basic circuit of a buck switching regulator

The output voltage is maintained by the controller by varying the duty cycle. The buck converter is also known as a step-down converter, since its output must be less than the input voltage [19,20].

The state of the converter in which the inductor current is never zero for any period of time is called the continuous conduction mode (CCM). It can be seen from the circuit that when the switch SW is commanded to the on state, the diode D is reverse-biased. When the switch SW is off, the diode conducts to support an uninterrupted current in the inductor [20].

Typical waveforms in the converter are shown in Figure 5 under the assumption that the inductor current is always positive.

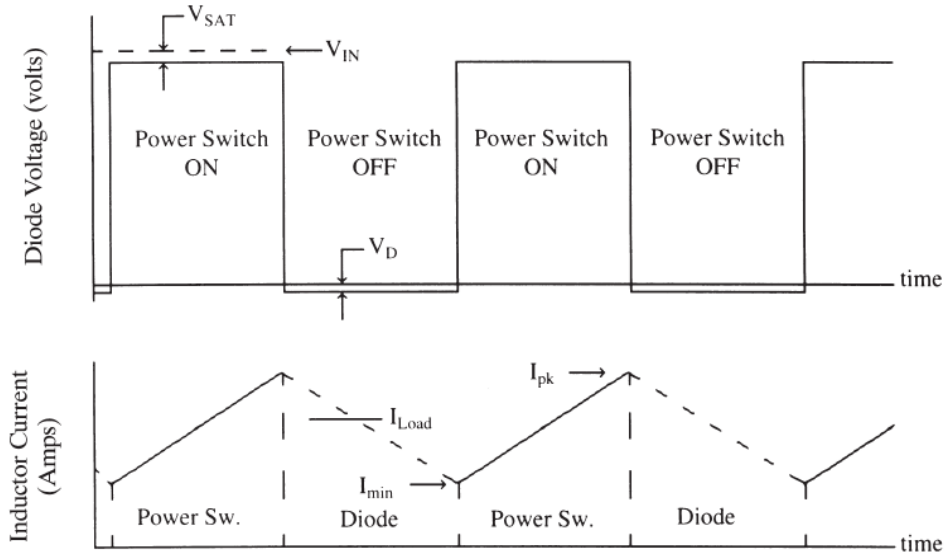

Figure 5. The voltage and current waveforms for a buck converter

The operation of the buck regulator can be seen by breaking its operation into two periods (refer to Figure 5). When the switch is turned on, the input voltage is presented to the input of the L-C filter. The inductor current ramps linearly upward and is described as

$$i_L\ (on) = \frac{(V_{in} - V_{out})t_{on}}{L_O} + i_{init} \tag{4}$$

The energy stored within the inductor during this period is

$$E_{stored} = {}^{1}\!/_{2} L_O (i_{peak} - i_{min})^2 \tag{5}$$

http://dx.doi.org/10.5772/51918

When SW turns off, the inductor will try to maintain the forward current constant, and the input voltage to the inductor wants to fly below ground and the diode. The current in inductor will now continue to circulate in the same direction as before with diode and the load. However, since the voltage now impressed across inductor has reversed, the current in inductor will now decrease linearly to its original value during the "off" period. The current through the inductor is described during this period by

$$i_L\ (off) = i_{peak} - \frac{V_{out} \cdot t_{off}}{L_O} \tag{6}$$

The current waveform, this time, is a negative linear ramp whose slope is $-V_{out}/L$. The dc output load current value falls between the peak and the minimum current values. In typical applications, the peak inductor current is about 150 percent of the dc load current and the minimum current is about 50 percent [20].

Condition for continuous inductor current and capacitor voltage: The voltage across the inductor L is, in general

$$e_L = L\ \frac{di}{dt} \tag{7}$$

Assuming that the inductor current rises linearly from I_{min} to I_{pk} in time t_{on}.

$$t_{on} = \frac{\Delta I\ L}{V_{in} - V_{out}} \tag{8}$$

And the inductor currents falls linearly from I_{pk} to I_{min} in time t_{off} .

$$t_{off} = \frac{\Delta I\ L}{V_{out}} \tag{9}$$

The switching period T can be expressed as

$$T = t_{on} + t_{off} = \frac{\Delta I\ L}{V_{in} - V_{out}} + \frac{\Delta I\ L}{V_{out}} = \frac{\Delta I\ L\ \ V_{in}}{V_{out}(V_{in} - V_{out})} \tag{10}$$

Which gives the peak-to-peak ripple current as

$$\Delta I = \frac{V_{out}(V_{in} - V_{out})}{fL\ V_{in}} = \frac{V_{in}k(1 - k)}{fL} \tag{11}$$

If I_L is the average inductor current, the inductor ripple current $\Delta I = 2I_L$. Using equations (3) and (11), we get

$$\frac{V_{in}k(1-k)}{fL} = 2I_L = 2I_a = \frac{2k\,V_{in}}{R} \tag{12}$$

Which gives the critical value of the inductor L_c as

$$L_c = \frac{(1-k)R}{2f} \tag{13}$$

The capacitor voltage is expressed as

$$v_c = \frac{1}{C}\int i_c dt + v_c\left(t=0\right) \tag{14}$$

If we assume that the load ripple current Δi_o is very small, $\Delta i_L = \Delta i_c$. The average capacitor current, which flows into $\frac{t_{on}}{2} + \frac{t_{off}}{2} = \frac{T}{2}$, is

$$I_c = \frac{\Delta I}{4} \tag{15}$$

From (14) and (15) the peak-to-peak ripple voltage of the capacitor is

$$\Delta V_c = v_c - v_c(t=0) = \frac{1}{C}\int_0^{T/2} \frac{\Delta I}{4} dt = \frac{\Delta I\, T}{8C} = \frac{\Delta I}{8fC} \tag{16}$$

From (11) and (16), we get

$$\Delta V_c = \frac{V_{out}(V_{in} - V_{out})}{8LC f^2 V_{in}} = \frac{V_{in}k(1-k)}{8LC f^2} \tag{17}$$

If V_c is the average capacitor voltage, the capacitor ripple voltage $\Delta V_c = 2V_{out}$. Using equations (3) and (17), we get

$$\frac{V_{in}k(1-k)}{8LC f^2} = 2V_{out} = 2kV_{in} \tag{18}$$

Which gives the critical value of the capacitor C_c as

$$C_c = C = \frac{1-k}{16L f^2} \tag{19}$$

The advantages of forward-mode converters are: they exhibit lower output peak-to-peak ripple voltages than do boost-mode converters, and they can provide much higher levels of output power. Forward-mode converters can provide up to kilowatts of power [18-20].

3.1.2.2. Boost regulators

In a boost regulator the output voltage is greater than the input voltage. Figure 6 shows the general arrangement of the power sections of a boost regulator. As one can notice, the boost-mode converter has the same parts as the forward-mode converter, but they have been rearranged. This new arrangement causes the converter to operate in a completely different fashion than the forward-mode converter [19, 20]. When SW turns on, the supply voltage will be impressed across the series inductor L. Under steady-state conditions, the current in L will increase linearly in the forward direction. Rectifier D will be reverse-biased and not conducting. At the same time, current will be flowing from the output capacitor Cout into the load. Hence, Cout will be discharging. Figures 7 and 8 show the current waveforms. The inductor's current wave form is also a positive linear ramp and is described by

$$i_L\ (on) = \frac{V_{in} t_{on}}{L} \tag{20}$$

When SW turns off the current in L will continue to flow in the same direction, rectifier diode D will conduct, and the inductor current will be transferred to the output capacitor and load. Since the output voltage exceeds the supply voltage, L will now be reverse-biased, and the current in L will decay linearly back toward its original value during the "off" period of SW. The inductor current during the power switch off period is described by

$$i_L\ (off) = i_{peak}(on) - \frac{(V_{out} - V_{in}) t_{off}}{L} \tag{21}$$

As with the buck regulator, for steady-state conditions, the forward and reverse volt-seconds across L must equate. The output voltage V_{out} is controlled by the duty ratio of the power switch and the supply voltage, as follows

$$V_{in} \times t_{on} = (V_{out} - V_{in}) \times t_{off} \ \rightarrow\ V_{out} = V_{in} \times \left(\frac{t_{off} + t_{on}}{t_{off}}\right) \overset{\frac{t_{off}+t_{on}}{t_{off}} = \frac{1}{1-k}}{\rightarrow} \quad V_{out} = \frac{1}{1-k} V_{in} \tag{22}$$

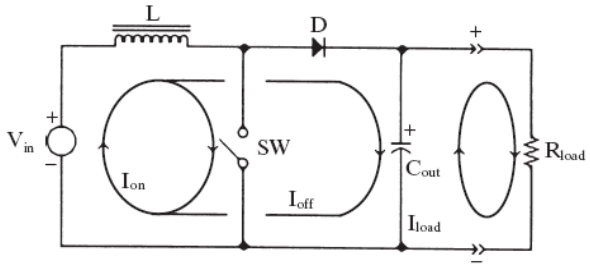

Figure 6. Basic circuit of a boost switching regulator

When the core's flux is completely emptied prior to the next cycle, it is referred to as the discontinuous-mode of operation. This is seen in the inductor current and voltage waveforms in Figure 7. When the core does not completely empty itself, a residual amount of energy remains in the core. This is called the continuous mode of operation and can be seen in Figure 8. The majority of boost-mode converters operate in the discontinuous mode since there are some intrinsic instability problems when operating in the continuous mode. The energy stored within the inductor of a discontinuous-mode boost converter is described by

$$E_{stored} = \frac{1}{2} L \; i_{pk}^2 \tag{23}$$

The energy delivered per second (joules/second or watts) must be sufficient to meet the continuous power demands of the load. This means that the energy stored during the ON time of the power switch must have a high enough I_{pk} to satisfy equation (24):

$$P_{load} < P_{out} = f\left[\frac{1}{2} L \; I_{pk}^2\right] \tag{24}$$

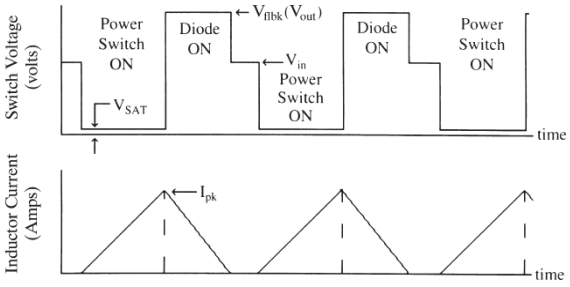

Figure 7. Waveforms for a discontinuous-mode boost converter.

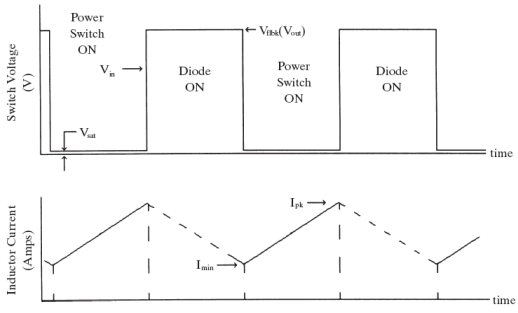

Figure 8. Waveforms for a continuous-mode boost converter.

http://dx.doi.org/10.5772/51918

Condition for continuous inductor current and capacitor voltage: Assuming that the inductor current rises linearly from I_{min} to I_{pk} in time t_{on}.

$$t_{on} = \frac{\Delta I\ L}{V_{in}} \tag{25}$$

And the inductor currents falls linearly from I_{pk} to I_{min} in time t_{off}.

$$t_{off} = \frac{\Delta I\ L}{V_{out} - V_{in}} \tag{26}$$

The switching period T can be expressed as

$$T = t_{on} + t_{off} = \frac{\Delta I\ L}{V_{in}} + \frac{\Delta I\ L}{V_{out} - V_{in}} = \frac{\Delta I\ L\ \ V_{out}}{V_{in}(V_{out} - V_{in})} \tag{27}$$

Which gives the peak-to-peak ripple current as

$$\Delta I = \frac{V_{in}(V_{out} - V_{in})}{fL\ \ V_{out}} = \frac{V_{in}k}{fL} \tag{28}$$

If I_L is the average inductor current, the inductor ripple current $\Delta I = 2I_L$. Using equations (22) and (28), we get

$$\frac{V_{in}k}{fL} = 2I_L\ = 2I_a = \frac{2\ V_{in}}{(1 - k)R} \tag{29}$$

Which gives the critical value of the inductor L_c as

$$L_c = \frac{k(1 - k)R}{2f} \tag{30}$$

When the SW is on, the capacitor supplies the load current for $t = t_{on}$. The average capacitor current during time t_{on} is $I_c = I_{out}$ and peak-to-peak voltage of the capacitor is

$$\Delta V_c = v_c - v_c(t = 0) = \frac{1}{C}\int_0^{t_{on}} I_c dt = \frac{1}{C}\int_0^{t_{on}} I_{out} dt = \frac{I_{out} t_{on}}{C} \tag{31}$$

Substituting $t_{on} = (V_{out} - V_{in})/(V_{out} f)$ in (31) gives

$$\Delta V_c = \frac{I_{out}(V_{out} - V_{in})}{V_{out} fC} = \frac{I_{out} k}{fC} \tag{32}$$

If V_c is the average capacitor voltage, the capacitor ripple voltage $\Delta V_c = 2V_{out}$. Using equations (32), we get

$$\frac{I_{out}k}{fC} = 2V_{out} = 2I_{out}R \tag{33}$$

Which gives the critical value of the capacitor C_c as

$$C_c = C = \frac{k}{2fR} \tag{34}$$

To the boost regulator's advantage, the input current is now continuous (although there will be a ripple component depending on the value of the inductance L). Hence less input filtering is required, and the tendency for input filter instability is eliminated [18-20].

3.1.2.3. Buck-boost regulators

A buck-boost regulator provides an output voltage that may be less than or greater than the input voltage. The output voltage polarity is opposite to that of the input voltage. Figure 9 shows the power circuit of a typical buck-boost regulator which operates as discussed below [18-20]

When SW is on, current will build up linearly in inductor L. Diode D is reverse-biased and blocks under steady-state conditions. When SW turns off, the current in L will continue in the same direction, and diode D is brought into conduction, transferring the inductor current into the output capacitor C and load. During the off period, the voltage across L is reversed, and the current will decrease linearly toward its original value. The output voltage depends on the supply voltage and duty cycle (t_{on} / t_{off}), and this is adjusted to maintain the required output. The current waveforms are the same as those for the boost regulator shown in Figure 10. As previously, the forward and reverse volt-seconds on L must equate for steady-state conditions, and to meet this volt-seconds equality

$$V_{in} \times t_{on} = V_{out} \times t_{off} \rightarrow V_{out} = V_{in} \times \left(\frac{t_{on}}{t_{off}}\right) \rightarrow V_{out} = -\frac{k}{1-k} V_{in} \tag{35}$$

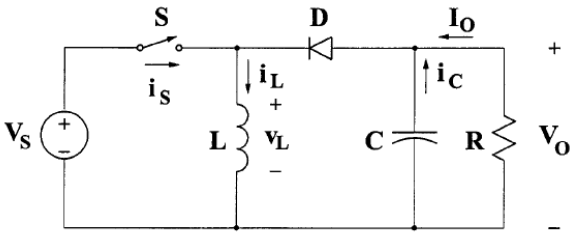

Figure 9. Basic circuit of a buck-boost switching regulator

http://dx.doi.org/10.5772/51918

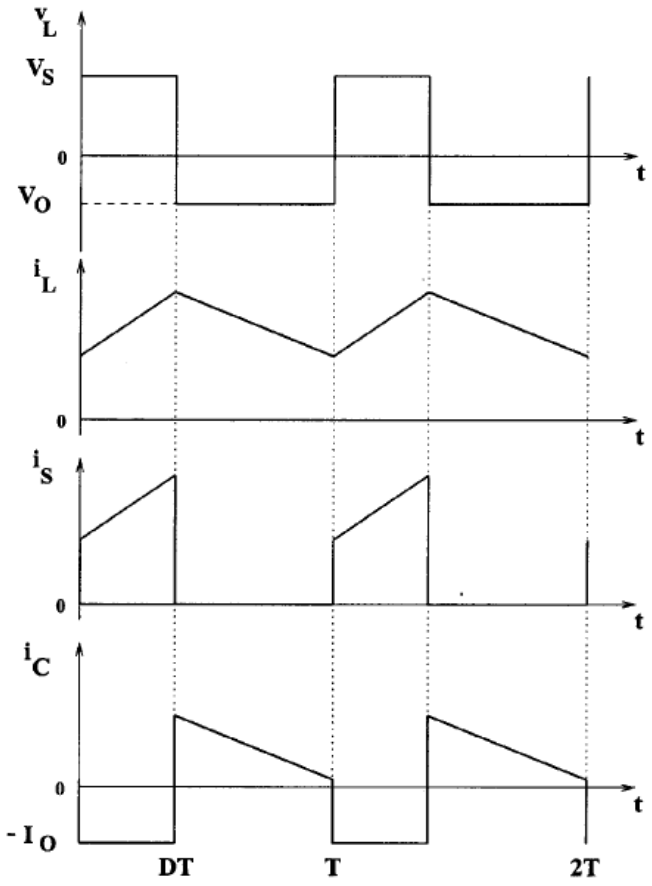

Figure 10. The voltage and current waveforms for a buck-boost converter

Condition for continuous inductor current and capacitor voltage: Assuming that the inductor current rises linearly from I_{min} to I_{pk} in time t_{on}.

$$t_{on} = \frac{\Delta I_L}{V_{in}} \tag{36}$$

And the inductor currents falls linearly from I_{pk} to I_{min} in time t_{off}.

$$t_{off} = \frac{-\Delta I_L}{V_{out}} \tag{37}$$

The switching period T can be expressed as

$$T = t_{on} + t_{off} = \frac{\Delta I\ L}{V_{in}} + \frac{-\Delta I\ L}{V_{out}} = \frac{\Delta I\ L\ (V_{out} - V_{in})}{V_{in} V_{out}} \tag{38}$$

Which gives the peak-to-peak ripple current as

$$\Delta I = \frac{V_{in} V_{out}}{fL\ (V_{out} - V_{in})} = \frac{V_{in} k}{fL} \tag{39}$$

If I_L is the average inductor current, the inductor ripple current $\Delta I = 2I_L$. Using equations (35) and (39), we get

$$\frac{V_{in} k}{fL} = 2I_L = 2I_a = \frac{2k\ V_{in}}{(1 - k)R} \tag{40}$$

Which gives the critical value of the inductor L_c as

$$L_c = \frac{(1 - k)R}{2f} \tag{41}$$

When the SW is on, the capacitor supplies the load current for $t = t_{on}$. The average capacitor current during time t_{on} is $I_c = I_{out}$ and peak-to-peak voltage of the capacitor is

$$\Delta V_c = v_c - v_c(t = 0) = \frac{1}{C}\int_0^{t_{on}} I_c dt = \frac{1}{C}\int_0^{t_{on}} I_{out} dt = \frac{I_{out} t_{on}}{C} \tag{42}$$

Substituting $t_{on} = V_{out} / [(V_{out} - V_{in}) f]$ in (42) gives

$$\Delta V_c = \frac{I_{out} V_{out}}{(V_{out} - V_{in}) fC} = \frac{I_{out} k}{fC} \tag{43}$$

If V_c is the average capacitor voltage, the capacitor ripple voltage $\Delta V_c = 2V_{out}$. Using equations (43), we get

$$\frac{I_{out} k}{fC} = 2V_{out} = 2I_{out} R \tag{44}$$

Which gives the critical value of the capacitor C_c as

$$C_c = C = \frac{k}{2fR} \tag{45}$$

Note that the output voltage is of reversed polarity but may be greater or less than V_{in}, depending on the duty cycle. In the inverting regulator, both input and output currents are discontinuous, and considerable filtering will be required on both input and output [18-21].

http://dx.doi.org/10.5772/51918

3.1.2.4. Cuk regulators

Similar to the buck-boost regulator, the cuk regulator provides an output voltage that is less than or greater than input voltage, but the output voltage polarity is opposite to that of the input voltage. Figure 11 shows the general arrangement of the power sections of a cuk regulator. The voltage and current waveforms for the cuk regulator are shown in Figure 12.

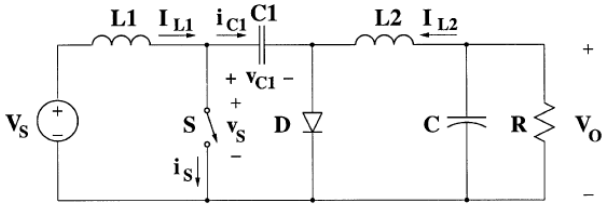

Figure 11. Basic circuit of a cuk switching regulator

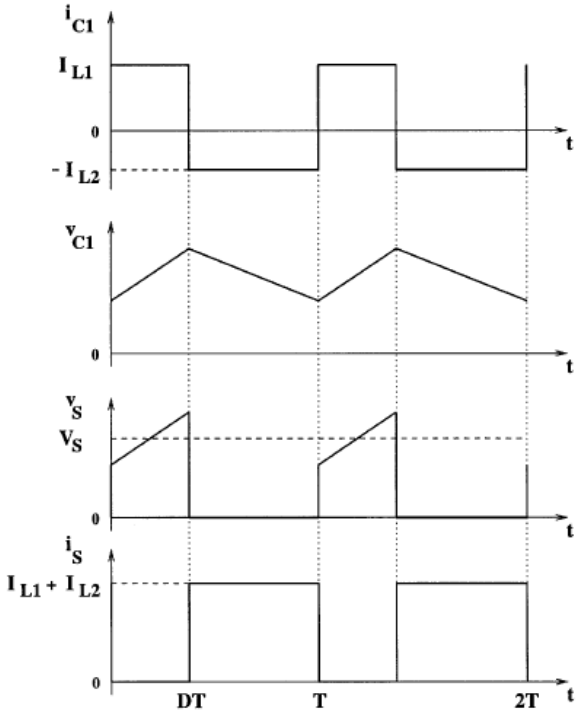

Figure 12. The voltage and current waveforms for a cuk converter

An important advantage of this topology is a continuous current at both the input and the output of the converter. Disadvantages of the cuk converter are a high number of reactive components and high current stresses on the switch, the diode, and the capacitor C1. When the switch is on, the diode is off and the capacitor C1 is discharged by the inductor L2 current. With the switch in the off state, the diode conducts currents of the inductors L1 and L2, whereas capacitor C1 is charged by the inductor L1 current [18-21].

To obtain the dc voltage transfer function of the converter, we shall use the principle that the average current through a capacitor is zero for steady-state operation. Let us assume that inductors L1 and L2 are large enough that their ripple current can be neglected. Capacitor C1 is in steady state if

$$I_{L\ 2}kT = I_{L\ 1}(1 - k)T \tag{46}$$

For a lossless converter

$$P_S = V_S I_{L\ 1} = -V_O I_{L\ 2} = P_O \tag{47}$$

From (46) and (47), the dc voltage transfer function of the cuk converter is

$$V_{out} = -\frac{k}{1 - k} V_{in} \tag{48}$$

The critical values of the inductor L_{c1} and L_{c2} determined by

$$L_{c1} = \frac{(1 - k)^2 R}{2kf} \tag{49}$$

$$L_{c2} = \frac{(1 - k)R}{2f} \tag{50}$$

And the critical values of the capacitor C_{c1} and C_{c2} determined by

$$C_{c1} = \frac{k}{2fR} \tag{51}$$

$$C_{c2} = \frac{1}{8fR} \tag{52}$$

3.1.3. Inverters

DC-to-ac converters are known as inverters. The function of inverter is to change a dc input voltage to symmetric ac output voltage of desired magnitude and frequency. The output voltage could be fixed or variable at a fixed or variable frequency. A variable output voltage can be obtained by varying the input dc voltage and maintaining the gain of inverter con-

http://dx.doi.org/10.5772/51918

stant. The output voltage waveforms of ideal inverters should be sinusoidal. However, the waveforms of practical inverters are non-sinusoidal and contain certain harmonics [18, 22].

For sinusoidal ac outputs, the magnitude, frequency, and phase should be controllable. Inverters generally use PWM control signals for producing an ac output voltage. According to the type of ac output waveform, these topologies can be considered as voltage source inverters (VSIs), where the independently controlled ac output is a voltage waveform. These structures are the most widely used in small-scale wind power applications. Similarly, these topologies can be found as current source inverters (CSIs), where the independently controlled ac output is a current waveform. These structures are not widely used in small-scale wind power applications [18].

Inverters can be broadly classified into two types: single-phase inverters, and three-phase inverters.

3.1.3.1. Single-phase bridge inverters

A single-phase bridge voltage source inverter (VSI) is shown in Figure 13. It consists of four switches. When S_1 and S_2 are turned on, the input voltage V_d appears across the load. If S_3 and S_4 are turned on, the voltage across the load is $-V_d$. Table 1 shows five switch states. If these switches are off at the same time, the switch state is 0. The rms output voltage can be found from

$$V_O = \sqrt{\left(\frac{2}{T_0}\int_0^{T_0/2} V_d^2 dt\right)} = V_d \tag{53}$$

Output voltage can be represented in Fourier series. The rms value of fundamental component as

$$v_O = \sum_{n=1,3,\ldots}^{\infty} \frac{4V_d}{n\pi}\sin n\omega t \xrightarrow{n=1} V_1 = \frac{4V_d}{\sqrt{2}\pi} = 0.90V_d \tag{54}$$

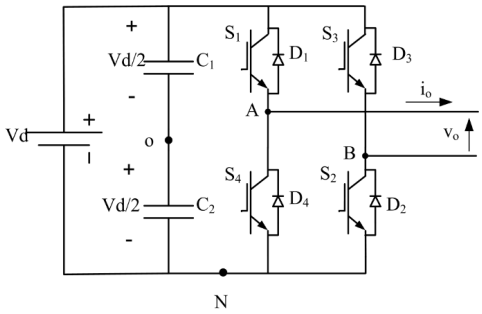

Figure 13. Single-phase full bridge inverter

When diodes D_1 and D_2 conduct, The energy is fed back to the dc source; so, they are known as feedback diodes. The instantaneous load current i_o for an RL load becomes

$$i_o = \sum_{n=1,3,\ldots}^{\infty} \frac{4V_d}{n\pi\sqrt{R^2 + (n\omega L)^2}} \sin(n\omega t - \theta_n) \tag{55}$$

Where $\theta_n = \tan^{-1}(n\omega L / R)$.

State No.	Output Voltage Level	State of (S_1, S_2, S_3, S_4)	Components Conducting
1	$+V_d$	(1, 1 , 0 , 0)	S_1 and S_2 if $i_o > 0$ D_1 and D_2 if $i_o < 0$
2	$-V_d$	(0, 0 , 1 , 1)	D_3 and D_4 if $i_o > 0$ S_3 and S_4 if $i_o < 0$
3	0	(1, 0 , 1 , 0)	S_1 and D_3 if $i_o > 0$ D_1 and S_3 if $i_o < 0$
4	0	(0, 1 , 0 , 1)	D_4 and S_2 if $i_o > 0$ S_4 and D_2 if $i_o < 0$
5	$-V_d$ $+V_d$	(0, 0 , 0 , 0)	D_4 and D_3 if $i_o > 0$ D_4 and D_2 if $i_o < 0$

Table 1. Switches states for a single-phase full-bridge inverter.

To control of the output voltage of inverters is often necessary to compensate the variation of dc input voltage, regulate the output voltage of inverter, and to adjust the output frequency to the desired value. There are various techniques to vary the inverter gain. The most operational method of controlling the gain and output voltage waveform is sinusoidal pulse-width modulation (SPWM) technique. In SPWM approach, the width of each pulse is varied in proportion to the amplitude of sine wave compared at the center of the same pulse. The gating signals in this approach are shown in Figure 14. The gating signals are generated by comparing a sinusoidal wave as reference signal with triangular carrier wave of frequency f_c. The frequency of reference signal f_r determines the output frequency f_o of inverter, and the peak amplitude of it A_r specifies the modulation index M. Comparing the bidirectional carrier signal v_{tri} with to sinusoidal reference signals $v_{control}$ and $-v_{control}$ results gating signals g_1 and g_4. The output voltage is $v_o = V_d(g_1 - g_4)$. However, g_1 and g_4 can not be released at the same time. The same gating signals can be generate by using unidirectional triangular carrier wave as shown in Figure 15. This method is easy to implementation [18,22,23].

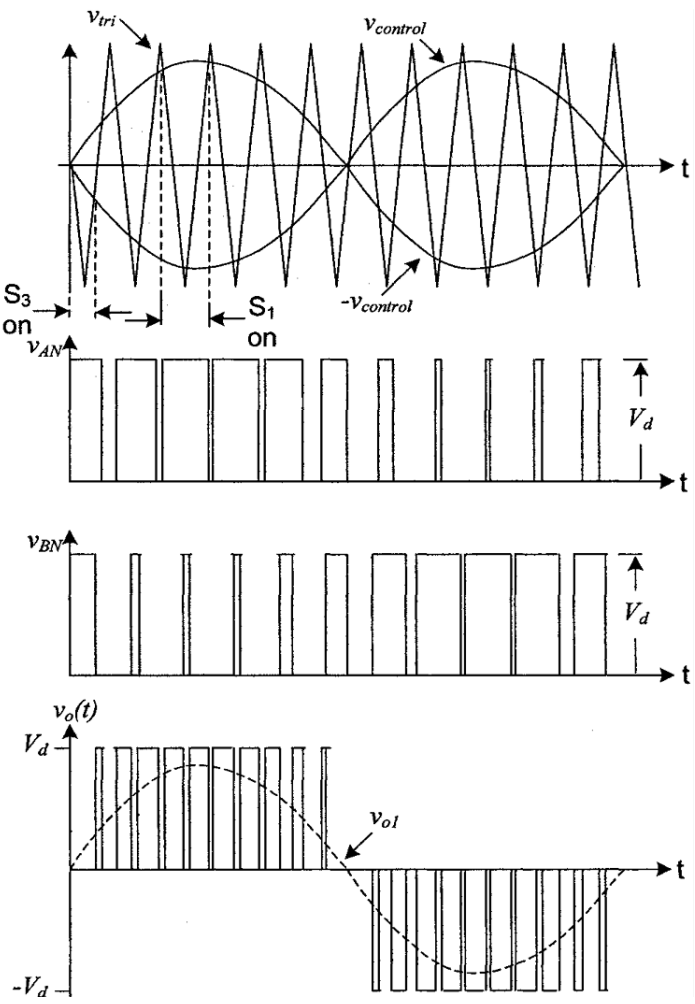

Figure 14. Bidirectional SPWM.

3.1.3.2. Multi-level inverters

The voltage source inverters generate an output voltage levels either 0 or $\pm V_d$. They are called two-level inverter. To obtain a quality output voltage or a current waveform with a minimum amount of THD[1], they require high-switching frequency and various pulse-width modulation (PWM) techniques. However, Switching devices have some limitations in operating at high frequency such as switching losses and device ratings [18].

1 Total Harmonic Distortion

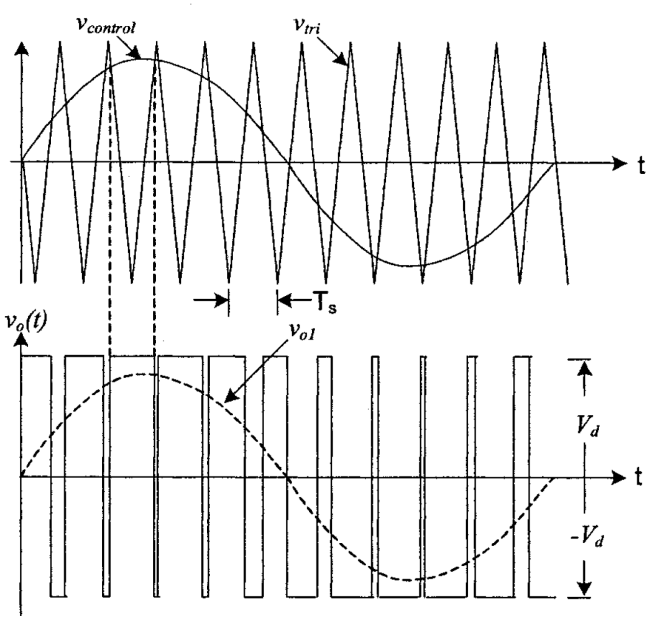

Figure 15. Unidirectional SPWM.

The most significant advantages of multilevel converters in comparison with two-level inverters are incorporating an output voltage waveform from several steps of voltage with significantly improved harmonic content, reduction of output $\frac{dv}{dt}$, electromagnetic interference, filter inductance, etc [24]. The general structure of multilevel converter is to synthesize a near sinusoidal voltage from several levels of dc voltages, typically obtained from capacitor voltage sources [18]. With increasing of levels, the output waveform has more steps, which produce a staircase wave that approaches a desired waveform. Also, as more steps are added to the waveform, the total harmonic distortion (THD) of output wave decreases.

Multilevel converters can be classified into three general types which are diode-clamped multilevel (DCM) converters, cascade multicell (CM) converters, and flying capacitor multicell (FCM) converters and its derivative, the SM converters [24].

3.1.3.2.1. Diode-clamped multilevel (DCM) converter

The n-level diode-clamped multilevel inverter (DCMLI) produces n-levels on the phase voltage and consists of $(n - 1)$ capacitors on the dc bus, $2(n - 1)$ switching devices and $(n - 1)(n - 2)$ clamping diodes. Figure 16 shows a 3-level diode-clamped converter. For a dc bus voltage E, the voltage across each capacitor is $\frac{E}{2}$, and each switching device stress is limited to one capacitor voltage level $\frac{E}{2}$ through clamping diodes.

http://dx.doi.org/10.5772/51918

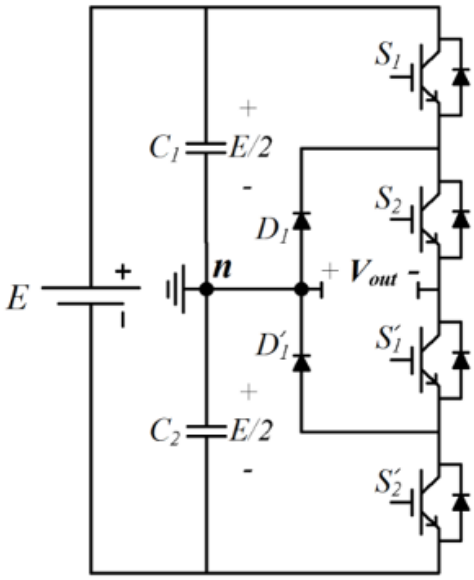

Figure 16. level diode-clamped converter.

To produce a staircase output voltage, for output voltage $V_{out} = \frac{E}{2}$, S_1 and S_2 power switches must be turned on. When $S_1^{'}$ and $S_2^{'}$ power switches are turned on, the output voltage $V_{out} = -\frac{E}{2}$ appears across the load. For output voltage $V_{out} = 0$, $S_1^{'}$ and S_2 power switches must be turned on [18,23].

The significant advantages of DCM inverter can be expressed as follows:

- When the number of levels is high enough, the harmonic content is low enough to avoid need for filters.
- Inverter efficiency is high because all devices are switched at the fundamental frequency.
- The control method is simple.

The significant disadvantages of DCM inverter can be expressed as follows:

- Excessive clamping diodes are required when the number of levels is high.
- It is difficult to control the real power flow of the one converter in multi converter systems [18,23].

3.1.3.2.2. Cascade multilevel (CM) converter

A cascade multilevel inverter consists of series of H-bridge inverter units. The general operation of this multilevel inverter is to synthesize a desired voltage from several separate dc sources, which may be obtained from wind turbines, batteries, or other voltage sources. Figure 17 shows the general structure of a cascade multilevel inverter with isolated dc voltage sources.

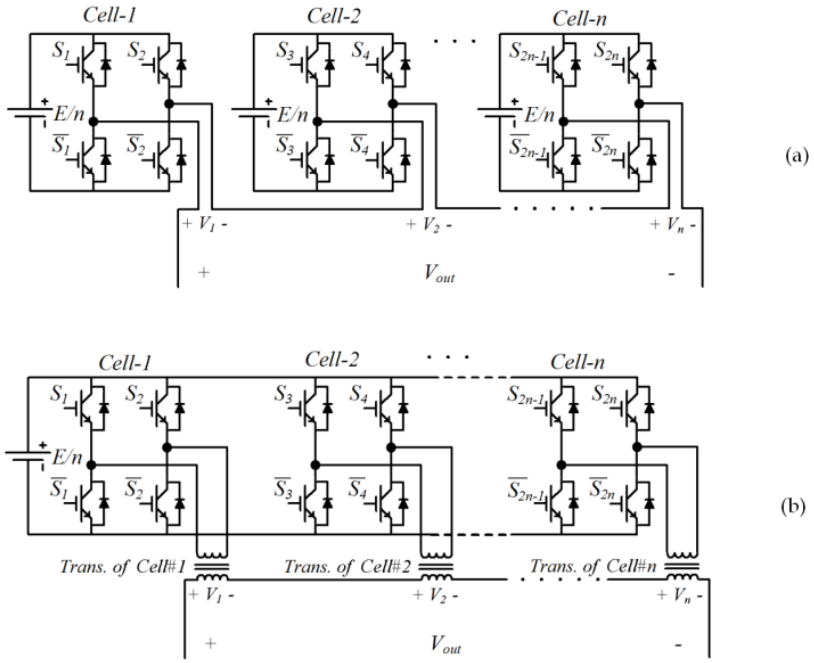

Figure 17. The 2n+1 levels cascade multilevel inverter: (a) with separated dc voltage sources. (b) with one dc voltage source and isolator transformers.

Each inverter can produce three different levels of voltage outputs, $+E$, 0, and $-E$, by connecting the dc source to the ac output side by different states of four switches, S_1, S_2, $\bar{S}_1$, and $\bar{S}_2$. Table 1 shows five switch states for H-bridge inverter. The phase output voltage is obtain by the sum of inverter outputs. Hence, the CM inverter output voltage becomes

$$v_{out} = \sum_{i=1}^{n} v_i \tag{56}$$

where n is number of cells and v_i is the output voltage of cell i.

If n is number of cells, the output phase voltage level is $2n + 1$. Thus, a five-level CM inverter needs 2 bridge inverters with separated dc voltage sources. Table 2 shows the switches states for five-level CM inverter [18,23].

Output Voltage Level	State of (S_1, S_2, S_3, S_4)	Number of States
$+\frac{2}{2}E$	(1, 0 , 1 , 0)	1
$+\frac{1}{2}E$	(1, 0 , 1 , 1) , (1, 0 , 0 , 0) , (1, 1 , 1 , 0) , (0, 0 , 1 , 0)	4
0	(1, 1 , 1 , 1) , (1, 1 , 0 , 0) , (0, 0, 0, 0) , (0, 0 , 1 , 1)	4
$-\frac{1}{2}E$	(0 , 1 , 1 , 1) , (0, 1 , 0 , 0) , (1, 1 , 0 , 1) , (0, 0 , 0 , 1)	4
$-\frac{2}{2}E$	(0, 1 , 0 , 1)	1

Table 2. Switches states for a five-level CM inverter.

The significant advantages of the CM inverter can be expressed as follows:

- Compared with the DCM and FCM inverters, it requires the minimum number of components to achieve the same number of voltage levels.
- Soft-switching techniques can be used to reduce switching losses and device stresses.

The significant disadvantage of the CM inverter can be expressed as follows:

- It needs separate dc voltage sources for real power conversions [18,23].

3.1.3.2.3. Flying capacitor multicell (FCM) converter

The FCM converters consist of ladder connection of cells while each cell in FCM is made up of a flying capacitor and a pair of semiconductor switches with a complimentary state. The commutation between adjacent cells with their associated flying capacitors charged to the specific values generates different levels of chopped input voltage at the output side of converter [24]. The voltage balancing of flying capacitors which guarantees the safe operation of the converter is a important subject in these topologies [23, 24]. The capacitors voltage balancing which is called self-balancing occurs if phase-shifted carrier pulse-width modulation (PSC-PWM) technique is applied to the converter control pattern [24]. Figure 18 and Figure 19 show the general structure of a flying capacitor multilevel (FCM) inverter and the phase-shifted carrier pulse-width modulation (PSC-PWM) technique for five-level FCM inverter, respectively.

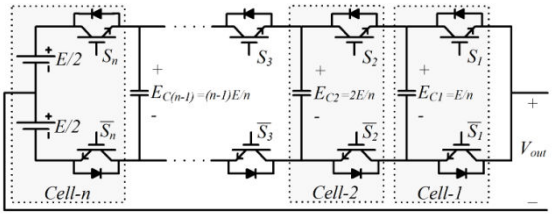

Figure 18. The *n* cells (*n* + 1 levels) FCM inverter.

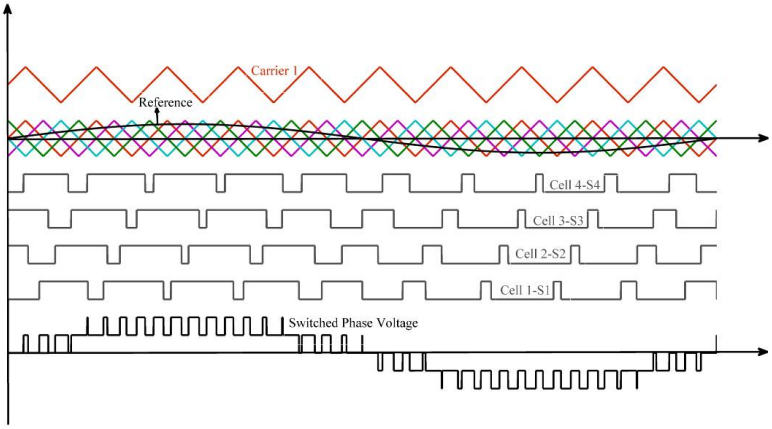

Figure 19. The phase-shifted carrier pulse-width modulation (PSC-PWM) technique for five-level FCM inverter.

The significant advantages of the FCM inverter can be expressed as follows:

- No need for isolation of dc links and transformerless operation capability.
- No need for clamping diodes.
- Availability of redundant states balance and inherent self-balancing property of the voltage across flying capacitors.
- Equal distribution of switching stress between power switches.

The significant disadvantages of the FCM inverter can be expressed as follows:

- A large number of flying capacitors is required when the number of levels is high.
- The inverter control can be very complicated [18,23,24].

Table 3 shows the switches states for five-level FCM inverter.

http://dx.doi.org/10.5772/51918

Output Voltage Level	State of (S_4, S_3, S_2, S_1)	Number of States
$+\frac{2}{4}E$	(1, 1 , 1 , 1)	1
$+\frac{1}{4}E$	(1, 1 , 1 , 0) , (1, 1 , 0 , 1) , (1, 0 , 1 , 1) , (0, 1 , 1 , 1)	4
0	(1, 1 , 0 , 0) , (1, 0 , 0 , 1) , (0, 0, 1, 1) , (0, 1 , 1 , 0)	4
$-\frac{1}{4}E$	(0, 0 , 0 , 1) , (0, 0 , 1 , 0) , (0, 1 , 0 , 0) , (1, 0 , 0 , 0)	4
$-\frac{2}{4}E$	(0, 0 , 0 , 0)	1

Table 3. Switches states for a five-level FCM inverter.

4. Small-scale wind energy conversion system

Small-scale wind conversion system may be integrated into loads or power systems with full rated power electronic converters. The wind turbines with a full scale power converter between the generator and load give the extra technical performance. Usually, a back-to-back voltage source converter (VSC) is used in order to achieve full control of the active and reactive power. But in this case, the control of whole system would be a difficult task. Since the generator has been decoupled from electric load, it can be operated at wide range frequency (speed) condition and maximum power extract. Figure 20 shows two most used solutions with full-scale power converters. Both solutions have almost the same controllable characteristics since the generator is decoupled from the load by a dc link [1,17].

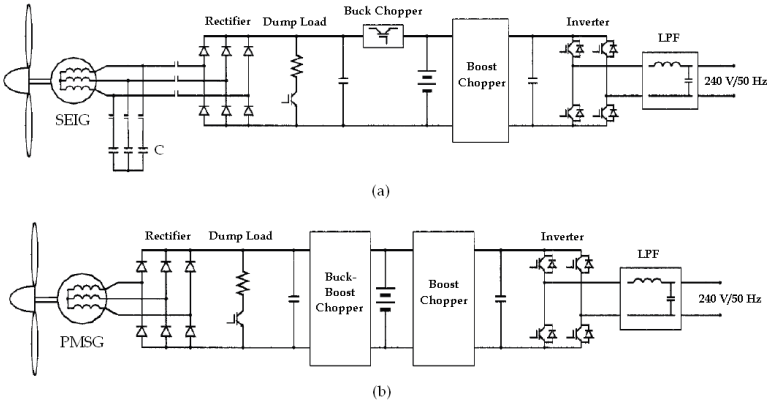

Figure 20. Small-scale wind energy conversion system. (a)self-excited induction generator with gearbox. (b)direct coupled permanent magnet synchronous generator.

The configuration shown in Figure 20(a) is characterized by having a gearbox. The wind turbine system with a SEIG and full rated power electronic converters is shown in Figure 20(a). Multipole systems with the permanent magnet synchronous generator without a gearbox is shown in Figure 20(b).

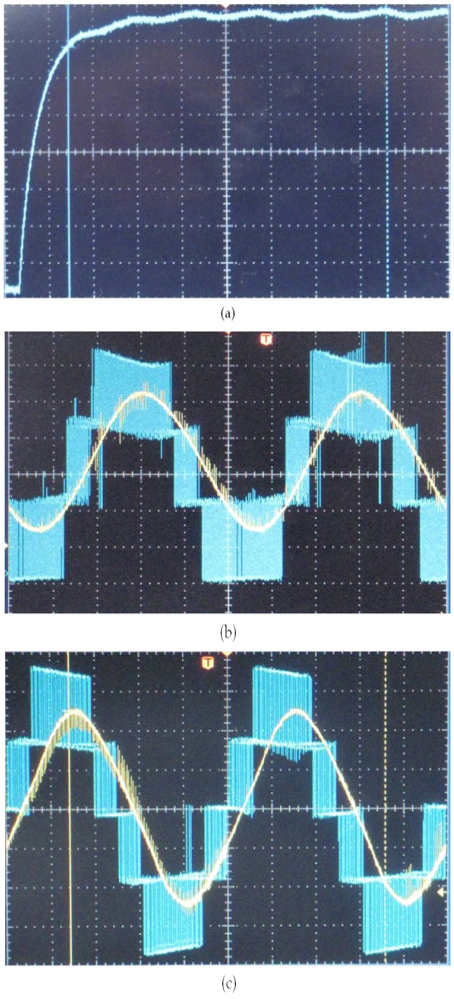

Figure 21. a) output regulated voltage of DC/DC boost converter. (b) output AC voltage and current of DC/AC 4 levels FCMC. (c) output AC voltage and current of DC/AC 5 levels FCMC [23].

The grid connected 1 KW small scale wind generation system has been modelled, designed and implemented in renewable energy research center of sahand university of technology. In this project the maximum power point tracking method has been used to control of varia-

ble speed small scale wind turbine. Wind turbine consist of axial flux permanent magnet synchronous generator (AFPMSG), rectifier, DC/DC boost chopper, maximum power point tracking controller, inverter and load. Tracking system is embedded in boost chopper controller in order to regulate wind turbine shaft at optimum speed to extract maximum power from wind. Two inverters such as: 4 and 5 levels flying capacitor multi-cell converter (FCMC) have been implemented. The small scale wind generation system has been simulated on MATLAB/Simulink platform. Simulation results clearly demonstrate that designed small scale wind generation system can operate correctly under various wind speeds. The regulated output DC voltage of DC/DC boost chopper has been converted to AC voltage with 4 and 5 levels flying capacitor multi-cell converter (FCMC). The DC/DC boost chopper and inverter include IGBT transistors, interfacing board, driver boards, voltage and current sensors and ATMEGA16 microcontroller board. The phase shifted pulse width modulation (PSPWM) and pulse width modulation (PWM) techniques have been implemented on multicell inverters and DC/DC boost chopper respectively [23]. The experimental results of the 1 KW small scale wind generation system have been shown in Figure 21. Figure 21(a) shows the output regulated voltage of DC/DC boost converter. Whereas, Figure 21(b) shows the output AC voltage and current of DC/AC 4 levels FCMC, and Figure 21(b) shows the output AC voltage and current of DC/AC 5 levels FCMC.

5. Conclusion

This chapter has reviewed different power electronic converters for small-scale wind turbine systems. Various arrangements of small scale wind generators with different generators and control systems are described. In compare with gearbox-connected wind generators, the main advantages of direct–drive wind generator systems are higher overall efficiency, reliability, and availability due to omitting the gearbox. Considering the improved performance and reduced cost of PM materials over recent years, direct drive PMSG have gained more attention in small scale wind generation systems. Different types of DC/DC converter for small-scale wind turbine output voltage regulation are described.

Several topolgies of DC/AC inverter for DC/DC converter output voltage conversion are investigated. The most significant advantages of multilevel converters in comparison with two-level inverters are low harmonic contents, low output $\frac{dv}{dt}$ and electromagnetic interference, and reduced size of filter inductance. Even though all types of multi-level converters such as DCMC, CMC, and FCMC present major advantages for small-scale wind energy conversion applications, but FCMCs have gained more attention in small-scale wind energy conversion systems.

Two most used solutions with full-scale power converters are investigated. Since the generator is decoupled from the load by a dc link, so both solutions have almost the same controllable characteristics. The wind turbines with a full scale power converter between the generator and load give the extra technical performance. The provided ex-

perimental results verify the good performance and feasibility of the proposed full-scale power electronic converter.

Author details

Mostafa Abarzadeh[1*], Hossein Madadi Kojabadi[1] and Liuchen Chang[2]

*Address all correspondence to: mst.abarzadeh@gmail.com

1 Renewable Energy Research Center, Sahand University of Technology, Tabriz, Iran

2 Department of Electrical & Computer Engineering, University of New Brunswick, NB, Canada

References

[1] Abarzadeh, M., Madadi, kojabadi. H., & Chang, L. Small Scale Wind Energy Conversion Systems In: Al-Bahadly I. (ed.) Wind Turbines: InTech; (2011). , 639-652.

[2] Yuan Lo K., Ming Chen Y., Ruei Chang Y. MPPT Battery Charger for Stand-Alone Wind Power System. Power Electronics, IEEE Transactions on. 2011;26(6) 1631 - 1638.

[3] Smith J., Thresher R., Zavadil R., DeMeo E., Piwko R., Ernst B., and Ackermann T. A mighty wind. IEEE Power Energy Mag.2009;7(2) 41-51.

[4] Nayar C., Dehbonei H., Chang L. A Low Cost Power Electronic Interface for Small Scale Wind Generators in Single Phase Distributed Power Generation System: conference proceedings, December 14-17, 2008, The University of Tasmania, Hobart, Tasmania, Australia: AUPEC; 2005.

[5] Pathmanathan, M., Tang, C., Soong, W. L., & Ertugrul, N. Comparison of Power Converters for Small-Scale Wind Turbine Operation: conference proceedings, September 25-28, (2005). Sydney,Australia: AUPEC; 2008.

[6] American Wind Energy Association Annual Wind Industry Report (year ending(2008). AWEA. http://www.awea.org

[7] Borowy B. S., Salameh Z. M., Dynamic response of a stand-alone wind energy conversion system with battery energy storage to a wind gust, IEEE Trans. Energy Convers. 1997;12(1) 73–78.

[8] Billinton R., Bagen, Cui Y., Reliability evaluation of small standalone wind energy conversion systems using a time series simulation model. IEE Proc.-Generat. Transmiss. Distrib. (2003). , 150(1), 96-100.

[9] Bagen, Billinton R., Evaluation of different operating strategies in small stand-alone power systems.IEEE Trans. Energy Convers. (2005). , 20(3), 654-660.

[10] Singh, B., & Kasal, G. K. Power Electronics in Small Scale Wind Turbine Systems. IEEE Trans. Power Electron. (2008). , 23(3), 1170-1177.

[11] Chen, Z., & Spooner, E. Power Electronics in Small Scale Wind Turbine Systems. IEE Proc. Electr. Power Appl. (1998). , 145(4), 273-283.

[12] Chen, Z., & Spooner, E. Grid Power Electronics in Small Scale Wind Turbine Systems. bines. IEEE Trans. Energy Convers.(2001). , 16(2), 148-154.

[13] Probst, O., Martinez, J., Elizondo, J., & Monroy, O. Small Wind Turbine Technology In: Al-Bahadly I. (ed.) Wind Turbines: InTech; (2011). , 107-136.

[14] Muljadi, E., Forsyth, T., & Butterfield, C. P. Power Electronics in Small Scale Wind Turbine Systems. conference proceedings: April May 1,(1998). Windpower '98 Bakersfield, CA., 27.

[15] Muljadi, E., Pierce, K., & Migliore, P. (2000). Power Electronics in Small Scale Wind Turbine Systems. *Journal of Wind Engineering and Industrial Aerodynamics*, 85(3), 277-291.

[16] Bialasiewicz J.T.Furling control for small wind turbine power regulation: conference proceedings, (9-11 June 2003). Industrial Electronics, 2003. ISIE '03. 2003 IEEE International Symposium on., 9-11.

[17] Blaabjerg, F., Liserre, M., & , K. Power Electronics in Small Scale Wind Turbine Systems. ine Systems. Power Electronics, IEEE Transactions on. (2012). , 48(2), 708-719.

[18] Rashid M.H. Power Electronics, circuits, devices and applications, third edition.Prentice-Hall; (2007).

[19] Keith, H., & Billings, . Power Electronics in Small Scale Wind Turbine Systems. McGraw-Hill; (1999).

[20] Marty Brown. Power Supply Cookbook, second edition.Butterworth-Heinemann; (2001).

[21] Czarkowski D. DC-DC Converters In: Rashid M.H. (ed.) Power Electronics Handbook: ACADEMIC PRESS; 2001. P211-223.

[22] Espinoza J.R. Inverters In: Rashid M.H. (ed.) Power Electronics Handbook: ACADEMIC PRESS;. (2001). 225-267.

[23] Abarzadeh, M., Modelling, Design., Implementation, of., Grid, Connected., Small, Scale., Wind, Generation., & System, . Msc thesis. Sahand University of Tech; (2011).

[24] Dargahi, V., Khoshkbar, Sadigh. A., Abarzadeh, M., Alizadeh, Pahlavani. M. R., & Shoulaie, A. Power Electronics in Small Scale Wind Turbine Systems. Power Electronics, IEEE Transactions on. (2012). , 27(9), 3875-3887.

Chapter 14

Advanced Wind Generator Controls: Meeting the Evolving Grid Interconnection Requirements

Samer El Itani and Géza Joós

Additional information is available at the end of the chapter

http://dx.doi.org/10.5772/51953

1. Introduction

1.1. Grid interconnection requirements

Reliable power system operation requires the continuous, instantaneous balance of supply and demand. Traditionally, power system planners have been familiar with a limited, well-understood amount of variability and uncertainty in demand and conventional generation. The large-scale integration of variable generation, such as wind power, gives rise to new challenges, requiring grid planners and operators to modify their traditional activities to maintain a secure, reliable operation of the power system.

1.1.1. Proliferation of wind power

For more than a decade now, wind power has been driving the change in electric grids worldwide. Currently, wind energy serves 22% of the load energy in Denmark, 17% in Portugal, 16% in Spain, 10.5% in Ireland and 9% in Germany. Also, with 86 GW of installed wind capacity in Europe, 42 GW in China, and 40 GW in the United States, it is fair to say that wind power has come to stay.

Each year wind power is increasing its share of the global electricity production, Figure 1. As penetration levels increase to the extent that conventional generators are displaced,

- is there a technical limit on the manageable wind penetration level?
- what are the technical characteristics hindering the integration of wind power?
- what are the needed reforms in technical design or operational trends of the grid to allow further accommodation of wind power?

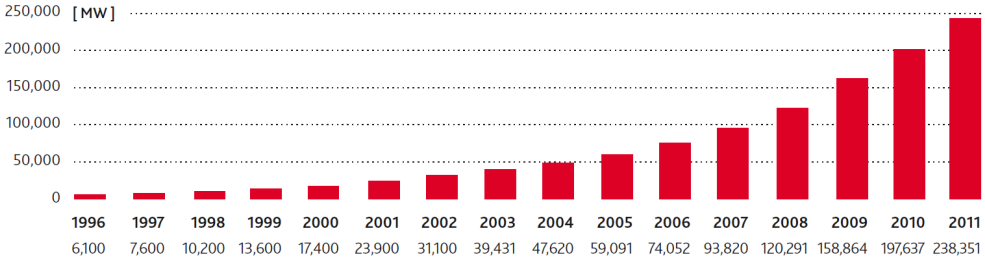

Figure 1. Global cumulative installed wind capacity, 1996-2011 [1].

In this chapter, we attempt at answering these questions to shed light on the main integration challenges that wind power is facing and the opportunities that lie within.

1.1.2. Grid integration challenges & opportunities

The grid impact of the connection of a wind power plant depends on several factors. These include the technology of the turbines, the plant collector system, the required interconnection features/capabilities, and the wind–grid penetration level.

Due to its intermittent nature, wind power blurs the distinction between dispatchable generation resources and variable system load. Since the fuel source of wind plants is uncontrollable and depends on meteorology, it must be dealt with operationally through mechanisms other than the traditional dispatch or commitment instructions. The challenging characteristics of wind power itself can be summarized in the following four elements [2]:

- **Variability:** The output of wind generation changes in time frames that range from seconds to hours
- **Uncertainty:** The magnitude and timing of variable generation output is less predictable than it is for conventional generation
- **Location:** Wind farms are often located in relatively unpopulated, remote regions that require long transmission lines to deliver the power to load centers
- **New technologies:** New technologies are often needed for wind turbines (e.g., doubly fed induction generators), requiring special assessment of their voltage and frequency regulation capabilities, harmonic emissions, contribution to sub-synchronous resonances, and protection coordination.

The nature of wind power, however, is not the only source of challenge. Some power systems attempting at wind integration are already weak, have limited dispatch flexibility and balancing capabilities, or suffer shortage in transmission infrastructure. In some systems, the gap between peak and valley loads is already big and the ramping capabilities are already exhausted,

http://dx.doi.org/10.5772/51953

leading to a tight load-following capability (e.g. China). The situation is exacerbated by wind integration because the wind power peaks typically occur at load off-peak [3].

In order to tackle these technical challenges while responding to the pressure to accommodate wind power, power system planners and operators have to alter their traditional planning methods and operational practices. The dominant philosophy is that wind power plants should have all the technical capabilities needed to contribute to the secure operation of the power system in the same manner as conventional generators do. Thus new grid codes are written, often with supplementary provisions for wind power plants. This is discussed in detail in the following sections.

1.1.3. Grid code development

In the rush of promoting wind energy, little attention was paid to grid interconnection issues in many countries. There were no requirements for wind farms to regulate voltage, ride through grid disturbances, or support the system frequency. Even in regions were interconnection requirements for wind farms where relatively advanced (e.g. Denmark or Germany), the provisions were moderate, reflecting the low wind penetration levels and the technology limitations at the time. At several occasions, these wind farms produced unacceptable voltage fluctuations during normal operation and caused major loss-of-generation events in response to otherwise minor system disturbances [5].

Through extensive experience with interconnection studies, power system operators and planners became increasingly familiar with the concept of a wind power plant; its performance characteristics, capabilities, and limitations. Grid codes were updated, requesting that wind plants exhibit similar operational features as conventional synchronous generators and abide by the same minimum performance criteria. The object of these provisions is to maintain the same level of operational security and reliability while minimizing curtailment of wind power. The main requirements relate to fault ride-through, reactive power and voltage control, dynamic behavior, active power and frequency control, and power quality. These requirements are met (either at the level of the wind turbine or the wind plant) through supplementary control loops that are triggered when specific events occur, such as contingencies resulting from grid faults, instabilities or loss of generation. These topics are treated in detail later in this chapter. Other generation controls not yet required from wind power plants include power system stabilizers (PSS), frequency regulation, and automatic generation control. These controls may in the future be incorporated into the core function or provided as ancillary services.

The technical requirements and performance specifications laid out in grid codes relate to the Point of Interconnection (POI), which is the border of responsibility between the network operator and the wind plant owner. As an example, Figure 2 and Table 1 describe the points of application of the technical rules of the grid operator in the Canadian province of Alberta (AESO). Similarly, Figure 3 shows the points of measurement for voltage ride-through and reactive power requirements according to the grid operator in the Canadian province of British Columbia.

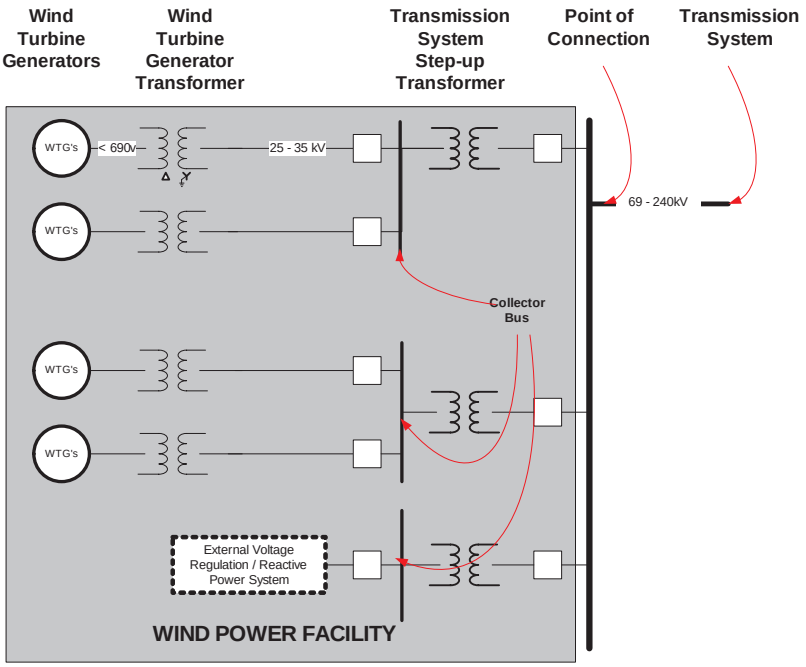

Figure 2. Wind power facility diagram – AESO [7].

Requirement	Performance Point		
Collector Bus	POI	WTG	
Maximum authorized MW	X		
Gross MW	X		
MW & ramp rate limiting		X	
Over-frequency control	X		
Off-nominal frequency		X	
Reactive power requirements	X		
Voltage regulation	X		
Voltage operating range	X		
Voltage ride-through		X	
Real-time monitoring	X	X	
Meteorological signals			X

Table 1. Points of measurement of performance criteria – AESO [7].

http://dx.doi.org/10.5772/51953

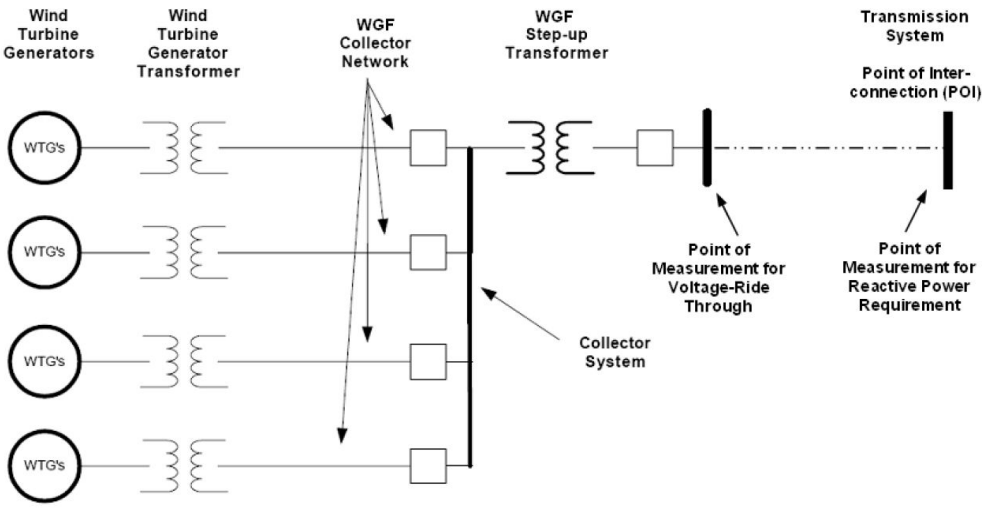

Figure 3. Wind power facility diagram – BC Hydro [24]. WGF: Wind generation facility.

For offshore wind power plants, there are two possibilities for the POI depending on how the grid connection is embedded in the regulatory framework. In some countries (e.g. Germany), the local utility is responsible for extending its transmission network offshore to enable the connection. In this case, the POI is at the offshore substation of the wind plant so all the offshore transmission assets are in the scope of responsibility of the network operator. In other countries (e.g. USA), the wind plant developer is responsible for grid connection up to the onshore POI, thus the submarine cables are within the wind power plant in this case [8].

It is challenging to design a wind plant, consisting of many turbines distributed over a large geographical area, so that it behaves like a conventional power plant as seen by the system at the POI. In the following sections, we discuss the different grid code requirements, design considerations, and industry implementations with reference to provisions from several European and North American grid codes. Emphasis is placed on the more sophisticated codes that come from countries and regions with high wind penetration levels. For each required control function, solutions are cited from the industry and reserach community.

1.1.4. Power coordination & energy storage

In addition to requiring a behavior similar to conventional generators from wind power plants, grid operators are looking into energy storage and coordinated generation as intelligent solutions to facilitate the connection of wind power. The power coming from conventional generation can be coordinated with the intermittent power from the wind to reduce the minute-to-minute variations. This has been employed in Portugal on multiple occasions where this solution was found technically viable and cost-effective [4]. A recent study performed in Ireland concluded that pumped hydro storage becomes economically attractive at an average annual wind power penetration of approximately 50% [14].

Short-term energy storage facilities (flywheels and batteries) are also gaining momentum in providing ancillary services to assist in power system stabilization and controlled islanding. In one example in the USA [13], a multi-MW battery energy storage system (BESS) was added in the grid to allow a large network to operate as a self-powered "island" in the event of transmission feeder loss. The BESS served radially fed distribution feeder loads for several hours during a permanent fault that was experienced on the grid. The BESS was also employed for peak shaving, thus helping defer costly transmission and substation transformer upgrades. In another example [14], a 21 MW wind power plant in Hawaii is was designed to utilize a 4 MW BESS to help regulate the variability of the plant's output, thus enhanced the stability of the local grid.

1.2. Steady-state tolerance ranges

1.2.1. Frequency & voltage operation ranges

Wind power plants are required to ride through prolonged frequency excursions without disconnection. This is typically defined through tolerance curves and extended time ranges around the nominal operating point of the power system. When the deviations are large, a reduction of the output power or operation for a limited period may be allowed. For example, Figure 4 shows the frequency tolerance curve of the Northeast Power Coordinating Council (NPCC)[1] and that of Hydro-Québec TransÉnergie (HQTE), the system operator in Québec.

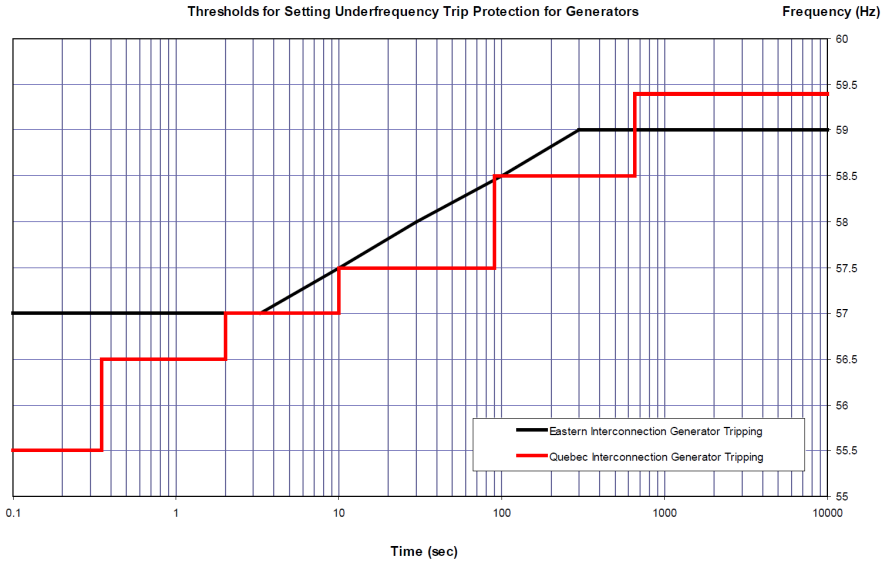

Figure 4. Required settings of under-frequency protection (log scale) – NPCC [18].

1 NPCC is responsible for the reliability of the bulk power system in Northeastern North America, governing the grids of several American and Canadian provinces.

http://dx.doi.org/10.5772/51953

The stability of the electric grid can be disturbed if a wind plant is disconnected as a consequence of a failure due to a voltage perturbation. Thus, a wind plant must be able to run at rated voltage plus an extended voltage range. In Europe, the required voltage and frequency tolerance ranges are often specified simultaneously. For example, the Nordic code[2] [19] demands from wind plants to operate in the voltage-frequency regions described in Figure 5.

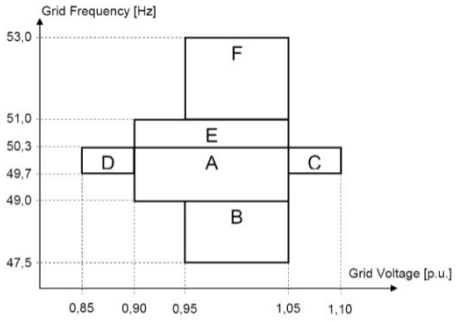

Region	Requirements	
	Operation	Active Power Reduction
A	Continuous	Not allowed.
B	Continuous for 30 minutes	Allowed as a linear function from (0%, 49.0 Hz) to (15%, 47.5 Hz)
C / D	Continuous for 60 minutes	Allowed to be reduced to 10%
E	Continuous for 30 minutes	Allowed to be slightly reduced
F	Continuous for 3 minutes	Allowed to be reduced to any level but the WTGs must stay connected

Figure 5. Voltage / frequency regions for wind power plants – Nordic code [20].

Figure 6 shows the different operation regions as specified by one of the German system operators.

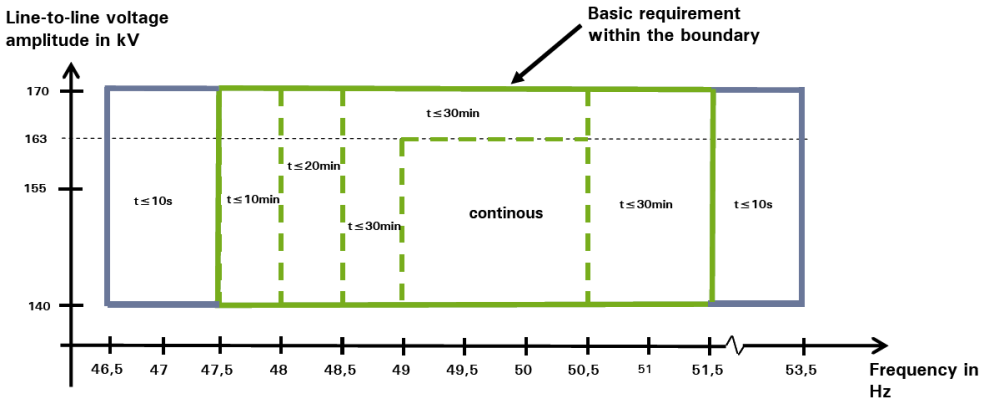

Figure 6. Voltage/frequency tolerance regions of one German system operator. Green: onshore wind plants, Green & blue: offshore wind plants [16], [17].

2 Until the publication of the ENTSO-E grid code in Fall 2013 [12]-[13], the Nordic code governs the operation of the transmission systems of Denmark, Finland, Iceland, Norway and Sweden .

In offshore and isolated power systems with weak interconnections, the frequency limits tend to be wider to ensure that wind plants (and other forms of generation) can continue to deliver their power and grid support functionalities. This is evident in the blue section of Figure 6, which shows that offshore wind plants are asked to stay connected between 46.5 Hz to 53.5 Hz (± 7%) for up to 10 sec. In Ireland, where the grid is infamous for its wide frequency excursions, wind plants are required to remain connected for frequency deviations down to 47.0 Hz and during a rate of change of frequency up to 0.5 Hz/sec. These are the most extreme frequency limits specified for 50Hz grids.

1.3. Active power control

Wind power plants are required to have an active power control system capable of receiving set-point commands from the grid operator to limit active power and ramp rate. This is typically achieved through pitch angle control and/or by disconnecting some wind turbines.

1.3.1. Set-point curtailment

During periods of transmission congestion or extremely low system loads, constraining conditions can result in deflated (or even negative) market prices, especially in regions with sophisticated wholesale electricity markets. One technique to address the lack of available transmission, or the excess of wind power at any given time, is to curtail wind plants to lower output levels during periods when it is less economic to keep them producing at full capability.

To accomplish this, several system operators have integrated wind energy into their security-constrained economic dispatch (SCED). Within the available power from the wind, the output power can be regulated to a specific MW value or a percentage of the available power. A fast, robust response of the active power control is important during normal operation to avoid frequency excursions and during transient fault situations to guarantee transient and voltage stability.

In one example, AESO specifies that wind plants must be able to limit their active power to real-time MW set-points with an average resolution of 1 MW and accuracy of 2% of rated power on a 1-minute average. It is also specified that wind gusts should not lead to exceeding the active power limit by more than 5% of rated power [18]. One of the German codes requires wind plants to be capable of operating at a reduced power output without exceeding 1% change of rated power per minute across the entire range between minimum and rated power [15]. The Irish code requires wind plants to commence the implementation of any set point within 10 sec of receipt of the signal [26].

1.3.2. Ramp rate limits

Requirements for active power control include the limitation of the ramp rate (rate of change) of active power. Ramp rates are possible for power increase, but operation with a power reserve is necessary in output power decrease, which necessitates sub-optimal economic operation.

http://dx.doi.org/10.5772/51953

For example, wind plants in Québec are required to be able to ramp up rate and down between 0 MW and rated power in an adjustable 2 to 60 second interval [23]. In Alberta, AESO specifies that wind plants must be capable of maintaining their ramp up between 5 and 20 %/min of the rated power, taking into account all losses in cables and transformers [19]. The Irish code requirespower curtailment capability with a ramp rate defined project-specifically in the range 1 – 30 MW/min [26]. The Nordic code [20] requires the ability to regulate active power up or down from 100% to 20% of rated power in less than 5 seconds.

1.4. Frequency control

System events that include load-generation mismatches often result in transient fluctuations of the system frequency. This can be caused by mechanical failures of generators, sudden load changes, or line losses in the transmission system. The rate and depth of frequency decline and the time for frequency to return to its target value are all critical bulk power system performance metrics that are affected by the dynamics of the generation mix.

1.4.1. Inertial response

With the increasing penetration of inverter-based generation technologies, such as modern wind plants, the primary frequency response of several North American and European grids has been declining for years. The concern is most pronounced during simultaneous light load and high wind, where economics dictates that fewer synchronous generators will be operating, and the overall grid inertia will consequently be reduced.

This was confirmed by a study performed in late 2010 by the Lawrence Berkeley National Lab and sponsored by the Federal Energy Regulatory Commission (FERC) in USA. The objective of the study was to examine the status of the American grids with respect to frequency regulation capabilities [38]. Among other results, the study concluded that:

- frequency-insensitive wind generation does have an impact on the minimum frequency observed following a loss of major generation
- This influence is not the sole cause for the deteriorated primary frequency response. Other causes include the low quality of the frequency response provided by the conventional generators
- The performance of demand-based primary frequency response reserves was superior to that of conventional governor-controlled generators in arresting the frequency decline due to significant loss of generation.

It was thus concluded that the approach for maintaining adequate frequency responsive reserves should not involve only new requirements for wind generation, but also innovative solutions on the demand side and improvements in the frequency response of the existing conventional generation.

In another case, the integration of wind energy in Québec has triggered an added need for frequency support in order to avoid reaching the low-shedding thresholds under critical

generation loss scenarios. The power system of Québec is connected to its neighboring systems asynchronously, thus it is responsible for its own frequency regulation as an independent region of the North American Electric Reliability Corporation (NERC). With the current inertia of Québec's system, large post-contingency frequency excursions up to ±1.5 Hz for extended periods can potentially occur. In a recent study [30], HQTE concluded that if 2000MW of hydro generation is replaced by wind turbine generators without inertial response, the frequency nadir will deteriorate by about 0.2 Hz within the first 10 seconds. As a result, HQTE requires wind plants to be equipped with an inertia emulation system to support system frequency following a major frequency event [23]:

- The system should respond to major frequency deviations only
- The performance should be at least as much as that of a conventional synchronous generator whose inertia constant (H) equals 3.5 sec.

The requirement can be satisfied if the active power is increased rapidly by 5% for about 10 sec following a major frequency deviation. A similar provision is stipulated by the Independent Electric System Operator (IESO) of Ontario.

Similar investigations are carried out in Europe. A study by the Irish grid operator forecasts deficiencies in system performance in terms of frequency and voltage control due to the increasing share of non-synchronous generation by 2020 [27]. The analysis concluded that:

- The projected levels of synchronous inertia available in 2020 will be less than the amount needed to meet the statutory system requirements
- At high instantaneous non-synchronous generation, there is a risk of excessive activation of Rate of Change of Frequency (RoCoF) protection relays that shut down wind turbines under certain scenarios.

The solutions that involve the replacement of the RoCoF relays on the distribution networks with alternative protection schemes or increasing the RoCoF thresholds. New commercial mechanisms and financial models are also being studied to allow for advanced ancillary services.

In the UK, the system operator performed a technical assessment of the available options for the management of frequency response with the integration of wind power [22]. The recommendations called for:

- A faster frequency response capability in the first 5 seconds following a load-generation mismatch
- A closer examination of the sensitivity of the frequency response with respect to the ramping capability of the existing generation
- A clearer rephrasing of the grid code provisions addressing frequency control
- A reexamination of the existing RoCoF settings.

In recognition of the grid's need for frequency response, wind turbine manufacturers have developed control functions that temporarily increase power output when frequen-

http://dx.doi.org/10.5772/51953

cy declines by withdrawing energy from the rotating inertia of the turbine. [39]-[46] contain descriptions of several implementations sought in the industry (and in research) with and without auxiliary storage. [47] provides a comprehensive summary and comparison of the different implementations to date. A common aspect among all these implementations, irrespective of the wind turbine generator (WTG) topology or electric concept, is that the amount of power boost is not constant but rather a function of the wind condition. This is because all modern WTGs are variable-speed machines that regulate their rotational speed to optimize power capture from the wind. Another feature is the recovery period that follows the power boost when the WTG is operating at below-rated conditions. During the recovery period, the WTG withdraws active power from the grid to recover its pre-event rotational speed. The design considerations for inertial response emulation include: (a) the optimal amount of power that can be drawn from the rotating masses; (b) the duration of the momentary injection; and (c) the duration of the speed and energy recovery phase.

A long-term overproduction is more challenging for WTGs. Since they are designed to capture the maximum amount of power from the wind at any given moment, it is not possible to maintain an increase in the output power. Leaving "headroom" to increase production would necessitate spilling wind energy when wind speeds are below the turbine's rating, thereby incurring an economic penalty due to reduced annual production levels. The utilization of such a capability therefore comes down to economics, i.e., the value of primary frequency response relative to the value of the wind energy. This technical option is discussed in the following section in the context of the British frequency control requirements.

1.4.2. Primary reserve for under-frequency

The British grid code contains the most advanced (and complex) frequency control requirements to date. Several operation modes are asked from wind plants whose installed capacity is beyond 50 MW depending on the actual value of the system frequency relative to the system Target Frequency (50 ± 0.1 Hz.

The system operator will send to the wind plant a signal with the Target Frequency and an instruction of whether to operate in the Frequency Sensitive Mode (FSM) or Limited Frequency Sensitive Mode (LFSM). If FSM is specified, the control system has to automatically regulate the active power output as a function of the deviation of the actual frequency from the target frequency, in a direction assisting in the recovery to the target frequency.

When the system operator expects an under-frequency situation, the wind plant is curtailed prior to the frequency drop via a separate command from the system operator. When the frequency drops below the target frequency, the wind plant must exhibit a Primary (P) and Secondary (S) response as defined in Figure 7. The new active power set point can be obtained from Figure 7 for a 0.5 Hz deviation. For smaller deviations, the response should be at least proportional to the requirement specified for the 0.5 Hz deviation [21].

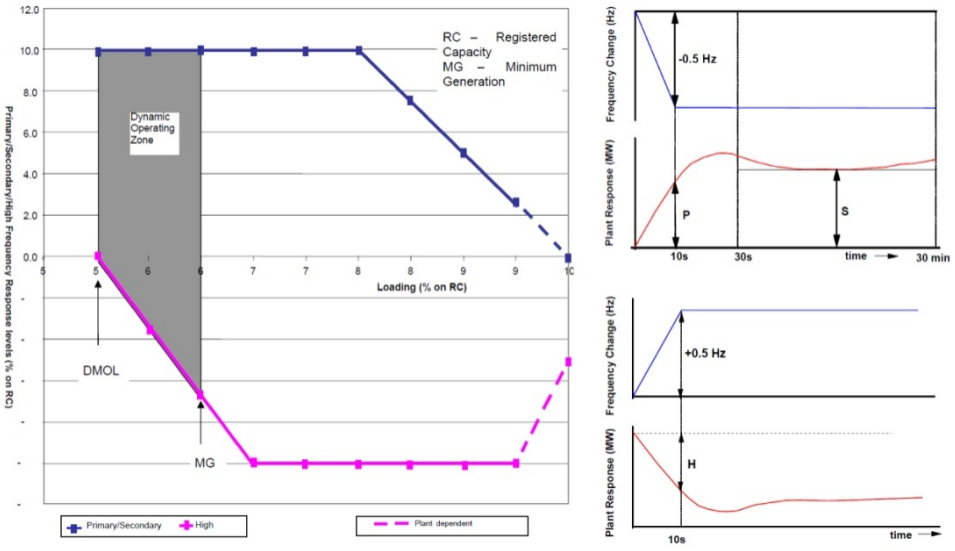

Figure 7. a) Minimum frequency response requirement for 0.5Hz frequency change from target frequency. (b) Interpretation of Primary (P), Secondary (S), and High-Frequency response values [21].

If the LFSM operation mode is specified by the system operator, only an over-frequency response is required. The active power control system must withhold the output for frequencies in the range between the target frequency and 50.4 Hz. Beyond 50.4 Hz, it must be reduced at a rate of at least 2% of actual active power per 0.1 Hz. The response should last until the frequency drops again below 50.4 Hz, with as much as possible delivered within the first 10 sec from the rise [21].

1.4.3. Over-frequency response

Wind plants are commonly asked to limit their active power as a function of the system frequency in over-frequency situations. For example, wind plants in the Canadian province of Alberta are required to have an over-frequency control system that:

- continuously monitors the grid frequency at a sample rate of 30/sec and a resolution of at least 4 mHz
- automatically controls the active power in a manner proportional to the frequency increase by a factor of 33% per Hz of actual active power output
- responds at a rate of 5%/second of the actual active power output
- has control priority over the other power limiting control functions like ramp rate limitations and curtailment set-point, and must reduce the active power output for an over-frequency condition even when these requirements are in effect

http://dx.doi.org/10.5772/51953

• has no intentional time delay, but may have a deadband of up to 36 mHz.

In Ireland, whose grid is known for its notorious frequency profile due to weak interconnection with the neighboring systems, the grid code demands from wind plants to control active power as close to real-time as possible according to the response curve described in Figure 8. The rate of response should be 1% of rated power per second for each online WTG [26]. Similar requirements exist in other European grid codes.

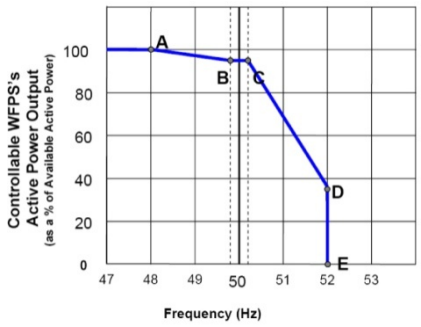

Point	f (Hz)	Active power (% of available power)	
		Capacity > 10MW	5MW < Capacity ≤ 10MW
A	47.0 – 51.0	50 – 100	100
B	49.5 – 51.0	50 – 100	100
C	49.5 – 51.0	50 – 100	100
D	50.5 – 52.5	20 – 100	20 – 100
E	50.5 – 52.5	0	0

Figure 8. Power-frequency response curve - Irish code [26]. WFPS: Wind farm power station.

1.5. Reactive power & voltage regulation

Voltage regulation in a power system is directly related to the flow of reactive power and is dependent on the short circuit capacity and impedance of the network. Large and quick variations of wind output can cause transient disturbances of the system voltage and tie line flows, both of which can lead to voltage stability issues especially in congested transmission corridors [2].

Conventional generation facilities have traditionally provided reactive power to support system voltage. These facilities have synchronous machines capable of operating in power factor ranges of +/-0.90 or +/-0.95. Voltage regulators on their excitation systems provide the primary voltage control function [6]. Older wind plants have been interconnected without these capabilities; occasionally leading to problems such as depressed voltages, excessive voltage fluctuation, and inability to deliver full power [6].

1.5.1. Steady-state reactive power range

In addition to the capability of operating within an extended voltage bandwidth around unity, modern wind plants are required to offer advanced reactive power and voltage control capabilities. The supplied reactive power should compensate for the reactive power loss and line charging inside the wind plant and up to the POI. It is often also required to regu-

late the POI voltage using dynamic reactive power in-feed, either automatically or in response to real-time instructions from the operator.

According to the British grid code, wind power plants must be capable of operating continuously at any point in the ranges illustrated in Figure 9. They must also be capable of continuous operation between a power factor of 0.95 lag and 0.95 lead when supplying rated MW.

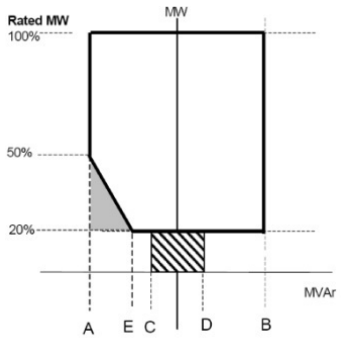

Point	Power factor / reactive power
A	0.95 lead at rated MW
B	0.95 lag at rated MW
C	Q = -5% of rated MW
D	Q = 5% of rated MW
E	Q = -12% of rated MW

Figure 9. Minimum requirements for reactive power range - British code [21].

Figure 10 shows the reactive power and power factor ranges specified in the Irish code [26].

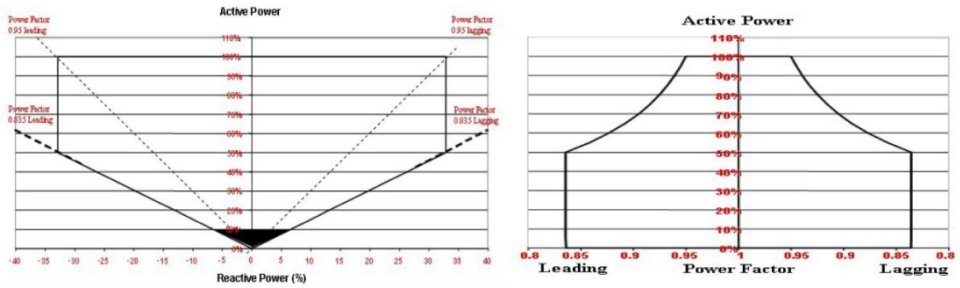

Figure 10. Requirements for reactive power capability of wind plants - Irish code [26].

Figure 11 shows the required static and dynamic reactive power ranges in the Canadian province of Alberta [19]. The requirement applies at the low-voltage side of the transmission step-up transformer. The dynamic capability is defined as the short-term reactive power response in a period of up to 1 second.

A supervisory control is normally present within a wind plant translating the reactive power or voltage demands at the connection point to operational set points for the individual WTGs. In some implementations, identical set points are dispatched to all turbines to keep

http://dx.doi.org/10.5772/51953

the design of the controller simple. In others, the set point is optimized for each individual turbine [6].

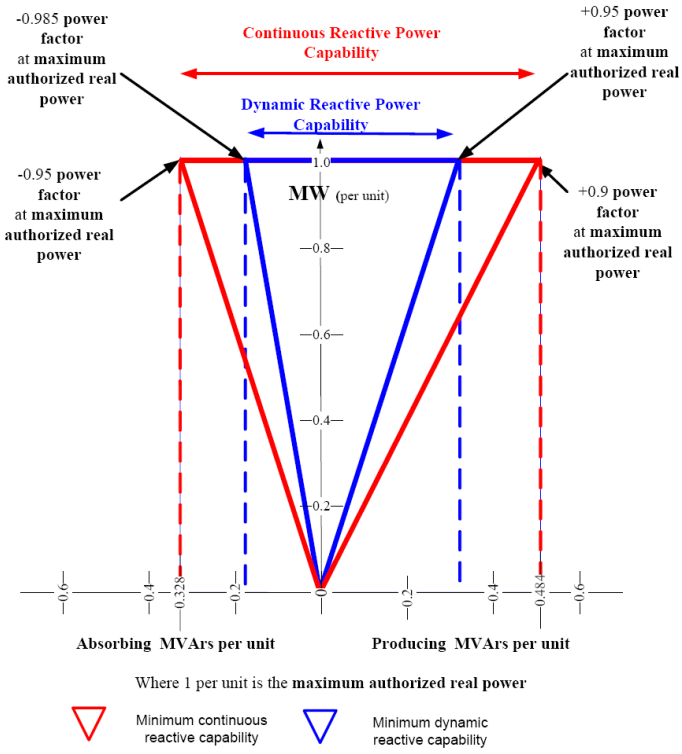

Figure 11. Requirements for reactive power capability of wind plants - AESO code [19].

Power flow calculations are performed to assess if the reactive power capabilities of the WTGs are enough to comply with the steady-state requirements. Although the collector system design work may be considered a separate activity, some iteration will usually be required. Transformers equipped with on-load tap changers are another system component that affects the voltage profile and reactive power flows. The speed of response of the tap changer, the size of the first step and those of subsequent steps are all relevant parameters that need to be optimized for a cost-efficient, grid code compliant wind plant-level control scheme.

Reactive power compensation equipment, such as static var compensators (SVCs) and static compensators (STATCOMs), may also help compliance with grid codes when there is little wind, or when the requirement is beyond the capability range of the WTGs. In offshore wind plants with lengthy submarine ac cables, high charging currents necessitate the injection of a large amount of apparent power. This greatly reduces the reactive power supply

and absorption margin at the on-shore POI under different operating conditions. Therefore, reactive power compensation elements are often needed in these cases at the high-voltage level.

1.5.2. Voltage regulation & dynamic response

Although the main focus is on the quasi-steady-state behavior of the wind plant, system operators also impose certain dynamic performance criteria. In general, there are three common reactive power control modes for wind plants:

1. Fixed reactive power mode, in which a set point reactive power flow is maintained as specified by the system operator
2. Fixed power factor mode, in which the ratio between active and reactive power is maintained. This mode is common for small wind plants or those connected to the distribution system and operated as distributed generation (DG)
3. Voltage control mode, in which the wind plant contributes reactive power to regulate the voltage magnitude at the connection point.

Voltage control is gaining more and more popularity, especially for large wind plants. For instance, wind plants in the UK connected to a line rated 33kV or above are required to contribute to voltage control with a predefined reactive power–voltage droop characteristic, as shown in Figure 12. If a sudden voltage change occurs in the grid, the wind plant is required to start reacting no later than 200 ms after the change and should provide at least 90% of the required reactive power within 1 second. After 2 seconds from the event, the oscillations in the reactive power output may be no larger than ±5% of the target value.

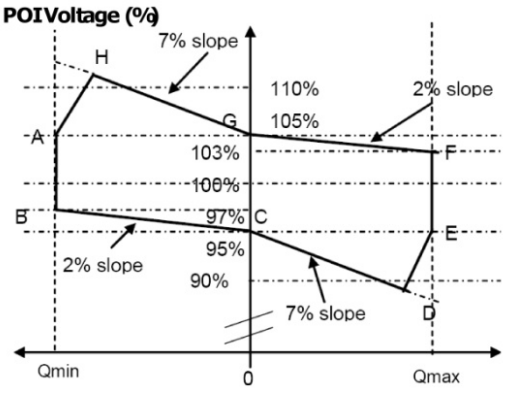

Figure 12. Voltage-reactive power envelope for voltage levels >33kV - British code [21].

The code of the Canadian province of Alberta requires from wind plants to have a continuously acting, closed-loop control voltage regulation system capable of responding to any

http://dx.doi.org/10.5772/51953

voltage set-point sent by the system operator between 95% and 105% of rated voltage. The system must also be able to regulate voltage according to an adjustable droop from 0 to 10%. The dynamic response must be such that a change in reactive power will achieve 95% of its final value no sooner than 0.1 second and no later than 1 second following a step change in voltage [18]. Specific dynamic criteria such as these are becoming more common together with the droop characteristics and steady-state specifications.

1.6. Voltage disturbance requirements

Unsurprisingly, special emphasis is placed in grid codes on the ability of wind plants to survive grid faults and contribute to supporting the grid during and after such events.

1.6.1. Fault ride-through

Although fault ride-through (FRT) profiles for WTGs were introduced more than 15 years ago, the discussions on how they should be established, interpreted and applied in practice are still hot. Early FRT requirements were mere adaptations from those of conventional generators and consisted of specifications of minimum connection durations as a function of voltage drop/rise magnitude. Contemporary provisions evolved to different levels of complexity and degrees of flexibility.

Figure 13 shows the FRT requirements in Québec [23]. Wind power plantss are also required to remain in service up to 0.15 seconds for double-phase-to-ground faults and 0.30 seconds for single-phase-to-ground faults.

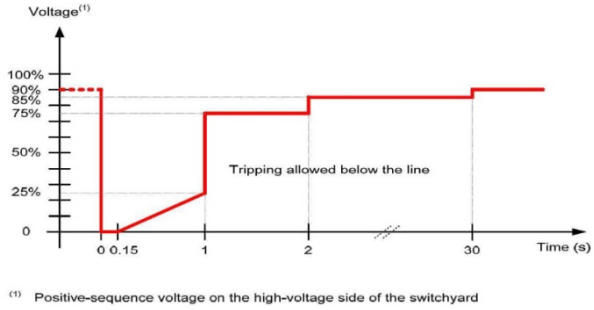

Over-voltage (p.u.)[1]	Minimum Duration (seconds)
1.00 ≤ V ≤ 1.10	Extended[2]
1.10 ≤ V ≤ 1.15	300.0
1.15 ≤ V ≤ 1.20	30.00
1.20 ≤ V ≤ 1.25	2.000
1.25 ≤ V ≤ 1.40[3]	0.100
V > 1.40[3]	0.033

Figure 13. FRT capability required from wind plants - HQTE code [23]; [1] Positive-sequence voltage on HV side of switchyard; [2] Up to hours, depending on time needed to bring grid voltage back to steady-state range; [3] Temporary blocking is allowed beyond 1.25p.u. but normal operation must resume once voltage drops back below 1.25p.u.

Figure 14 shows the FRT curve of one for the German codes [16]. Wind power plants must remain connected without instability above limit line 1 for all symmetrical or unsymmetrical voltage dips. Voltage drops within the area between limit lines 1 and 2 should not lead to disconnection, but short-time disconnection is allowed case of WTG instability. Disconnection is allowed below limit line 2.

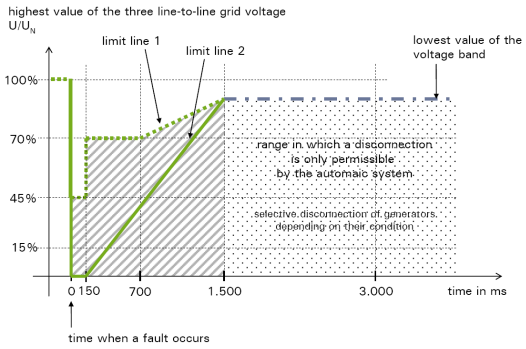

Figure 14. Low-voltage ride-through requirements for wind plants - German code [16].

The Australian grid code stipulates that wind plants must be capable of continuous uninterrupted operation in voltage transients caused by high speed auto-reclosing of transmission lines, irrespective of whether or not a fault is cleared during a reclosing sequence. Thus the wind power plant must be capable of riding through multiple faults as shown in Figure 15, which might be difficult for some FRT implementations due to excess stress on the drive-train of the WTG.

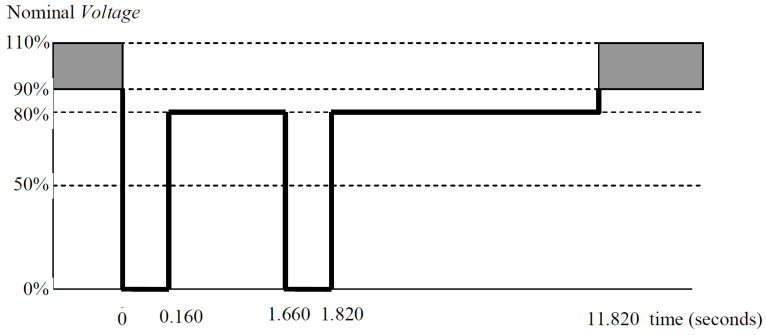

Figure 15. Low-voltage ride-through capability during auto-reclose operation - Western Power [27].

1.6.2. In-fault and post-fault requirements

In addition to remaining connected through the fault, some FRT provisions contain specifications for reactive current in-feed during the fault as well as precise criteria for active power recovery once the fault is cleared.

One German code [16] requires wind plants to support the grid voltage with additional reactive current in proportion to the voltage deviation, as shown in Figure 16. The in-feed must start within 20 msec of the occurrence of the voltage dip and must be maintained for a

http://dx.doi.org/10.5772/51953

further 500 milliseconds after the voltage returns to the 10% voltage dead band. Resynchronization must take place within up to 2 sec and active power must increase with a rate not less than 10% of rated power after fault clearance.

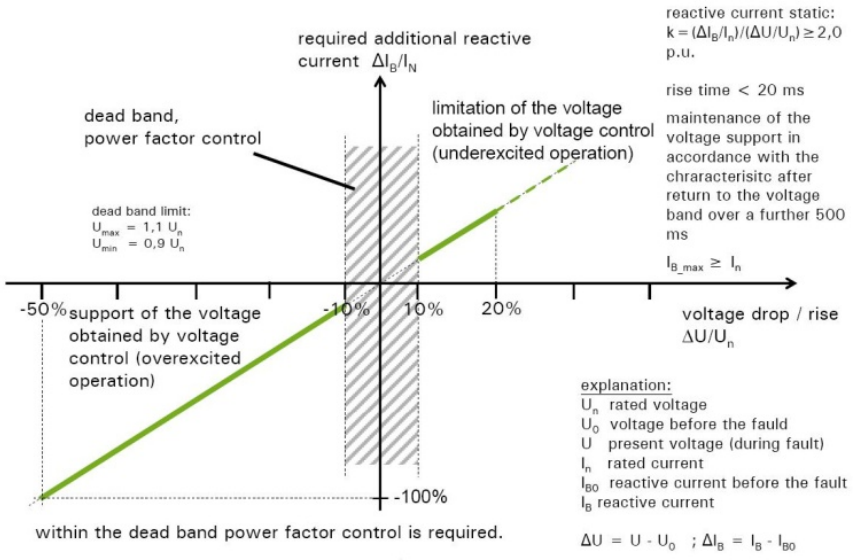

Figure 16. Required voltage support during disturbances in onshore wind plants - German codes [16].

Grid codes of UK and Ireland code [21] requires offshore wind power plants to provide active power output during voltage dips at least in proportion to the retained balanced voltage [26]. The Spanish code [25] has requirements for both active and reactive power consumption during a fault. Wind plants are not allowed to absorb active power during a balanced 3-phase fault or during the voltage recovery period after clearance. Absorption of active and reactive power is accepted for 150 msec interval after the beginning of the fault and 150 msec after clearance, as shown in Figure 17 (a). During the rest of the fault time, active power consumptions must be limited to 10% of the plant rated power. Within the 150 msec, the reactive power injection should be controlled as shown in Figure 17 (b).

Implementing the low-voltage ride-through in WTGs implies a proper management of the power being converted by the machine in the absence of the load or power sink provided by the grid [33]. This power needs to be curtailed, dissipated or stored, to avoid generator overspeeding. A number of technical possibilities are available: (a) acting on the blade capture rate by changing, for example, the blade angles, thus reducing the amount of wind power captured; (b) acting on the generator so that it no longer produces power and that the power does not flow from the stator into the grid; (c) dissipating the power produced by the generator, by means of resistances on the dc bus or using storage devices (seldom implemented). A combination of these solutions can be used concurrently.

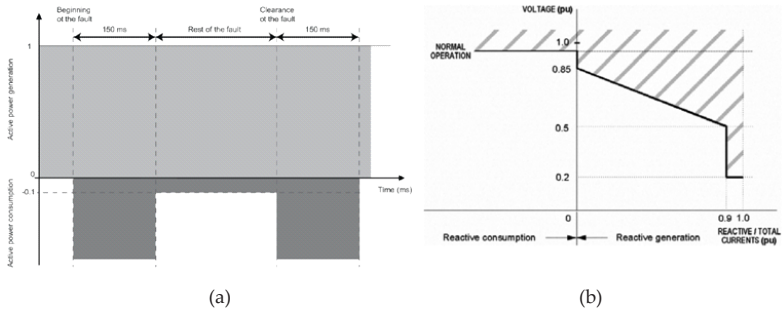

(a) (b)

Figure 17. Active power under balanced 3-phase faults - Spanish code [24].

1.7. Harmonic emissions of wind power plants

The influence of a wind power plant on the current/voltage harmonic distortion should be considered in the design process since all system operators have maximum allowed emission levels for single order and total harmonic distortion at the connection point. The three sources contributing to the harmonic levels in a wind power plant are [8]:

1. the wind turbine generators
2. the dynamic reactive power compensation equipment (if any)
3. the collector system feeders, and
4. the electric grid itself

The contribution of each of these four sources to the total harmonic voltage distortion can be determined separately but should not be added arithmetically because they are not in phase. Therefore, summation laws, such as those of the IEC 61400-21 standard, can be applied for a more realistic account for angular differences and randomness of the harmonics.

Reactive power compensation elements will also affect the harmonic performance. SVCs and STATCOMs inject harmonics into the grid just as the wind turbines do. The collector system cables can also act as amplifiers for the harmonic emissions, especially in offshore wind power plants. The long ac submarine cables have frequency characteristics that could trigger critical resonances with the power system at relatively low frequencies.

Adequate modeling of the grid impedance as seen from the wind plant is also very important to quantify the grid's contribution to the harmonic emissions. The grid's impedance is not static; it's rather a function of the switching state and loading level in the grid. The dominant approach is to obtain (through simulation) the network impedance for a wind range of system states and plot them as a set of impedance loci in the complex impedance (R–X) plane. An example of this plot is given in Figure 18. For each harmonic frequency corresponds an R–X plane, where the points p_1 through p_4 are usually fixed whereas Z_{max} is different for each harmonic order.

http://dx.doi.org/10.5772/51953

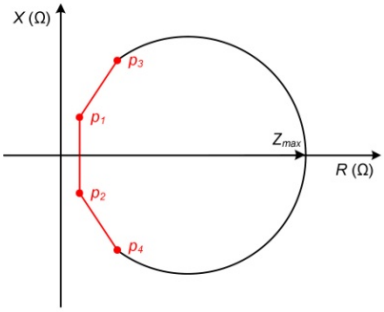

Harmonic	p_1 (Ω)	p_2 (Ω)	p_3 (Ω)	p_4 (Ω)	Z_{max} (Ω)
2					
3					
4					
. . .					
50					

Figure 18. Typical impedance plane as provided by network operators.

The wind plant's contribution to the harmonic voltage distortion at the POI has to be determined by assuming the worst-case network impedance in terms of resonances, which is generally different from the value resulting in the highest wind turbine contribution. If the harmonic performance analysis indicates that emission limits are likely to be exceeded, mitigation measures must be carried out. In order to mitigate the problem at the WTG level, some vendors equip their turbines with specific control schemes whose objective is to displace the phase angle between turbines to minimize the distortion at the connection point. At the wind plant level, one or more filters can typically be added to the design to diminish the emission at the most critical harmonic frequencies.

1.8. Other interconnection concerns

1.8.1. Power system stabilizers

Some of the recent grid codes include references to the capability of wind power plants in contributing to power oscillation damping in the grid through power system stabilizers (PSS). The grid code of HQTE, for example, stipulates that wind plants must be designed and built so that they can be equipped with a stabilizer in case it was imposed later during the lifetime of the wind power plant.

In synchronous generators, PSSs are used to damp oscillations arising from interactions between generators in a power plant, generators and the network and between generation areas. These functions are implemented using a supplementary control loop acting on the generator excitation system or voltage regulator. Damping is achieved through modulation of the reactive power produced by the generator. Modulating the real power flow through the governor would be slow with cost impacts on the turbine design and performance. However this is easier with wind power plants. The active and reactive power can be modulated independently by means of two separate supplementary control loops on the power converter regulator [48]-[50]. In the case of a DFIG, the control of higher frequency oscilla-

tions is limited by the rating of the rotor side converter, however, in the case of full converters, the control range can be significantly wider and the control can be made more effective.

There are options for implementing and triggering PSS functions in wind plants. One of them is based on the frequency deviation. Studies were carried out to demonstrate that both active and reactive power control could be used effectively to damp inter-machine oscillations and to investigate the impact of the wind plant location on the damping effectiveness [33], [48]. It was found that, in general, active power control is less dependent on location, but still more effective when the point of POI of the wind plant was located close to a synchronous generator plant.

1.8.2. Operational monitoring & communication

Wind plants are required to send a wide range of real-time data points to the control and dispatch centers of the grid operator. These include status indications and measurements collected through the supervisory control and data acquisition (SCADA) system. The data points include:

- electrical measurements the at POI and/or collector system feeders, including: phase and line voltages and currents, actual and available MW and Mvar outputs, and average MW.hr yields
- operating status signals, including: transformer tap positions, status of dynamic compensation systems, and the action of main switchgear and protection systems
- meteorological data at the wind farm, including: wind speed and direction at individual turbines, ambient temperature, atmospheric pressure, and precipitation.

Increasingly, the real-time (electrical and meteorological) data is being used by grid operators/planners for wind power forecasting. In one example, the New York Independent System Operator (NYISO) has developed a program that integrates wind forecast into the real-time dispatch [32]. NYISO uses its wind forecast to predict the output level over the next hour, broken up into 5-minute time steps. At each time step, NYISO determines the output level at which the wind plant is economic to operate by using an economic offer curve supplied by the wind plant. If the wind plant is economic at an output level lower than the forecast level, NYISO will send a curtailment signal to commanding the wind plant to reduce its output. In China, the National Electric Power Dispatching and Communication Center (NEPDCC) uses the real-time wind power operation information from the different regional and provincial grids in China to perform its online transmission reliability and generation adequacy studies [10].

1.9. Grid compliance validation

Studies are performed to investigate the impact of any the new generation added to the grid. The connection of a new wind power plant will be authorized only if the performed connection impact assessments and associated tests show that the integration of new generation does not lead to a deterioration of the reliability and operational security of the system.

http://dx.doi.org/10.5772/51953

1.9.1. System impact studies

In general, the studies performed for the connection of wind plants are similar to those for a conventional thermal or hydroelectric plant. The purpose of these studies is to verify that the coordinated operation of all the units within the plant complies with the general and project-specific requirements stipulated by the grid operator. Those studies typically include [8]:

- Power flow studies to see the impact of the wind plant integration on system steady-state flows, voltages profiles, and transfer capabilities
- Contingency analysis to see the behavior of the wind plant during grid events that involve the loss of transmission circuits, transformers, or other generators so as to ensure that post-contingency flows and voltages are within their respective limits
- Low-voltage ride-through analysis to show compliance with the required durations and fault severities
- Short-circuit studies to ensure that the new plant does not cause over-duty of breakers or other equipment in nearby substations
- Dynamic studies to verify that the wind plant has enough static/dynamic reactive power to meet the requirements of voltage control
- Transient stability analysis to test the response of the wind plant and nearby system to faults occurring on the power system and to ensure that generation remains on synchronism and performs in an acceptable manner.
- Subsynchronous control instability studies addressing the interaction of wind turbines and their control systems with series-compensated lines on the transmission grid
- Load rejection study to evaluate the impact on the wind plant in ac interconnections
- Power quality studies, including harmonic and flicker analysis to determine the potential impact of wind fluctuations on the voltages at nearby substations and load centers.

1.9.2. Wind generator models

System planners and operators use simulations to assess the potential impact of contingency scenarios on system performance and to assess the ability of the power system to withstand such events while remaining stable and intact. As discussed in Sections 1.3–1.8, the wind plant control is composed of several levels with different response characteristics, including the WTGs, wind plant controller, reactive power compensation equipment, and on-load tap changers. Thus, it can be quite challenging to design a collective control scheme for the wind plant to meet the required dynamic response at the POI under all operating conditions. This is typically examined in transient stability studies, where all relevant components and their control loops are modeled. For this type of study, generic simulation models often do not exhibit the necessary level of precision. Thus user-written, validated models are generally needed.

1.9.3. Grid connection testing

Passing the field validation tests is a prerequisite for the permission of interconnection of some grid operators. These tests are performed in order to:

- Demonstrate that the overall wind plant and its constituting elements, including the WTGs, compensating equipment, and substation transformer meet the technical requirements of the grid operator
- Validate the simulation models and the associated parameters by comparing the model behavior to the field measurements.

Figure 19 shows the main areas of wind power plant and wind turbine testing. Type tests are tests of representative equipment performed by the manufacturer in the presence of third party certifiers. The intent is to demonstrate that a particular equipment design exhibits its specific performance that can be generalized to all other equipment of that same design [33]. These include validations of the power performance, load calculations, noise levels, and voltage/frequency operation ranges. Long-term harmonic measurements are also performed to establish the harmonic emission spectrum. These measurements are generally repeated for each wind plant at the POI to account for the emissions of auxiliary equipment and the amplifications caused by the collector system and the grid itself.

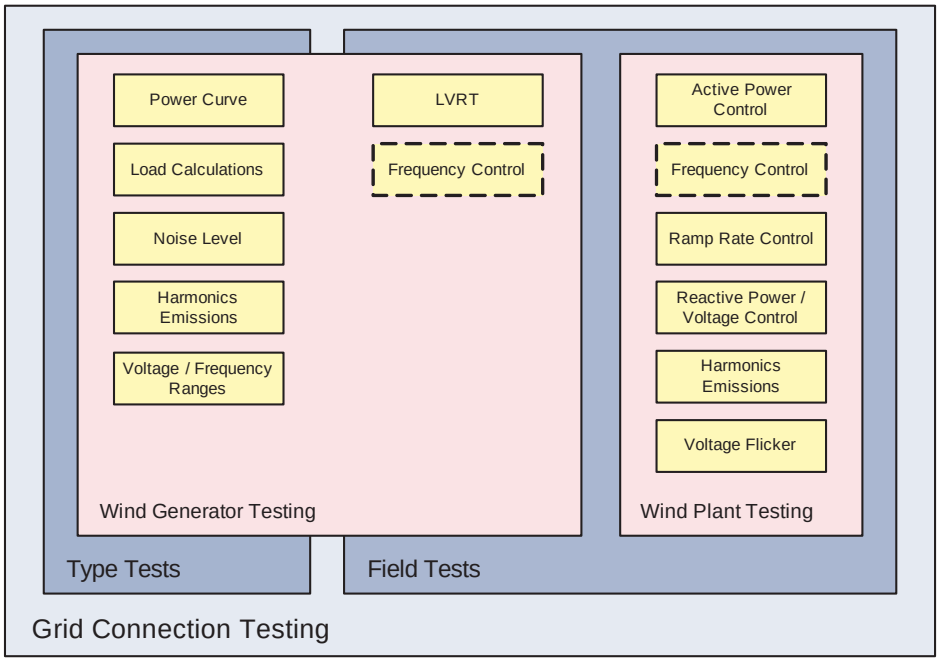

Figure 19. Grid connection tests of wind plants and wind turbine generators.

http://dx.doi.org/10.5772/51953

Other wind plant field tests include active power and ramp rate control. Depending on the approach of the grid operator, frequency control capabilities (including inertia control and over-frequency response) are either tested at the WTG level (e.g. HQTE) or wind plant level (e.g. UK). The reactive power range and voltage control are also tested to verify the capability of the central wind plant controller and any compensation equipment to respond to voltage deviations as quickly and sufficiently as required.

The data gathered through the online monitoring systems during the life-time of wind plants is also used for performance evaluation. This data, including snapshots of the wind plant behavior taken during external and unscheduled events (such as disturbances or large wind changes) is particularly useful in fine-tuning the wind plant parameters for optimal grid compatibility. The large-scale deployment of phasor measurement units (PMU) by system operators would also open the door for a variety of advanced monitoring and control applications.

1.10. Chapter summary

As grid operators worldwide continue to face a rapid growth of the installed capacity of wind power, the following key items should be observed in order to be able to accommodate high penetration levels while maintaining the same level of operational security and reliability:

- Clearer grid codes and standards addressing system issues such as transient stability, voltage collapse, and reactive power support
- Better market practices employing different scheduling periods and incorporating wind power forecasts
- Enhanced interconnections among generation areas with transmission upgrades and optimization of grid utilization
- Wider balance areas and new power exchange mechanisms
- Increased system flexibility through faster response from conventional generation, better demand-side management, and intelligent incorporation of storage technologies
- Improved system operational tools and models for more complex power systems with high wind penetration.

Author details

Samer El Itani[1] and Géza Joós[2]

1 Grid Integration & Electrical Modeling, REpower Systems Inc., Canada

2 Electrical & Computer Engineering, McGill University, Canada

References

[1] Global Wind Energy Council. (2012, February). Global Statistics 2011[Online]. Available: http://www.gwec.net/index.php?id=103&L=0%25252525B4.

[2] M. Ni and Z. Yang, "By leaps and bounds," *IEEE Power and Energy Magazine*, vol. 10, no. 2, pp. 37-43, 2012.

[3] I. M. Dudurych, A. Rogers, R. Aherne, L. Wang, F. Howell and X. Lin, "Safety in numbers," *IEEE Power and Energy Magazine*, vol. 10, no. 2, pp. 62-70, 2012.

[4] A. Tuohy and M. O'Malley. (2011, February). Pumped storage in systems with very high wind penetration. *Energy Policy* [Online]. Available: http://erc.ucd.ie/publications/.

[5] H. Holttinen, A. G. Orths, P. B. Eriksen, J. Hidalgo, A. Estanqeiro, F. Groome, Y. Coughlan, H. Neumann, B. Lange, F. van Hulle and I. Dudurych, "Currents of change," *IEEE Power and Energy Magazine*, vol. 9, no. 6, pp. 47-59, 2011.

[6] R. Piwko, P. Meibom, H. Holttinen, B. Shi, N. Miller, Y. Chi and W. Wang, "Penetrating insights," *IEEE Power and Energy Magazine*, vol. 10, no. 2, pp. 44-52, 2012.

[7] J. Kehler, "Wind Technical Rule" *AESO Market Service Stakeholder Session*, Jan. 2010.

[8] J. Feltes, R. Hendriks, S. Stapleton, R. Voelzke, B. Lam and N. Pfuntner, "Twixt land and sea," *IEEE Power and Energy Magazine*, vol. 10, no. 2, pp. 53-61, 2012.

[9] M. de la Torre, T. Domínguez, G. Juberías, E. Prieto and O. Alonso, "Operation of a power system with large integration of renewable energies," *in Proc. 7th Int. Workshop on Large-Scale Integration of Wind Power into Power Systems*, Madrid, Spain, May 26–27, 2008, pp. 13–18.

[10] J. Jiang, Y. Chi, H. Qin, Z. Pei, Q. Li, M. Liu, J. Bai, W. Wang, S. Feng, W. Kong, and Q. Wang, "Wind energy in China," *IEEE Power and Energy Magazine*, vol. 9, no. 6, pp. 36-46, 2011.

[11] M. Lauby, M. Ahlstrom, D. Brooks, S. Beuning, J. Caspary, W. Grant, B. Kirby, M. Milligan, M. O'Malley, M. Patel, R. Piwko, P. Pourbeik, D. Shirmohammadi and J. Smith, "Balancing act," *IEEE Power and Energy Magazine*, vol. 9, no. 6, pp. 75-85, 2011.

[12] F. Van Hulle, P.W. Christensen, S. Seman and V. Schulz, "European grid code development – the road towards structural harmonization" *Proc. 9thInt. Workshop on Large-Scale Integration of Wind Power*, Canada, Oct. 2010.

[13] A. Nourai and D. Kearns, "Batteries Included," *IEEE Power and Energy Magazine*, vol. 8, no. 2, pp. 49-54, 2010.

[14] *Sempra BP Wind to Develop Hawaii Wind Project with Wind Storage*, Connected, The Utility Variable Generation Integration Group (UVIG), vol. 6, no.5, pp. 4, 2012.

[15] *ENTSO-E Draft Network Code for Requirements for Grid Connection applicable to all Generators*, ENTSO-E AISBL, Brussels, Jan. 2012.

[16] *Grid Connection Code–Extra High Voltage*, Transpower stromübertragungs GmbH, Bayreuth, Germany, April 2009.

[17] *Requirements for Offshore Grid Connections in The Transpower Grid*, E.ON Netz GmbH, Bayreuth, Germany, April 2010.

[18] *Standard PRC-006-NPCC-1 Automatic Underfrequency Load Shedding*, Northeast Power Coordinating Council Inc., New York, USA, Sept. 2012.

[19] *ISO Rules, Section 502.1 – Wind Aggregated Generating Facilities*, Alberta Electric System Operator, Alberta, Canada, August 2011.

[20] *Nordic grid code*, Nordel, January 2007.

[21] *The Grid Code, Issue 4, Revision 10*, National Grid Electricity Transmission plc, UK, January 2012.

[22] National Grid Electricity Transmission plc. (2011). Frequency Response Technical Sub-Group Report, Version 1.0 [Online]. 34 pp. Available: http://www.nationalgrid.com/NR/rdonlyres/2AFD4C05-E169-4636-BF02-EDC67F80F9C2/50090/FRTSGGroupReport_Final.pdf

[23] *Transmission Provider Technical Requirements for the Connection of Power Plants to the Hydro-Quebec Transmission System*, Hydro-Québec TransÉnergie, February 2009.

[24] *60kV to 500kV Technical Interconnection Requirements for Power Generators*, BC Hydro, February 2012.

[25] *Procedimientos De Verificación, Validación Y Certificación De Los Requisitos Del Po 12.3 Sobre La Respuesta De Las Instalaciones Eólicas Y Fotovoltaicas Ante Huecos De Tensión, PO 12.3, Version 9*, Red Eléctrica de España (REE), Spain, May 2011.

[26] *Grid Code – Version 4.0*, EirGrid, Ireland, December 2011.

[27] *Technical Rules*, Western Power, Australia, December 2011.

[28] EirGrid (2010). All Island TSO Facilitation of Renewables Studies. [Online]. 77 pp. Available: http://www.eirgrid.com/media/FacilitationRenewablesFinalStudyReport.pdf

[29] IEA. (2011). Integration of Renewables—Status and Challenges in China [Online]. Available: http://www.iea.org/papers/2011/Integration_of_Renewables.pdf.

[30] U.S. Department of Energy. (2011, June). 2010 wind technologies market report. [Online]. Available: http://www1.eere.energy.gov/wind/pdfs/51783.pdf.

[31] J. Brisebois and N. Aubut, "Wind farm inertia emulation to fulfill Hydro-Québec's specific need," *2011 Power & Energy Society General Meeting*, Detroit, USA, 24-29 July 2011.

[32] M. Ahlstrom, J. Blatchford, M. Davis, J. Duchesne, D. Edelson, U. Focken, D. Lew, C. Loutan, D. Maggio, M. Marquis, M. McMullen, K. Parks, K. Schuyler, J. Sharp and D. Souder, "Atmospheric pressure," *IEEE Power and Energy Magazine*, vol. 9, no. 6, pp. 97-107, 2011.

[33] S. El Itani and G. Joós, "Wind turbine generator controls: meeting present and future grid code requirements" *2012 CIGRE Session*, Paris, August 2012.

[34] R. Zavadil, N. Miller, A. Ellis, E. Muljadi, P. Pourbeik, S. Saylors, R. Nelson, G. Irwin, M. Sahni and D. Muthumuni, "Models for change," *IEEE Power and Energy Magazine*, vol. 9, no. 6, pp. 86-96, 2011.

[35] WECC REMTF. (2010, Aug.). WECC Wind Power Plant Dynamic Modeling Guide [Online]. Available: www.wecc.biz.

[36] Working Group Joint Report—WECC Working Group on Dynamic Performance of Wind Power Generation and IEEE Working Group on Dynamic Performance of Wind Power Generation, "Description and technical specifications for generic WTG models—A status report," *In Proc. IEEE PES PSCE*, Mar. 2011.

[37] M. Asmine; J. Brochu; J. Fortmann, R. Gagnon, Y. Kazachkov, C. E. Langlois, C. Larose, E. Muljadi, J. MacDowell, P. Pourbeik, S. A. Seman and K. Wiens, "Model validation for wind turbine generator models," *Inst. Elect. Eng.Trans. Power Syst.*, to be published.

[38] Lawrence Berkeley National Laboratory, "Use of frequency response metrics to assess the planning and operating requirements for reliable integration of variable renewable generation," Lawrence Berkeley National Lab, Berkeley, CA, LBNL-4142E, Dec. 2010.

[39] M. Dernbach, D. Bagusche and S. Schrader, "Frequency control in Québec with DFIG wind turbines," *9th International Workshop on Large-Scale Integration of Wind Power into Power Systems*, Québec City, Canada, October 2010.

[40] S. El Itani, M. Dernbach and M. Kosbab, "Supplementary grid functions in DFIG wind turbines to meet Québec's frequency requirements," *2012 CIGRÉ Canada Conference*, Montréal, Canada, October 2012.

[41] N. Miller, K. Clark and M. Shao, "Impact of frequency responsive wind plant controls on grid performance," *9th International Workshop on Large-Scale Integration of Wind Power into Power Systems 2010*, Québec City, Canada, October 2010.

[42] L.-R. Chang-Chien and Y.-C. Yin, "Strategies for operating wind power in a similar manner of conventional power plant," *IEEE Trans. Energy Conv.*, vol. 24, no. 4, pp. 926-934, December 2009.

[43] S. El Itani, U. Annakkage and G. Joós "Short-Term Frequency Support utilizing Inertial Response of DFIG Wind Turbines," *In Proc. 2011 IEEE Power & Energy Society General Meeting*, Detroit, USA, July 2011.

http://dx.doi.org/10.5772/51953

[44] R. Doherty, A. Mullane, G. Nolan, D.J. Burke, A. Bryson and M. O'Malley, "An assessment of the impact of wind generation on system frequency control," *IEEE Trans. Power Syst.*, vol. 25, no. 1, pp.452-460, February 2010.

[45] D. Gautam, L. Goel, R. Ayyanar, V. Vittal and T. Harbour, "Control strategy to mitigate the impact of reduced inertia due to doubly-fed induction generators on large power systems," *IEEE Trans. Power Syst.*, vol. 26, no. 1, pp. 214-224, February 2011.

[46] N. Ullah, T., Thiringer and D. Karlsson, "Temporary primary frequency control support by variable speed wind turbines — Potential and applications" *IEEE Trans. Power Syst.*, vol. 23, pp. 601-612, 2008.

[47] P.W. Christensen and G.C. Tarnowski, "Inertia for Wind Power Plants – State of The Art Review – Year 2011," *10th International Workshop on Large-Scale Integration of Wind Power into Power Systems*, Aarhus, Denmark, November 2011.

[48] C. Martinez, G. Joós, and B.T. Ooi, "Power System Stabilizers in Variable Speed Wind Farms" *In Proc. 2009 IEEE Power & Energy Society General Meeting*, Calgary, Canada, July 2009.

[49] I. Kamwa, R. Grondin and G. Trudel, "IEEE PSS2B versus PSS4B: the limits of performance of modern power system stabilizers" *IEEE Trans. Power Syst.*, vol. 20, pp. 903-915, 2005.

[50] F. Hughes, O. Anaya-Lara, N. Jenkins and G. Strbac, "A power system stabilizer for DFIG-based wind generation" *IEEE Trans. Power Syst.*, vol. 21, pp. 763-772, 2006.